DOCTOR OF PHILOSOPHY

High Contrast Imaging: Exoplanet and Low Stellar Mass Populations

Durkan, Stephen

Award date:
2018

Awarding institution:
Queen's University Belfast

High Contrast Imaging: Exoplanet and Low Stellar Mass Populations

A thesis submitted for the degree of
Doctor of Philosophy

by

Stephen Durkan, MSci
(Queen's University Belfast, 2014)

Faculty of Engineering and Physical Sciences

School of Mathematics and Physics
Queen's University Belfast
Belfast, Ireland

April 2018

Acknowledgements

Firstly, I would like to thank Dr. Markus Janson, I could not have asked for a better supervisor. Thank you Markus, for your invaluable guidance and support and always making time for me despite your own commitments in Stockholm. Thank you for giving me the opportunities to visit some of the most amazing places in the world, they're experiences I'll never forget. You're surprise visit to congratulate me on passing my Viva really sums up how kind and how much of a friend you are. It was a privilege to be your first PhD student.

I also want to thank Dr. Chris Watson. Thanks Chris, for your continual help and taking me under your wing despite your insane workload and having your own PhD students. Your guidance and advice helped immensely in the writing of this thesis. Thank you to all the members of ARC for creating a great work environment, especially my fellow PhD students.

To my Mummy, I owe you more than I can ever repay. You're the bravest, most selfless person I know. I don't know how you do it. Thanks so much for all you've done and continue do for me. I wouldn't be where I am without you. To my Daddy, you shaped me into the person I am today and still continue to influence me. You inspired my love for nature and the Universe through our many adventures. I'll never forget our time together.

I want to thank all the other amazing women that I'm so lucky to have in my life. To Pauline, you've been so much more than a grandparent, you've been a second parent to me. I'm eternally grateful for your love and support. You're an inspiration, always putting others before yourself. And thanks for the fortune you've spent lighting candles over the years. To Cait, this is as much your achievement as mine. I couldn't have done it and wouldn't have made it this far in life without you. You've always been there for me no matter what, constantly supporting and loving me. Thanks for being my best friend. I'm so proud of you and I'll be forever grateful for the amazing life you've made for us. To Shiv, thanks for our sneaky days off. They gave me much needed respite at times. Thanks for inspiring my own inquisitiveness through your amazing curiosity.

Abstract

In this thesis I report the results of a re-analysis of archival Spitzer IRAC direct imaging surveys encompassing 121 nearby stars. While the small size of Spitzer provides a lower resolution than 8 m class AO-assisted ground-based telescopes, which have been used for constraining the frequency of $0.5 - 13$ M_J planets at separations of $10 - 10^2$ AU, its exquisite infrared sensitivity provides the ability to place unmatched constraints on the planetary populations at wider separations. Sophisticated high-contrast techniques are applied to the sample in order to remove the stellar point-spread function and to open up sensitivity to planetary mass companions down to $5''$ separations. This enables sensitivity to $0.5 - 13$ M_J planets at physical separations on the order of $10^2 - 10^3$ AU, allowing a parameter space to be probed that has not previously been systematically explored to any similar degree of sensitivity. Based on a colour and proper motion analysis, no planetary detections are recorded. Exploiting this enhanced survey sensitivity with Bayesian analysis, the population of $0.5 - 13$ M_J planets at separations of $100 - 1000$ AU is constrained with an upper frequency limit of 9% (at 95% confidence).

I also report the results of a FEROS radial velocity survey of low-mass binaries, the majority of which are high probability young moving group (YMG) members. YMGs are prime targets for exoplanet imaging due to their youth ($\sim 10 - 100$ Myr), as any potential orbiting planet will be equivalently young and therefore luminous. Lucky imaging multiplicity surveys have recently identified hundreds of new YMG low-mass binaries, where a subsample of M-dwarf multiples have estimated orbital periods less than 50 years. Radial velocity measurements for 29 such targets are presented here, complementing the astrometric data. This will allow enhanced orbital determinations and precise dynamical masses to be derived in a shorter timeframe than possible with astrometric monitoring alone. Derived dynamical masses will enable binary systems to be isochronally dated to a good level of precision. This dating can then potentially be applied to the YMG of which they are members, for improved age constraints on the full population of stars. Improved YMG age constraints are critical for estimating the mass or initial entropy of imaged planets using mass-luminosity evolutionary models.

Contents

List of Figures

List of Tables

Publications

Durkan, S., Janson, M., Ciceri, S., Brandner, W., et al.
A Radial Velocity Survey of Spatially Resolved, Low Mass Binaries
2018 accepted to A&A

Durkan, S., Janson, M., Carson, J.
High Contrast Imaging with Spitzer: Constraining the Frequency of Giant Planets out to 1000 au Separations
2016 ApJ 824 58

Janson, M., **Durkan, S.,** Hippler, S., Dai, X., et al.
Binaries among low-mass stars in nearby young moving groups
2017 A&A 599 70

Rodet, L., Bonnefoy, M., **Durkan, S.**, Beust, H., et al.
Dynamical masses of M-dwarf binaries in young moving groups I - The case of TWA 22 and GJ 2060
2018 accepted to A&A

Calissendorff, P., Janson, M., Köhler, R., **Durkan, S.,** et al.
The discrepancy between dynamical and theoretical mass in the triplet-system 2MASS J10364483+1521394
2017 A&A 604 82

Henning, T., Mancini, L., Sarkis, P., Bakos. G.A., et al.
HATS-50b through HATS-53b: four transiting hot Jupiters orbiting G-type stars discovered by the HATSouth survey
2018 accepted to AJ

Bento, J., Schmidt, B., Hartman, J.D., Bakos, G.A., et al.
HATS-22b, HATS-23b and HATS-24b: three new transiting super-Jupiters from the HATSouth project
2017 MNRAS 468 835

Chapter 1

Introduction

For centuries, philosophers and scientists alike have contemplated the existence of planets outside our solar system and wondered, could such worlds host extraterrestrial life? However, what do we understand by the term planet? An IAU resolution in 2006 adopted the following definition; a planet is a celestial body that is in orbit around the Sun, has sufficient mass so as to assume a hydrostatic equilibrium (spherical) shape under self-gravity, and has cleared the local neighbourhood around its orbit (Perryman, 2011). It would seem reasonable to adopt the same definition for an exoplanet, a planet outside our solar system, albeit that the body orbits a star other than the Sun.

However, this definition was brought into question with the discovery of the first exoplanet system. Wolszczan & Frail (1992) demonstrated that the timing variations in the pulsation period of the pulsar PSR 1257+12 were due to the gravitational influence of at least two terrestrial mass companions. Hence, the first exoplanet system discovered was around a stellar remnant. Subsequent exoplanet discoveries have revealed a diversity of companion masses and system architectures, and accompanied by an increasing brown dwarf population, have introduced ambiguity to the exoplanet definition. The IAU adjusted its working definition of a planet accordingly. It now defines a planet as a celestial body below the limiting mass for the onset of thermonuclear fusion of deuterium, $\sim$ 13 Jupiter masses (Burrows et al., 2001), that orbits a star or stellar remnant, with the previous caveat that the object must be massive enough to achieve hydrostatic equilibrium and have cleared out its local neighbourhood. Sub-stellar companions above the $\sim$ 13 Jupiter mass limit are therefore considered brown dwarfs. However, this upper mass limit is not a rigid boundary and the distinction between the exoplanet and brown dwarf populations can be blurred depending on the host star metallicity (Spiegel et al., 2011). It has

been argued (Basri & Brown, 2006) that mass limits could be dispensed of in favour of a definition based on a companions formation and evolutionary history, however, these mechanisms are still not well understood over the entire parameter space of the current exoplanet population.

Three years after the discovery of the PSR 1257+12 planetary system came the first confirmation of a planet orbiting a sun like star, 51 Peg b (Mayor & Queloz, 1995). However, this planet is in a configuration drastically different to anything in our own solar system, the gas giant has 0.47 Jupiter masses yet orbits its host star in ~ 4 days. The current exoplanet population is dominated by 51 Peg b analogues, gas giants with orbital separations much shorter than the Earth-Sun distance. The prevalence of these highly irradiated 'hot Jupiters' can be explained by the observational bias inherent in the most effective planet detection techniques. In fact, a statistical analysis of a population of bound microlensing discovered planets suggests that other planetary configurations are much more common throughout the galaxy (Cassan et al., 2012). In the orbital range of 0.5 - 10 AU, $52^{+22}_{-29}\%$ and $62^{+35}_{-37}\%$ of Milky Way stars host Neptune and super-Earth sized planets respectively, compared to $17^{+6}_{-9}\%$ of Jupiter hosting stars. Cassan et al. (2012) also find that on average each Milky Way star hosts $1.6^{+0.72}_{-0.89}$ planets in the 0.5 - 10 AU orbital range. These findings suggest that stars host planetary systems as a rule, rather than the exception, promising a population of billions of planetary systems waiting to be discovered and characterised.

As our technology and observational methods constantly advance, we continue to broaden our sensitivity to the full exoplanet population, facilitating the discovery of a broad diversity of planetary systems, enabling planet formation and evolutionary theories to be tested and constrained, and allowing for the potential to probe for extraterrestrial life.

In this Thesis I investigate the planetary population over a previously elusive parameter space, wide separations beyond 100 AU, through enhancing high contrast imaging capability from space. I perform a re-analysis of archival imaging surveys with increased sensitivity and present the first constraints on the planet population over separations of 100 - 1000 AU. In addition, I investigate a population of low mass M-dwarf binaries to derive isochronal age estimates that can then be applied to the full young moving group (YMG) of which they are members. Improved YMG ages are highly useful for a range of astrophysical purposes, in particular, for constraining

the properties of directly imaged planets. I present the results of a radial velocity survey for a sample of M-dwarf binaries, essential for a robust isochronal analysis of the components, and highlight individual survey discoveries. Finally, I demonstrate a preliminary isochronal analysis of the M-dwarf binary GJ 3305AB, a wide companion to the exoplanet host 51 Eri.

In the continuation of this chapter I introduce the main planetary detection techniques and give an overview of planet formation and evolution mechanisms. In Chapter 2 I give a more focused overview of the direct imaging method, highlighting discoveries and high contrast techniques. I then discuss current limitations in the imaging field, leading to the motivation behind my investigations.

1.1 Planet Detection Methods

To date (January 2018), the known exoplanet population consists of 3726 confirmed planets in 2792 planetary systems.[1] Planet detection is currently viable via several different methods, each sensitive to a specific parameter space of the exoplanet population and with their own individual benefits and constraints. Figure 1.1 displays the full exoplanet population as function of mass and orbital period, differentiating between planets discovered by separate detection methods. In the following subsections the four most effective detection methods will be discussed.

1.1.1 Radial Velocity

The radial velocity technique has played a pivotal role in shaping the field of exoplanet study. It enabled the confirmation of the first planet around a solar like star, 51 Peg b (Mayor & Queloz, 1995), galvanising the field, and to date is credited with the discovery of over 700 additional planets. This accounts for $\sim 20\%$ of the entire planet population, and it terms of sheer number of discoveries, the radial velocity technique is only surpassed by the transit method, largely due to the success of NASA's Kepler mission.

This technique exploits the motion of a host star around the common barycentre it shares with its planetary companion. As the companion orbits the common barycentre, the host star experiences a reflex motion about the same point. As the

[1]The Extrasolar Planets Encyclopaedia (Schneider et al., 2011)

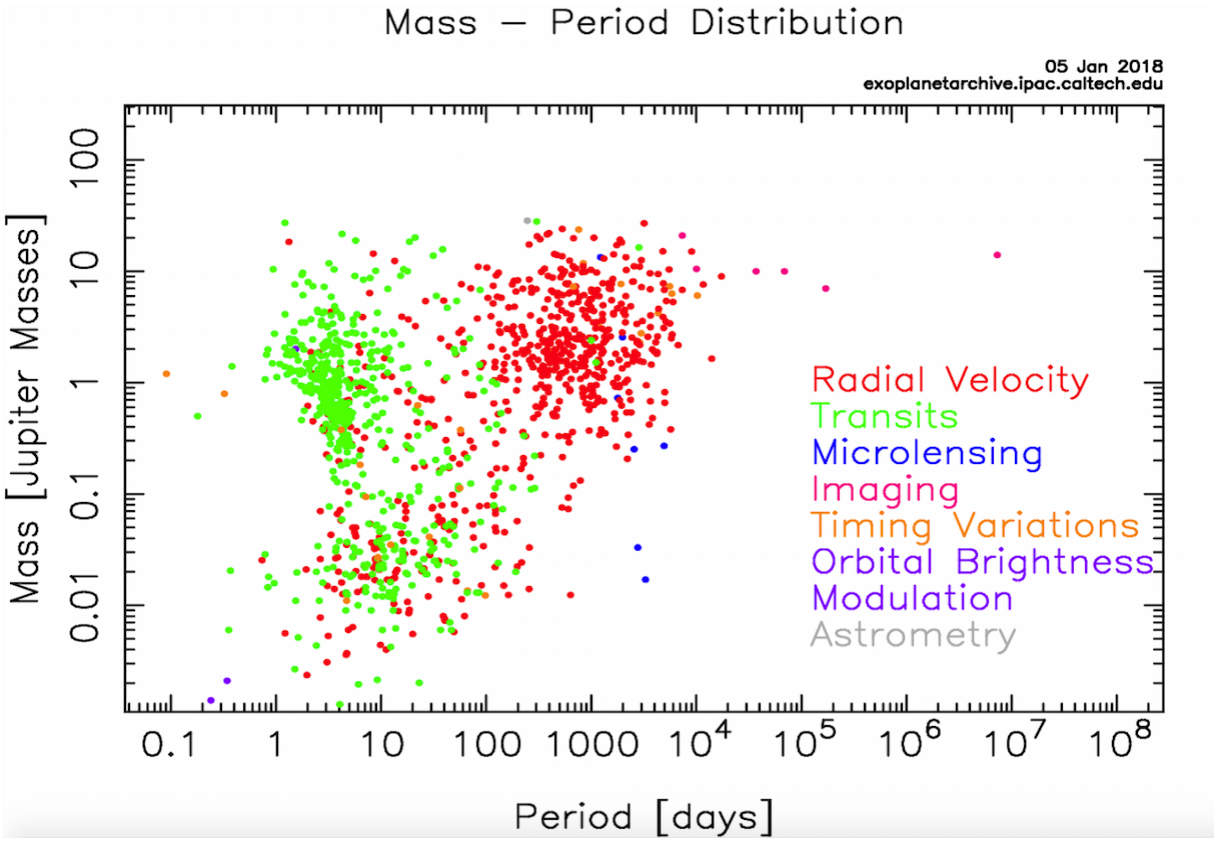

Figure 1.1: Mass - Period distribution of the currently confirmed exoplanet population. The colour code identifies the method used to detect each planet. The distribution of points highlight the parameter space each detection method is currently sensitive to, a result of the bias inherent in the individual techniques. Image: NASA Exoplanet Archive

star moves along the line of sight towards an observer, the stellar light is compressed, shifting to bluer wavelengths in the observer's frame. As the star then moves away from the observer the light is stretched, shifting to redder wavelengths. This phenomenon is known as the Doppler effect. Figure 1.2 depicts this effect. The shift in wavelength is directly related to the line-of-sight velocity, termed radial velocity, of the star v through the non-relativistic Doppler shift equation:

$$v = \frac{\lambda - \lambda_0}{\lambda_0} c \tag{1.1}$$

where c is the speed of light, λ is the observed wavelength, and λ_0 is the rest wavelength in the frame of the host star. Measuring this wavelength shift then allows us to calculate the radial velocity of a star, and record its periodic change across a full orbit. This is done using a spectrograph, an instrument that disperses incoming light

into its component wavelengths. Radial velocity studies typically use high resolution échelle spectrographs which are capable of resolving thousands of stellar absorption lines in the black-body continuum of dispersed light. The high resolution spectra can then be cross-correlated with a standard or theoretical template spectra with known radial velocity. The cross-correlation determines the shift in the stellar absorption lines with respect to the template lines, allowing the radial velocity to be calculated.

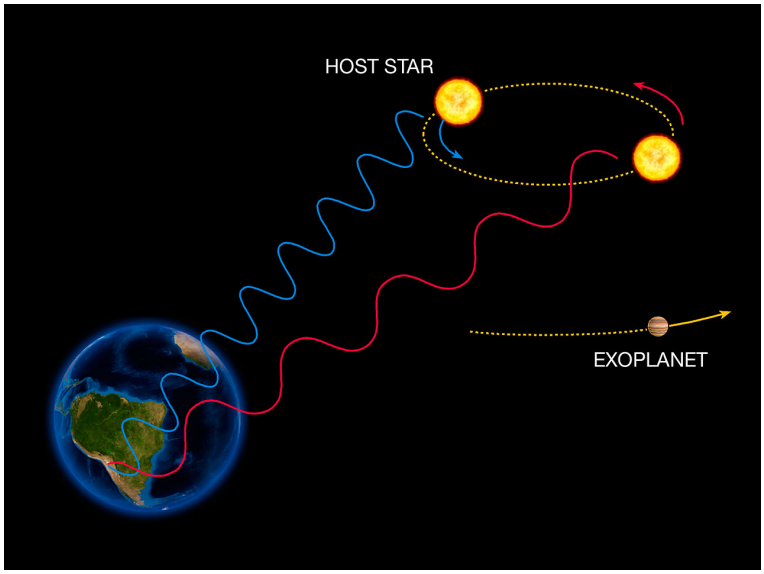

Figure 1.2: Planetary system displaying planet in orbit around system barycentre and the resultant reflex motion of the host star. Light is blue shifted as the host moves towards the observer, and red shifted as in moves away. Image: ESO Press Photo

Calculating the stellar radial velocity over multiple orbits with good phase coverage allows a radial velocity curve to be plotted. An example radial velocity curve is plotted in Figure 1.3. The curve's periodic signal relates to the period of the reflex motion of the star, and hence the orbital period of the planetary companion P. The planet eccentricity e and argument and time of periapsis can be determined from the specific shape of the radial velocity curve, with a zero eccentricity planet generating a purely sinusoidal signal. If the eccentricity is non-zero, the signal will differ from a pure sinusoid in a well-defined manner. The planet mass can then be determined from the semi-amplitude of the radial velocity signal K through the equation (Borucki & Summers, 1984):

$$K = \left(\frac{2\pi G}{P}\right)^{1/3} \frac{M_p \sin i}{(M_\star + M_p)^{2/3}} \frac{1}{(1-e)^{1/2}} \tag{1.2}$$

where M_p is the planetary mass, $M_\star$ is the stellar mass, P is the orbital period of the system, G is the gravitational constant and i is the inclination of the orbital axis with respect to the observer. Accounting for the various constants in Equation 1.3, for a zero eccentricity planet this reduces to:

$$K(ms^{-1}) = 28.4 \left(\frac{P}{1yr}\right)^{-1/3} \left(\frac{M_p \sin i}{M_{Jup}}\right) \left(\frac{M_\star}{M_\odot}\right)^{-2/3} \tag{1.3}$$

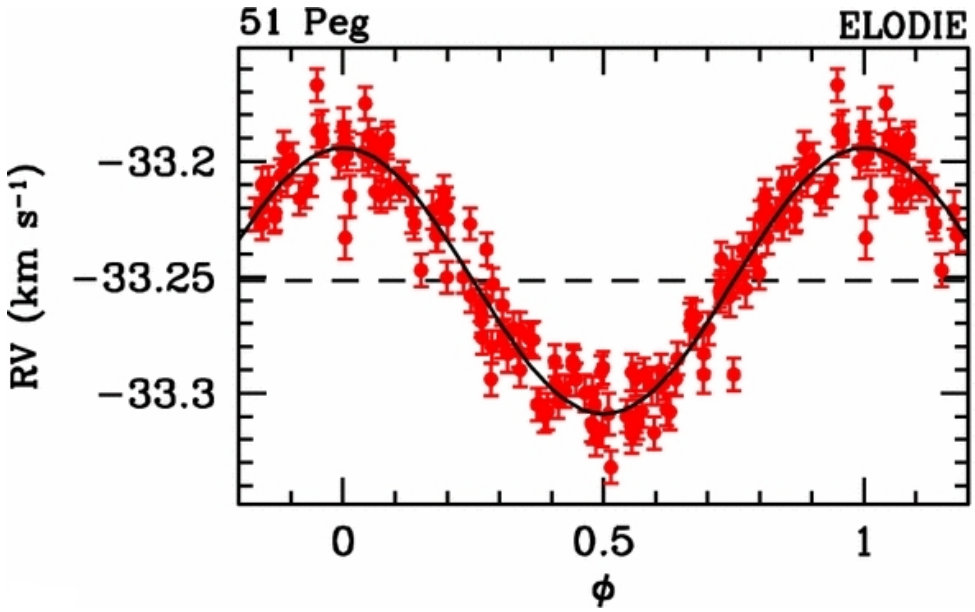

Figure 1.3: Phase-folded radial velocity curve of 51 Peg (Naef et al., 2004). Measurements taken with the ELODIE spectrograph. The orbit of 51 Peg b is almost perfectly circular and therefore the data is well fit with a pure sinusoid.

If the stellar mass is well-defined, $M_p \sin i$ can be determined. The $\sin i$ term accounts for the fact that it is the radial component of the stellar velocity that is measured and that the companions orbital plane is inclined with respect to an observer. If the orbital plane is edge-on, $i = 90°$, then the total stellar velocity due to reflex motion will be along the radial direction and $M_p \sin i$ will give the true companion mass. However, as the orbital plane approaches a face-on configuration, the majority of the stellar reflex motion becomes confined to the plane of the sky and only a small component of the stellar velocity will be along the radial direction. The

true companion mass will then be much greater than $M_p \sin i$. Therefore, in isolation the radial velocity technique only allows for the minimum companion mass to be measured. Complimentary techniques, such as the transit method, allow for the orbital inclination to be measured, breaking the degeneracy between inclination and companion mass, allowing the true mass to be determined.

As shown in Equation 1.3, the RV semi-amplitude is sensitive to planetary mass, orbital period and host star mass. More massive, shorter orbital period planets orbiting low-mass stars generate larger amplitude radial velocity signals, which are easier to detect. Hence, the radial velocity technique is biased to the discovery of such planets. This bias, along with current spectrograph limitations, explains the distribution of radial velocity discovered planets plotted in Figure 1.1. From Equation 1.3, a Jupiter analogue orbiting a solar mass star with a period of 12 years would produce a 12.4 ms^{-1} semi-amplitude. However, an Earth analogue with an orbital period of a year would produce just a $\sim$ 0.1 ms^{-1} semi-amplitude. Current high resolution spectrographs such as HARPS (Mayor et al., 2003) cannot resolve radial velocity shifts smaller than $\sim$ 0.5 ms^{-1} (e.g., Dumusque et al., 2012). Whilst this capability has enabled the discovery of hundreds of gas giants and allowed for the detection of terrestrial mass planets around low-mass stars (e.g., Anglada-Escudé et al., 2016), detection of earth analogues in the habitable zone around solar-like stars will only be possible with near-future spectrographs, such as ESPRESSO (Pepe et al., 2014) and the E-ELT's HIRES (Marconi et al., 2016), with radial velocity precisions ≤ 0.1 ms^{-1}.

1.1.2 Transits

The transit method of exoplanet detection came to fruition somewhat later than the radial velocity technique. The first detection of a transiting planet was HD 209458 b in 1999 (Charbonneau et al., 2000), although the companion was previously known through radial velocity discovery. It wasn't until several years later that OGLE-TR-56 b became the first exoplanet to be discovered via the transit method (Konacki et al., 2003). However, since then the population of planets discovered via transits has grown exponentially. This is due to the success of dedicated transit surveys performed from both the ground, e.g. WASP (Pollacco et al., 2006), and space, e.g. the Kepler mission (Koch et al., 2010). The number of confirmed planets discovered via the transit method now numbers $\sim$ 2800, $\sim$ 75% of the entire exoplanet population,

with thousands more transiting candidates awaiting confirmation.

This detection method exploits the orbital geometry of a planet with an inclination close to 90°. Such an orbit will ensure that the planet passes directly between its host star and an observer. As the planet passes in front of (transits) the star, it occults a fraction of the stellar disk, blocking a portion of the stellar emission from reaching an observer. The observer then notices a distinct decrease in the stellar flux, compared to the out of transit flux. This change in observed flux ΔF is given by the ratio of the total occulted area to the total area of the stellar disk, or more simply:

$$\Delta F = \left(\frac{R_p}{R_\star}\right)^2 \tag{1.4}$$

where R_p and $R_\star$ are the planetary and stellar radii respectively. Therefore, if the stellar radius is well-defined, the planetary radius can be calculated from the decrease in flux. Monitoring a transiting planet host photometrically across a sufficiently large fraction of a planet orbit allows for a transit light curve to be plotted, and ΔF to be measured. An example of a transit light curve is plotted in Figure 1.4.

The shape of the transit light curve is dependent on the impact factor, b, along with other factors such as stellar limb darkening; the drop in brightness from the centre of the star to its limb due to the effects of optical depth and decreasing temperature with radius. The impact factor is a dimensionless parameter defining the apparent separation between the planet centre and stellar equator at mid-transit. The impact parameter is dependent on the planets orbital inclination and semi-major axis, a, and is given by:

$$b = \frac{a \cos i}{R_\star} \tag{1.5}$$

Planets with a larger impact factor will experience a larger apparent separation between their centre and stellar equator. This results in a shallower, V - shaped transit due to longer ingress / egress times and the planet occulting a darker region of the star towards the limb. Fitting a transit model to the specific shape of the light

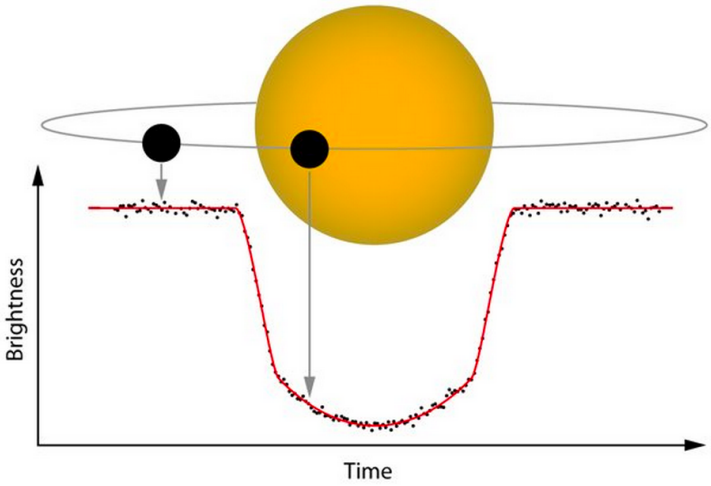

Figure 1.4: Light curve of the transiting planet WASP-10b (Johnson et al., 2009). The overlaid diagram displays the expected star-planet configuration over the transiting event. Out of transit WASP-10 displays near uniform brightness. Between the planet disc just touching the stellar limb until the full planet disc occults the star, the stellar brightness decreases steadily. This period is referred to as planetary ingress. The light curve then appears flat-bottomed until the planet disc just touches the edge of the opposite stellar limb. Brightness then increases steadily until the entire planet passes outside the stellar disc. This period is referred to as planetary egress. The flat-bottomed portion of the WASP-10b light curve appears slightly curved due to stellar limb darkening. Image: John Johnson, Harvard-Smithsonian Center for Astrophysics

curve allows for a model dependent estimate of the impact parameter. Using equation 1.5, the orbital inclination can then be calculated. This information allows the degeneracy between planetary mass and inclination inherent in RV data to be broken. The transit and RV methods therefore provide complimentary data that allow for the true planetary mass, and consequently bulk density, to be determined.

An impact factor of unity describes a transiting planet whose centre just touches the limb of the star at mid-transit. In such a scenario:

$$\cos i = \frac{\mathrm{R}_\star}{\mathrm{a}} \tag{1.6}$$

Therefore, for a grazing transit, where the limb edge of the planet disc just touches the limb of the star, the following equation must be valid:

$$\cos i \leq \frac{\mathrm{R}_\star + \mathrm{R}_\mathrm{p}}{\mathrm{a}} \tag{1.7}$$

And for a full transit, where the entire planet disc occults the star at mid-transit, the following equation must be valid:

$$\cos i \leq \frac{\mathrm{R}_\star - \mathrm{R}_\mathrm{p}}{\mathrm{a}} \tag{1.8}$$

For a randomly aligned planet on a circular orbit, and in the typical case where $R_p \ll R_\star$, the probability of a full or grazing transit, P, is then given by:

$$P \simeq 0.005 \left(\frac{R_\star}{R_\odot}\right)\left(\frac{1\,au}{a}\right) \tag{1.9}$$

From equations 1.4 and 1.9 the transit technique is clearly biased towards more massive planets with short orbital periods. This bias explains the distribution of transit discovered planets plotted in Figure 1.1. More massive planets with larger radii will produce larger dips in the stellar light curve, which are easier to detect. The same is true for planets around low-mass stars with smaller radii. This bias can be overcome as instrumentation improves, pushing sensitivity towards smaller, terrestrial planets. The bias towards shorter period planets is a result of the greater likelihood that a short separation planet will appear to transit its host. This bias is inherent in the transit method and cannot be overcome with increasing instrument capability. In addition, shorter period planets will generate multiple transit events over a short timescale, leading to a better assessment of false positive scenarios and an evaluation of the planet candidancy within a reasonable timeframe. A false positive scenario refers to an alternative event that causes a dip in the stellar light curve mimicking a planetary transit. Figure 1.5 highlights some potential false positive sources. The likelihood of these scenarios must be evaluated, from high-contrast imaging and radial velocity measurements in addition to multiple transit analysis, before a firm

planet detection can be confirmed.

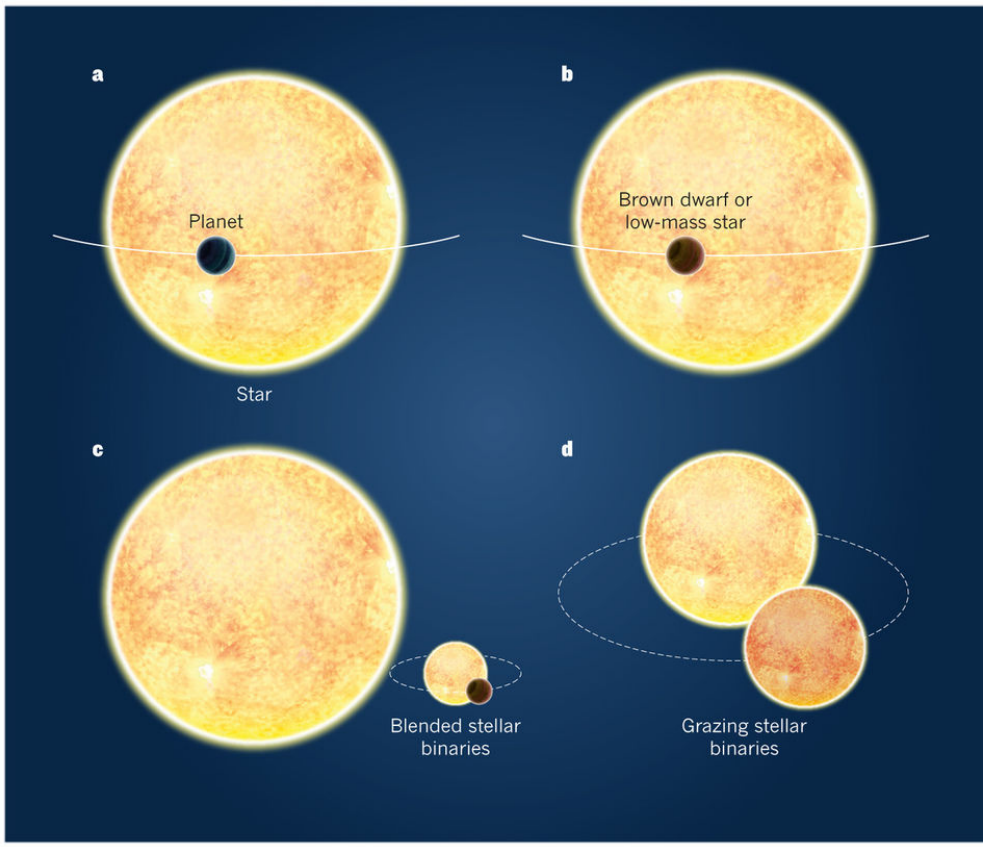

Figure 1.5: Planet transit and false positive sources. Panel a: Planetary transit. Panel b: Brown dwarf or low-mass stellar companion transit. Such bodies have similar radii to planetary objects, and therefore occult a similar fraction of the stellar disk, generating the same transit profile as a planetary companion. Panel c: Blended stellar binary. Background, or faint bound, eclipsing binaries blend with the target star due to limited telescope resolution. The deep eclipses of the binary become sufficiently diluted that they mimic shallower planetary transits. Panel d: Grazing stellar binary. These are binaries with orbital configurations such that one component only grazes the face of its companions disk, generating a shallow eclipse that mimics a planetary transit. Image : Cameron (2012)

From equation 1.4, a Jupiter sized planet around a sun like star will have a transit depth on the order of $\sim 10^{-2}$. Both ground and spaced based transit surveys have easily achieved photometric precision to this level, leading to a vast population of confirmed transiting gas giants. However, terrestrial sized planets around solar analogues generate a transit depth on the order of $\sim 10^{-5}$. Whilst this photometric precision is not currently feasible from the ground, it has been achieved from space with the

Kepler telescope, leading to the detection of Kepler-452b, a potentially rocky Earth sized planet ($R_p = 1.6\,R_\oplus$) within the habitable zone of a sun like star (Jenkins et al., 2015). However, a major drawback to the Kepler mission is that the typical target is quite faint (V > 12), limiting the possibility for RV follow up to determine a potential companions true nature and mass. This obstacle will be overcome with the launch of TESS (Ricker et al., 2014) in 2018 and PLATO 2.0 (Rauer et al., 2014) within the next decade, transiting survey missions with a photometric precision capable of detecting Earth-analogues orbiting bright ($4 \leq I_c \leq 13$ and $4 \leq V \leq 11$ respectively) stars, allowing for in depth candidate follow-up and characterisation.

1.1.3 Microlensing

Microlensing is a unique but relatively inefficient planet detection technique . Although the microlensing method was first conceived $\sim$ 50 years ago (Liebes, 1964), the first planet detection did not come until 2004 with the discovery of OGLE 2003-BLG-235 (Bond et al., 2004). Since then, microlensing has yielded a further $\sim$ 60 planet discoveries, accounting for $\sim$ 2% of the current exoplanet population.

This method exploits a gravitational lensing event, arising as a consequence of general relativity, to detect and characterise planetary companions. When a background source star passes behind a foreground lens star the trajectory of the source light is slightly bent as it passes through the gravitational potential of the lens. As the light bends around the lens, multiple distorted and highly magnified images of the source star are formed. These separate images cannot be resolved and are instead observed as a magnification of the source star, resulting in an increase in brightness by up to several orders of magnitude. Figure 1.6 shows an example light curve of a microlensing event. This magnification can last from weeks to months depending on the lens mass and the relative motion between the source and lens.

If the lens were to host a planetary companion with a projected separation that coincides with the position of a magnified image, the planet will act as a further lens, forming further unresolved images of the source, resulting in additional magnification. This effect is short lived, typically on the order of hours, and produces a sharp deviation in the microlensing light curve, referred to as a caustic event. An example caustic event due to the planet OGLE-2005-BLG-390Lb can be seen in Figure 1.6.

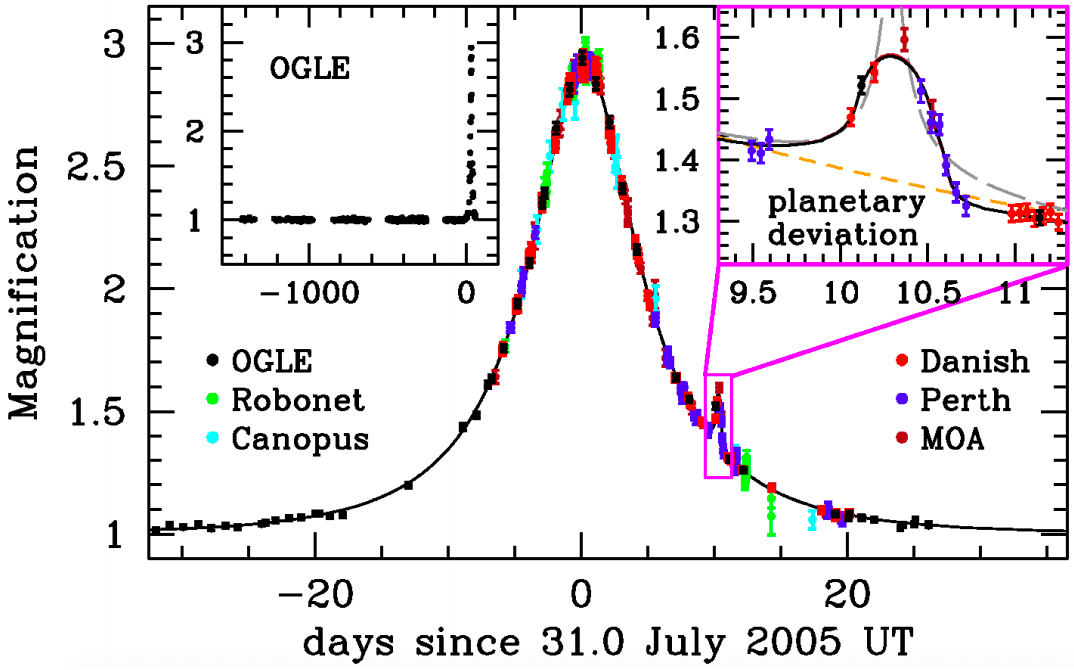

Figure 1.6: Observed light curve of the OGLE-2005-BLG-390 microlensing event and best fit model. Colour identifies the different sources of photometric measurements. The top left inset shows the OGLE light curve for this source covering the previous four years. The top right inset highlights the caustic event due to the planetary companion OGLE-2005-BLG-390Lb, with an estimated 5.5 Jupiter masses and a projected separation of 2.6 AU (Beaulieu et al., 2006).

The duration of a caustic event due to the presence of a planet, t_p is given by:

$$t_p = \frac{q^{1/2}}{t_E} \tag{1.10}$$

where t_E is the total duration of the primary microlensing event and q is the planet - lens star mass ratio. Modelling the light curve to determine t_p and t_E then allows for the mass ratio to be determined. Light curve modelling can also generate an estimate of the planet's angular separation, which is given by the time delay between peak magnification and the caustic event. Due to the required precise alignment of the source and lens stars, microlensing events are extremely rare and unpredictable. Microlensing studies constantly monitor a large population of stars towards the galactic centre, due to increased stellar density, to overcome this restriction and increase the chance of a microlensing detection. As the lens is typically very faint with respect to

the source, it is invisible in almost all regards and cannot be targeted for follow up observations. Planet detection via this method is therefore a one-off event, providing non repeatable results. This also ensures host star parameters, such as mass, are difficult to determine and must be evaluated statistically using galactic models. Planetary mass derived from the measured mass ratio and host star mass is also therefore model dependent.

However there are some major advantages to this technique over other detection methods. Whilst duration, and therefore detectability of the caustic is dependent on planet mass, the amplitude is independent of planetary mass. This is true up until a planets zone of gravitational influence is smaller than the angular size of the source, where caustic events become suppressed and rendered undetectable (Gaudi, 2010). This enables sensitivity down to Earth mass planets for main-sequence sources (e.g., Bond et al., 2017). Microlensing is also sensitive to planets at much wider separations than the transit and RV method. The sensitivity of this technique peaks for planets at a projected separation equal to the Einstein radius, the radius of a ring-like image of the source formed when the source is located exactly behind the lens. For the typical source and lens distance, this Einstein ring radius, r_E, corresponds to a physical distance of (Gaudi, 2012):

$$r_E \sim (2-4)\mathrm{AU}\left(\frac{\mathrm{M}}{\mathrm{M}_\odot}\right)^{1/2} \tag{1.11}$$

This technique is therefore sensitive to planets around the snow line, where temperatures are cold enough for volatile compounds such as water to condense into solid grains. Sensitivity drops off for separations significantly shorter and larger than the Einstein radius. Microlensing is also one of the only detection techniques capable of probing the population of free-floating planets, allowing for valuable statistical analysis of the full planet population (e.g., Cassan et al., 2012). It is also the only method currently sensitive to planets at large galactic distances on the order of kiloparsecs, and is even capable of detecting exoplanets beyond the Milky Way (Ingrosso et al., 2009).

The current population of ~ 60 microlensing planets has been discovered solely via the OGLE (e.g., Udalski, 2009) and MOA (Sumi et al., 2003) microlensing surveys.

The WFIRST mission, set to launch within the next decade, aims to significantly expand this population and open up sensitivity to terrestrial planets down to $0.1 M_{\oplus}$ within habitable zone separations (Spergel et al., 2013).

1.1.4 Direct Imaging

The RV, transit and microlensing methods are all considered indirect planet detection techniques. Imaging however, enables a direct detection of a planetary companion by spatially resolving the light from the planet from its parent star. This feat was first achieved in 2004 with the detection of 2M1207b (Chauvin et al., 2004, 2005), a $\sim$ 5 M_J planet orbiting a brown dwarf host at a project separation of $\sim$ 50 AU (Song et al., 2006). Figure 1.7 displays an image of 2M1207A and its resolved planetary companion. Advancements in imaging instrumentation and techniques then led to the first direct exoplanet detections around stellar primaries, β Pic b (Lagrange et al., 2010) and the HR 8799bcde multiple planet system (Marois et al., 2008b, 2010).

To date, $\sim$ 90 planet candidates have been discovered via direct imaging [2]. However, less than one - two dozen (depending on interpretation) of these have been truly unequivocal detections. This disparity between potential candidates and robust confirmations is due to the difficulty in differentiating between a companion in the planetary regime and low-mass brown dwarf regime, constraints with common proper motion testing to discern whether a candidate is bound to the host star, and ambiguity in the nature of the light source e.g. source could be explained as emission from a planetary companion or as stellar light reflected from a localised dust feature in a debris disk (e.g., Janson et al., 2012b). The number of unambiguous directly imaged planets accounts for less than 1% of the entire exoplanet population, highlighting the difficulty in the imaging technique.

Whilst recording an image of a planet around its host may be a conceptually simple detection technique, in reality it is extremely challenging. This is due to the large brightness contrast and small angular separation between a faint planet and its luminous host star, ensuring the planetary point source is engulfed in the stellar glare, or point spread function (PSF). For example, the planet-star contrast ratio for an earth analogue around a sun-like star would be 10^{-10} in the optical and 10^{-7} in the infrared

[2]The Extrasolar Planets Encyclopaedia (Schneider et al., 2011)

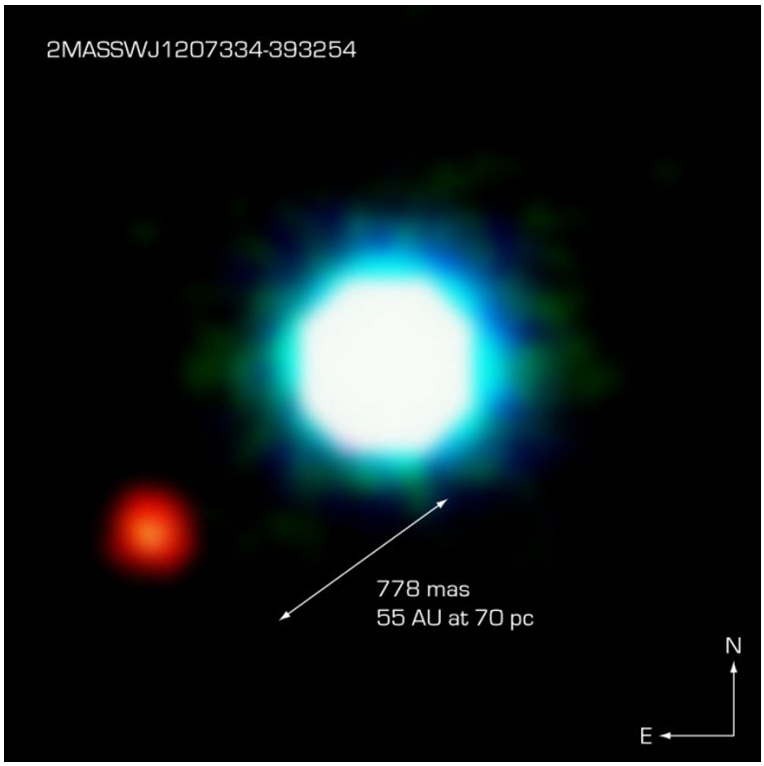

Figure 1.7: Brown dwarf 2M1207A (centre of image) and its planetary companion 2M1207b. Image is a composite of three near-infrared exposures (H, K and L') using NACO on the VLT (Chauvin et al., 2004). 2M1207b is extremely red in colour in comparison to the brown dwarf host, indicating a low temperature, and therefore low mass object. The 778 mas angular separation equates to a $\sim$ 55 AU projected separation at 70 pc, although this distance has since been revised (e.g., Song et al., 2006; Biller & Close, 2007; Dupuy & Liu, 2012)

(Traub & Oppenheimer, 2010), a 25 and 17.5 magnitude difference respectively. At a modest system distance of 10 pc, the angular separation of this planet would be 0.1 arc seconds. Such an extreme contrast ratio at this separation is far beyond the detection capabilities of the most advanced imaging instruments currently available such as SPHERE (Beuzit et al., 2008) and GPI (Macintosh et al., 2008).

The imaging method faces a range of additional challenges. Ground based studies experience image degradation and distortion due to atmospheric turbulence. Space-based studies are limited by the small telescope aperture diameter, D, which produce large diffraction limited PSF's (the full width at half maximum, a measurement of the extent of the stellar PSF, scales with 1/D). Imperfections in the optical elements of both ground and space-based facilities lead to wavefront interference, introducing a broad sea of spurious speckles to the resultant image which further act to obscure a

planetary point source. Imaging constraints and the techniques, instrumentation and post-processing solutions for stellar PSF and speckle subtraction will be discussed in detail in Chapter 2.

Direct imaging studies typically target young, nearby stars. Such targets prove favourable to imaging searches for planetary companions as young giant planets are intrinsically bright in the near infrared due to heat retention from formation and gravitational contraction. These bright, self-luminous planets offer a more achievable contrast with their host and are therefore easier to detect. Planet brightness then decreases over time (e.g., Baraffe et al., 2003; Fortney et al., 2008), due to radiative cooling, resulting in a more challenging contrast ratio. Nearby stars are also favourable targets for exoplanet detection as imaging searches can probe much shorter orbital separations than they can for distant targets – sensitivity across a certain range of angular separations translates into a range of shorter physical separations.

Therefore, some of the best environments to directly image planetary companions are young moving groups (YMGs). These are young ($\sim 10 - 100$ Myr) co-moving associations of stars in the solar neighbourhood ($\sim 10 - 100$ pc) originating from a common birth cluster (e.g., Zuckerman & Song, 2004; Torres et al., 2008). An additional benefit to targeting systems in YMGs is that the group provides an age estimate of member stars that is potentially much more reliable than any accessible technique for individual stars. Although direct imaging enables all system orbital parameters to be determined, through monitoring an orbit over its full duration, and provides information of planetary radius and temperature, from bolometric luminosity and spectral energy distribution, companion mass can not be directly derived. Rather, an estimate of the mass is generated using mass-luminosity evolutionary models (e.g., Baraffe et al., 2003, 2015) which are age dependent. A well constrained system age then enables a well constrained estimate of companion mass.

As seen from Figure 1.1 this technique is biased to massive planets at large orbital separations. Massive planets are hotter, due to a greater wealth of energy liberated from gravitational contraction, and therefore brighter in the near-infrared and easier to detect. Planets at larger orbital separations are also easier to detect as stellar flux decreases as a function of angular distance. The stellar glare is minimised at large separations and the required contrast is more achievable. Imaging is therefore sensitive to exoplanet populations over a unique parameter space, with the ability

to effectively probe for giant planets at separations beyond $\sim$ 10 AU. The origin of such wide orbit planets remains challenging to explain and the discovery of planetary mass companions at separations of 1000's of AU (e.g GU Psc b; 2000 AU (Naud et al., 2014), 2M2126b; $>$ 4500 AU (Deacon et al., 2016)) has fueled the theory of novel formation and migration mechanisms. These mechanisms will be discussed in detail in section 1.2. Sensitivity to smaller mass and / or shorter separation planets via direct imaging will be significantly enhanced with the dawn of next generation imagers such as the largest ever space based facility JWST (6.5m; Gardner et al., 2006), due for launch in 2020, and ground based instruments on future 30m class telescopes (e.g ELT, TMT). This is due the higher angular resolution and greater image sensitivity (more photons collected) afforded by larger telescope diameters.

An additionally benefit to the imaging technique is the ability to spectroscopically characterise resolved companions. As the recorded photons originate directly from the planetary atmosphere, unparalleled information on the chemical composition, atmospheric properties and formation and early evolution can be obtained from intermediate resolution spectroscopy (e.g., Bowler et al., 2017; Daemgen et al., 2017).

1.2 Planet Formation and Evolution

As discussed in the Section 1.1, the plethora of confirmed exoplanets to date is dominated by a population within 5 - 6 AU of their host star. This has been due to the success of large-scale RV and transit surveys, which are biased to short separation planets and whose typical duration limit their ability to detect periodicities on the order of 10's of years. Such surveys account for a combined detection of $\sim$ 3500 planets, $\sim$ 95% of the current exoplanet population. This sample enables statistically significant trends to be uncovered between planetary / host star properties and planet frequency, which in turn allows for planet formation and evolution theories to be stringently tested and constrained. However formation scenarios and evolutionary paths for wide giant planets with separations $>> 5-6$ AU, the parameter space currently accessible via direct imaging, continue to prove challenging to constrain. This is due to the small population of unambiguous planet detections over this separation range and a lack of systematic explorations by surveys with a sufficient degree of sensitivity and statistically robust population analyses.

Understanding of relevant formation and evolutionary theories can be of fundamental importance to the interpretation of a sub-stellar companion. It is evident that brown dwarfs and giant planets represent two distinct populations which arise from two (or more) different formation channels (Chabrier et al., 2014). As each formation mechanism leaves some imprint on a companion that is observationally detectable (e.g. mean density, atmospheric properties), it is possible that the two populations can be differentiated by their formation history. For example, (Konopacky et al., 2013) found that enhanced C/O ratio and depleted C and O levels in the atmosphere of HR 8799c favoured a core accretion formation scenario, confirming the planetary nature of the companion. Objects formed through gravitational instability or cloud collapse track the chemical abundance of the original star-forming material (and therefore the host star), whilst core accretion planetary atmospheres may deviate from a stellar composition due to post-formation capture of solid material. However, it must be noted that planet migration and chemical evolution within the disk can complicate conclusions based on composition (Lodders, 2004).

Still, constraining formation mechanism is a much more robust method of distinguishing between the two populations than using a mass cut-off of $\sim 13 M_J$, based on the minimum mass required for the onset of deuterium burning. This is because, in addition to a metallicity and composition dependence on this mass cut-off (Spiegel et al., 2011), the mass domains of the two populations overlap and it has been shown that even planets as massive as $\sim 25 M_J$ can form, where deuterium burning is possible in the H/He layers above the planet core (Baraffe et al., 2008).

Therefore, developing, testing and constraining formation and evolutionary theories relevant across the full parameter space of the exoplanet population is of vital significance, in addition to its own scientific merit, for the interpretation and confirmation of candidate planets. In this section the current assortment of planet formation and migration theories will be discussed with a focus on the mechanisms that can explain the origin of wide giant planets at separations of 10s out to 1000s of AU.

1.2.1 Formation

1.2.1.1 Core Accretion

Core accretion is one of the main competing theories explaining planet formation. This mechanism is characterised by a bottom-up formation scenario which can be

conceptualised as a two stage process. In the first stage, small dust grains in the circumstellar disk collide and coalesce to form larger bodies, growing from sub-micron particles to km-sized structures.

One barrier to this mechanism is the radial drift experienced by mm to m sized bodies. Circumstellar gas orbits at sub-Keplerian velocities, due to the pressure gradient in the disk. However, particles in the mm to m range do not feel the effects of the pressure gradient and travel at Keplerian velocities. The solid material therefore experiences an aerodynamic drag due to a continuous headwind of gas. This results in a loss of angular momentum, causing the particles to spiral inward and eventually escape the disk due to photoevaporation. This can lead to depletion of mm to m sized bodies on a timescale on the order of ~ 1000 years (e.g., Alexander & Armitage, 2007). This barrier can be overcome with vortices (e.g., Klahr & Bodenheimer, 2003) and local pressure maxima (e.g., Johansen et al., 2009) which act to trap the dust, preventing radial drift and enabling continual particle coagulation. Streaming instabilities (Youdin & Goodman, 2005), resulting from the drag interaction between solid particles and the gas, may generate overdense concentrations of dust which are susceptible to fragmentation and contraction, allowing formation of km sized bodies on a rapid timescale, also bypassing the radial drift barrier.

As bodies grow to km-sized planetesimals, they become gravitationally focusing, increasing the rate of material capture and growth. If the body can reach a critical ~ 10 Earth masses, while sufficient gaseous material remains in the disk, it will trigger runaway gas accretion (Pollack et al., 1996) and the core body captures a large gaseous envelope, becoming a gas giant planet. This is the second stage of core accretion. The gas accretion rate increases exponentially, whilst the increasing difficulty associated with accreting planetesimals reaching the core intact, as a result of drag, dynamical pressure and evaporation in the captured atmosphere, ensures core growth plateaus. The mass of the gaseous envelope then dominates the total mass of the planet. The formation of such massive cores is only possible beyond the snow line where temperatures are cold enough for volatile compounds such as water to condense into solid grains, substantially increasing the surface density and amount of material available for growth in a planetesimals feeding zone.

However, an additional barrier to gas giant formation is the conflicting formation and gaseous disk depletion timescales. The lifetime of the gaseous component of the

disk is on the order of ~ 10 Myr (Hernández et al., 2008), with half of stars in young clusters losing their discs within 3 Myr (Haisch et al., 2001), whilst classical formation of a critical core mass and runaway gas accretion requires a similar timescale of ~ 10 Myr (Pollack et al., 1996). These timescales represent an obstacle to gas giant formation as there does not seem to be sufficient time for gas giants to form before the gaseous material is lost to the system in most cases. One mechanism to overcome this barrier is turbulent migration. As a planetesimal in a fixed orbit quickly depletes the solid material available for growth in its surrounding feeding zone, formation proceeds slowly over the classical timescales mentioned. However, accounting for the migration history of the core can significantly broaden the feeding zone, enabling access to a wealth of solid material and therefore formation on much more rapid timescales, on the order of ~ 1 Myr (Alibert et al., 2005). Several planet migration mechanisms will be discussed in section 1.2.2.

Pebble accretion (Lambrechts & Johansen, 2012) is another mechanism allowing for the formation of critical mass cores and exponential gas accretion on short timescales. It is also a potential solution to the challenge faced by classical theory in explaining planet formation beyond ~ 20 AU, where the low surface density of solid material and long collisional timescales result in the core being unable to reach critical mass before the gas dispersal (Dodson-Robinson et al., 2009). Pebble accretion refers to the capture of solid material through gas friction in the presence of a thin gaseous atmosphere around the planetesimal. This effect captures material at a much higher efficiency than possible solely via gravitational focusing and gas giant cores can form on timescales potentially orders of magnitude shorter. However, simulations have shown that this mechanism is ineffective at giant core formation at very wide orbital separations, $\gtrsim 50$ AU (Bitsch et al., 2015).

Gas accretion, the end phase of gas giant planet formation, finally halts when the gas supply is exhausted, either when the gaseous component of the disk dissipates, or when the planet opens a gap in the circumstellar disk. If the core cannot achieve critical mass, in general or before gas dissipation, the core ends its formation as a terrestrial or ice giant planet.

Observational evidence, and investigations into competing formation modes, suggests that core accretion is the dominant mechanism for the formation of terrestrial and giant planets. Formation via core accretion is consistent with the planet-

metallicity correlation (e.g., Santos et al., 2004; Fischer & Valenti, 2005), the increase in giant planet frequency with increasing stellar metallicity. Higher metallicity indicates a larger abundance of volatiles and refractory material in the disk and therefore higher disk surface density. This supports critical core formation on shorter timescales, allowing for the onset of runaway gas accretion before disk dissipation. The planet-metallicity correlation weakens for lower mass companions, again in agreement with core accretion as lower mass companions have a weaker dependance on disk density as critical core masses do not need to be reached. The apparent relationship between planet frequency, and mass, with stellar mass for RV planets (e.g., Hekker et al., 2008; Johnson et al., 2010) also favours the core accretion mechanism, as a more massive star will harbour a more massive disk, providing more material to form a larger core in a shorter timeframe. However, this relationship is somewhat debatable. As high mass stars on the main sequence are hostile to precise RV measurement (due to substantial rotation, temperature and activity) planet searches rely on high mass stars that have evolved off the main sequence in to giants, which are more susceptible to RV measurement. Lloyd (2011) proposed that the discrepancy in rotational velocity and observationally inferred mass between exoplanet hosting giants and the distribution of field stars can be explained by erroneous mass determinations of giant exoplanet hosts. Having revised these masses, Lloyd (2011) suggests that there is no valid relationship between planet frequency and stellar mass.

1.2.1.2 Gravitational Instability

Gravitational instability (disk instability) is an alternative, top-down formation mechanism. This theory is founded on the principle that protoplanetary gas disks are likely to be gravitationally unstable over some phase of their lifetime. Such instabilities produce over dense regions in the disk, which can rapidly grow to alter the structure and evolution of the disk through self-gravity. These over dense regions induce density perturbations in the disk, which may develop into spiral arms through Keplerian rotation (Laughlin & Bodenheimer, 1994), transferring mass inwards and angular momentum outwards through gravitational torque. If these instabilities can cause disk fragmentation, dense self gravitating clumps of gas and dust can form and remain bound to the host star. These clumps are referred to as giant gaseous protoplanets which can then undergo further collapse and contraction to directly form gas giant planets (Boss, 1997, 2001). This entire process can occur rapidly, on the timescale of several hundred years (e.g., Mayer et al., 2002), well within the lifetime

of the disk.

The ability to induce an instability in the disk is governed by the Toomre criterion which must be satisfied (Toomre, 1964):

$$Q = \frac{c_s \Omega}{\pi G \Sigma} < 1 \tag{1.12}$$

Where Q is the Toomre parameter, c_s is the speed of sound in the disk, Σ the surface density and Ω the disk angular velocity. The Q parameter is a measure of the competition between the destabilizing self-gravity of the circumstellar gas, and the pressure gradient and Coriolis forces which have a stabilising effect on the disk. The requirement that the Q parameter must be small for an instability to occur translates to a minimum mass on the resultant planet (e.g., Matsuo et al., 2007). For the Toomre criterion to be satisfied around a solar type star the surface density of the disk would have to be (Chabrier et al., 2014):

$$\Sigma > \frac{c_s \Omega}{\pi G} \approx 10^5 \, g \, cm^{-2} \left(\frac{AU}{r} \right)^{7/4} \tag{1.13}$$

This density is more than an order of magnitude larger than that of the commonly adopted minimum mass solar nebula (e.g., Davis, 2005), a protoplanetary disk with the minimum mass to form all the solar system planets. This suggests that this mechanism operates preferentially during the early phase of the disk lifetime when the mass is still high.

An additional criterion that must be satisfied for disk fragmentation to proceed is the cooling criterion (Gammie, 2001):

$$\tau_c \lesssim \frac{3}{\Omega} \approx \tau_{orb} \tag{1.14}$$

Where τ_c is the cooling time and τ_{orb} is the orbital timescale. This criterion is a measure of the competition between radiative cooling, which lowers entropy of the gaseous material, reducing the pressure supporting collapse and enabling fragmentation, and thermal pressure due the dissipation of gravitational turbulence, which acts to resist fragmentation. Dissipation of gravitational turbulence occurs over the shearing timescale, which is of the same order as the orbital timescale (Janson et al., 2011).

The main barrier to this formation mechanism is that it is very difficult to simultaneously fullfill both the Toomre and cooling criteria. In fact it is only theoretically possible over a small parameter space of companion masses and orbital separations. An example of the parameter space over which this mechanism is possible is shown in Figure 1.8. From Figure 1.8 it can be seen that this mechanism preferentially forms brown dwarfs, with only a small section of the viable parameter space in the planetary regime, if we assume two distinct populations based on mass. Formation of planetary mass objects at separations on the order of 100 AU becomes increasingly unlikely (e.g., Boss, 2006) due to low disk surface density. Furthermore, this parameter space is readily accessible to direct imaging surveys. The lack of detections over this range, and statistically robust population analyses, tells us that objects across this parameter space are rare (on the order of $\sim 1-5$ % (e.g., Vigan et al., 2017)), implying that planet formation via gravitational instability is also rare. Indeed, Janson et al. (2012a) found that $< 10\%$ of stars could host disk instability-formed companions. These conclusions were found to be valid even when subsequent companion migration was considered. Since a much more substantial fraction of stars than this host known planets likely to have formed via core accretion (Mayor et al., 2011; Batalha et al., 2013), gravitational instability can not be a dominant planet formation mechanism.

1.2.1.3 Cloud Fragmentation

As mentioned in Section 1.1.4, the direct imaging technique has enabled the discovery of planetary mass companions at separations of 100's to 1000's of AU (e.g., Lafrenière et al., 2008; Kraus et al., 2014a; Naud et al., 2014; Deacon et al., 2016). As discussed in the sections 1.2.1.1 and 1.2.1.2, both core accretion and gravitationally instability mechanisms have considerable difficulty in explaining the formation of such wide separation planets (without considering migration scenarios), due to the low surface

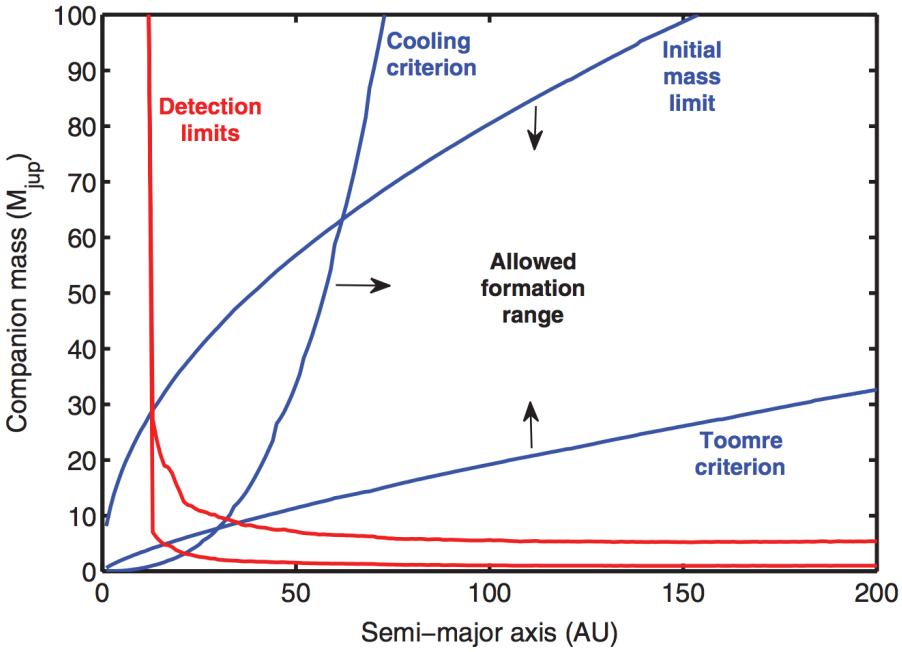

Figure 1.8: Gravitational instability formation limits for the K0V star HIP 7235 (Janson et al., 2012a). The parameter space over which gravitational instability is possible is constrained by the Toomre and cooling criteria, as well as an initial mass criterion which considers the upper mass limit on the initial fragment from the local available mass in the disk as a function of separation. Also presented are the direct imaging detection limits for this system. The two separate limits correspond to the lower and upper age limits of HIP 7235.

density of the disk and long collisional timescales. However, a viable mechanism proposed to explain the in situ formation of such wide giant planets has been molecular cloud fragmentation. In such a scenario, giant planets form via the same pathway as stellar and sub-stellar (brown dwarf) objects.

This process begins with the gravitational collapse of overdense gas clumps in giant molecular clouds, possibly generated from supersonic turbulent flows (McKee & Ostriker, 2007) or radiation driven implosion due to an external bright star (Getman et al., 2009). These collapsing overdense clumps fragment into protostellar embryos with masses of several M_J (Low & Lynden-Bell, 1976). The embryos then accrete material from the surrounding gas reservoir to form stellar-mass objects. However, if the embryo can be ejected from the densest regions of gaseous material before they can accrete substantial mass, their formation phase can end in the brown dwarf and planetary mass regime (Bate, 2009, 2012). Multiple cloud fragmentation during collapse (Burkert et al., 1997) can potentially form planetary mass companions grav-

itationally bound to brown dwarf and stellar hosts.

There is currently strong evidence that cloud fragmentation is a viable mechanism for producing > 10 AU separation giant planets. 2M0441+2301AabBab is a a hierarchical quadruple system consisting of a low-mass star, two brown dwarfs, and a planetary mass companion whose system architecture, low-mass ratios and young age ($\sim 1 - 3$ Myr, possibly too young to have formed through core accretion) are broadly consistent with formation through cloud fragmentation, analogous to higher-mass quadruple star systems (Todorov et al., 2010; Bowler & Hillenbrand, 2015).

However, this mechanism has difficulty in explaining the formation of planetary systems with extreme planetary mass ratios, such as planetary companions to low-mass brown dwarfs (e.g., Chauvin et al., 2004; Barrado Y Navascués et al., 2007). The efficiency and prevalence of this mechanism have not been robustly assessed, due to a lack of systematic explorations and population synthesis comparing direct imaging observations to predictions of cloud fragmentation theory, and a lack of realistic initial conditions in fragmentation simulations (Chabrier et al., 2014). There may also be a large degree of ambiguity in the interpretation of a planetary mass companion ($< 13\mathrm{M}_J$) formed via this mechanism. Can such an object be considered a planet if it has formed via the same pathway as stars and brown dwarfs, rather than in a protoplanetary disk? Until this process is better understood it cannot be considered a dominant mechanism for wide giant formation.

1.2.2 Migration

As discussed in the previous sections there are many obstacles to wide ($\gtrsim 50$ AU) giant formation in situ, particularly via core accretion which is considered the dominant formation mechanism. The population of planets at separations of 100's to 1000's of AU may instead be explained by formation at relatively small separations, which is well understood, accompanied by an outward orbital migration. There are currently several mechanisms theorised to induce this outward migration.

1.2.2.1 Planet-Disc Interactions

Orbital migration can be induced through gravitational interactions between the planet and the protoplanetary disk in which it forms. Such migration can be categorised into two main class. The first class is referred to as Type I migration and is

relevant for terrestrial sized planets with $M_P < 10M_\oplus$. Such planets are not massive enough to form a gap in the disc, a phenomena that requires the planetary Hill sphere radius, which defines the planets sphere of gravitational influence, to be larger than the disk thickness. The surface density profile of the gaseous component of the disk then remains approximately unperturbed. However these bodies are capable of gravitationally exciting spiral density waves in the disk through Lindblad and corotation resonances (Goldreich & Tremaine, 1979). These density waves form spiral arms interior and exterior to the planet orbit whose asymmetry produces a net torque, which predominately causes an inward migration (e.g., Tanaka et al., 2002).

The second class is referred to as Type II migration and is relevant for giant planets. The large angular momentum of such massive planets and their strong tidal interactions with the disk can repel gas in an annular region around the planet faster than viscosity can replenish it, clearing a gap in the disk along its orbit (Goldreich & Tremaine, 1980; Lin & Papaloizou, 1986). However, gas continues to flow in a stream across the gap past the planet, locking the planets radial drift to the viscous evolution of the gas (Ward, 1997). The planet tracks the motion of the gas, typically migrating inwards with gas accretion. However, for gas accretion and subsequent inward migration to proceed, gaseous material in outer regions of the disk must move outwards to conserve angular momentum (Martin et al., 2007). Therefore, if a planet were to have formed within these outer regions, it will migrate outwards, tracking the motion of the gas. Simulations have found that for giant planets forming around ~ 10 AU, a favourable environment for formation via core accretion, this process can migrate planets out to ~ 50 AU separations (Veras & Armitage, 2004). After the gaseous material has dissipated, further outward migration can occur due to the planets interaction with a disk of planetesimals. The planet experiences recoil motion as it gravitationally scatters surrounding planetesimals (Levison et al., 2007), resulting in an increase in orbital separation. This process is thought to have caused the outward migration of Saturn, Uranus and Neptune to their current location (Tsiganis et al., 2005).

Therefore, Type II outward orbital migration and subsequent planetesimal scattering is a viable theory for explaining the population of wide separation giants discovered via direct imaging at separations out to the order of 100 AU. However, it cannot explain the presence of giants at separations on the order of 10^3 AU as these separations lie beyond the typical confines of the disk (e.g., Isella et al., 2009), where

there is no material to interact with. Alternative migration mechanisms are required to explain exoplanet existence over this parameter space.

1.2.2.2 Planet-Planet Scattering

Gravitational interactions between multiple planetary bodies can occur long after the gaseous component of the disk has dissipated and the planetesimal disk has been depleted. In fact, gas dissipation is a necessary requirement for planet-planet scattering as gas in the disk acts to damp eccentricity excitation, which prevents orbit crossing and close encounters of planetary bodies (Chatterjee et al., 2008). Once the gas has dissipated, eccentricity excitation can proceed, leading to orbit crossing, close encounters and subsequent gravitational scattering.

Numerical simulations show that as one of two gravitationally interacting planets is scattered inwards, the other may be ejected out to stable orbits of hundreds of AU (e.g., Rasio & Ford, 1996; Veras & Armitage, 2004; Chatterjee et al., 2008; Jurić & Tremaine, 2008). The population of hot Jupiters with large eccentricities, spin-orbit misalignments and retrograde orbits is a consistent outcome of inward planet-planet scattering (e.g., Nagasawa et al., 2008; Naoz et al., 2011). Wide giants produced by outward scattering would also be on highly eccentric orbits, however if sufficient solid material remains in the outer regions of the disk, the planet orbit may be circularised through dynamical friction (Ford & Chiang, 2007).

Circularisation becomes very difficult for companions scattered beyond the typical confines of the disk, producing a population of highly eccentric wide planets. Dynamical simulations by Veras et al. (2009) have shown planet-planet scattering capable of migrating planets out to separations on the order of $10^2 - 10^5$ AU. However, they find the population on stable orbits to be smaller than the population of planets that eventually end up in unbound orbits, passing through these wide separations before being ejected. Although a sizeable population of wide and highly eccentric planets is found at ages of 10-50 Myr in the models, the population decreases on timescales of ~ 10 Myr to produce a significantly depleted population at ages > 50 Myr, when the majority of planets have been ejected from the system, enhancing the free-floating planet population. However, even at 500 Myr some planets remain in orbit beyond 1000 AU. Planet-Planet scattering is therefore a viable mechanism to explain the wide giant population out to separations of 1000's AU.

1.2.2.3 Planet Capture

The capture mechanism was initially conceived to explain the population of wide ($> 10^3$ AU) stellar binaries. Conventional stellar formation theories and dynamical interactions cannot explain the formation and survival of such wide bound systems in stellar clusters due to dynamical disruption (e.g., Parker et al., 2009). However, these binaries could form during dispersal of a stellar cluster or association. In such a scenario, stars that are initially unbound become bound as the cluster expands and the gravitational influence of the other members of the cluster diminishes (e.g., Kouwenhoven et al., 2010; Moeckel & Bate, 2010). For this process to proceed, the pair must be at a sufficiently close separation and have similar velocities.

The formation of wide planet companions was proposed as a natural extension of this mechanism. In this scenario stars and brown dwarfs capture free-floating planets into bound orbits during stellar cluster dispersal. Statistical analysis of microlensing studies have suggested the existence of a large population of free-floating planets (e.g., Sumi et al., 2011; but see also Mróz et al., 2017) that would be available for recapture. This large population may be a result of planet-planet scattering, cloud fragmentation, ejection from dynamically unstable multiple protostellar systems or due to a close encounter with a large cluster star (e.g., Kroupa & Bouvier, 2003; Veras et al., 2009; Bate, 2012). Simulations have found this mechanism capable of producing bound planets at separations of > 50 AU (Parker & Quanz, 2012) and $10^2 - 10^5$ AU with $3 - 6$ x $(f_{FFP}/1)\%$ of all stars capturing companions over this separation range (Perets & Kouwenhoven, 2012), where f_{FFP} is the number of free-floating planets per star in the cluster. Perets & Kouwenhoven (2012) also found that multiple planets can be captured by the same host through independent consecutive captures, and binary systems can also effectively capture companions onto both circumstellar and circumbinary orbits. Planet capture is therefore also a viable mechanism to explain the wide giant population out to separations of 1000's AU.

Chapter 2

High Contrast Imaging

As discussed in Section 1.1.4, direct imaging is a unique and highly rewarding planet detection technique. It yields a wealth of information, revealing planetary motion, allowing all orbital parameters to be derived, enabling an estimate of planetary temperature, radius and mass (although model dependent), and facilitates the spectroscopic characterisation of resolved companions, providing information on atmospheric constituents. Direct imaging also provides the most viable method to probe for planets at separations greater than $\sim$ 10 AU, a parameter space that continues to challenge planet formation and evolutionary theories (as discussed in Section 1.2). Systematic explorations by imaging surveys, enabling planet detection and robust population analyses, is essential for assessing the relevance of various competing theories, and allowing for stringent constraints to be placed on formation and evolution modes out to thousands of AU.

However, as previously mentioned, this technique is inherently difficult due to the large brightness contrast and small angular separation between a faint planet and its luminous host star, often ensuring the planet is engulfed within the stellar PSF. Imaging faces a range of additional challenges such as image degradation and distortion due to atmospheric turbulence and wavefront interference due to instrument imperfections, which introduces a broad sea of spurious speckles to the resultant image, further obscuring any planetary point source.

This Chapter focuses on these challenges and the techniques, instrumentation and post-processing solutions that are employed to overcome them and enhance high contrast imaging capability through PSF and speckle subtraction. I then discuss current limitations in the imaging field, leading to the motivation behind my investigations.

2.1 Atmospheric Turbulence

Under ideal conditions, the full width at half maximum (FWHM), a measure of the spatial extent of the stellar PSF, is governed by the diffraction limit of the telescope. This diffraction-limited resolution scales linearly with telescope size, via the following relationship:

$$FWHM \propto \frac{\lambda}{D} \tag{2.1}$$

Where λ is the observing wavelength and D is the aperture diameter. Therefore, telescope size is of critical importance for imaging studies as larger apertures produce smaller PSF's (in the diffraction-limited case), pushing sensitivity to planetary mass companions at smaller angular separations from their host. Consequently, imaging studies typically favour the use of 8m class ground based telescopes, which are $\sim 4-5$ larger than the largest (visible/near-infrared) space based telescope (Hubble Space Telescope: D = 2.4m), due to the expense associated with launching facilities into orbit.

However, the ideal conditions required for diffraction-limited imaging cannot be achieved from the ground due to the presence of the Earth's atmosphere. Localised variations of temperature and pressure in the Earth's atmosphere generate turbulent flows of gas. These flows generate spatially and temporally varying cells of gas with different temperatures and densities. As the refractive index of air is temperature and density dependent, these turbulent cells create an inhomogeneous medium of spatially and temporally varying refractive indices. As a plane wavefront from an an astronomical source enters the atmosphere, the varying refractive indices introduce different phase shifts to different segments of the wavefront. This results in aberration, a deterioration in wavefront quality as the plane wave becomes bent and distorted traveling towards the Earths surface. At the telescope this aberration results in a broadening and blurring of the PSF. The interference of varying wavefront segments also introduces a sea of speckles to the resultant image. Furthermore, due to the temporal variation of the pattern of turbulent cells, consecutive images of a target can display vastly different PSF and speckle pattern structure and shape.

The strength of the wavefront aberrations caused by atmospheric turbulence is measured by the Fried parameter, r_0 (Fried, 1965, 1966). It is effectively a measure of the coherence length of the wavefront errors, the diameter over which the root-mean-square phase variations do not exceed one radian, and represents the average size of a turbulent cell. Observations conducted using telescopes with D $< r_0$ are not affected by turbulence and are effectively diffraction limited, observations where D$>> r_0$ are strongly affected by turbulence. The FWHM of a Stellar PSF imaged under the latter condition is then given by:

$$FWHM \propto \frac{\lambda}{r_0} \tag{2.2}$$

Typical values for r_0 at $\lambda = 500$ nm are in the range of 10 - 20 cm (Perryman, 2011), with $r_0 \propto \lambda^{6/5}$. Therefore, in the visible and near-infrared, 8m class ground based telescopes produce PSF's that are $\sim 40 - 80$ times broader than the diffraction limited case, with FWHMs on the order of $1''$. Broadening of a stellar PSF from the diffraction limited case to the seeing limited case as a function of D/r_0 is shown in Figure 2.1. Such broad PSF's and temporally varying PSF structure would severely limit ground based exoplanet imaging capability, as the extent of the stellar glare and speckle pattern would obscure any planetary point source. To avoid this obstacle of atmospheric turbulence, space based telescopes could be utilised. However, as previously mentioned such facilities have relatively small apertures and therefore produce large diffraction limited PSF's, which similarly limit imaging capability. This has motivated the optimisation of imaging from the ground, with the development of techniques and instrumentation to negate PSF broadening and improve wavefront quality, ensuring the feasibility of direct planet detection. These techniques will be discussed in the following sections.

2.1.1 Lucky Imaging

Lucky imaging is one such technique for minimising the effect of atmospheric turbulence and enhancing the resolution of ground-based telescopes. The technique, first proposed ~ 40 years ago by Fried (1978), exploits the temporally varying nature of the turbulence. As the pattern of turbulent cells encountered by a wavefront varies with time, the strength of the aberrations, and therefore wavefront quality at the telescope

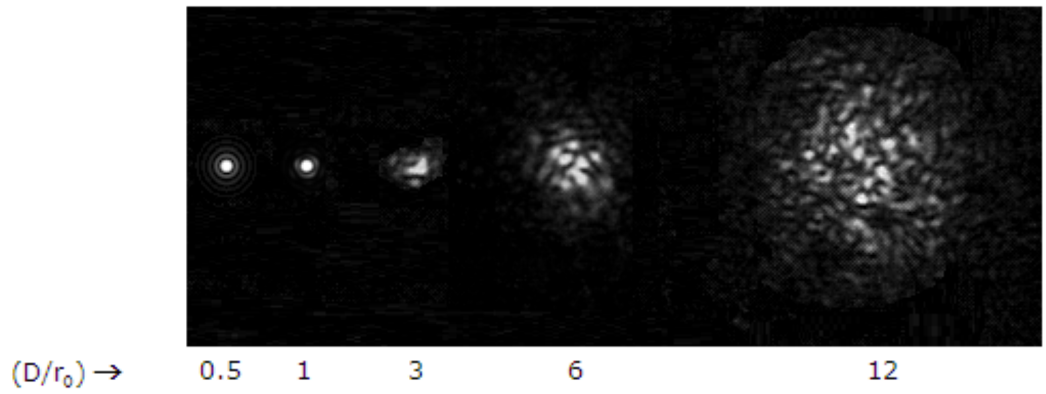

Figure 2.1: PSF broadening as a function of D/r_0 for a fixed telescope diameter. To the left of the image $D < r_0$ and therefore atmospheric turbulence is not a limiting factor. The PSF is purely diffraction limited and therefore appears as an Airy disk surrounded by diffraction rings. As D becomes $>> r_0$, moving to the right of the figure, the PSF becomes seeing limited, significantly broadening, blurring and developing a speckle pattern. Image: telescope-optics.net

also varies as a function of time. Occasionally, the combined phase variations across the length of a telescope aperture, δ, will be minimal i.e., less than 1 radian, and the PSF of an imaged source will enter the near-diffraction limited regime, with a Strehl ratio $\gtrsim 0.37$ (Strehl $\approx exp(-\delta^2)$). Strehl ratio is a measurement of image quality and is the ratio of the peak intensity of an abberated PSF imaged at the telescope, to a perfect diffraction limited PSF. The probability, P, of the wavefront variance being less than 1 radian across the full telescope aperture, and therefore achieving a Strehl ratio $\gtrsim 0.37$ approaching the diffraction limited regime, is given by (Fried, 1978):

$$P \sim 5.6\, exp\,[-0.1557(D/r_0)^2] \tag{2.3}$$

From Equation 2.3, for a telescope aperture $D = 7\, r_0$, the probability of obtaining a 'lucky image' with Strehl $\geq 0.37 \approx 2.72 \times 10^{-3}$. In other words, one exposure in ~ 350 would be in the near-diffraction limited regime. Lucky imaging exploits this phenomenon by selecting the best quality, highest Strehl ratio frames from a large number of exposures, whilst rejecting the majority of the seeing-limited, distorted frames. The best quality frames are then combined, producing a substantial gain in spatial resolution and signal to noise, to achieve almost diffraction-limited PSF's. A comparison between a seeing limited image and the corresponding 'lucky' version of

the image can be seen in figure 2.2. In a typical lucky imaging sequence, $\sim$ 10000 exposures are taken. This would generate $\sim$ 27 frames with Strehl ratios $\geq$ 0.37 for final image combination for a $D = 7\,r_0$ aperture. However, in practice there is no restriction on minimum Strehl for image combination and typically the best 1% or 10% of frames are selected, which increases image depth whilst still allowing for a substantial improvement in image resolution. Whilst $D > 7\,r_0$ would allow for a higher image resolution, the frequency of 'lucky' near-diffraction limited exposures decreases as a function of $exp\,[-(D/r_0)^2]$. For example, for $D = 10\,r_0$, the frequency drops to one in 10^6. $D = 7\,r_0$ provides the optimal trade-off between angular resolution and 'lucky' frequency (Hufnagel, 1966), which directly translates into image depth. For typical values of r_0, $D = 7\,r_0$ translates to telescope apertures of 1.4 m at 500 nm and 2.5 m at 800 nm (Baldwin et al., 2001).

An additional consideration critical to the lucky imaging technique is exposure integration time. Single frame exposure time must be short enough to capture a frozen state of the wavefront distortion, i.e. the distortion and speckle pattern do not vary as a function of time across one exposure. Otherwise, the speckle pattern would smear out and high resolution spatial information would be lost – obtaining 'lucky' near-diffraction limited frames would become unfeasible. Therefore, exposure times must be shorter then the speckle coherence time (a timescale describing the temporal decorrelation of the speckle pattern), where the speckle pattern remains fixed. As speckle coherence times are typically on there order of $\sim$ 10 ms (e.g., Dainty et al., 1981; Vernin & Munoz-Tunon, 1994), lucky imaging exposures must have similar integration times of $\sim$ 10 ms or shorter.

For a 1% selection, 10000 frames and a 10 ms integration time, the total effective integration of the final combined image is 1 second. The sensitivity of such images typically limits exoplanet imaging capability as the required contrast cannot be achieved, however, lucky exoplanet imaging is possible. For example, Janson et al. (2017) recorded one of the shortest wavelength images of a planetary mass companion with the detection of the deuterium burning boundary object 2MASS J01033563-5515561(AB)b in the SDSS z' band ($\sim$ 900 nm). Detecting and characterising stellar binaries has been much more successful using this technique (e.g., Hormuth et al., 2007; Schnupp et al., 2010; Janson et al., 2012c; Jódar et al., 2013; Janson et al., 2017), as the smaller brightness contrast between components is much

more achievable.

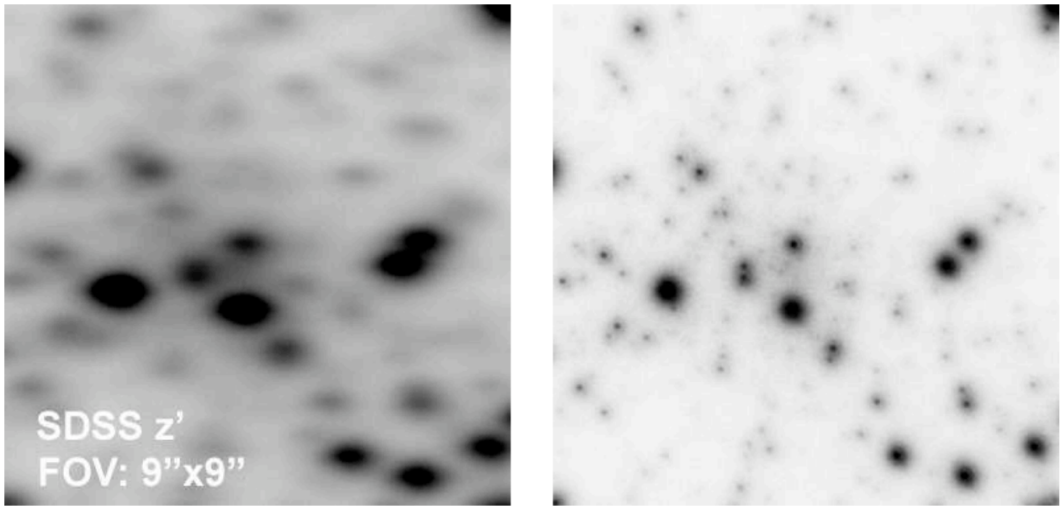

Figure 2.2: Comparison between seeing limited image (left frame) and 'lucky' image (right frame) of the core of the globular cluster M15. Taken with AstraLux Norte on the Calar Alto 2.2m telescope (Hormuth et al., 2008). Lucky image is the combination of the best 5% of 10000 frames. Although the lucky image contains 20 times less photons, it is clearly superior in terms of angular resolution and point source detection.

As mentioned, the effectiveness of this technique drops off rapidly for $D > 7\,r_0$ as the 'lucky' probability scales with $exp\,[-(D/r_0)^2]$. For typical values of r_0, 10 - 20 cm for $\lambda = 500$ nm (with $r_0 \propto \lambda^{6/5}$), $D >> 7\,r_0$ for 8m class telescopes. Therefore, this technique is totally ineffective on the largest ground based telescopes that have the potential to produce the highest angular resolution images. In order to push the imaging capability of these telescopes from the seeing limited to the diffraction limited regime, other techniques must be employed, such as adaptive optics.

2.1.2 Adaptive Optics

Adaptive optics (AO; Babcock, 1953) is a technique used to improve wavefront quality and achieve near-diffraction limited imaging by actively compensating for the wavefront aberrations caused by atmospheric turbulence. This process can be broken down into two main phases. In the first phase, the nature of the wavefront aberrations are measured using a wavefront sensor (WFS). A portion of incoming light is directed towards the WFS using a beamsplitter, whilst the remainder travels to the science camera. AO systems typically use dichroic beamsplitters, analysing visible light for

wavefront correction whilst imaging in the near infrared. The WFS generally consists of a phase-sensitive optical device and a high efficiency photon detector. Three different types are currently in use: the Curvature WFS, Pyramid WFS and Shack-Hartmann WFS. The Shack-Hartmann is the most common WFS and is employed by AO imaging instruments on 8m class telescopes e.g. NACO (Lenzen et al., 2003; Rousset et al., 2003), SPHERE (Beuzit et al., 2008), GPI (Macintosh et al., 2008). It consists of an array of lenses (lenslets) which each form an image of a source on a position sensitive photon detector, typically a charge-coupled device (CCD). Any wavefront phase perturbation, which manifests as a local wavefront tilt, will then produce a shift in the recorded source image. Therefore, the local tilt can be measured from the image position. As wavefront aberration can be approximated by a discrete set of wavefront tilts, sampling local tilt over the entire lenslet array allows the full wavefront distortion to be measured.

In the second phase, information from the WFS is passed to a high-performance, real-time computer, which calculates the wavefront shape. The computer then outputs a voltage, shaping a deformable mirror which alters the path lengths of different wavefront segments to correct for phase perturbations (tilts) and recovering a plane, unperturbed wavefront. The precise shape of the mirror is controlled by an array of voltage sensitive actuators connected to an optical surface that deforms under actuator expansion. In order to effectively sample wavefront distortion and produce an effective wavefront correction, the number of actuators and sensor elements (e.g., Shack-Hartmann lenslets) must be on the order of $(D/r_0)^2$ (Perryman, 2011). With an 8m telescope and under V-band seeing of $0.6''$, this would translate to ≈ 2300 actuators in the V-band, but only ≈ 66 in the K-band (Hormuth, 2007). However, a significantly smaller number of actuators can still enhance wavefront quality and produce images with sharp cores (e.g., Roddier et al., 1991). Extreme adaptive optics systems (ExAO) however employ vast arrays of actuators and lenslets which allow for very fine sampling of wavefront distortion, contributing to excellent wavefront correction. For example, the ExAO system on board SPHERE, SAXO (Fusco et al., 2006; Petit et al., 2014), employs a 41 x 41 actuator array and a 40 x 40 lenslet WFS, enabling almost diffraction limited imaging with H-band ($\sim 1.6\,\mu$m) Strehl ratios in excess of 90% (under median conditions).

The deformable mirror is placed before the beamsplitter in the optical pathway, creating a continuous closed loop of wavefront sensing, analysis and correction. This

loop must be executed on the order of milliseconds, shorter the timescale for atmospheric coherence (time in which wavefront variations deviate less than one radian), in order for the system to effectively analyse specific wavefront distortion and correspondingly shape the deformable mirror for wavefront correction, before the nature of the distortion changes. A schematic displaying a typical AO system configuration can be seen in figure 2.3. Figure 2.4 shows an example of the immense improvement that can be achieved with AO.

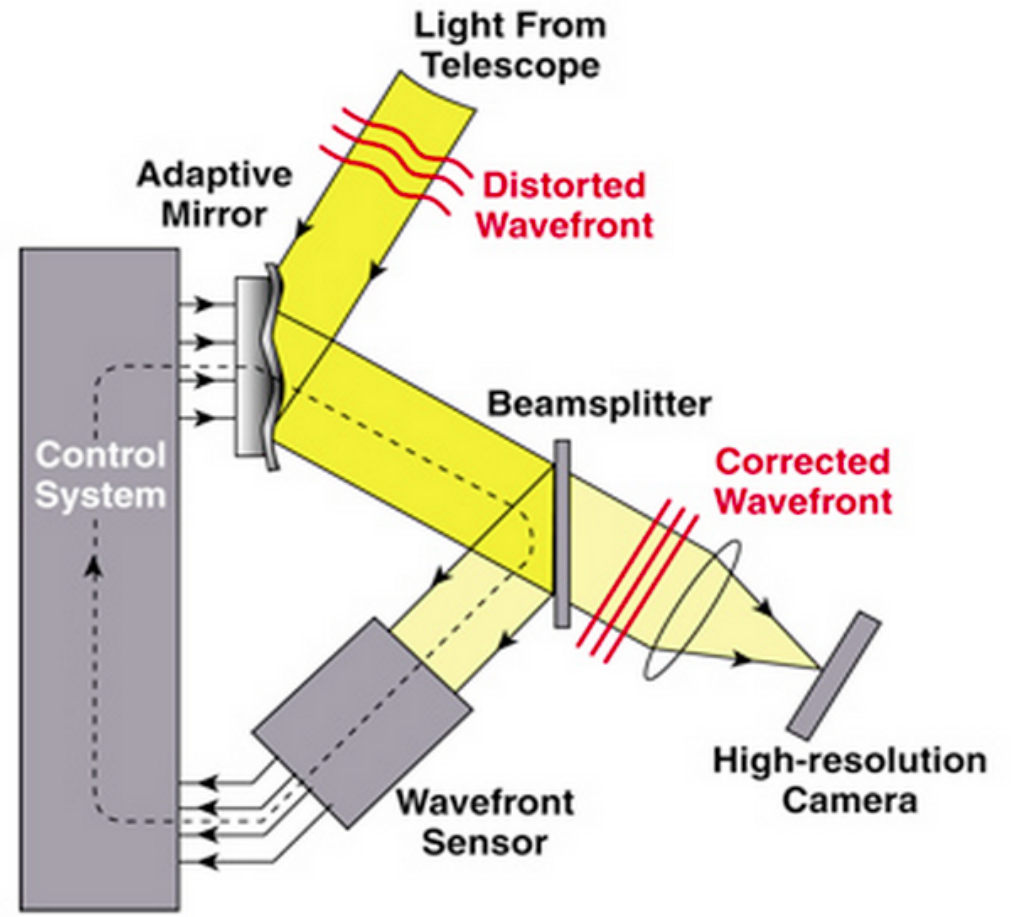

Figure 2.3: Schematic of a typical AO system configuration. A beamsplitter is used to send a portion of a distorted wavefront to a WFS. This passes information on the nature of the distortions to a high-performance computer control system, converting wavefront shape to voltage. This voltage drives actuators which shape a deformable (adaptive) mirror to correct for wavefront distortion. The corrected wavefront is then passed to the science camera. Image: Claire E. Max, UCSC

Optimal AO performance requires wavefront sensing with good signal to noise

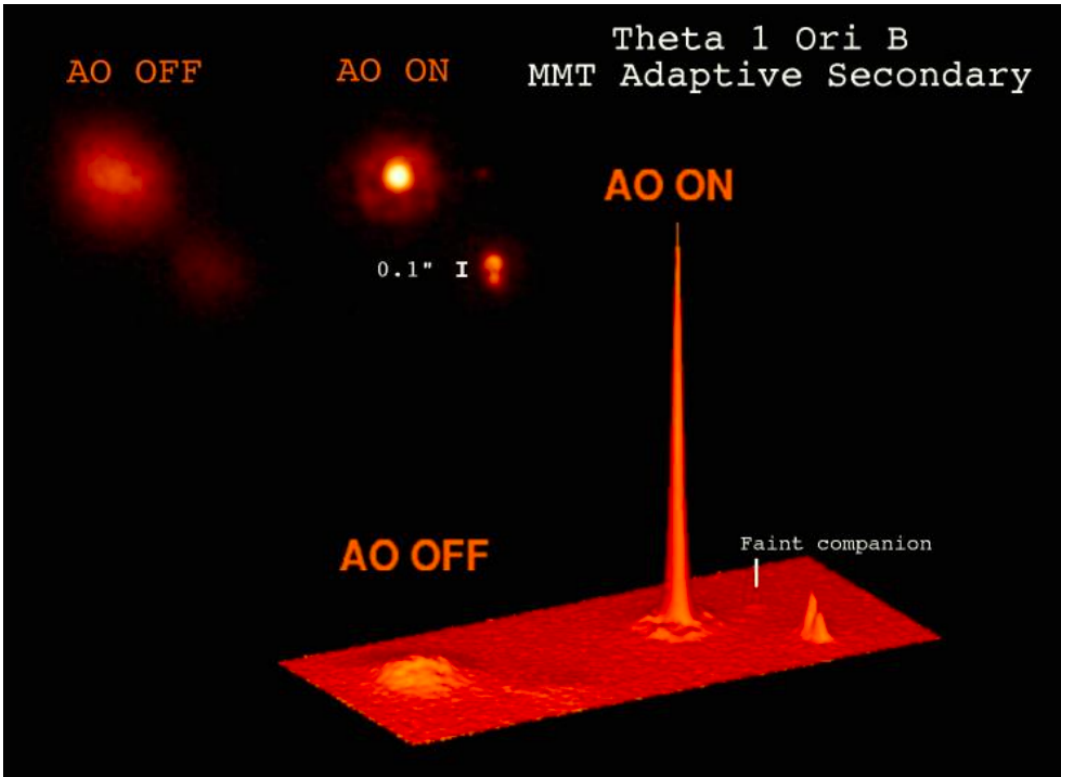

Figure 2.4: AO imaging of the Theta 1 Ori B multiple star system using the 6.5m MMT. With AO off, this system appears as just 2 stars, with broad PSF's and Strehl ratios of 0.5%. With AO on, Strehl ratios of 10% are achieved and the much narrower PSF's allow the system to be identified as a tight group of 4 visual stars – a single star has been resolved into two components with a 0.1″ separation and an additional faint companion has been revealed. Image: Laird Close, CAAO, Steward Observatory

ratio, and therefore bright source ($V \lesssim 15$) observation is essential. Imaging studies simultaneously observe a bright reference (guide) star for wavefront sensing in order to perform wavefront correction for a typically fainter target star. This guide star must lie within the isoplanatic angle from the target, so that the guide star statistically experiences the same wavefront distortion as the target. The isoplanatic angle, θ_0, defines the angle at which optical path variations cause phase aberration deviations less than one radian. It is related to the Fried parameter, r_0, via (Bozza et al., 2016):

$$\theta_0 \propto \cos\gamma \, \frac{r_0}{h} \tag{2.4}$$

Where γ is the zenith angle and h is the characteristic height of the turbulence.

If the angular separation between the guide star and the target star is $> \theta_0$, the wavefront of each star will travel through the same turbulent layers at low altitudes, experiencing the same distortion, however, wavefront paths increasingly deviate with increasing atmospheric height. Therefore, significantly different turbulent layers will be probed at high altitudes, resulting in a substantial variation in guide - target wavefront distortion. Wavefront sensing and correction made for the guide star will subsequently produce a substandard, or even adverse, target wavefront correction. A diagram highlighting this effect of anisoplanatism can be seen in figure 2.5.

Typical values for the isoplanatic angle, where distortion is statistically uniform allowing for good AO correction, are $10'' - 20''$ in the near-infrared (Sandler et al., 1994; Fritz et al., 2010). This angle severely restricts AO application as bright stars are not so common in the sky. The sky coverage that provides suitably bright natural guide stars (NGS) within θ_0 from a random target is, on average, only $\sim 10\%$ (Davies & Kasper, 2012), although this figure varies significantly between the galactic plane (tens of percent) and the galactic pole (tenths of a percent) (Ellerbroek & Tyler, 1998).

This restriction has been overcome with the use of artificial, laser guide stars (LGS e.g., Beckers, 1993). This technique applies a laser beam pulsed from the ground to create an artificial light source at an arbitrary position in the sky, extending the sky coverage of AO accessibility to nearly 100% (e.g., van Dam et al., 2006). These lasers can be tuned to Rayleigh scatter ($\sim$ 350 nm) in dense regions of atmosphere at altitudes up to 30 km, or to excite sodium atoms ($\sim$ 589 nm) concentrated in a $\sim$ 5 km thick layer at an altitude of $\sim$ 90 km (Chapman, 1939). However, single LGS posses a substantial drawback with respect to NGS. LGS are created at some finite height in the atmosphere and therefore the backscattered beam will not sample the full atmospheric turbulence experienced by a target star at infinity (with respect to atmospheric height). This cone-effect reduces the maximum achievable Strehl ratio.

Single guide star systems also suffer from a restricted field of view (FOV), on the order of 10" - 20", i.e. θ_0, where AO offers optimal wavefront correction. Beyond these separations image quality would experience substantial degradation as AO performance deteriorates due to anisoplanatism. Alternative AO systems have been designed to negate this effect such as ground layer adaptive optics (GLAO e.g., Tokovinin, 2004) and multi conjugate adaptive optics (MCAO e.g., Berkefeld et al.,

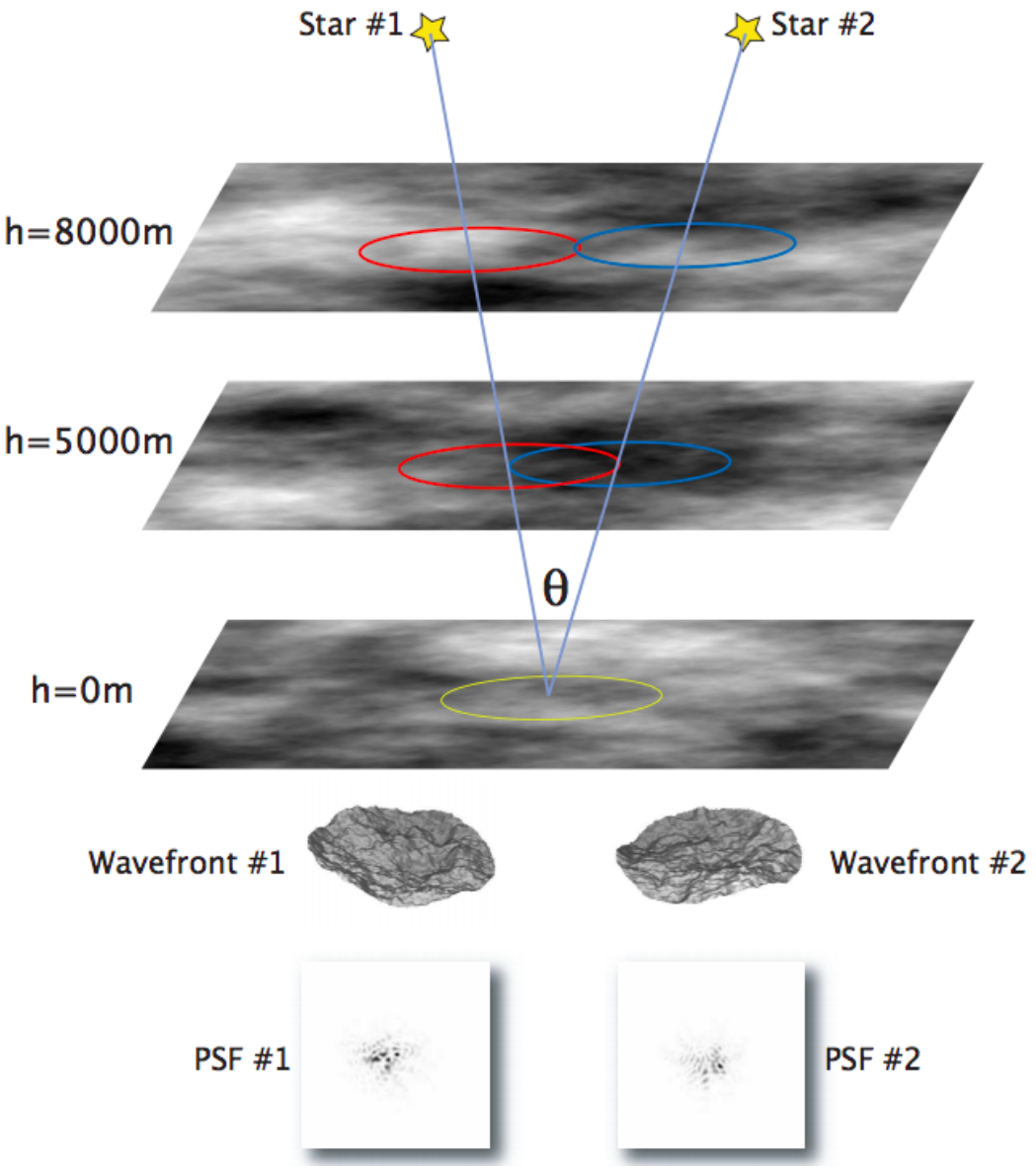

Figure 2.5: Diagram of anisoplanatic effects due to turbulent layers at varying height. Ovals represent projected telescope aperture seen by each star at different altitudes. For a given target - guide star separation θ, both wavefronts see the same projected aperture at ground level and travel through the same turbulent material, experiencing equivalent distortion. With increasing high projected apertures become increasingly separated. At high-altitudes, the separate wavefronts travel through completely different turbulent material, experiencing different distortion. At the telescope, the cumulative distortion experienced by each wavefront produces vastly different wavefront shapes, and therefore different PSF's. Image: (Hormuth, 2007).

2001). GLAO corrects the component of wavefront distortion due to ground layer turbulence only. This correction is done by combining wavefront errors from a number

of well separated reference stars with separate wavefronts traveling through different turbulent layers at high altitudes, but the same layers at the ground level. Whilst GLAO systems can not reach the performance of conventional AO systems (as higher altitude distortion is not corrected), they offer reasonable wavefront correction (Strehl $\sim 10\%$) over a wide FOV (up to 10'). MCAO utilises different NGS or LGS positioned so that the different columns of turbulence that they probe are fully superimposed at low altitudes and partially superimposed at high altitudes. Wavefront aberrations caused by separate turbulent layers are then corrected for separately with multiple conjugated deformable mirrors. Whilst MCAO in principle is able to provide Strehl ratios $> 50\%$ over a FOV on the order of arc minutes, the technology is currently limited by its complexity and expense. The Gemini Multi-Conjugate Adaptive Optics System (GeMs; Rigaut et al., 2014) is currently only capable of providing Strehl ratios of 10%, 15% and 30% in J, H and K respectively, over a FOV of more than 1 arcminute. However, advanced MCAO systems are being designed for AO application on the future generation of 30m class telescopes, e.g TMT (Gilles et al., 2006), ELT (Diolaiti et al., 2010).

2.2 PSF Subtraction

As mentioned in the previous section, AO is a powerful imaging tool. In fact, using exclusively AO on the VLT enabled the first direct image of a planetary mass object, 2M1207b (see figure 1.7). However, this planet is particularly susceptible to direct detection. Its youth (10 ± 3 Myr TW Hya YMG member e.g., Gagné et al., 2015; Bell et al., 2015) and substantial mass (~ 5 M_J) ensure a significant near-infrared brightness. Furthermore, it is in wide orbit around a faint brown dwarf host. The subsequent contrast ratio is extremely favourable, e.g. an L'-band magnitude contrast ~ 4 (Chauvin et al., 2004), and easily achieved with AO imaging.

The broader population of young (< 1 Gyr) Jupiter mass planets around stellar hosts are much more difficult to detect, and are typically inaccessible to AO imaging in isolation. Whilst AO corrects for atmospheric turbulence and allows for near diffraction-limited imaging, the resultant PSF – a diffraction limited core surrounded by Airy rings superimposed on a wide scattered light halo, remains problematic. These Airy rings represent several percent of the stellar flux over separations of significant interest to imaging studies, typically separations on the order of 10 AU. For example, at just four resolution elements (λ/D) from the core, ~ 100 mas for an

8m telescope operating at 1μm , the PSF is 3 x 10^{-4} the central peak brightness (Oppenheimer & Hinkley, 2009). This is orders of magnitudes brighter than any potential faint planetary companion which would then be completely obscured and undetectable. Therefore, the bright diffraction core and surrounding Airy pattern severely limit exoplanet imaging capability.

A further limitation to AO imaging in isolation is speckle noise, the random intensity pattern produced by wavefront interference. Whilst rapidly varying speckles due to atmospheric turbulence are attenuated by AO, optical imperfections in the telescope / instrument system introduce phase shifts to different wavefront segments, subsequently leading to wavefront interference that generates speckle noise that can be an order of magnitude larger than the residual photon noise (e.g., Bloemhof, 2003; Marois et al., 2008a). In fact, these speckles can be as bright as 4×10^{-3} of the host star brightness at separations of $\sim 7\lambda/D$ (Oppenheimer & Hinkley, 2009), mimicking and obscuring any orbiting planetary companion and therefore limiting imaging capability to an even greater degree than the Airy pattern. The intensity distribution of the speckle pattern is dependent on physical properties of the telescope / instrument system, such as temperature, mirror imperfections and optical alignment, which evolve over a relatively long timescale, producing slowly evolving, quasi-static speckles. This speckle noise is spatially correlated (Soummer et al., 2007) and cannot be averaged out over time into a smooth background.

To significantly enhance imaging capability and open up sensitivity to a broader population of planets, the limiting nature of the bright diffraction core, Airy pattern and speckle noise must be negated with the application of starlight and speckle suppression and subtraction techniques. These techniques will be discussed in the following sections.

2.2.1 Coronagraphy

Coronagraphy is the collective name for techniques that act to attenuate on-axis stellar light, rejecting it from the area of interest, whilst transmitting off-axis light that may be due to a potential planetary companion. In this manner the PSF core and Airy pattern are suppressed, leaving planetary photons well isolated from the stellar light and easier to detect. This attenuation is achieved in the imaging instruments hardware. This technique was first employed to study the faint coronal emission

around the bright Sun (Lyot, 1939) and is how the name is derived.

The classical coronagraph used by Lyot (1939) was later optimised for high contrast imaging application (Sivaramakrishnan et al., 2001) and is briefly described here. A schematic of a Lyot coronagraph configuration is shown in figure 2.6. It consists of two 'masks' and three lenses which are used to achieve PSF suppression. In the first stage, a lens forms an image of the target at the centre of an circular opaque focal plane mask / occulting spot, in place of a detector that usually records the image. The core diffraction peak of the stellar light is largely absorbed by this mask, however, diffraction around the edges transmits a significant portion of starlight down the optical train. In the next stage, the beam of light is brought back out of focus by a second lens, forming an image of the telescope pupil. In this plane, residual light not absorbed by the occulting mask has been concentrated into bright diffraction rings. These rings are well spatially separated from any transmitted off-axis light, and therefore diffraction has been exploited to isolate any companion signal from the stellar PSF. These rings can additionally be filtered out, without subtracting substantial planetary emission. This is done in the third stage of the optical train using a Lyot stop. It effectively acts as a downsized telescope aperture, blocking light from the wide diffraction rings whilst transmitting the remaining light to a third lens, which forms the final image on a detector. This final image contains only $\sim 0.5\%$ of the initial starlight, whilst off-axis planet throughput is typically 80%, i.e. 20% of light has been lost to coronagraph suppression (Bozza et al., 2016).

Since the conception of the optimised Lyot coronagraph a variety of additional coronagraphic techniques have been developed. They can be categorised into four broad classes (e.g., Guyon et al., 2006): amplitude-based Lyot coronagraphs, phase-based Lyot coronagraphs, pupil-apodization coronagraphs and interferometric coronagraphs. Each individual coronagraph is characterised by how it operates, its off-axis throughput and inner and outer working angles (IWA, OWA), angular separations at which off-axis throughput reaches half of the peak throughput. Typical coronagraph designs have IWAs of $\sim 2 - 4\ \lambda/D$ (Bozza et al., 2016). Planetary light is rapidly suppressed or obscured by residual starlight at separations approaching this IWA.

Amplitude-based coronagraphs improve on the original Lyot design by introducing band-limited masks e.g., band-limited coronagraph (Kuchner & Traub, 2002), in the image plane or by entrance pupil apodization e.g., Apodized Pupil Lyot Coronagraph

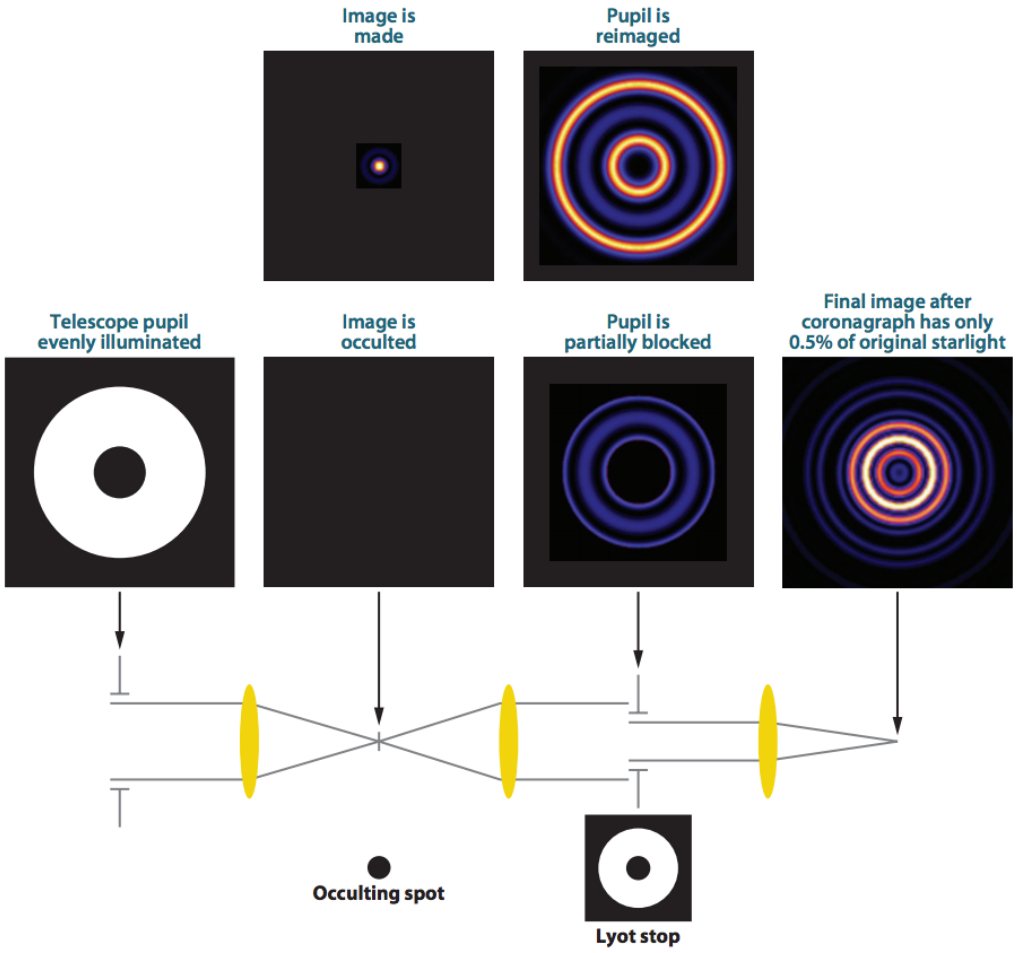

Figure 2.6: Schematic of a classical lyot coronagraph. The tops images display the stellar intensity distribution at each point along the optical train shown below. See text for details. Image: Oppenheimer & Hinkley (2009)

(APLC, Soummer et al., 2003). APLCs modify the standard entrance pupil with a tapered transmission mask, smoothly reducing the sharp discontinuity in wavefront profile at the edges of the telescope aperture, subsequently suppressing the amplitude of the diffraction rings. APLCs are currently in use on the most advanced imaging instruments such as SPHERE (Beuzit et al., 2008) and GPI (Macintosh et al., 2008). Phase-based coronagraphs similarly improve on the original Lyot design by introducing phase shifts to the wavefront in the focal plane, leading to the destructive interference of diffracted light leaking past the occulting mask. As the name implies, the 4-Quadrant Phase Mask (4QPM, Rouan et al., 2000) achieves destructive interference by positioning a four quadrant phase mask in the focal plane. The mask is transparent with adjacent quadrants differing in optical thickness by $\lambda/2$, introducing a π phase change to different wavefront segments which then are eliminated by in-

terference. A 4QPM is also available for coronagraphy on SPHERE and can achieve contrast ratios of 10^{-6} to 10^{-8}. Interferometric coronagraphs also work to attenuate the stellar PSF by destructively interfering on-axis light. For example the Achromatic Interferometric Coronagraph (Baudoz et al., 2000) achieves this using a beam splitter to introduce a π phase shift between two copies of the image resulting in destructive interference on their recombination. Pupil apodization coronagraphs (e.g., Kasdin et al., 2003) are characterised by the optimisation of the pupil transmission function to focus and suppress starlight, rather than making use of an occulting mask in the image plane as in Lyot coronagraphy.

Coronagraphy requires excellent wavefront stability, and is a very powerful tool when coupled with AO imaging. AO corrected, high contrast coronagraphic images acquired with e.g., GPI provide excellent sensitivity, enabling the detection of 51 Eri b, a ~ 2 M_J planet orbiting at ~ 13 AU from its F0 host (Macintosh et al., 2015). However, as was the case for 51 Eri b, further high-contrast techniques in addition to AO and coronagraphy are required to improve achievable imaging contrast and open up sensitivity to a broader range of planetary companions.

2.2.2 Angular Differential Imaging

Coronagraphy improves the contrast performance of imaging instruments by suppressing the diffraction peak reconstructed by AO. However, such systems significantly suffer from quasi-static speckles (see section 2.2), due to optical imperfections and misalignments within the telescope, AO module, coronagraph and camera system which severely limit imaging capability. Angular differential imaging (ADI, Marois et al., 2006) is an innovative high-contrast technique that attenuates this quasi-static speckle noise, facilitating the detection of faint planetary companions.

During conventional observations the science camera rotates, tracking a targets apparent rotation across the night-sky from the ground (due to the rotation of the Earth). In this fashion the orientation of the field is kept constant, and sequences of images can be easily combined. On the contrary, during an ADI sequence the instrument field derotator is switched off and the telescope pupil is fixed to the science camera. The fixed optical alignment of the telescope-instrument system locks the quasi-static speckle pattern to the pupil plane, improving stability of the PSF / speckle pattern throughout the sequence. However, as the camera no longer tracks the sky, the FOV rotates throughout the sequence, if an altitude-azimuth telescope

is used. Any unseen planetary companion to the target will also rotate with the field, providing a sequence of images in which the speckle pattern remains stable but where a planet would appear at different position angles. This rotation causes the planet to smear azimuthally during observation, slightly decreasing the PSF intensity, although this effect can be overcome with short exposure times relative to the rate of field rotation. For each image, a reference PSF is constructed and subtracted to remove quasi-static PSF structure. This reference is constructed from the stack of remaining images, either conventionally by computing the median of the image stack, or by more sophisticated post-processing algorithms (see section 2.3). If the FOV has rotated sufficiently throughout the sequence, the reference image will not contain any companion signal, and the planetary PSF will be preserved upon reference subtraction. Marois et al. (2006) have shown that subtraction of a conventional median reference can reduce quasi-static speckle noise by a factor of 5 in each individual image. After individual reduction, each image can be rotated to align the FOVs and then combined, providing an additional gain in signal to noise on the order of square root the number of individual images. A diagram of the ADI process is shown in figure 2.7.

Imaging with AO, coronagraphy and ADI is an immensely powerful planet detection tool. In fact, it has been employed by numerous direct imaging surveys, systematically achieving contrast ratios on the order of 10^6 across a broad range of targets (e.g., Lafrenière et al., 2007a; Biller et al., 2013; Brandt et al., 2014; Chauvin et al., 2015), enabling constraints to be placed on the wide giant population and facilitating the discovery of several companions, including the multiple planet system HR 8799 (Marois et al., 2008b, 2010) shown in figure 2.8. A variant of ADI is also possible from space, where the nominal roll across a space telescope orbit can provide several images of a target at different rotation angles, allowing PSF construction and subtraction whilst preserving any potential planetary signal (e.g., Janson et al., 2012b, 2015).

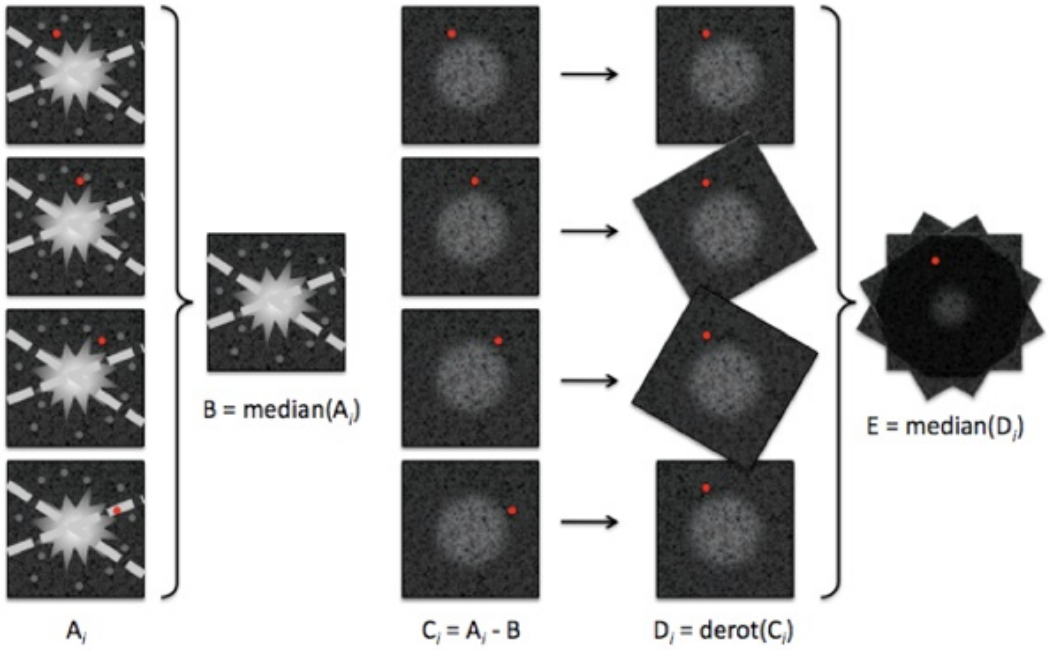

Figure 2.7: Diagram highlighting the crucial ADI steps. In the first panel, a series of A_j images are taken with the instrument field derotator switched off. The PSF and speckle pattern (grey dots) are fixed to the pupil plane and remain stable across the sequence. However a planetary companion to the target, highlighted in red, rotates with the field across the sequence. In the second panel, a median reference, B, is constructed from the A_j images and consequently contains no planetary signal. In the third panel, the median reference is subtracted from each individual image, removing the quasi-static PSF structure whilst leaving the planetary signal relatively unperturbed in a series of C_j images. In the final two panels the C_j images are rotated, aligning the FOVs in a series of D_j images which are then median combined, producing a final image, E, with increased signal to noise of the planetary companion. Image: Christian Thalmann

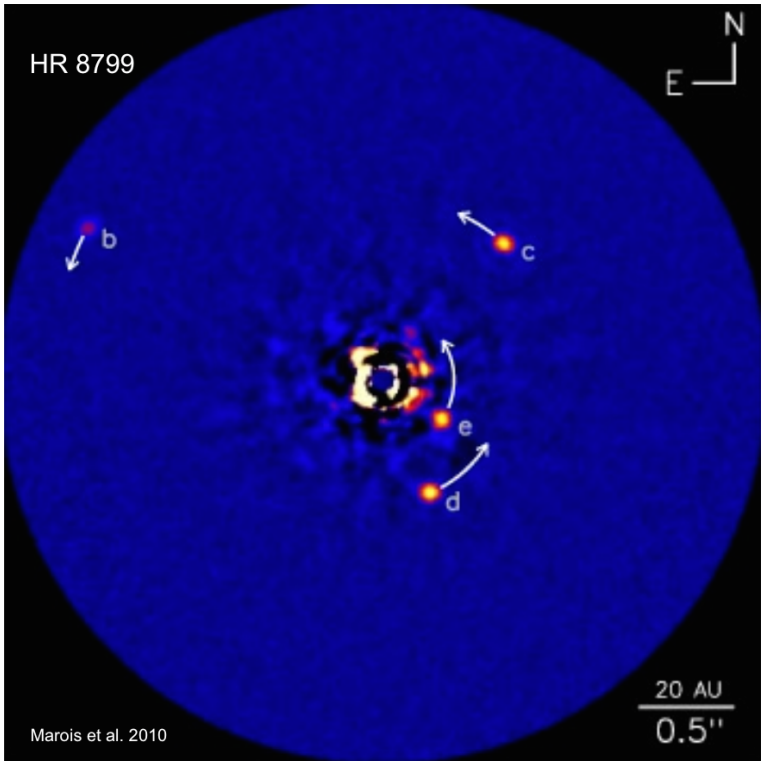

Figure 2.8: HR 8799 multiple planet system. Planets have separations on the order of 15, 25, 40, and 70 AU. Image taken with the Keck telescope using ADI with a LOCI PSF construction (see section 2.3). However, the three outer planets were previously detected using ADI with a median PSF construction. Image: Marois et al. (2010)

2.2.3 Chromatic Speckle Suppression

Chromatic speckle suppression refers to the suite of techniques which act to attenuate speckle noise by exploiting the chromatic behaviour of the speckle pattern and the contrasting spectral energy distributions of a host star and its planetary companion.

Simultaneous spectral differential imaging (SDI e.g., Racine et al., 1999; Marois et al., 2000) is one such technique which achieves speckle suppression by exploiting absorption or emission features due to molecules exclusively present in cool planetary atmospheres. Two images of the target are acquired across two narrow band filters closely separated in wavelength, one inside the absorption / emission feature, the other just outside. Any planetary companion for which this feature is present will be significantly brighter in one of the images whilst the stellar PSF and speckle pattern will be largely identical across both filters due to their narrow separation; if the images can be acquired simultaneously, ensuring no temporal speckle variation. This can be achieved for example using a Wollaston prism to split incoming light based on polarisation state, sending the two components down different optical paths, passing through the separate filters before being placed side by side on a detector. The two images can then be subtracted, removing the bulk of the stellar PSF and speckle pattern whilst preserving the majority of the planetary signal, and therefore improving the achievable contrast.

One molecule expected to be prevalent in cool planetary atmospheres is methane (e.g., Burrows et al., 2001; Geballe et al., 2002), and therefore narrow band filters inside (e.g., CH_4L: 1.643 μm to 1.788 μm) and just outside (e.g., CH_4S: 1.486 μm to 1.628 μm) the 1.6 μm methane absorption band are particularly suitable for SDI. SDI exploiting this absorption band has facilitated the discovery of a low mass sub-stellar companion (Biller et al., 2006), improved the contrast at small angular separations of typical imaging surveys when used in combination with ADI (Biller et al., 2013) and provided the detection of a deep methane absorption feature in the atmosphere of the previously detected planetary companion GJ 504 b (Janson et al., 2013). CH_4S and CH_4L band images of GJ 504 b acquired in SDI mode can be seen in figure 2.9.

Significantly increasing the spectral resolution of the observations allows speckle suppression via a somewhat different technique, spectral deconvolution (SD, Sparks & Ford, 2002). Speckle noise is chromatic and the pattern moves radially outward as a function of wavelength, as the PSF scales with λ/D. However, any true planetary

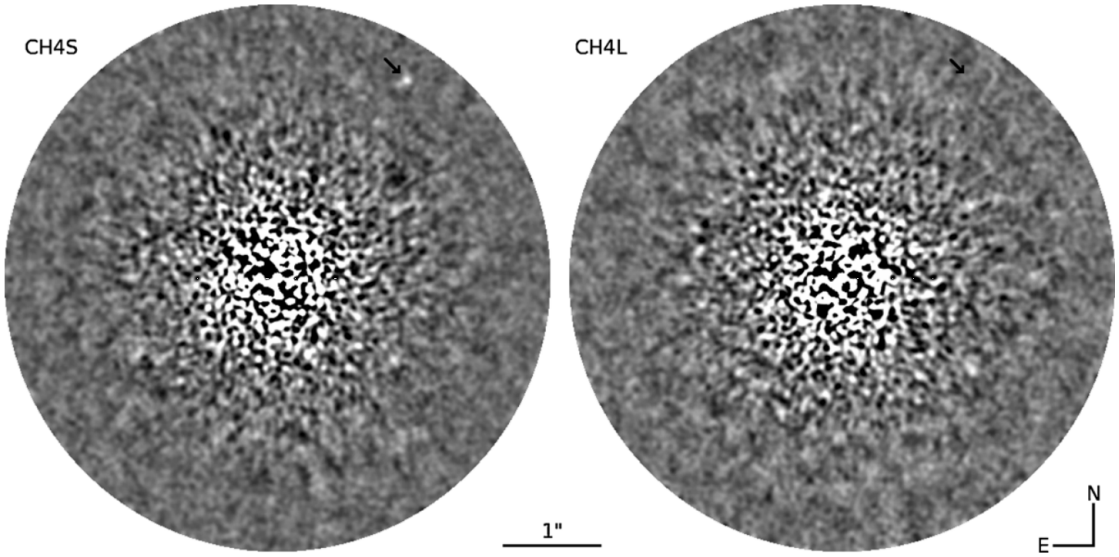

Figure 2.9: Simultaneous images of GJ 504 taken in CH_4S (left image) and CH_4L (right image) narrow band filters (Janson et al., 2013). Filters are closely separated in wavelength, however an ADI reduction has been performed contributing to the variance in the residual speckle noise between images. The planet, GJ 504 b, appears bright in the CH_4S band (outside methane absorption filter - top right of the image) but disappears entirely in CH_4L, indicating strong methane absorption.

companion will have a fixed position, independent of observing wavelength. Simultaneously imaging the target across a relatively broad range of spectral bands then produces a stack of images in which the speckle pattern moves radially out along diagonal paths whilst an orbiting planet remains stationary. SD achieves speckle suppression by subtracting any wavelength dependent artefacts. This is done by spatially scaling each spectral band image by a factor proportional to its wavelength. This spatial manipulation results in speckle alignment throughout the image stack and a radial drift in planet position as a function of wavelength. Similar to ADI, the speckle patterns and PSFs are now aligned and stable across each individual image, whilst the planetary signal location varies. A reference PSF can then be constructed from the image stack and subtracted from each individual image, removing the speckle pattern whilst preserving the planetary PSF. Each image can then be rescaled so the planet position remains fixed as a function of wavelength.

Simultaneous imaging across a broad range of spectral bands is possible with the use of an integral field spectrograph (IFS e.g., Berton et al., 2006), an instrument with a spatially segmented FOV which disperses incoming light to generate spatially resolved, low-resolution spectra. IFSs generate image data cubes in which spatial in-

formation is contained along two dimensions and spectral information along the third. With SD achieving speckle and PSF subtraction, this data cube provides a wealth of information on any resolved planetary companion, allowing spectral characterisation without the need for follow-up observations, any a priori knowledge on planetary location or assumptions on spectral features (e.g. methane absorption). SD using the IFS on SPHERE is capable of reaching contrast ratios on the order of $\sim 10^{-6}$ (Mesa et al., 2015), enabling the spectral characterisation of the planetary object 51 Eridani b (Samland et al., 2017).

2.3 Post-Processing Algorithms

As discussed in section 2.2, speckle suppression techniques such as ADI, SDI and SD act to improve achievable contrast and enhance imaging capability through reference PSF subtraction. This reference is constructed from a library of PSF's, typically imaged at neighbouring states of the telescope-instrument system (e.g., fixed optical alignment observations over a period of time, ADI, or simultaneous observations at different wavelengths, SDI, SD), such that speckle noise is attenuated whilst planetary signal is preserved upon subtraction. Conventional PSF construction is made from taking a pixel-wise median of the library stack, which will effectively represent the stable speckle pattern whilst not containing any planetary signal, if the library has been assembled using one of the aforementioned suppression strategies.

However, as instrumentation and observing strategies continually improve, more efficient methods of PSF modelling are required in order to overcome residual speckle noise limitations and take full advantage of higher quality data. This has led to the development of several sophisticated, empirical post-processing algorithms which generate optimised reference PSF's for each target image, effectively modelling individual PSF variance, providing an optimal PSF / speckle subtraction and further enhancing sensitivity to any faint planetary companions. Two main families of high-contrast algorithms have been developed and are in widespread use across a variety of imaging surveys.

One family of algorithms is the Locally Optimised Combination of Images (LOCI, Lafrenière et al., 2007b). LOCI builds a reference PSF specific to each individual image through the linear combination of library PSF's. The linear coefficients of each library PSF are optimised using a least-squares fit to minimise the residual noise upon

subtraction. This optimisation is computed independently in local subsections across the target image, as the correlation between the target PSF and an individual library PSF will vary as a function of position, i.e. a library PSF may effectively represent the target PSF at a particular separation but exhibit relatively large variation at other separations (due to e.g. speckle evolution). LOCI is a powerful alternative to conventional PSF construction, providing a factor of ~ 3 improvement in sensitivity at small angular separations in ADI reductions (Lafrenière et al., 2007b) which enabled the detection of HR 8799 e (Marois et al., 2010), the inner most planet in the HR 8799 system (see figure 2.8). LOCI can also be readily applied to SD reductions using IFS (e.g., Pueyo et al., 2012).

The second family of algorithms is Principal Component Analysis (PCA, Soummer et al., 2012; Amara & Quanz, 2012). Similar to LOCI, individual model PSF's are constructed from a linear combination of references. However, for PCA these references are not individual library PSF's, but rather the principal orthogonal components of the entire library stack. These principal components are sets of orthonormal basis, linearly independent sets of vectors that span the image dimensions, and represent features that occur systematically throughout the data. The first few of the components contain the most common and stable structures with the least noise throughout the library stack, e.g., the diffraction core of the PSF, prominent quasi-static speckles and spider features (spike-like features caused by diffraction around the physical structure holding the secondary telescope mirror in place). Each individual target image can be reconstructed from a linear combination of the library principal components and the linear coefficients can be calculated by projecting the target onto each basis set. Decomposition of the reference library into its principal components can be achieved through singular value decomposition (PynPoint, Amara & Quanz, 2012) or a Karhunen-Loéve transform (KLIP, Soummer et al., 2012). An example of a PCA PSF construction highlighting individual principal components can be seen in Figure 2.10. Whilst Amara & Quanz (2012) have shown that PCA can provide a factor of five sensitivity improvement at small angular operations with respect to LOCI, other studies have found comparable PSF and speckle suppression between the two. However, the PCA algorithm offers a significant speed enhancement in image reduction over LOCI (e.g., Soummer et al., 2012; Janson et al., 2015), as once the orthonormal basis sets have been generated the linear coefficients can be calculated with relatively minimal computational burden via target projection.

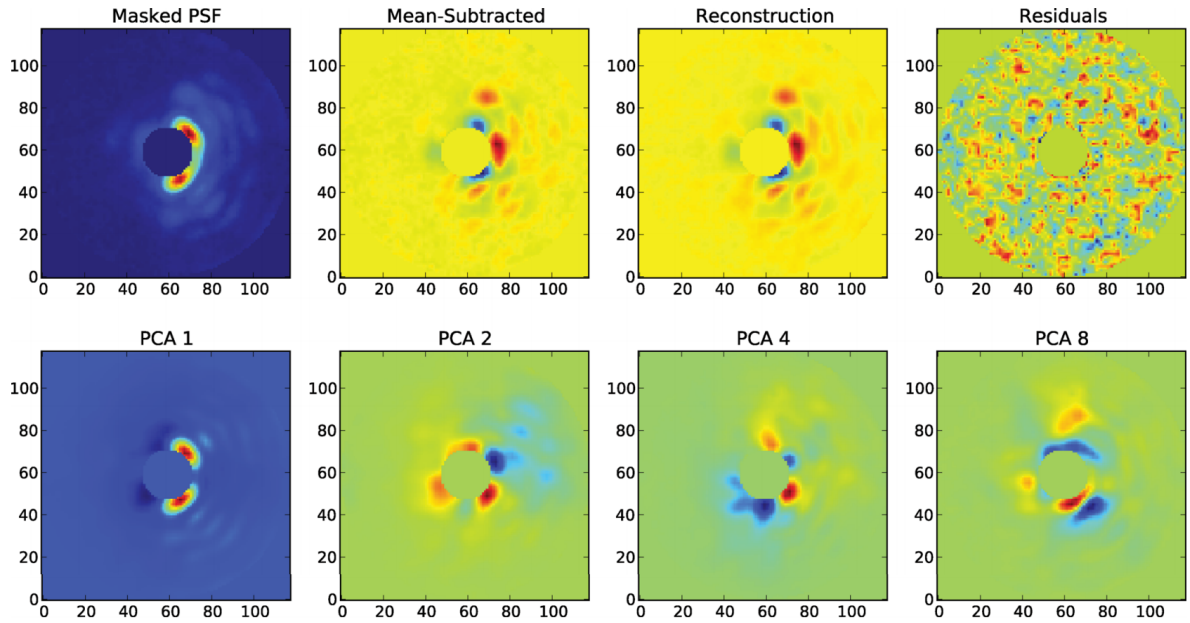

Figure 2.10: Example of PCA PSF construction using Pynpoint (Amara & Quanz, 2012). The top left panel shows an individual masked target PSF taken from a library assembled through ADI. The second top panel shows the same PSF with the pixel-wise average library PSF subtracted. The third top panel shows the optimal reference PSF constructed using 100 PCA modes. The construction effectively represents the targets residual speckle and PSF features leaving minimised residuals upon subtraction, these residuals are shown in the final top panel. The bottom panels highlights four examples of various PCA modes, the principal components of the library stack. Each component represents different PSF and speckle features that occur systematically throughout the data.

Therefore, in this thesis where I investigate the planetary population at separations beyond 100 AU by enhancing high contrast imaging capability from space, I favour the use of a PCA post-processing solution over LOCI. As will be described in Chapter 3, this investigation will involve the reanalysis of archival Spitzer imaging surveys. Studies with Spitzer by Janson et al. (2015) have found a KLIP-based algorithm to provide image reduction with a signal-to-noise ratio greater than a factor of ≈ 2 than that achievable with Pynpoint. Therefore, I focus on a KLIP based analysis in my subsequent investigations. A more detailed mathematical description of the KLIP algorithm is given below.

2.3.1 PCA - KLIP

The KLIP algorithm is formulated as follows. Any astronomical PSF can be understood as an N-dimensional stochastic function representative of the state of the telescope-instrument system, ψ, and therefore dependent on factors such as observing wavelength, optical alignment, temperature, wavefront distortion, exposure time, stellar magnitude etc. In the first stage of the KLIP reduction, each two dimensional image in the library is collapsed into a one dimensional array of n pixels. The intensity distribution of any PSF can then be written as;

$$I_{\psi}(n) = I(n, \psi) \tag{2.5}$$

Any target that contains a faint astronomical signal, $A(n)$, that could potentially be due to a planetary companion, can then be written as;

$$T(n) = I_{\psi_0}(n) + A(n) \tag{2.6}$$

Whilst the set of N_R reference PSF's, assembled through some speckle suppression method, can be written as;

$$\{R_k(n) = I_{\psi_k}(n)\}_{k=1.....N_R} \tag{2.7}$$

ψ_0 and ψ_k represent realisations of the state of the telescope-instrument system for the target PSF and library of reference PSF's respectively. With the library typically assembled at neighbouring states of the telescope-instrument system, $|\psi_i - \psi_j| < \delta$ for all $i, j \in [0, N_R]$ where δ is small (but may be adjusted to suit the needs of individual studies). This ensures the PSF and speckle pattern remain stable across the library and principal components that effectively model the target PSF can be generated. References are selected so that they do not contain any bright astronomical signal within the area in which PCA is to be performed (optimisation region) to prevent

the generation of PCA modes containing the signal which could lead to subtraction of any real companion PSF within the target image, or the injection of a fake PSF, mimicking a planetary companion.

The next step in the KLIP algorithm is to subtract a pixel-wise mean library image from the target image and library stack. As the images are of zero mean over the optimisation region, the orthogonal basis set that produces an optimal reconstruction of $I_{\psi_0}(n)$ can be computed with a Karhunen-Loéve transform (Karhunen, 1947; Loève, 1948) of $\{R_k(n)\}_{k=1.....N_R}$;

$$Z_k(n) = \frac{1}{\sqrt{\Lambda_k}} \sum_{p=1}^{N_R} c_k(\psi_p) R_p(n) \tag{2.8}$$

Where Z_k is the optimal orthonormal basis set, $c_k(\psi_p)$ and Λ_k are the eigenvectors and eigenvalues respectively of the N_R-dimensional covariance matrix of the reference stack $\{R_k(n)\}_{k=1.....N_R}$. Whilst increasing the number of orthonormal bases, PCA modes, used for PSF construction helps to remove a greater portion of the PSF and speckle pattern, it also adds to the background noise and subtracts a greater portion of any planetary signal. However, as the first few PCA modes contain the most dominant, common structures throughout the reference stack, with each subsequent mode representing realisations of the PSF of decreasing importance, the number of modes used in the reduction can be truncated and optimised to provide a favourable trade-off between PSF subtraction, background noise and planetary throughput (e.g., Meshkat et al., 2014; Wahhaj et al., 2015). This optimisation can be performed by injecting synthetic planet signals into target images and evaluating signal-to-noise upon reduction as a function of number of PCA modes. The coefficient of each PCA mode is then computed by projecting the target image onto each orthonormal base. As the modes are combined linearly, the optimal realisation, $\hat{I}_{\psi_0}(n)$, of the target PSF, $I_{\psi_0}(n)$, is given by;

$$\hat{I}_{\psi_0}(n) = \sum_{k=1}^{K_{klip}} < T(n), Z_k(n) > Z_k(n) \tag{2.9}$$

Where K_{klip} is the truncated number of PCA modes ($K_{klip} < N_R$) and $< T(n), Z_k(n) >$ is the inner product of $T(n)$ and $Z_k(n)$ i.e. the target projection onto the orthonormal base ($T_1 Z_{k1} + T_2 Z_{k2} + ... + T_n Z_{kn}$) . The final reduced image, F(N), providing PSF and speckle subtraction with minimised residuals, enhancing detectability of any potential planetary signal ($A(n)$), is simply calculated by;

$$F(N) = T(n) - \hat{I}_{\psi_0}(n) \tag{2.10}$$

2.4 Imaging Limitations - Study Motivation

In this section I further expand on two specific limitations faced by the direct imaging field, leading to the motivations behind the investigations presented in this thesis; a survey probing and statistically constraining the planetary population beyond 100 AU, through enhancing high contrast imaging capability from space, and an investigation into a population of low mass M-dwarf binaries contributing to the eventual derivation of isochronal age estimates that can then be applied to the full YMG of which they are members.

2.4.1 High Contrast Imaging with Spitzer

As discussed in section 1.1, the plethora of confirmed exoplanets to date is dominated by a population within 5 - 6 AU of their host star, accounting for $\sim 95\%$ of the entire population. This sample enables statistically significant trends to be uncovered between planetary/host star properties and planet frequency, which in turn allows for planet formation and evolution theories to be stringently tested and constrained. However, formation scenarios and evolutionary paths for wide giant planets with separations $>> 5 - 6$ AU continue to prove challenging to constrain. This is due to a lack of systematic explorations by surveys with a sufficient degree of sensitivity and statistically robust population analyses.

Direct imaging provides the most viable technique to probe for giant planets at such wide separations. Extensive work has been carried out to expand the sample of wide giant planets through detection in large-scale direct imaging surveys (e.g.,

Masciadri et al., 2005; Biller et al., 2007; Kasper et al., 2007; Lafrenière et al., 2007a; Chauvin et al., 2010; Ehrenreich et al., 2010; Leconte et al., 2010; Carson et al., 2011; Janson et al., 2011; Delorme et al., 2012; Vigan et al., 2012; Biller et al., 2013; Chauvin et al., 2015; Bonavita et al., 2016; Vigan et al., 2017). While these surveys typically record non-detections, several planetary mass wide companions have been found, indicating that although these types of planets may be rare (e.g., Nielsen & Close, 2010), they do exist with some frequency throughout the galaxy. By subjecting these imaging surveys to statistical analysis, an upper limit on this frequency can be determined. Concurring frequency upper limits have been found for wide giant planets over a separation range on the order of $10^1 - 10^2$ AU, corresponding to the parameter space at which observations are sensitive to Jupiter mass companions. Examples of these limits for companions in the mass range $\sim 1 - 13$ M_J are shown in table 2.1.

Table 2.1: Wide Planet Frequency Upper Limits

		Planet Frequency	
Mass Range (M_J)	Separation Range (AU)	Fractional Upper Limit	Study
0.5 - 13.0	50 - 250	0.093	(Lafrenière et al., 2007a)
0.5 - 13.0	25 - 100	0.110	(Lafrenière et al., 2007a)
1.0 - 13.0	20 - 150	0.100	(Chauvin et al., 2010)
1.0 - 20.0	10 - 150	0.060	(Biller et al., 2013)

Sensitivity is confined to this separation range due to instrumental limitations. Imaging surveys typically favour the use of AO corrected instruments on 8m class ground-based telescopes. The high angular resolution afforded by such instruments provides sensitivity to planetary mass companions at small separations, down to the order of 10 AU, inside of which the required contrast becomes unachievable as one approaches the core of the near diffraction limited PSF. The outer sensitivity limit stems from anisoplanatism (see section 2.1.2) , where AO delivers poor wave front correction at increasing separation due to the different propagation paths and hence varying wave front distortion experienced by off-axis light. This substandard correction results in a decrease in image quality and therefore a reduction in sensitivity at

large separations. Typical values for the isoplanatic angle, where distortion is statistically uniform allowing for good AO correction, are $10'' - 20''$ in the near-infrared (Sandler et al., 1994; Fritz et al., 2010), and thus imaging instruments are typically restricted to this FOV where AO offers optimal wavefront correction. Examples of the FOVs for several imaging studies that have availed of a variety of telescopes, instruments, and instrument modes (speckle suppression methods) are shown in table 2.2. This table does not include ongoing surveys with the most advanced imaging instruments, such as SHINE with SPHERE on the VLT (e.g., Chauvin et al., 2017) which utilises the IRDIS dual-band imager with a FOV of $11'' \times 11''$.

Table 2.2: Imaging Survey FOV

Study	Telescope	Instrument	Mode	FOV (" × ")
(Biller et al., 2007)	VLT	NaCo	SDI	5 × 5
(Kasper et al., 2007)	VLT	NaCo	Sat-Im	28 × 28
(Lafrenière et al., 2007a)	Gemini-N	NIRI	ADI	22 × 22
(Vigan et al., 2012)	VLT	NACO	ADI	14 × 14
(Biller et al., 2013)	Gemini-S	NICI	Cor-ASDI	18 × 18
(Brandt et al., 2014)	Subaru	HiCIAO	ADI	20 × 20

Sat-Im: saturated imaging, Cor-ASDI: coronagraphic imaging with ADI and SDI.
Table modified from Chauvin et al. (2015).

Conducting imaging surveys from space-based telescopes would negate this effect and provide a large FOV; however, as previously mentioned their small aperture diameters produce large diffraction limited PSF's, severely limiting their application for direct imaging of exoplanets. Still, Marengo et al. (2006, 2009) have shown that the Spitzer space telescope is capable of sensitivity to planetary mass companions at large angular separations with their studies of ϵ Eri and Fomaulhaut. Recent studies of Vega, Fomalhaut, and ϵ Eri by Janson et al. (2012b, 2015) have demonstrated that sensitivity to planetary mass companions is achievable with Spitzer within the PSF noise-limited regime, with the application of sophisticated high-contrast reduction techniques.

Therefore, I envisioned the implementation of a sophisticated post-processing solution, PCA - KLIP, in order to subtract the large-scale PSF structure associated with Spitzer and enhance the sensitivity of archival imaging surveys, enabling sensitivity to planetary mass companions over a separation on the order of $10^2 - 10^3$ AU. This parameter space has not previously been systematically explored by surveys to a sufficient degree of sensitivity, leaving the population of giant planets at these separations poorly constrained.

The origin of such wide orbit planets remains challenging to explain, but their detection, e.g., 1RXS J1609-2105 b, 330 AU (Lafrenière et al., 2010); FW Tau b, 330 AU (Kraus et al., 2014a); HD106906 b, 650 AU (Bailey et al. 2014); and GU Psc b, 2000 AU (Naud et al., 2014), 2M2126b; $>$ 4500 AU (Deacon et al., 2016), has fueled the theory of novel formation and migration mechanisms (see section 1.2). Constraining the population of giant planets at separations of $10^2 - 10^3$ AU is essential for assessing the relevance of these theories, and allowing for stringent constraints to be placed on formation and evolution modes out to thousands of astronomical units. As previously discussed, this is of critical importance to the interpretation of substellar companions; a better understanding of formation pathways, and the observationally detectable imprints they leave on companions, may provide a much more robust method of differentiating between exoplanet and brown dwarf populations than a deuterium burning mass cut-off.

In this thesis I present the results of a re-analysis of archival Spitzer imaging surveys with enhanced sensitivity and the first robust constraints on the population of $0.5 - 13$ M_J over separations of 100 - 1000 AU.

2.4.2 AstraLux Multiplicity Survey

Low-mass stars in multiple systems are increasingly playing an important role in stellar astrophysics. Statistically constraining their multiplicity characteristics and population properties provides clues on their formation and evolutionary pathways (e.g., Burgasser et al., 2007; Bate, 2012; Duchêne & Kraus, 2013), potentially connecting higher mass stars to brown dwarfs (e.g., Luhman et al., 2007; Chabrier et al., 2014). The identification and characterisation of low-mass multiples is also highly relevant to several fields of exoplanet study, particularly direct imaging. For example, imaging surveys typically exclude visual binaries (Lafrenière et al., 2007a; Janson et al., 2011; Vigan et al., 2012; Rameau et al., 2013; Vigan et al., 2017) due to the

intricacies of planet detection within the combined PSF patterns of multiple stars, alongside the formation and long-term stability barriers faced by any possible planet orbiting such systems. Recently however, efforts have also been made to probe the population of wide separation circumbinary planets through dedicated imaging studies of stellar multiples (e.g., Thalmann et al., 2014; Bonavita et al., 2016). Binary identification aids target selection for such studies.

As discussed in section 1.1.4, also of fundamental importance to any imaging study is a good estimate of target age. This is critical for estimating the mass or initial entropy of planets and brown dwarfs using mass-luminosity evolutionary models. Such objects are maximally hot, and therefore luminous, directly after formation and gradually cool – becoming less luminous as the planet ages (Baraffe et al., 2003; Burrows et al., 2003; Fortney et al., 2008). Imaging surveys therefore typically target stars in $\sim 10 - 100$ Myr YMGs (e.g Biller et al., 2013; Brandt et al., 2014; Durkan et al., 2016), where any planet will be equivalently young and therefore luminous, offering the best chance of detection. YMGs also provide age estimates of stars that are potentially much more reliable than any accessible technique for individual stars, translating to a more reliable and precise mass estimate of any imaged companion using age dependent mass-luminosity evolutionary models (e.g., Baraffe et al., 2003, 2015).

However, uncertainties remain in the ages of YMGs. For instance, the age estimates in the AB Dor (e.g. Torres et al., 2008; Barenfeld et al., 2013; Bell et al., 2015) and USco (de Zeeuw et al., 1999; Pecaut et al., 2012; Song et al., 2012) associations vary by more than a factor of two between the lowest and highest reasonable estimates in the literature. Even self-consistent YMG studies produce age determinations with large uncertainties, emphasising the inherent difficulty in estimating ages. For example, the YMG age estimates of Bell et al. (2015) are shown in table 2.3. These age uncertainties, although relatively small compared to field star ages, dominate the mass uncertainty of an imaged sub-stellar companion and can lead to disparity in the mass estimates of analogous studies, potentially furthering ambiguity to its interpretation as a planet or brown dwarf. For example, Delorme et al. (2013) derive a deuterium burning boundary, $\sim 12 - 14$ Jupiter masses for the sub-stellar companion J01033563-5515561(AB)b using a system age of 30 Myr adopted from the Tucana-Horologium (Tuc-Hor) age reported in Torres et al. (2008), of which the host is a high probability member. However Janson et al. (2017) derive a $\sim 15-20$ Jupiter

mass for the companion using a Tuc-Hor age of $\sim 40 - 50$ Myr adopted from Bell et al. (2015). Clearly a better understanding of YMG ages is essential for more robust constraints to be placed on companion masses.

Table 2.3: Bell et al. (2015) YMG ages

YMG	Age (Myr)
AB Dor	130 - 200
β Pic	21 - 27
Carina	38 - 56
Columba	8 - 14
Tuc-Hor	41 - 49
TW Hya	7 - 13

In this regard, YMG M-dwarf multiples can be very useful. As M-dwarfs have long pre-main sequence lifetimes ($\sim$ 100 Myr Baraffe et al., 1998), they are continually evolving along a mass-luminosity track throughout the YMG phase, providing ideal laboratories for precise isochronal dating. Such dating analysis can be conducted using spectral properties alone; bolometric luminosity and effective temperature (e.g., Janson et al., 2007), however, the large degree of uncertainty in the ultra-cool M-dwarf temperature scale introduces a source of systematic error into the analysis. Relating a model independent mass, such as dynamical masses derived from orbitally monitoring M-dwarf multiples, to luminosity allows for a much more robust isochronal analysis. This has been demonstrated for a few YMG binaries (e.g., Bonnefoy et al., 2009; Köhler et al., 2013; Montet et al., 2015) however, a broader comprehensive study is of fundamental importance to cover a wider sample of YMGs and to assess dating robustness and coevality within individual YMGs. Model independent M-dwarf masses can also be derived through high precision photometric and spectroscopic observations of double-lined, eclipsing binaries (e.g., Zhou et al., 2014, 2015). However, such systems are rare and typically much older than any YMG and the M-dwarf $\sim$ 100 Myr pre-main sequence lifetime.

Precise dynamical M-dwarf masses are also essential for calibrating low-mass stellar models. This is particularly relevant in the era of earth sized planet discovery in 'temperate orbits' around low-mass hosts (e.g., Quintana et al., 2014; Anglada-Escudé et al., 2016; Gillon et al., 2017), where a better understanding of the stellar physical properties will allow more reliable planetary parameters to be derived.

These arguments for low-mass multiplicity studies and binary characterisation have motivated our AstraLux Large M-dwarf Multiplicity surveys, systematic lucky imaging studies of > 1000 X-ray active young M-dwarfs, many of which are also high probability YMG members (e.g., Bergfors et al., 2010; Janson et al., 2012c, 2014b, 2017). As one would expect roughly 30% of these were identified as multiple systems, significantly increasing the number of close YMG M-dwarf binaries. The continual astrometric monitoring of these systems will allow orbital parameters to be stringently constrained with the aim of deriving dynamical masses for individual components. This has recently been achieved by Calissendorff et al. (2017) for the young triplet 2MASS J10364483+1521394. A combined dynamical mass of 0.48 ± 0.14 $M_{\odot}$ and a mass ratio of 1.00 ± 0.03 was derived for the low-mass pair orbiting the M-dwarf primary, allowing for an isochronal analysis of this system using resolved photometry. This isochronal analysis is shown in figure 2.11. Exploiting such dynamical masses for model calibration and YMG age dating is the underlying goal of our AstraLux multiplicity surveys.

However, astrometric monitoring alone is often not enough to derive precise dynamical masses and enable a robust isochronal analysis, a complementary RV analysis is equally important for a range of purposes. Whilst relative astrometry provides the means to constrain orbital parameters, it is limited to providing the total system mass. An RV analysis provides information about the mass ratio of the system, allowing individual component masses to be derived when coupled with the astrometric information. RV data also provides a third dimension of information, outside the plane of the sky, providing much stronger constraints on mutual orbital parameters (e.g. period, eccentricity, argument of periapsis etc.) in a shorter timeframe than would be possible with either method in isolation (Tuomi et al., 2009). An additional importance to the RV observations is the ability to efficiently detect further close companions in the system that are unresolved in the images. Identifying such companions is of critical importance for isochronal analysis as any unresolved

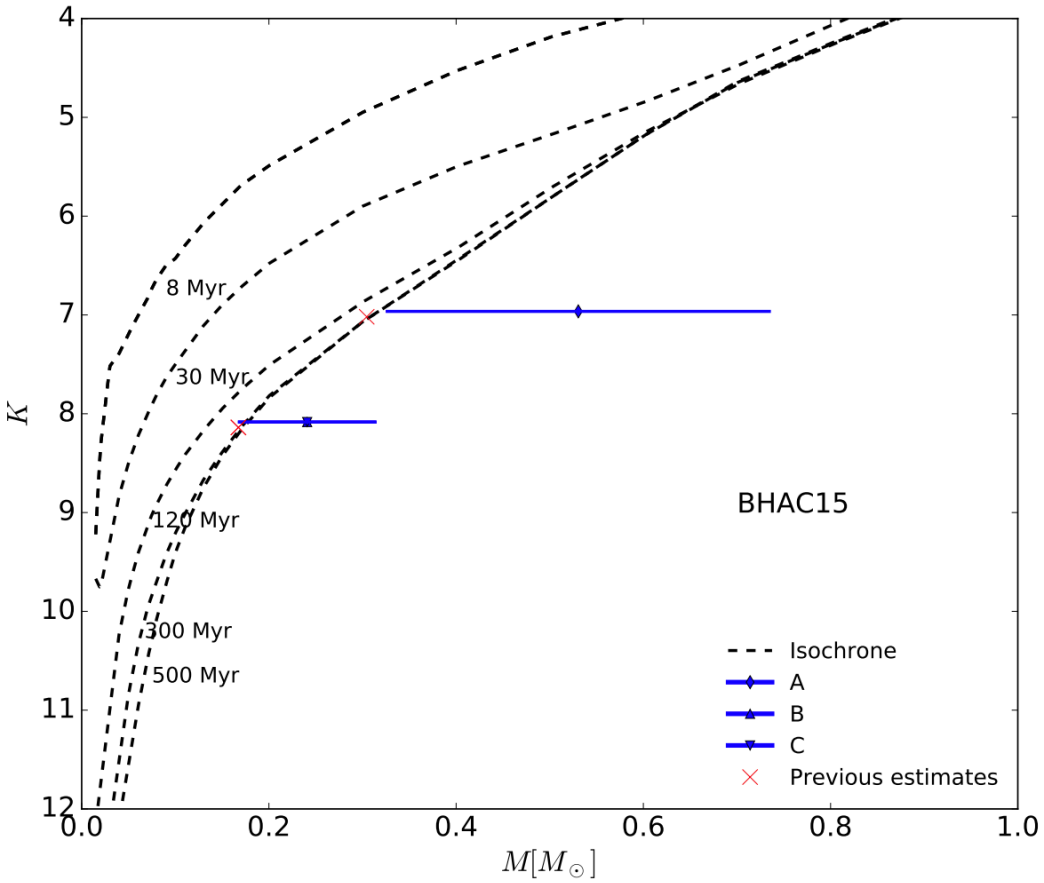

Figure 2.11: Ursa-Major moving group triplet 2MASS J10364483+1521394 individual component mass and magnitude plotted against BHAC15 (Baraffe et al., 2015) evolutionary models with isochrones ranging from 8-500 Myr (Calissendorff et al., 2017). Isochrones are well separated in such a plot allowing for precise age dating. However, the discrepancy between dynamical and theoretical masses for J1036 noted in this work, in addition to the large mass uncertainty dominated by the error from the distance measurement (20.1 ± 2.0 pc), makes it difficult to place an age estimate on this particular system based solely on photometry. Resolved bolometric luminosities would enable a much more robust isochronal analysis. Note, B and C components have a mass ratio of 1.00 ± 0.03 and therefore the data points overlap in this figure.

pair treated as a single star will lead to an incorrect age estimate or model calibration.

Motivated by this reasoning we have conducted an RV monitoring survey of high-utility M-dwarf binaries to complement our astrometric observations. In this thesis I present RV measurements we have derived for a sample of binaries over several epochs, highlighting new discoveries and a population analysis of the data. A demonstration of a preliminary isochronal analysis of the M-dwarf binary GJ 3305AB, a wide companion to the exoplanet host 51 Eri, is also presented.

Chapter 3

High Contrast Imaging with Spitzer I: Archival Re-analysis

The contents of chapter 3 and 4 have been published in the Astrophysical Journal, Volume 824, as the paper entitled 'High Contrast Imaging with Spitzer: Constraining the Frequency of Giant Planets out to 1000 AU Separations' (Durkan et al., 2016). All of the work presented is my own. In this chapter I present the results of a re-analysis of archival Spitzer imaging surveys with enhanced sensitivity. I give a description of the Spitzer space telescope and target sample, before detailing the observations, data reduction and PSF subtraction. I then present the survey sensitivity limits, highlighting the sensitivity improvement provided with PCA, and the results of planet candidacy vetting.

3.1 Spitzer Space Telescope

Spitzer (Werner et al., 2004) is the final member of NASA's family of 'Great Observatories' a group of four space based facilities designed to carry out astronomical investigations over a broad range of wavelengths i.e., the Hubble Space Telescope (visible), Compton Gamma Ray Observatory (gamma ray), Chandra X-Ray Observatory (X-ray) and Spitzer Space Telescope (infrared). Spitzer was launched on 25^{th} August 2003 into an Earth-trailing heliocentric orbit. It is an infrared telescope consisting of three instruments; the Infrared Array Camera (IRAC, Fazio et al., 2004), capable of broad band imaging at 3.6, 4.5, 5.8 and 8.0 μm, the Infrared Spectrograph (IRS, Houck et al., 2004), capable of low (R $\sim 60 - 130$) and moderate (R ~ 600) resolution spectroscopy between ~ 5 and 40 μm, and the Multiband Imaging Photometer for Spitzer (MIPS, Rieke et al., 2004), capable of broad band imaging at 24, 70 and 160 μm as well as low-resolution spectroscopy between ~ 55 and 95 μm. A liquid

helium coolant was employed to cool these instruments to temperatures of $\sim$ 5.5 Kelvin, ensuring optimal instrument performance by preventing thermal infrared radiation due to heat generated by the telescope itself from flooding the detectors. A schematic of the telescope is shown in figure 3.1. Designed for a lifetime of five years, the helium coolant was depleted in May 2009. However, whilst MIPS and IRS are no longer functional, the 3.6 and 4.5 μm IRAC cameras remain operational. With relatively warmer conditions ($\sim$ 30 Kelvin) this phase of the mission became known as the 'warm' phase, whilst the pre-May 2009 period became known as the 'cryogenic' phase. 13 years after its launch and well beyond its envisioned lifetime, NASA granted the mission a two and half year extension in October 2016 in what it has called the 'beyond' phase.

Whilst Spitzer's array of instruments enable explorations into a broad range of astrophysical phenomena, most relevant to exoplanet imaging is the IRAC, particularly the 4.5 μm camera. Based on evolutionary model predictions, non-irradiated jovian mass planetary companions are at their peak luminosity within the 4.5 μm band (e.g., Baraffe et al., 2003). Complemented by Spitzer IRACs exquisite infrared sensitivity at 4.5 μm, this channel potentially offers excellent planet detection capability. A further benefit to direct imaging with Spitzer IRAC is its FOV. As Spitzer does not suffer from the anisoplanatism limitations of ground based, AO assisted imagers (restricting FOV's to the order of $10'' - 20''$), IRAC can afford a large FOV, $5.2' \times 5.2'$ (on the order of 10^3 larger than the SPHERE IRDIS FOV). Spitzer IRAC therefore provides an ideal tool to probe the planetary population at wide separations out to 1000s of AU, facilitating planet detection within a previously elusive parameter space and enabling stringent constraints to be placed on the wide giant population.

However, Spitzers relatively small telescope diameter, 0.85 m, ensures a large diffraction limited PSF. At 4.5 μm the PSF FWHM is $1.72''$ during the cryogenic phase and rising to $2.02''$ during the warm phase of the mission. This broad PSF has previously severely limited Spitzer's direct imaging capability. Still, Marengo et al. (2006, 2009) have shown that the Spitzer space telescope is capable of sensitivity to planetary mass companions at large angular separations with removal of the stellar PSF by subtracting observations taken at two different roll angles (see section 2.2.2). Recent studies of Vega, Fomalhaut, and ϵ Eri by Janson et al. (2012b, 2015) have demonstrated that sensitivity to planetary mass companions is achievable with Spitzer within the PSF noise-limited regime with the application of sophisticated

high-contrast reduction techniques, namely multi-roll angle ADI accompanied by a PCA reduction. They attained sensitivity down to ~ 2 M_J at 150 AU for Vega and ~ 1 M_J at 30 - 35 AU for ϵ Eri, although these stars are very nearby which places even modest physical separations at large angular separations.

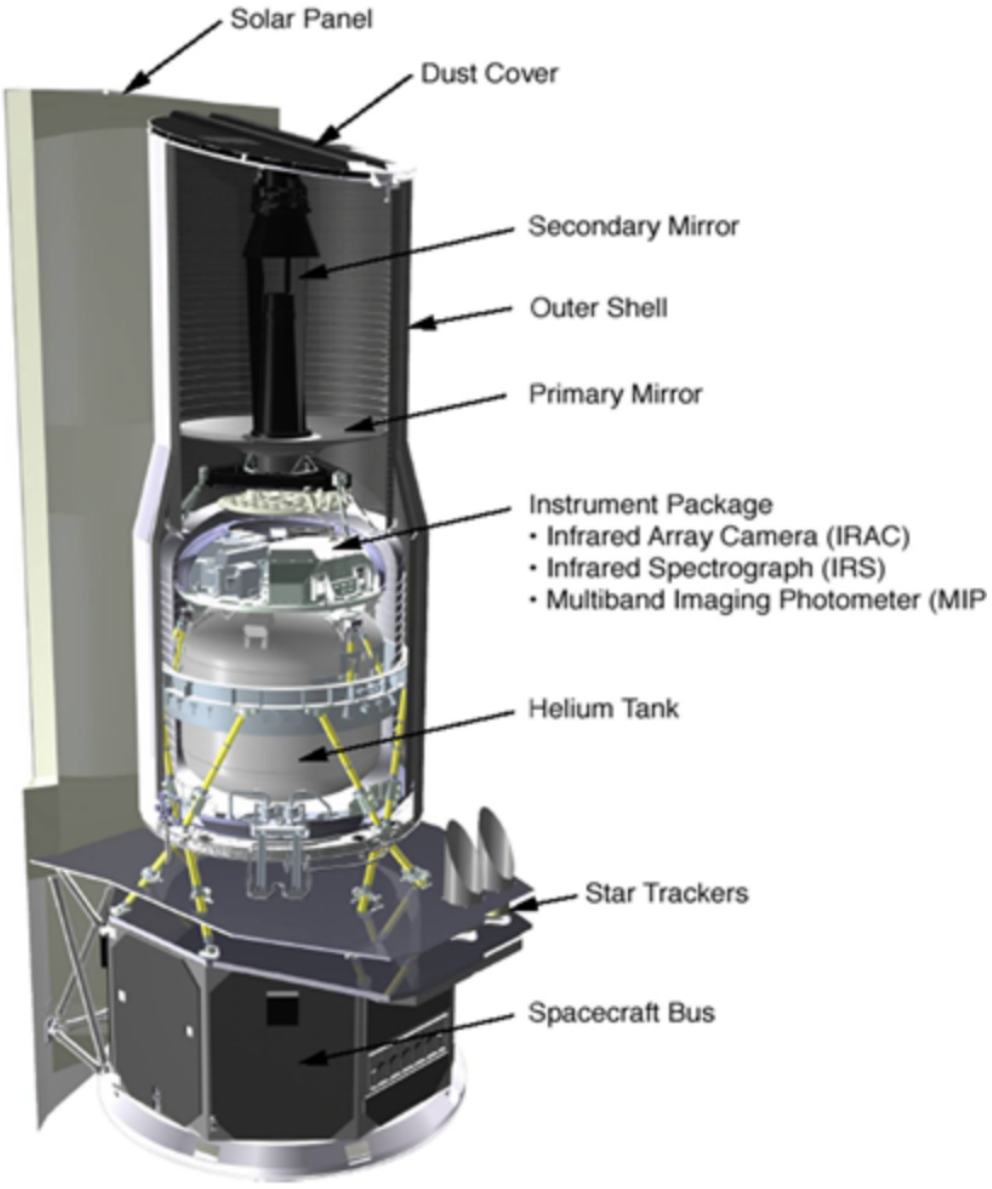

Figure 3.1: Spitzer space telescope schematic. The outer shell encompasses the Cryogenic Telescope Assembly (CTA) which holds the telescope, the instruments and the helium coolant. The spacecraft bus houses the avionics, power and telemetry components. The dust cover was jettisoned several days after launch. Image: Spitzer Telescope Handbook - Schuyler Van Dyk

Extending these high-contrast studies with Spitzer to a much broader sample of targets will significantly enhance the prospect of exoplanet detection at separations beyond 100 AU and enable robust population analyses that will place constraints on the planet population out to 1000's of AU, a statistic currently lacking and of vital importance to assessing the relevance and constraining various planet formation and evolution modes. Such studies are also ideal precursors to future imaging surveys with Spitzer's successor the JWST (due for launch 2019), aiding in target selection and optimising post-processing algorithms for space based imaging. Therefore, I implemented a sophisticated post-processing solution, PCA - KLIP, in order to subtract the large-scale PSF structure associated with Spitzer and enhance the sensitivity of readily available archival imaging surveys, providing sensitivity to planetary mass companions over a separation on the order of $10^2 - 10^3$ AU. As discussed in section 2.3, I favour the use of PCA - KLIP due to its speed enhancement over LOCI and its generation of higher signal-to-noise ratio images with respect to Pynpoint in previous Spitzer studies.

3.2 Target Sample

The target list is compiled from archival Spitzer data based on proximity and youth. As mentioned in section 1.1.4, such targets prove favourable to imaging searches for planetary companions as young giant planets are intrinsically bright in the near-infrared, due to heat retention from formation and gravitational contraction, whilst stars within close proximity to Earth provide sensitivity to companions over a greater range of physical separations for a given detection threshold at a specific angular separation, compared to a relatively distant target, allowing for detection of shorter period planets.

This motivates the choice of stars from the archival Spitzer program 34 (P34) for enhanced imaging analysis. This program targeted 73 nearby (< 30 pc), young stars and therefore provides an ideal basis for the sample for re-analysis. Multiple age indicators, including X-ray luminosity, chromospheric activity, Lithium abundance, rotation, and photometric colour, were originally used to select targets for P34 with ages below 120 Myr. These age estimates are overly optimistic. Using a number of YMG catalogues (e.g., Montes et al., 2001b; Zuckerman & Song, 2004; Torres et al., 2008; Maldonado et al., 2010; Malo et al., 2013), 55 of these targets are identified

as YMG members. Conservative age limits are then placed on each of these 55 targets corresponding to reliable literature age estimates of the YMG of which they are a member; these age estimates are given in Table 3.1. The validity of two YMGs merit attention. It has been proposed that the Argus YMG association, along with the IC 2391 Supercluster and Carina-Vela MG, is an extension of the halo of the nearby IC 2391 open cluster (De Silva et al., 2013). However, these groups are quite distinct in terms of membership and properties, suggesting that Argus is indeed a real co-eval association (Riedel et al., 2014). There is also significant evidence that the sample of Local Association (LA) YMG candidates is heavily contaminated by old field stars, by as much as 50%(López-Santiago et al., 2009). However true LA members can be identified from additional signatures of youth which all LA targets in this sample exhibit. Conservative age limits are placed on the remaining targets by combining literature age estimates encompassing several of the previously mentioned dating techniques (e.g., Barnes, 2007; Mamajek & Hillenbrand, 2008; Plavchan et al., 2009; Tetzlaff et al., 2011; Vican, 2012). Whilst the refined age limits now span a range from 8 to 1050 Myr, the sample remains relatively young with a median target age of 85 Myr. The exception to this is HD 124498. Malo et al. (2013) identifies this target as a probable member of the β Pic YMG. However, Chauvin et al. (2010), using age diagnostics including Lithium abundance and X-ray luminosity, reclassify HD 124498 as an older system with an age $\geq$ 100 Myr. Therefore, for this study HD 124498 is assigned an age of 12 Myr (lower limit on β Pic YMG) - 10 Gyr (upper limit on old field stars, see following paragraph) to ensure any statistics encompassing age estimations produce conservative results. The median target distance, spectral type, and H-band magnitude are 23.3 pc, G5 and 5.289 mag respectively.

A further archival Spitzer program was additionally chosen to add to the target sample, program 48 (P48). This program targeted 48 nearby ($<$ 35 pc) stars with known planetary companions, discovered via radial velocity. As such, these planets are on relatively short orbits, spanning a parameter space currently inaccessible to direct imaging techniques. These exoplanet host stars are relatively old and no confident age limits can be found for the majority of the sample throughout the literature.

Table 3.1: Moving Group Age Estimates

YMG	Age Estimate (Myr)	Age Reference
Local Association (LA)	20 - 150	(Montes et al., 2001b; Brandt et al., 2014)
β Pictoris	12 - 22	(Malo et al., 2013)
Ursa Major	400 - 600	(King et al., 2003)
Castor	100 - 300	(Barrado y Navascues, 1998; Montes et al., 2001b)
IC2391	45 - 55	(Stauffer et al., 1997)
Hyades	575 - 675	(Perryman et al., 1998)
Her-Lyr	211- 303	(Eisenbeiss et al., 2013)
AB Dor	70 - 120	(Malo et al., 2013)
Octans-Near	30 - 100	(Zuckerman et al., 2013)
Argus	30 - 50	(Malo et al., 2013)
TW Hydrae	8 - 12	(Malo et al., 2013)
Tuc-Hor/Columba/Carina	20 - 40	(Malo et al., 2013)

Bell et al. (2015) presented revised ages for several of these groups, see table 2.3, after this Spitzer study had already been accepted for publication.

For consistency, and to justify that any derived statistical result represents a conservative limit, we adopt a conservative age of $1 - 10$ Gyr for all P48 stars. This age range spans the breadth of poorly constrained literature ages for the majority of the sample. The exceptions to this are HD 13507, HD 1237, and AF Hor, which are identified as members of YMGs with independent literature age estimates that support the association membership. Reliable literature age estimates of the relevant YMGs are adopted for these stars. While these targets may prove unfavorable to a deep imaging study, due to their extended ages, the strength in their addition to the sample is that they provide an additional 48 references to aid in PSF reduction of the 73 P34 stars, contributing to an increase in achievable contrast and sensitivity to smaller mass companions. P48 was executed under the exact observational parameters as P34. Along with P48 encompassing a similar spectral sample of stars as P34, median spectral type and H-band magnitude G5 and 4.957, respectively, this ensures P48 targets provide sufficient P34 PSF references. The median distance of P48 stars is 22.6 pc. So while the age range of P48 stars limit sensitivity to low-mass planets, their proximity ensures sensitivity to larger mass planets over a wide range of separations. Therefore, their inclusion in the sample for reduction and analysis as well as providing additional references is justified. However, we note the potential bias introduced to any population constraint statistically derived from a deep imaging search encompassing a sample of stars hosting short period planets. If we consider

planet-planet scattering to be a relevant mechanism for giant planet production at $10^2 - 10^3$ AU separations, the presence of a detected planet at a separation comparable to where a wide giant planet is expected to initially form and migrate or scatter inwards, incorporates some degree of bias into our statistics that we cannot quantitatively evaluate. Therefore, we do not correct for this possible bias. The combined target properties are given in table 3.2.

Table 3.2. Target Sample Properties

HD	HIP	Other	R.A.	decl.	H Mag	Spectral Type	Distance (pc)	YMG	Age (Myr)	YMG / Age Reference	Binarity
48189	31711		06 38 00.366	-61 32 00.19	4.747	G1/G2V	21.3	AB Dor	70 - 120	Z04a, M13	Y/0.6″/810″
	106231	LO Peg	21 31 01.713	+23 20 07.37	6.524	K8	24.8	AB Dor	70 - 120	Z04a, L06, M13	
113449	63742		13 03 49.655	-05 09 42.52	5.674	G5V	21.7	AB Dor	70 - 120	Z04a, N12, M13	
102647	57632		11 49 03.578	+14 34 19.41	1.925	A3Vvar	11.0	Argus	30 - 50	Z11, M13	
	23200	GJ 182	04 59 34.831	+01 47 00.68	6.450	M0Ve	25.9	β Pictoris	12 - 22	T8, S12	
174429	92680		18 53 05.875	-50 10 49.88	6.486	K0Vp	51.5	β Pictoris	12 - 22	Z04b, T8	
196982	102141		20 41 51.159	-32 26 06.83	5.201	M4Ve	10.7	β Pictoris	12 - 22	Z04b, T8	Y/2.2″
197481	102409		20 45 09.531	-31 20 27.24	4.831	M1Ve	9.9	β Pictoris	12 - 22	Z04b, T8	Y/4600″
181296	95261		19 22 51.206	-54 25 26.15	5.148	A0Vn	48.2	β Pictoris	12 - 22	Z04b, M13	Y/4.2″
	108706	GJ 4247	22 01 13.125	+28 18 24.87	7.035	M4V	8.9	Castor	100 - 300	M01b, N12	
216803	113283		22 56 24.053	-31 33 56.04	3.804	K4V	7.6	Castor	100 - 300	M01b, N12	
	114252	GJ 890	23 08 19.550	-15 24 35.80	7.301	M0Ve	22.3	Castor	100 - 300	M01b, N12	
13507	10321		02 12 55.005	+40 40 06.02	5.649	G5V	26.9	Castor	100 - 300	M01b, N12	
217107	113421		22 58 15.541	-02 23 43.38	4.765	G8IV	19.9		1000 - 10000		
206860	107350		21 44 31.329	+14 46 18.98	4.598	G0V	17.9	Her-Lyr	211 - 303	L06, F08	Y/43.2″
35296	25278		05 24 25.464	+17 23 00.72	4.029	F8V	14.4		84 - 316	B07, M08, Mk08	Y/705.2″
41700	28764		06 04 28.440	-45 02 11.77	5.149	G0IV-V	26.6	Hyades	575 - 675	M01b	
173880	92161		18 47 01.274	+18 10 53.47	4.447	A5III	28.9	Hyades	575 - 675	B85	
1237	1292		00 16 12.678	-79 51 04.24	4.990	G6V	17.5	Hyades	575 - 675	M01b	
17051	12653		02 42 33.466	-50 48 01.06	4.323	G3IV	17.2		1000 - 10000		
40979	28767		06 04 29.942	+44 15 37.59	5.509	F8	33.1		1000 - 10000		Y/192.4″
75732	43587		08 52 35.811	+28 19 50.95	4.265	G8V	12.3		1000 - 10000		Y/85.1″
120136	67275		13 47 15.743	+17 27 24.86	3.546	F7V	15.6		1000 - 10000		Y/1.8″
179949	94645		19 15 33.230	-24 10 45.67	5.101	F8V	27.6		1000 - 10000		
1835	1803		00 22 51.788	-12 12 33.97	5.035	G3V	20.9	Hyades	575 - 675	M01b, M10, N12	
222143	116613		23 37 58.488	+46 11 57.96	5.123	G3/4V	23.3	Hyades	575 - 675	M01b, M10	
108799	60994		12 30 04.774	-13 23 35.46	4.932	G1/G2V	24.7	IC2391	45 - 55	N12	Y/2.1″
30495	22263		04 47 36.291	-16 56 04.04	4.116	G3V	13.3	IC2391	45 - 55	M10	
128987	71743		14 40 31.106	-16 12 33.44	5.629	G6V	23.7	IC2391	45 - 55	M10	

Table 1.2. Target Sample Properties

HD	HIP	Other	R.A.	decl.	H Mag	Spectral Type	Distance (pc)	YMG	Age (Myr)	YMG / Age Reference	Binarity
19994	14954		03 12 46.437	-01 11 45.96	3.768	F8V	22.6		1000 - 10000		Y/2.1″
	117410	GJ 9839	23 48 25.691	-12 59 14.86	6.485	K5Vke	28.2	Carina	20 - 40	Z06	
27045	19990		04 17 15.662	+20 34 42.93	4.577	A3m	28.9	Octans-Near	30 - 100	Z13	
197157	102333		20 44 02.334	-51 55 15.50	3.692	A9IV	24.2	Octans-Near	30 - 100	Z13	
166	544		00 06 36.785	+29 01 17.40	4.629	K0V	13.7	Her-Lyr	211 - 303	F04, L06	
17925	13402		02 52 32.128	-12 46 10.97	4.230	K1V	10.4	LA	20 - 150	M01a, M10	
	37766	GJ 285	07 44 40.174	+03 33 08.84	6.005	M4.5Ve	6.00	LA	20 - 150	M01b	
		EY Dra	18 16 16.776	+54 10 21.62	7.960	dM1.5e	30.0[a]	LA	20 - 150	J94	
197890	102626		20 47 45.007	-36 35 40.79	6.930	K0V	52.2	Tuc-Hor	20 - 40	K14	
10008	7576		01 37 35.466	-06 45 37.53	5.899	G5V	24.0	LA	20 - 150	M01b, M10	Y/612″
77407	44458		09 03 27.083	+37 50 27.53	5.534	G0V	30.5	LA	20 - 150	M01a, M01b	
171488	91043		18 34 20.103	+18 41 24.23	5.896	G0V	38.0	LA	20 - 150	M01b	
		V383 Lac	22 20 07.0258	+49 30 11.763	6.577	K1V	27.5[b]	LA	20 - 150	M01a, M01b	
130322	72339		14 47 32.727	-00 16 53.32	6.315	K0V	31.7		1000 - 10000		
217014	113357		22 57 27.980	+20 46 07.79	4.234	G5V	15.6		1000 - 10000		
92945	52462		10 43 28.272	-29 03 51.43	5.770	K1V	21.4	LA	20 - 150	M01b, L06	
129333	71631		14 39 00.210	+64 17 29.95	6.012	G1.5V	34.1	LA	20 - 150	M01a, M01b	Y/0.8″
181327	95270		19 22 58.943	-54 32 16.97	5.980	F5/F6V	51.8	β Pictoris	12 - 22	Z01, Z04b	
82443	46843		09 32 43.759	+26 59 18.70	5.242	G9V	17.8	Columba	20 - 40	B14	Y/64.7″
116956	65515		13 25 45.533	+56 58 13.78	5.481	G9V	21.6	Her-Lyr	211 - 303	F04, M10	
177724	93747		19 05 24.608	+13 51 48.52	3.048	A0Vn	25.5	TW Hydrae	8 - 12	N12	Y/1494.63″
29697	21818		04 41 18.856	+20 54 05.45	5.310	K3V	13.2	Ursa Major	400 - 600	M01a, M01b	
7590	5944		01 16 29.253	+42 56 21.90	5.258	G0	23.2	Ursa Major	400 - 600	F04, M10	
217813	113829		23 03 04.977	+20 55 06.87	5.232	G5V	24.7	Ursa Major	400 - 600	M01b, K03	
128311	71395		14 36 00.560	+09 44 47.46	5.303	K0	16.5		1000 - 10000		
147513	80337		16 24 01.289	-39 11 34.71	4.025	G3/G5V	12.8		1000 - 10000		Y/345″
150706	80902		16 31 17.585	+79 47 23.20	5.639	G0	28.2		1000 - 10000		
175742	92919		18 55 53.225	+23 33 23.93	5.762	K0V	21.4	Ursa Major	400 - 600	K03	
76644	44127		08 59 12.454	+48 02 30.57	2.763	A7Vn	14.5		450 - 1050	V12	Y/0.7″/2.4″

Table 1.2. Target Sample Properties

HD	HIP	Other	R.A.	decl.	H Mag	Spectral Type	Distance (pc)	YMG	Age (Myr)	YMG / Age Reference	Binarity
82558	46816		09 32 25.568	-11 11 04.70	5.596	K0V	18.6		50 - 75	F86, T11	
92139	51986		10 37 18.140	-48 13 32.23	3.170	F4IV	26.8		50 - 150	P09	Y/0.5″
112429	63076		12 55 28.548	+65 26 18.51	4.604	A5n	29.3		50 - 450	P09	
115383	64792		13 16 46.516	+09 25 26.96	4.107	G0V	17.6		130 - 160	M10, V12	
		GJ 3789	13 31 46.617	+29 16 36.72	7.002	M4V	7.9[c]	Carina/Columba	20 - 40	R14	
141795	77622		15 50 48.966	+04 28 39.83	3.440	A2m	21.6		220 - 820	V12	
124498	69562		14 14 21.357	-15 21 21.76	6.781	K4V	30.2	β Pictoris	12 - 10000	C10, M13	
220182	115331		23 21 36.513	+44 05 52.38	5.574	K1V	21.5		200-318	G00, B07, M08	
20630	15457		03 19 21.696	+03 22 12.72	3.039	G5Vvar	9.14		350-700	M08 , M10, V12	
130948	72567		14 50 15.811	+23 54 42.64	4.688	G2V	18.2		640-1001	D09	Y/0.1″/2.6″
142	522		00 06 19.175	-49 04 30.68	4.646	F7V	25.7		1000 - 10000		Y/4.1″
4208	3479		00 44 26.651	-26 30 56.45	6.243	G5V	32.4		1000 - 10000		
10697	8159		01 44 55.825	+20 04 59.34	4.678	G5IV	32.6		1000 - 10000		
3651	3093		00 39 21.806	+21 15 01.71	4.064	K0V	11.0		1000 - 10000		Y/42.9″
20367	15323		03 17 40.045	+31 07 37.36	5.117	F8V	26.7		1000 - 10000		
222404	116727		23 39 20.852	+77 37 56.19	1.190	K1III	14.1		1000 - 10000		Y/0.9″
27442	19921		04 16 29.029	-59 18 07.76	1.814	K2III	18.2		1000 - 10000		Y/13.1″
33636	24205		05 11 46.448	+04 24 12.73	5.633	G0	28.4		1000 - 10000		
39091	26394		05 37 09.892	-80 28 08.84	4.424	G0V	18.3		1000 - 10000		
50554	33212		06 54 42.825	+24 14 44.02	5.516	F8V	29.9		1000 - 10000		
75289	43177		08 47 40.390	-41 44 12.45	5.187	F9VFe+0.3	29.2		1000 - 10000		Y/21.5″
82943	47007		09 34 50.737	-12 07 46.37	5.245	F9VFe+0.5	27.5		1000 - 10000		
92788	52409		10 42 48.528	-02 11 01.52	5.798	G6V	35.5		1000 - 10000		
95128	53721		10 59 27.973	+40 25 48.92	3.736	G0V	14.0		1000 - 10000		
114386	64295		13 10 39.824	-35 03 17.21	6.497	K3V	28.9		1000 - 10000		
114783	64457		13 12 43.786	-02 15 54.13	5.623	K1V	20.5		1000 - 10000		
192263	99711		20 13 59.846	-00 52 00.77	5.685	K2.5V	19.3		1000 - 10000		
117176	65721		13 28 25.809	+13 46 43.64	3.457	G5V	18.0		1000 - 10000		
134987	74500		15 13 28.667	-25 18 33.65	5.121	G5V	26.2		1000 - 10000		

Table 1.2. Target Sample Properties

HD	HIP	Other	R.A.	decl.	H Mag	Spectral Type	Distance (pc)	YMG	Age (Myr)	YMG / Age Reference	Binarity
141937	77740		15 52 17.547	-18 26 09.84	5.866	G2/G3V	32.3		1000 - 10000		
143761	78459		16 01 02.662	+33 18 12.63	3.989	G2V	17.2		1000 - 10000		
145675	79248		16 10 24.314	+43 49 03.53	4.803	K0V	17.6		1000 - 10000		
160691	86796		17 44 08.701	-51 50 02.59	3.724	G5V	15.5		1000 - 10000		
216435	113044		22 53 37.932	-48 35 53.83	4.687	G0V	32.6		1000 - 10000		
210277	109378		22 09 29.866	-07 32 55.15	4.957	G8V	21.6		1000 - 10000		
216437	113137		22 54 39.482	-70 04 25.35	4.923	G1VFe+0.3	26.8		1000 - 10000		
74575	42828		08 43 35.538	-33 11 10.99	4.227	B1.5III	269.5		13.2 - 18.4	T11	
59967	36515		07 30 42.512	-37 20 21.70	5.253	G3V	21.8	Castor	100 - 300	N12	
73350	42333		08 37 50.294	-06 48 24.78	5.318	G5V	24.0	Hyades	575 - 675	M10, T12	
37124	26381		05 37 02.486	+20 43 50.84	6.021	G4IV-V	33.7		1000 - 10000		
52265	33719		07 00 18.036	-05 22 01.78	5.033	G0V	29.0		1000 - 10000		
		AF Hor	02 41 47.31	-52 59 30.7	7.851	M2Ve	27.0[d]	Tuc-Hor	20 - 40	M13, Z04b	Y/22.1″
36705	25647		05 28 44.830	-65 26 54.86	4.845	K0V	15.2	AB Dor	70 - 120	Z04a, L06, M13	Y/8.9″
21845	16563		03 33 13.491	+46 15 26.53	6.457	K2	34.4	AB Dor	70 - 120	Z04a, L06, M13	Y/9.6″
102077	57269		11 44 38.463	-49 25 02.75	6.642	K1V	48.6		30 - 120	W14	Y/0.2″
105963	59432		12 11 27.754	+53 25 17.45	5.867	K0V	30.2		242 - 302	B07, M08	Y/13.5″
139084	76629		15 38 57.543	-57 42 27.34	5.994	K0V	38.5	β Pictoris	12 - 22	Z04b, M13	Y/10.2″
172555	92024		18 45 26.900	-64 52 16.54	4.251	A7V	28.6	β Pictoris	12 - 22	Z04b, M13	Y/71.4″
202730	105319		21 19 51.990	-53 26 57.93	4.224	A5V	30.3		50 - 900	P09, V12	Y/7.3″
218738	114379		23 09 57.372	+47 57 30.13	5.788	G5Ve	23.7		12.7 - 48	P09, T11	Y/15.8″
51849	33560		06 58 26.051	-12 59 30.58	6.368	K4V	21.7		30 - 220	P09, T11	Y/0.7″
141272	77408		15 48 09.463	+01 34 18.27	5.610	G8V	21.3	LA	20 - 150	M01b, M10	Y/17.9″
155555	84586		17 17 25.505	-66 57 03.73	4.907	G5IV	31.5	β Pictoris	12 - 22	Z04b, M13	Y/34.04″
220140	115147		23 19 26.633	+79 00 12.67	5.512	G9V	19.2		16 - 50	Mk07, T11	Y/10.8″/962.6″
11131	8486		01 49 23.356	-10 42 12.86	5.289	G1Vk	22.6	Ursa Major	400 - 600	M01b, M10, N12	Y/192.9″
43162	29568		06 13 45.296	-23 51 42.98	4.863	G5V	16.7	IC 2391	45 - 55	M10, N12	Y/24.6″/164″
160934	86346		17 38 39.634	+61 14 16.03	6.998	K7Ve	33.1	AB Dor	70 - 120	Z04a, L06, M13	Y/0.12″

Table 1.2. Target Sample Properties

HD	HIP	Other	R.A.	decl.	H Mag	Spectral Type	Distance (pc)	YMG	Age (Myr)	YMG / Age Reference	Binarity
9826	7513		01 36 47.842	+41 24 19.64	2.957	F8V	13.5		1000 - 10000		Y/55.4″
13445	10138		02 10 25.934	-50 49 25.42	4.245	K0V	10.8		1000 - 10000		Y/2.4″
46375	31246		06 33 12.622	+05 27 46.53	6.072	K1IV	34.8		1000 - 10000		Y/11.2″
162020	87330		17 50 38.355	-40 19 06.07	6.649	K3V	29.4		1000 - 10000		
186427	96901		19 41 51.972	+50 31 03.08	4.695	G5V	21.2		1000 - 10000		Y/41.6″
190360	98767		20 03 37.406	+29 53 48.49	4.239	G7IV-V	15.9		1000 - 10000		Y/178.2″

Note. — Target right ascension (R.A.) and declination (decl.) values are taken from the revised Hipparcos catalogue (van Leeuwen, 2007) at equinox=J2000, epoch=J2000 computed by Vizier. H band magnitudes are taken from 2MASS All-Sky Catalog of Point Sources (Cutri et al., 2003). Distances taken from revised Hipparcos catalogue unless noted otherwise with indices [a,b,c,d], relevant references given below. Column 9 notes YMG membership. Age estimates for YMG targets are taken from estimates of the group age given in table 3.1. Targets with unconstrained ages are assigned an age of 1 - 10 Gyr. Column 11 notes literature sources identifying YMG membership, or the sources estimating age for several young targets with no known YMG membership. Column 12 notes Y for targets identified as part of a binary system (see section 4.2.1) and gives the separation of the binary companion. Identification and separation values are taken from the Washington double star catalogue (Mason et al., 2001).

[a](Plavchan et al., 2009)

[b](Montes et al., 2001a)

[c](Gliese & Jahreiss, 1991)

[d](Riaz et al., 2006)

References. — (B07) (Barnes, 2007); (B14) (Brandt et al., 2014); (B85) (Bubenicek et al., 1985); (C10) (Chauvin et al., 2010); (D09) (Dupuy et al., 2009); (F04, F08) (Fuhrmann, 2004, 2008); (F86) (Fekel et al., 1986); (G00) (Gaidos et al., 2000); (J94) (Jeffries et al., 1994); (K03) (King et al., 2003); (K14) (Kraus et al., 2014b); (L06) (López-Santiago et al., 2006); (M01a, M01b) (Montes et al., 2001a,b); (M08) (Mamajek & Hillenbrand, 2008); (M10) (Maldonado et al., 2010); (M13) (Malo et al., 2013); (Mk07, Mk08) (Makarov et al., 2007, 2008); (N12) (Nakajima & Morino, 2012); (P09) (Plavchan et al., 2009) ; (R14) (Riedel et al., 2014); (S12) (Schlieder et al., 2012); (T8) (Torres et al., 2008); (T11) (Tetzlaff et al., 2011); (T12) (Tabernero et al., 2012); (V12) (Vican, 2012); (W14) (Wöllert et al., 2014); (Z01, Z04a, Z04b, Z06, Z11, Z13) (Zuckerman et al., 2001, 2004; Zuckerman & Song, 2004; Zuckerman et al., 2006, 2011, 2013).

3.3 Observations and Data Reduction

The combined 121 targets were observed with Spitzer IRAC under archival programs 34 and 48 between 2003 and 2004, during the cryogenic phase of the mission. Images were obtained simultaneously at 3.6, 4.5, 5.8 and 8.0 μm (channels 1 - 4 respectively). Channel 2 was chosen as the primary channel to analyse based on evolutionary model predictions that planetary mass companions are at their peak luminosity within the 4.5 μm band. Therefore, this channel offers the best sensitivity for planet detection. Channel 1 images are also reduced and analysed as a means to vet potential companions (see section 3.5.2).

Each individual target was observed once across all channels. Each observation consisted of 10 exposures, executed as a five-position Gaussian dither pattern. Dithering is a deliberate shift of the pointing of the telescope between exposures which allows for the filtering of hot pixels, fixed noise patterns and cosmic ray hits upon data reduction. For example, hot pixels are individual pixels that appear overly bright due to oversensitivity or leakage of electrical charge into the pixel well. These pixels are fixed in position in the CCD detector and therefore occur at the same place across each exposure. However, dithering shifts the position of the target across each exposure. During data reduction individual exposures are aligned with respect to the target, and hot pixel location varies across the exposures. These pixels can then be identified as outliers by comparing pixel values at the same position across the aligned image stack, and discarded (e.g. by median filtration). Dithering to a sub-pixel accuracy also enables spatial oversampling. This allows for the reconstruction of information which may have been lost due to spatial under-sampling. At 3.6 and 4.5 μm the IRAC PSF, with FWHMs of 1.66″ and 1.72″ respectively, is particularly under-sampled with a pixel size of 1.2″ across all four wavelength bands. The five-point Gaussian pattern is accurate to a 1/2 pixel shift, and therefore the spatial resolution can be increased to 0.6″ per pixel upon image combination (mosaicking). Each exposure was executed with a 30 s frame time allowing for an effective exposure time of 26.8 s per dither position. The final effective exposure time for each target is then 268 s upon mosaicking of the 10 individual frames.

The Spitzer Science Center (SSC) IRAC Pipeline (version S18.25.0) performed data reduction for all observations. The level 1 pipeline takes raw data from the

IRAC detector and performs basic reduction steps such as flat-fielding, dark subtraction, cosmic ray detection and pointing determination, producing basic calibrated data frames (BCDs). An additional pipeline, the artifact-corrected BCD pipeline, performed further data reduction to mitigate commonly found IRAC artefacts such as; stray or scattered light from stars outside the FOV and filter ghosts (secondary, out of focus PSFs formed by reflection within the instrument optics) due to bright stars within the field, column pulldown in which a bright pixel triggers a bias shift within its column, generating a lower background value throughout the entire column with respect to surrounding columns, and muxbleed and muxstripe – easily noticeable 'ghosting' patterns along the pixel readout channels as a result of operating the detectors at such cold temperatures which causes a delay in the electronics returning to their quiescent state. This pipeline produces corrected BCDs (CBCDs) which have also been corrected for saturation by fitting an appropriate PSF that is matched to the unsaturated wings of the source. The level 2 IRAC pipeline, which accepts CBCD data products, preforms further advanced image processing, refining the telescope pointing and performing additional outlier rejection before mosaicking the frames to produce a single post-BCD (PBCD) sub-pixelated image with a $0.6''$ per pixel resolution over the $5.2' \times 5.2'$ FOV. These PBCD frames are readily available on the Spitzer Heritage Archive within the NASA/IPAC Infrared Science Archive[1].

However, the saturation correction performed by the artifact-corrected BCD pipeline generates images which are unsuitable for a close companion search as pixels toward the PSF core may have been replaced with model pixel values, ensuring that any information about potential companion sources at these separations is lost. Nonetheless, in this study the use of PBCDs over BCDs is favoured due to the additional artefact correction performed on the former by the SSC IRAC pipeline. Therefore, a composite frame is generated consisting of a PBCD image where saturation corrected regions, identified in the relevant mask files produced by the pipeline, have been replaced with pixel values generated from mosaicking the relevant level 1 BCD frames. These pixel values have been sub-pixelated to the equivalent $0.6''$per pixel resolution. Figure 3.2 shows an example of such a composite PBCD/BCD image.

[1]http://irsa.ipac.caltech.edu

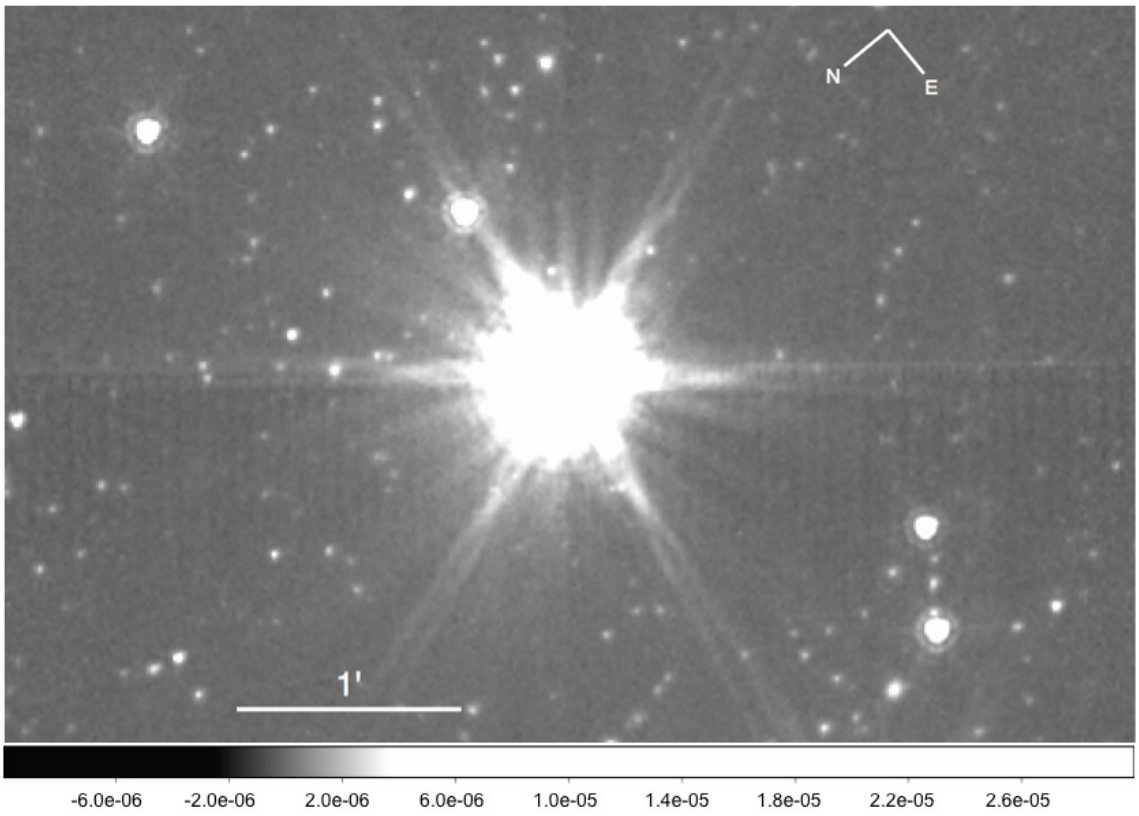

Figure 3.2: Example of a composite PBCD/BCD 4.5 μm image of HD 217813, displaying the extent of the PSF and Spitzer spider features. The wide FOV reveals a multitude of point sources, which must be vetted for planet candidacy. HD 217813 properties lie close to the median of the sample, H mag = 5.232, G5V star at 24.7 pc.

3.4 PSF Subtraction

The centre of each target PSF is initially calculated by the fitting of a two-dimensional Gaussian with a FWHM equal to 1.66″ and 1.72″ for 3.6 and 4.5 μm images respectively. The center of each image is then shifted to this position. Every image is then normalised by the central brightness of the stellar PSF, estimated from the saturation corrected images. This provides an image stack of target PSFs that have similar normalised flux values. The saturated cores of each image are then masked for subsequent image reduction. All images are then robustly centred with respect to the stack by subtraction of a median stack image over a range of sub-pixel offsets. The offset producing the minimum residuals is used to align each image. The image stack constitutes the library of PSFs used to construct a reference PSF for image subtraction. This accurate alignment of target PSFs provides better performance of any reference construction, ultimately leading to improved sensitivity in any final reduced image.

As discussed in previous sections, PCA is used to construct the optimal reference PSF to subtract from the target PSF. Although variations of PCA such as PynPoint and KLIP have the same underlying principle; a linear combination of orthogonal basis sets are used for reference construction, PCA performed here follows a KLIP-based analysis due to its generation of higher signal-to-noise ratio images with respect to Pynpoint in previous Spitzer studies (Janson et al., 2012b, 2015). See section 2.3.1 for a detailed description of the algorithm.

The PCA optimisation is limited to to a 201×201 pixel sub-section of each 3.6 and $4.5\,\mu$m image, centred on the star. This corresponds to a $2.01' \times 2.01'$ FOV encompassing separations out to $\sim 1'$ from each target. This reduced area is chosen as a favourable trade off between algorithm efficiency and sensitivity to wide separations, with $1'$ corresponding to separations on the order of 10^3 AU, at the typical target distance. PCA application beyond this separation would also prove fruitless as $> 1'$ separations are certainly within the background noise-limited regime which PCA cannot reference and effectively subtract due to its random nature. Similar to LOCI, the optimisation is computed independently in local subsections across the target image, as the correlation between the target PSF and an individual basis set varies as a function of position. These subsections are chosen to be concentric annuli centred on the target. The radii of the annuli are chosen such that each annulus contains 1500 pixels, with an inner 4 pixel radius mask covering saturated cores. This is an optimal trade-off between sub-section size, number of pixels encompassed, and algorithm efficiency: A large number of pixels is beneficial for providing the algorithm with enough data to generate representative basis sets, but a too large sub-section size will be less efficient at representing the local PSF conditions. Meanwhile, a larger number of sub-sections will significantly extend the execution time of the algorithm.

Reference annuli containing $\geq 5\sigma$ astronomical sources such as background stars, stellar companions, or surviving bad pixels are excluded to prevent the algorithm from subtracting any true planetary PSF, and to prevent any fake planetary signal being injected into the final image. The amount of reference frames per annulus available for PCA application after this exclusion ranges from 93 to 33, with a median of 56 frames. However, separations within $0.5'$ of the PSF core always have > 60 references available for PCA application. Figure 3.3 displays the number of available frames as a function of annulus position. As previously mentioned in section 2.3.1,

the number of PCA modes used in the reduction can be truncated and optimised to provide a favourable trade-off between PSF subtraction, background noise and planetary throughput. However, the computation of the eigenvectors of the covariance matrix of the library stack restricts the maximum number of PCA modes to that of the number of available reference frames. Therefore, for the median case, PCA generates 56 modes for an annular sub-section with 56 available reference frames. Janson et al. (2015) found that 203 modes provide the ideal amount to combine for optimising the total signal to noise in their PCA reduction of Spitzer IRAC images. As the number of modes available for this reduction are fewer, no truncation is applied and the maximum number of modes are combined for each sub-section.

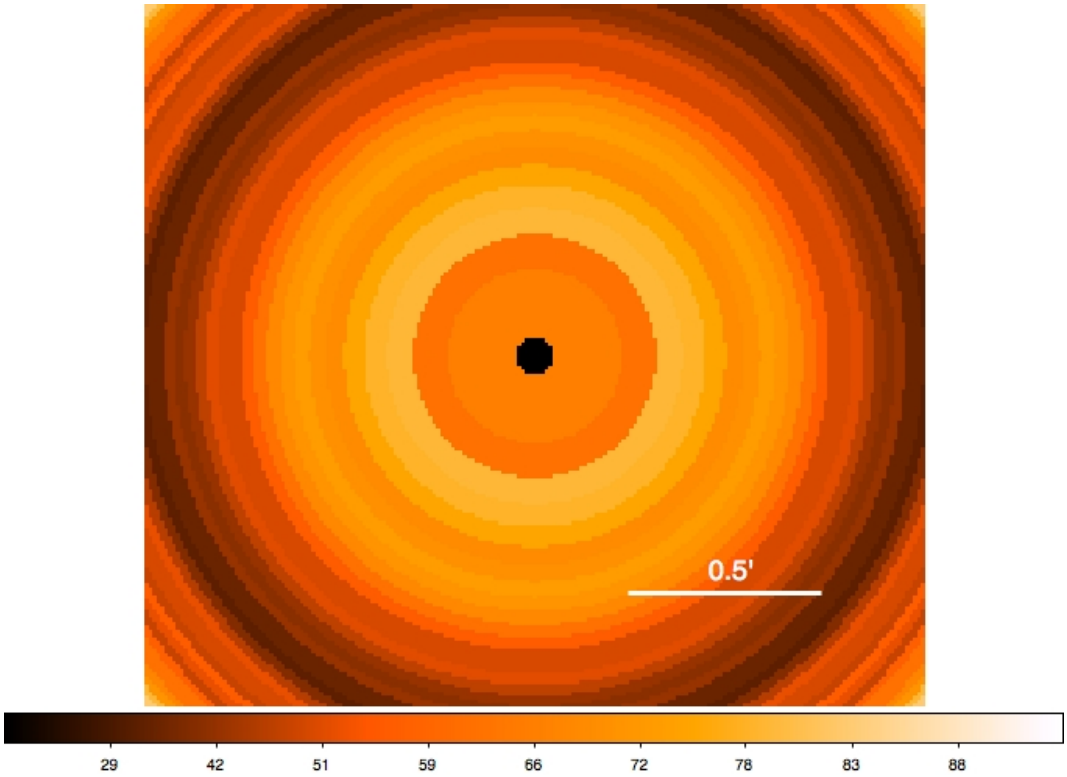

Figure 3.3: Number of reference frames available as a function of 1500 pixel annulus position. Image encompasses the $2.01' \times 2.01'$ optimisation region. Scale bar relates number of available frames to colour intensity. All separations within $0.5'$ of the PSF core have > 60 references available for PCA application. A four pixel radius mask covers the core of the image.

An example of an initial PCA reduced image can be seen in figure 3.4. This initial reduction suffers from some major drawbacks resulting in a sub-standard PSF subtraction. These drawbacks arise from the underlying principle of the PCA reduction,

which effectively acts to produce the lowest residuals in the PSF subtracted image. Therefore, particularly bright sources, $> 50\,\sigma$ upon inspection, dominate the weighting of the PCA modes, heavily weighting basis sets that effectively model the flux at the source position, but that may be a poor representation of PSF features contained in the rest of the annulus. This may produce the lowest residuals, but the vast majority of the annular region will have experienced a substandard reduction, producing an annulus with significant noise with respect to surrounding annuli as seen in figure 3.4. Furthermore, since flux increases toward the PSF core, the larger flux values toward the inner region of each annulus also dominate the weighting of the orthogonal basis sets. Again, this may produce the lowest residuals, but the outer annular regions will have experienced a substandard reduction. These algorithm deficiencies are dealt with by executing PCA several times under different conditions. After the initial reduction a second iteration is executed with $> 50\,\sigma$ sources masked in the target image. In this way annuli harbouring bright sources experience an optimal reduction and the two iterations can then be combined, generating a complete image. This bright source problem could also be solved by running the Algorithm on separate sectors of each annulus, although this may significantly increase total execution time. For each set of iterations the PCA reduction is carried out four times, increasing the radius of the inner saturation mask, and therefore shifting the radii of the 1500 pixel annuli. This ensures that each section of the 201×201 pixel optimisation region has been encompassed by an inner annular region and experienced a full quality reduction. A composite of these four separate PCA reduced frames is then generated whose constituent parts have experienced optimal reduction. This composite image of four reductions (8 iterations of the algorithm in total) constitutes the final reduced image for analysis. An example of a final PCA reduced image can be seen in figure 3.5.

As mentioned in section 2.3, PCA is typically performed at neighbouring states of the telescope/instrument system and provides optimal PSF subtraction when carried out in tandem with angular differential imaging application, where the PSF remains quasi-static over the observation. Here, PCA is applied to a sample observed at varying states of the telescope/instrument system taken over the course of one year, e.g., varying stellar magnitude, spectral type, telescope roll angle. Therefore, this study constitutes a trial of PCA on an unfavourable data set, testing its effectiveness at the limits of its application.

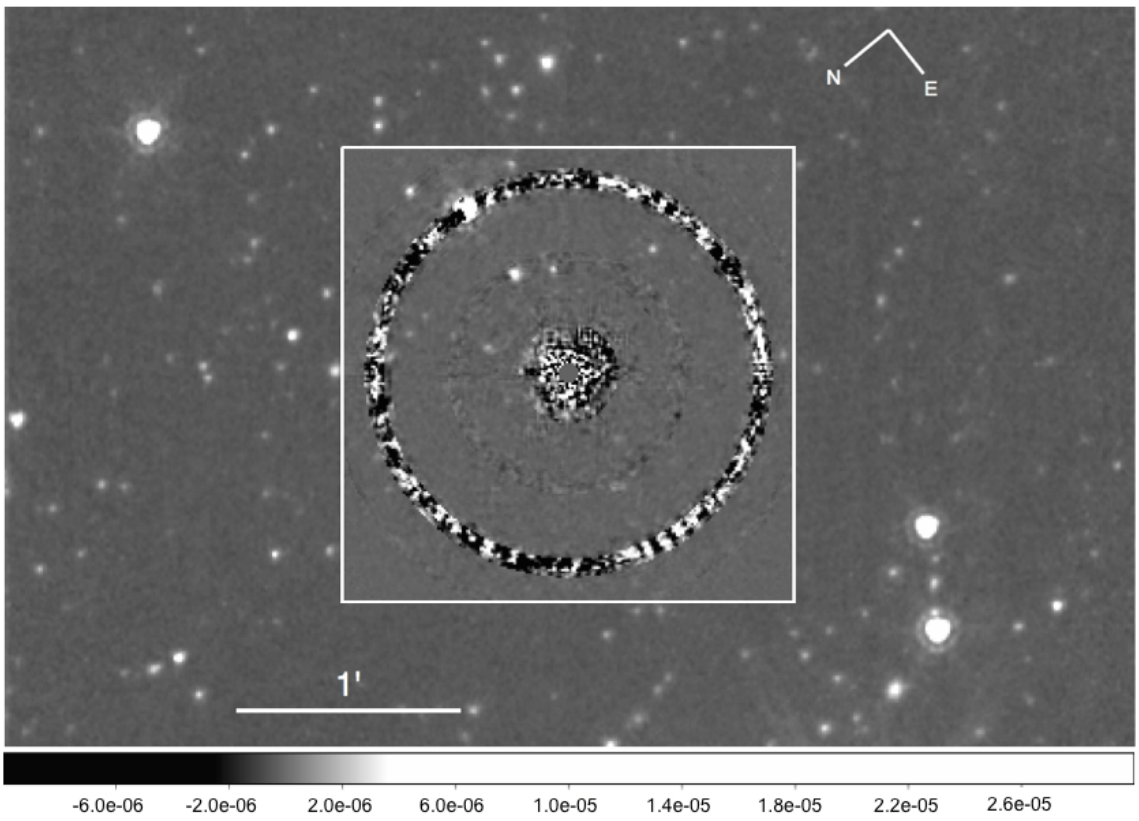

Figure 3.4: Initial reduced 4.5 μm image of HD 217813 depicting the same FOV as figure 3.2. The white box highlights the $2.01' \times 2.01'$ optimisation region. Regular PSF subtraction of a mean stack image has been performed outside the optimisation region. Outer annulus regions and annuli containing bright sources experience a sub-standard reduction generating particularly noisy annuli and distinct transitions between annular zones.

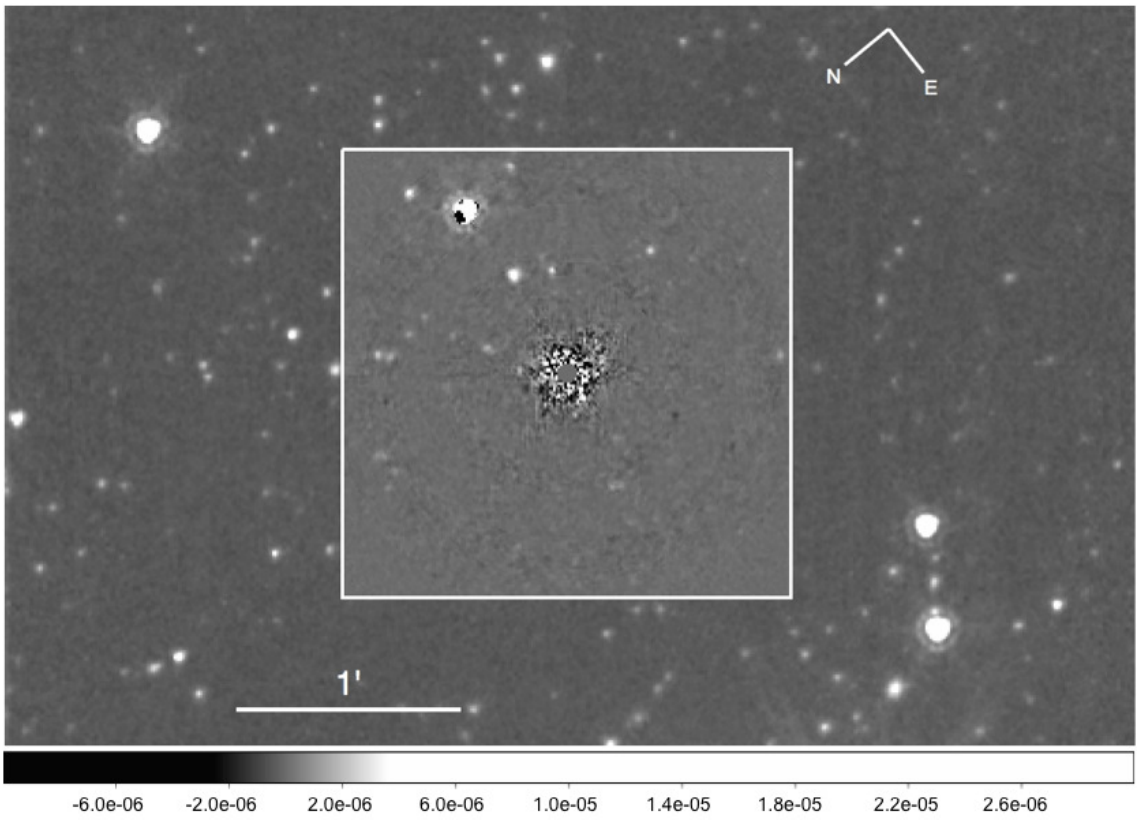

Figure 3.5: Final reduced 4.5 μm image of HD 217813 depicting the same FOV as figure 3.2. All regions of the image have experienced optimal reduction, generating an image in which the PSF has been effectively removed and there is a smooth transition between annular zones. Additional point sources have been revealed with respect to the pre-PCA image (see figure 3.2) which must be vetted for planet candidacy.

3.5 Results

3.5.1 Observational Sensitivities

The sensitivity in the final PCA reduced images is evaluated at $5\,\sigma$ detection limits by relating the standard deviation, σ, in concentric 1 pixel width annuli centred on the star, to the zero-point flux of Vega, $F_0 = 179.7$ Jy at $4.5\,\mu$m, using the method of Marengo et al. (2009);

$$m = -2.5\,log\,\frac{5\pi\,(\mathrm{FWHM}/2)^2\,\sigma}{F_0} \tag{3.1}$$

This generates sensitivity values in units of Vega magnitudes, m. As any potential companion will suffer from partial flux subtraction during the PCA reduction, source throughput must be accounted for in the sensitivity estimation. Synthetic companions are injected into each target image at position angles 0° and 90° in order to cover spider and non-spider regions, at five pixel intervals out to the edge of the optimisation region, and throughput after PCA application is recorded. The mean throughput is then calculated at each separation and linearly interpolated to produce throughput values for each pixel separation, consistent with sensitivity estimation in one-pixel width annuli. The mean throughput, τ, over the image stack is then used for sensitivity estimation via the equation;

$$m = -2.5\,log\,\frac{5\pi\,(\mathrm{FWHM}/2)^2\,\sigma}{F_0} + 2.5\,log(\tau) \tag{3.2}$$

The performance of the $4.5\,\mu$m PCA reduction is evaluated by computing sensitivity curves for both PCA optimised and conventional PSF subtracted images (i.e., subtraction of a mean stack image) and calculating the sensitivity improvement provided by PCA for each target. The median sensitivity improvement curve is then generated. This curve, displayed in figure 3.6, shows that PCA offers superior image sensitivity at separations less than $20''$, within the PSF noise-limited regime, and provides a median improvement of ~ 0.9 mag at separations less than $10''$. This validates the application of PCA in a study encompassing a diverse sample of stars, observed at varying states of the telescope/instrument system. The ~ 0.9 mag improvement in the contrast limited regime demonstrates the relevance of applying and

developing sophisticated high-contrast techniques to archival Spitzer data, where the sensitivity to planetary mass companions at relatively small angular separations has been enhanced. This allows for the possibility of subsequent planet detection within a previously elusive parameter space and enables more stringent constraints to be placed on the wide giant population. In the background noise-limited regime, separations greater than 20″, PCA does not provide any sensitivity improvement over regular PSF subtraction, due to the random nature of background noise which PCA cannot reference.

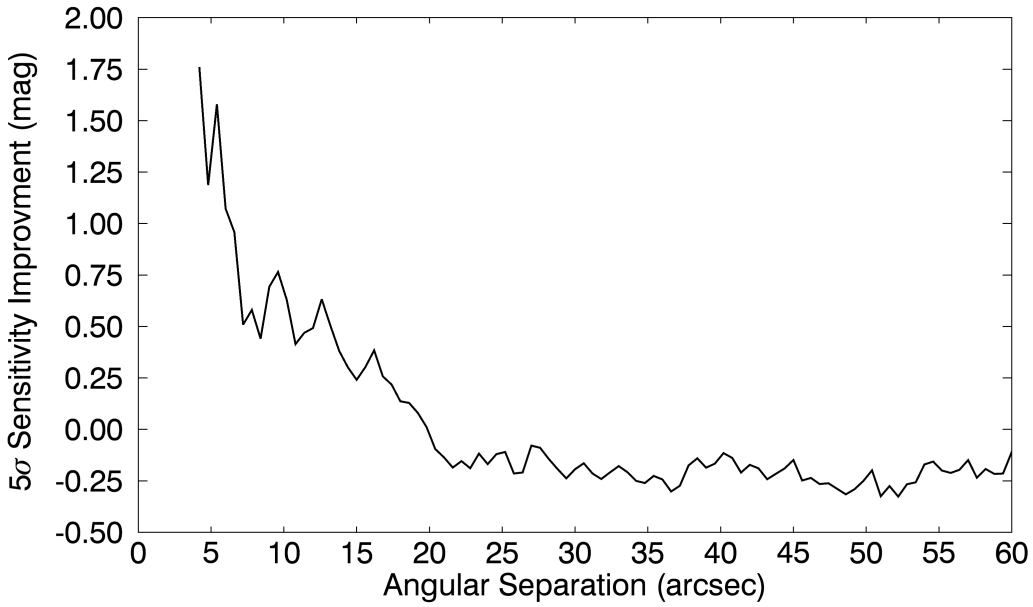

Figure 3.6: PCA sensitivity improvement with respect to conventional PSF subtraction, as a function of separation. The decrease in improvement around 20″ corresponds to the transition between the PSF noise-limited regime and the background noise-limited regime. The jagged nature of the curve stems from preferential reduction of inner annulus regions.

Figures 3.7 and 3.8 show the 4.5 μm median sensitivity curves for the PCA reduced P34 and P48 stars respectively. Within $\sim$ 20″ sensitivity decreases toward the PSF core where the residual PSF noise exhibits the largest variance, limiting sensitivity to lower magnitude companions. Outside $\sim$ 20″ PCA provides no sensitivity improvement in the background noise-limited regime, which tends to be constant, thus magnitude sensitivity at these separations is roughly constant. Figures 3.7 and

3.8 also map sensitivity as a function of projected physical separation out to ~ 1400 AU at the median distance of P34 and P48 stars, 23.3 pc and 22.6 pc respectively. P34 and P48 stars provide comparative magnitude sensitivity limits.

These magnitude sensitivity limits can be translated into mass sensitivities using mass-luminosity evolutionary models. One caveat is the discrepancy between hot-(Chabrier et al., 2000; Baraffe et al., 2003; Burrows et al., 2003) and cold-start (Marley et al., 2007; Fortney et al., 2008) models, where the later predict much fainter planets at young ages. Here we will consider hot-start models, which are consistent with existing observational data (Janson et al., 2011). However, it can be noted that the models converge on the order of tens of Myr for low-mass planetary companions ($\leq 2\,M_J$) and on the order of hundreds of Myr for higher mass planetary companions (Spiegel & Burrows, 2012). Thus the choice of model will not lead to significant disparity in mass sensitivity over the complete sample at the typical ages considered. COND-based models (Allard et al., 2001; Baraffe et al., 2003), applicable for companion temperatures below 1700 K, which is a relevant temperature range for 0.5-13 M_J companions over the sample age range, are used here.

The corresponding mass sensitivities for the median P34 and P48 magnitude sensitivities are shown in figures 3.7 and 3.8. With P34 targets, sensitivity down to $\leq 2\,M_J$ companions is achieved down to $\sim 5''$, corresponding to ~ 100 AU projected separation, while sensitivity down to 0.5 M_J companions is achieved for separations $\gtrsim 15''$ ($\gtrsim 350$ AU). While P34 and P48 stars provide comparative magnitude sensitivity limits, the extended ages of P48 stars ensure an equivalent low-mass sensitivity cannot be achieved. Sensitivity to below 4 M_J is typically not acquired, and sensitivity to $5\,M_J$ planets is limited to outside $20''$ (~ 500 AU). Taking $13\,M_J$ as the upper mass limit for planetary objects, sensitivity to planets within $10''$ (~ 200 AU) is typically not acquired for P48 targets.

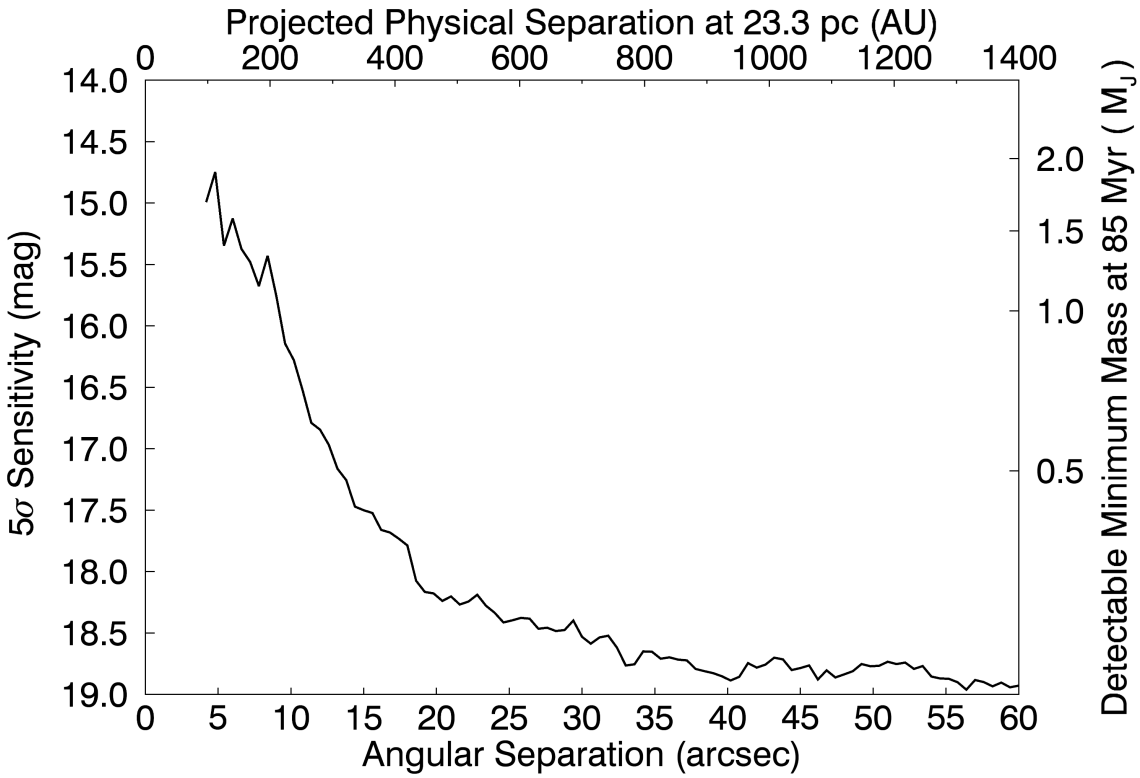

Figure 3.7: Median survey detection limits for P34 stars. Magnitude sensitivity is given as a function of angular separation. The right axis shows the corresponding minimum detectable mass at the median target age of 85 Myr. The top axis displays projected physical separation at median target distance 23.3 pc.

3.5.2 Candidate Vetting

The multitude of point sources revealed by PSF subtraction across the 121 target sample must be evaluated for planet candidacy. Two initial criteria are used to identify potential planetary mass companions. First, each 4.5 μm reduced image is visually inspected to identify realistic PSF shapes, allowing real sources to be distinguished from potential surviving bad pixels. Any realistic PSF is then vetted for planetary candidacy by comparison of the 4.5 and 3.6 μm images. The spectral energy distribution of a non-irradiated 0.5-13 Jupiter mass companion, at the typical ages of our sample, is such that planetary flux at 3.6 μm is typically > 1 mag fainter than at 4.5 μm where peak emission occurs (Baraffe et al., 2003; Spiegel & Burrows, 2012). In contrast to a background star, which is expected to be approximately equally bright in

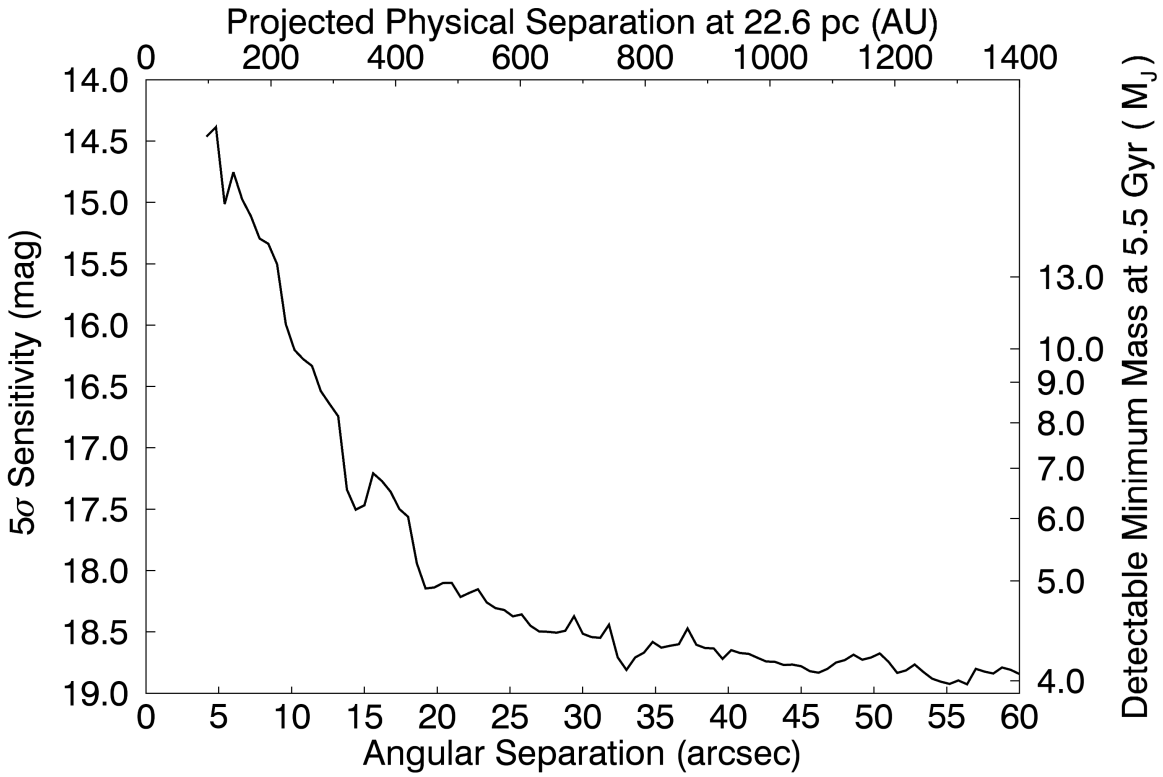

Figure 3.8: Median survey detection limits for P48 stars. The right axis shows the corresponding minimum detectable mass at the median target age of 5.5 Gyr. The top axis displays the projected physical separation at the median target distance 22.6 pc.

the 3.6 and 4.5 μm images, a planet detection recorded around the 5 σ limit at 4.5 μm is not expected to be recovered to any reasonable significance at 3.6 μm. This allows planetary sources to be distinguished from faint background stars initially without the need for a proper motion analysis. Therefore, we look for source non-detection at 3.6 μm to confirm planet candidacy.

Through comparison of 3.6 and 4.5 μm images, 36 candidates with realistic planetary mass colour were initially identified. Figure 3.9 shows a typical candidate identification through a 4.5 μm source non-detection at 3.6 μm. These candidates are further vetted with a common proper motion analysis using a second epoch combining archival Spitzer data and observations carried out during Spitzer Cycle 11 in 2015 under program 11102, repeating the original observations for several candidate host stars under the same observational parameters, with subsequent equivalent reduc-

tion. The target sample has a median total proper motion of 206 mas yr^{-1}, and over a baseline of $4 - 11$ years provided by the second epoch data, co-moving planetary companions can be confidently identified in an image with a $0.6''$ per pixel scaling. Four candidates recovered in a second epoch are revealed to be non-co-moving with the target star. Such sources are most likely rare background galaxies with unusual infrared colours, such as NGC 1377, which is brighter at $4.5\,\mu$m than $3.6\,\mu$m (Dale et al., 2005). Non-detection of the remaining sources and inspection of the raw CBCD frames leads to their identification as bad pixels surviving the Spitzer Science Center IRAC Pipeline reduction. Therefore, this survey records a null planet detection result.

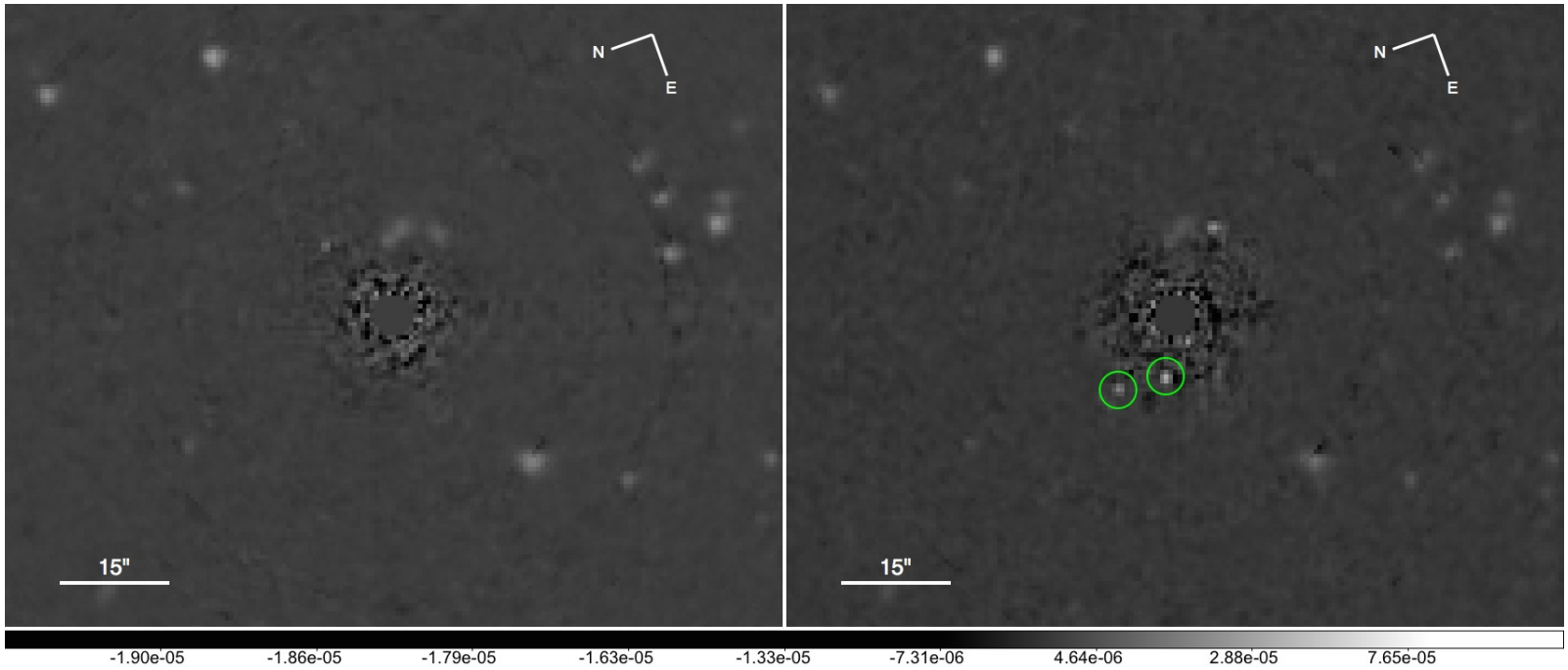

Figure 3.9: PCA reduced 3.6 μm (left) and 4.5 μm (right) images of HD 197890. The majority of point sources revealed appear at both wavelengths and therefore are likely background stars. Sources highlighted in green circles, however, only appear at 4.5 μm and are identified as potential planetary candidates. After further analysis these apparent sources were revealed to be surviving outlier pixel values.

Chapter 4

High Contrast Imaging with Spitzer II: Constraining the Frequency of Giant Planets out to 1000 AU Separations

As in previous direct imaging surveys, the null planet detection result and the magnitude detection limits of the Spitzer archival reanalysis can be exploited to place constraints on the wide giant population through statistical analysis, specifically the coupling of Monte Carlo simulations and Bayesian approximation. Effectively the Bayesian analysis determines the population of wide giants, as an upper fractional limit of stars that harbour such a companion, that is consistent with the derived planet detection probability and the null survey result. The relevance of this work is that with improved sensitivity in the PSF noise-limited regime, due to PCA application to archival Spitzer data, and the wide FOV providing background noise-limited sensitivity, sensitivity to planetary mass companions over separations on the order of $10^2 - 10^3$ AU has been achieved. This has been done for both young, P34, and relatively old, P48, stars, as seen in figures 3.7 and 3.8. With this enhanced sensitivity, significant constraints can be placed on the population of wide giants out to 1000 AU.

4.1 Statistical Formalism

The statistical analysis is formulated in the same fashion as previous works based on Lafrenière et al. (2007a). Consider the observation of the N, 121, targets in the archival reanalysis sample. The parameter j identifies individual targets in the sample such that $j = 1 - 121$. f denotes the fraction of stars that harbour at least one

planetary companion over a given mass and semi-major axis interval. The probability of detecting a companion orbiting star j over this mass and semi-major axis interval, given the survey detection limits and assuming such a companion exists, is denoted by p_j. The probability of detecting a planetary companion around star j, without any a priori knowledge of companion existence, is given by fp_j. Accordingly, the probability of a non-detection is given by $1 - fp_j$. The variable d_j is assigned a value of 1 or 0 to denote a planet detection or non-detection around star j respectively. The set $\{d_j\}$ across all N targets then represents the number of stars hosting planets that were detected in the survey. The probability of obtaining the observed number of detections $\{d_j\}$, or the likelihood of the data given f, is given by;

$$\mathcal{L}(\{d_j\}|f) = \prod_{j=1}^{N} (1 - fp_j)^{(1-d_j)} (fp_j)^{d_j} \tag{4.1}$$

In the case where a null planet detection result is achieved across the entire survey, as is the case in the Spitzer archival reanalysis, equation 4.1 reduces to;

$$\mathcal{L}(\{d_j\}|f) = \prod_{j=1}^{N} (1 - fp_j) \tag{4.2}$$

Bayesian inference then exploits the prior distribution $p(f)$, which in this case is an initial estimate of f, and the likelihood function $\mathcal{L}$, to derive the posterior distribution $p(f|\{d_j\})$. This is an updated, robust estimate of f in light of the observational data. Bayesian inference computes $p(f|\{d_j\})$ following Bayes' theorem;

$$p(f|\{d_j\}) = \frac{\mathcal{L}(\{d_j\}|f)p(f)}{\int_0^1 \mathcal{L}(\{d_j\}|f)p(f)\mathrm{d}f} \tag{4.3}$$

Initial systematic explorations and investigations into wide planet companion frequency, at separations $\lesssim 100$ AU, (e.g., Lafrenière et al., 2007a) had no prior knowledge of f and therefore adopted the most conservative prior distribution $p(f) = 1$. This conservative prior can also be adopted for a population analyses conducted using

the archival IRAC reanalysis data, as no prior knowledge concerning f exists over separations on the order of $10^2 - 10^3$ AU, the parameter space at which the observations are sensitive to planetary mass companions. A confident upper and lower bound for f, the credible interval, can then be evaluated from the posterior distribution. As a null planet detection result is recorded in the Spitzer archival reanalysis survey, the appropriate lower bound for f, $f_{\rm min}$, is 0. The upper limit on f is derived by solving the following equation;

$$\alpha = \int_0^{f_{\rm max}} p(f|\{d_j\})\mathrm{d}f \tag{4.4}$$

α is the credibility level of the derived result, which is chosen to be 95%. This formulation effectively questions, what is the range of f that will produce the null detection result 95% of the time, given the detection probability? If a survey were to record at least one planet detection, clearly $f_{\rm min} > 0$. In that case, equal-tail credible intervals must be solved to retrieve $f_{\rm max}$ and $f_{\rm min}$;

$$\frac{1-\alpha}{2} = \int_0^{f_{\rm min}} p(f|\{d_j\})\mathrm{d}f \quad \text{and} \quad \frac{1-\alpha}{2} = \int_{f_{\rm max}}^1 p(f|\{d_j\})\mathrm{d}f \tag{4.5}$$

Equation 4.4 can be solved analytically by recognising that $(1 - fp_j) \approx e^{-fp_j}$. This approximation is valid assuming $fp_j << 1$, which is a reasonable given the null detection result. If each individual p_j value is also approximated by the average detection probability across the sample, $\langle p_j \rangle$, equation 4.2 simplifies to;

$$\mathcal{L}(\{d_j\}|f) = e^{-Nf\langle p_j \rangle} \tag{4.6}$$

And equation 4.4 can now be easily solved to produce an estimate of $f_{\rm max}$;

$$f_{\rm max} \approx \frac{-\ln(1-\alpha)}{N\langle p_j \rangle} \tag{4.7}$$

This approximation can be also be derived using Poisson statistics (e.g., Carson et al., 2006; Chauvin et al., 2010), again valid for $fp_j << 1$. The average detection probability remains the only unknown in equation 4.7, and must be evaluated in order to determine $f_{\max}$.

4.2 Detection Probabilities

The probability of detecting a planetary companion within a given mass and semi-major axis interval must be evaluated for each target in order to determine the average detection probability across the survey sample. Each p_j value is dependent on the chosen mass and semi-major axis range, as well as the target age (e.g., younger planets will be brighter and easier to detect than older planets for a given mass) and the target distance (e.g., planets around nearby stars will be at larger angular separations, further from the residual PSF noise-limited core and easier to detect than planets around more distant stars for a given semi-major axis). Orbital eccentricity distribution, orbital orientation and orbital phase must also be accounted for as these parameters significantly impact planetary projected separation for a given semi-major axis. Similar to the argument concerning host star distance, larger projected separations will place planetary companions further from the residual PSF noise-limited core, providing a higher detection probability. This is true up to $\sim 20''$ projected separations as $> 20''$ is within the background noise-limited regime which typically provides a constant sensitivity level (see figures 3.7 and 3.8) and therefore detection probability, for a given mass.

As in previous wide giant statistical population analyses (e.g., Lafrenière et al., 2007a; Chauvin et al., 2010; Biller et al., 2013; Janson et al., 2012a), 10,000 synthetic planets are simulated for each target using a Monte Carlo approach to randomly sample planet mass, separation, orbital projection, and system age to derive the planet detection probability. Planet mass is sampled between 0.5 and 13 M_J. The 13 M_J boundary corresponds to the minimum mass required for the onset of deuterium burning and therefore an approximate upper mass limit for planetary objects. The 0.5 M_J boundary approximately corresponds to the surveys peak sensitivity limit, which is typically acquired within the background noise-limited regime of the young

P34 targets (see figure 3.7). This lower mass boundary is also the lowest mass for which COND-based evolutionary models provide magnitude predictions. The lack of constraints on the planet population over the parameter space explored here, 100 - 1000 AU, has ensured any constraints on mass distribution are correspondingly lacking. Therefore, a mass distribution of $dn/dm \propto m^{\alpha}$ is adopted, where $\alpha = -1.31$, extrapolated from a statistical analysis of radial velocity exoplanet studies (Cumming et al., 2008). In any case, Chauvin et al. (2010) find the choice of semi-major axis power-law index to dominate the derived detection probabilities in comparison to any variation in α.

Planet semi-major axis is sampled from a linear distribution between 100 and 1000 AU, corresponding to the parameter space over which the archival reanalysis is sensitive to planetary mass companions. Nielsen et al. (2008); Nielsen & Close (2010) found semi-major axis power laws reported by Cumming et al. (2008) to be invalid at the separations considered here ($>$ 100 AU), motivating the choice of a linear distribution. In any case the choice of semi-major axis distribution does not significantly impact the result as the uncertainty in stellar age completely dominates the uncertainty in detection probabilities.

Eccentricity distribution, orbital orientation and orbital phase are all accounted for with one parameter, the orbital projection factor of Brandeker et al. (2006). For companions on circular orbits, Brandeker et al. (2006) derives a probability density distribution describing the projected separation of a companion in units of its semi-major axis. This distribution is derived by generating a stochastic vector with a direction uniformly distributed over a unit sphere and calculating the projected distance between a planet and its host in the plane perpendicular to a random, uniformly distributed viewing direction. For companions on elliptical orbits, derivation of the projection factor probability distribution is more complicated as the radial separation between the companion and its host is nonlinear in time, and consideration must be given to the form of the eccentricity distribution. Brandeker et al. (2006) adopts an eccentricity distribution of $f(e) = 2e$ based on theoretical predictions and concurring observations of long period ($>$ 1000 days) binaries (Duquennoy & Mayor, 1991). As the probability distribution cannot be derived algebraically in this case, Brandeker et al. (2006) provides a numerical solution following a Monte Carlo approach. 10^8 binary orbits are simulated taking into account eccentricity, phase and orbital orientation and the resultant projection factor is recorded (by dividing the outputted

projected physical separation by the randomly generated semi-major axis). The probability density and distribution of the recorded projection factor is shown in figure 4.1. The probability density curve, $f_S(s)$, is well fitted with the following function;

$$f_S(s) = \frac{\pi}{4} \sin\left(\frac{\pi}{2}s\right) \tag{4.8}$$

Where $s \in [0, 2]$,. Accordingly, the probability distribution, $F_S(s)$, is given by;

$$F_S(s) = \frac{1}{2}\left[1 - \cos\left(\frac{\pi}{2}s\right)\right] \tag{4.9}$$

Similar to the argument concerning mass distribution, the lack of constraints on the planet population over 100 - 1000 AU, has ensured any constraints on eccentricity distribution over this parameter space are correspondingly lacking. Therefore, the $f(e) = 2e$ distribution observed for long period binaries is assumed to be relevant for the long period planet simulations. Hence, the elliptical orbit projection factor probability distribution of Brandeker et al. (2006) is adopted. A random projection factor, S, sampled from this distribution is generated via the following equation;

$$S = 2\pi^{-1} \arccos(1 - 2X) \tag{4.10}$$

Where $X \in U(0, 1)$. A projection factor is generated for each of the 10,000 simulated planets and used to translate true physical semi-major axis, randomly sampled between 100 - 1000 AU, to a projected physical separation. Projected separations, a_p, are then converted to angular separations, θ, using the known stellar distance (given in table 3.2) via $\theta = a_p/D$. Here we do not sample over any uncertainty in stellar distance as the revised Hipparcos measurements have good precision and thus the uncertainty in stellar age completely dominates the uncertainty in detection probabilities.

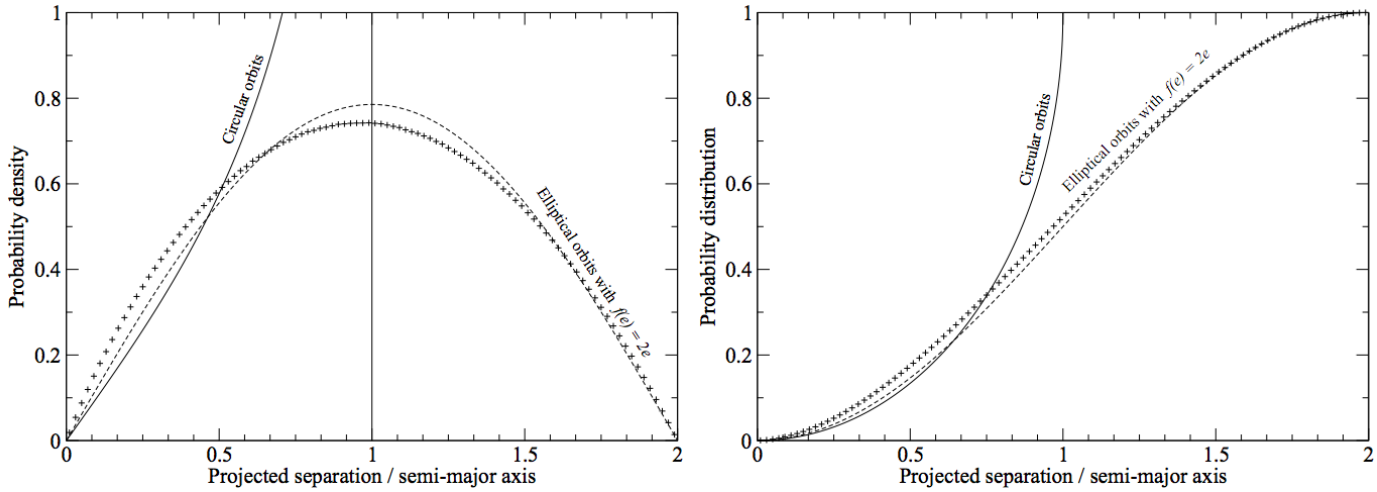

Figure 4.1: Left panel: probability density for the the orbital projection factor, i.e., the projected separation between a companion and its host in units of its semi-major axis. Right panel: corresponding probability distribution for the the orbital projection factor. Distributions for both circular orbits (solid line) and elliptical orbits (crosses for the Monte Carlo output and a dash line for the fit to the data) are presented. Image: Brandeker et al. (2006)

Age is sampled between limits of reliable estimates from the literature (typically YMG ages presented in table 3.1), or between 1 and 10 Gyr for the majority of P48 targets with ages that are not well constrained. These ages are given in table 3.2. Using the same COND-based evolutionary models (Allard et al., 2001; Baraffe et al., 2003) that allowed survey magnitude detection limits to be translated into mass detection limits (see section 3.5.1), the randomly sampled planet masses can be directly translated into Spitzer IRAC 4.5 μm magnitudes using the sampled target age. However, these models predict absolute magnitudes whilst the survey detection limits are given in apparent magnitudes. Therefore, to make the two compatible, the simulated absolute magnitudes, M, are translated into apparent magnitudes, m, using the known stellar distances via the following equation;

$$m = M + 5\,(log(D) - 1) \tag{4.11}$$

The Monte Carlo approach, generating planets in the mass range [0.5,13] M_J and the separation range [100, 1000] AU, and accounting for system age, distance, orbital eccentricity, orientation and phase, produces two outputs for each of the 10,000

planets; an angular separation and apparent Vega magnitude. These outputs are effectively coordinates that allow each of the 10,000 planets to be mapped on to the $5\,\sigma$ magnitude sensitivity curves, of which the median for P34 and P48 targets are presented in figures 3.7 and 3.8. The fraction of planets that lie above the detection limit provides the detection probability for each target. This process is repeated for every target in the sample, generating 10,000 discrete planets on each iteration. Mean detection probabilities for P34 and P48 stars for the mass range [0.5,13] M_J and the separation range [100, 1000] AU are 0.42 and 0.08 respectively. Mean detection probabilities over P34 targets are typically much greater than the mean over the entire sample, due to the superior mass sensitivity of P34 targets corresponding to their relatively young ages. However, as shown in section 4.3, the inclusion of P48 targets provides a favourable trade off between lower mean detection probability, $\langle p_j \rangle = 0.28$, and increased sample size, which leads to better statistical constraints on the wide giant population.

Monte Carlo simulations are additionally performed over varying mass and separation ranges in order to constrain the wide giant population as a function of mass and separation. The mass range is varied between [0.5, m_{max}] M_J with m_{max} ranging from 1.0 to 13.0 M_J in increments of 0.5 M_J. The separation range is varied between [a_{min}, a_{max}] with a_{min} = 75, 100, 125 AU, and a_{max} in the range [a_{min} + 25, 1000] AU, increasing in increments of 25 AU. Mean detection probabilities over the entire sample, as a function of upper mass and outer separation limit, are given in figure 4.2.

4.2.1 Binary Bias

It is noted that 43 targets in the archival reanalysis sample are identified as binary stars in the Washington double star catalog (Mason et al., 2001) that have been vetted for true companionship through a proper motion analysis. These targets are identified in table 3.1 where the angular separation between the primary and stellar companion are also given. These binaries account for $> 1/3$ of the entire sample. Rejecting such a large number of targets from the statistical analyses would have a significant impact on the population constraint. In the case of a null detection result, it increases the frequency upper limit by a factor of $\sim 3/2$ (see equation 4.7), if the mean detection probability remains constant. This motivates the inclusion of the binary sample in the planet frequency determination. However, this may introduce a

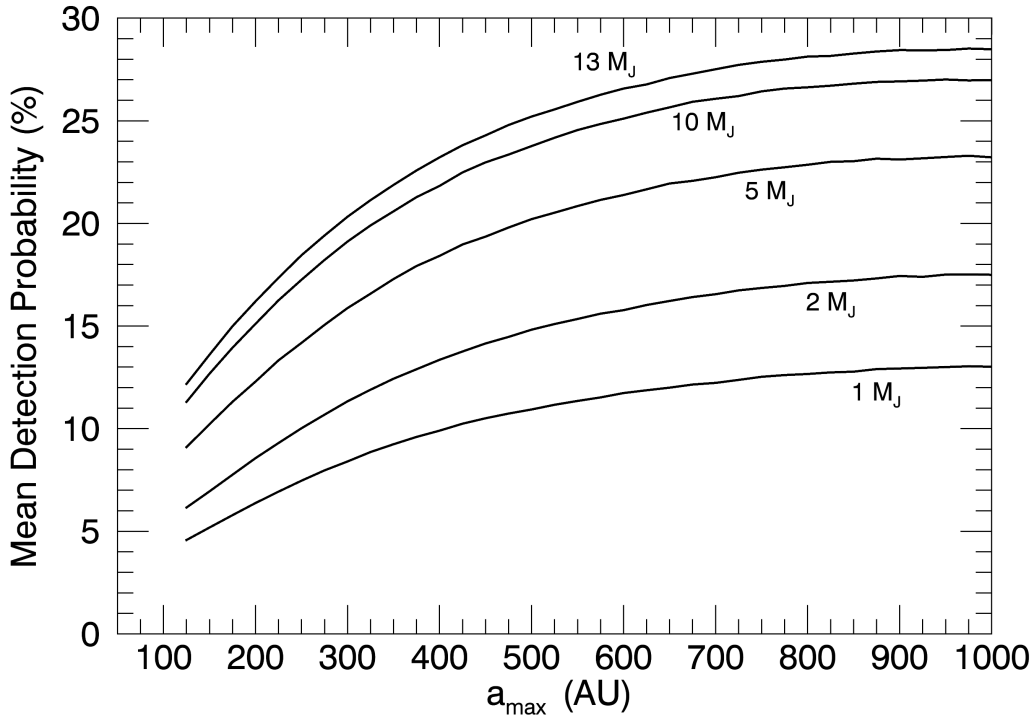

Figure 4.2: Mean planet detection probabilities over the combined P34 and P48 sample as a function of semi-major axis and mass. The x axis denotes the outer limit a_{max} over which planet separation is sampled with constant a_{min} = 100 AU. Curves are labeled with upper mass limit m_{max} over which planet mass is sampled in units of M_J, with constant m_{min} = 0.5 M_J.

bias to any astrophysical interpretation, which must be accounted for.

A null planet detection result is recorded in these binary systems, which is the basis of our statistical formalism. However, the binary companion will have introduced a parameter space of instability (due to the chaotic dynamics of three gravitationally attracting bodies) in which a planet would not be expected to orbit around its host star. To deal with this and remove the bias from the analysis, the stability criteria of Holman & Wiegert (1999) are used to determine the instability regions, for both potential S- and P-type systems. S-type systems refer to planetary orbits around only one of of the components of the binary, within the orbit of the pair. P-type systems refer to planetary orbits around both components, outside of the pairs orbit. The stability criteria for S-type systems is as follows;

$$
\begin{aligned}
a_c/a_b &= (0.464 \pm 0.006) + (-0.380 \pm 0.010)\mu + (-0.631 \pm 0.034)e \\
&\quad +(0.586 \pm 0.061)\mu e + (0.150 \pm 0.041)e^2 + (-0.198 \pm 0.074)\mu e^2
\end{aligned} \tag{4.12}
$$

Where a_c is the critical semi-major axis, a_b the binary semi-major axis and μ the binary mass ratio. For S-type systems a_c constitutes a maximum outer stability limit, such that orbits beyond a_c and inside of the secondary star are unstable. The stability criteria for P-type systems is as follows;

$$
\begin{aligned}
a_c/a_b &= (1.60 \pm 0.04) + (5.10 \pm 0.05)e + (-2.22 \pm 0.11)e^2 \\
&\quad +(4.12 \pm 0.09)\mu + (-4.27 \pm 0.17)e\mu + (-5.09 \pm 0.11)\mu^2 \\
&\quad +(4.61 \pm 0.36)e^2\mu^2
\end{aligned} \tag{4.13}
$$

For P-type systems a_c constitutes a maximum inner stability limit, such that orbits beyond the secondary star and inside of a_c are unstable. Therefore, a_c values calculated via equations 4.12 and 4.13 form the bounds of the instability region for a planet on an unknown orbit. Many of the binary orbits and companion masses are not well documented, so for algorithm simplicity, consistency and to ensure conservative results, the worst-case scenario of an equal mass binary system, which introduces the greatest range of instability, is assumed. The latest epoch separation given in the Washington double star catalog is also assumed to be the true physical separation. This is a reasonable assumption as for a random distribution of binary eccentricities, phases, and orientations the most likely true physical separation is given by the projected separation (Brandeker et al., 2006, see left panel in figure 4.1). Since the eccentricity distribution of this sample is unknown, circular orbits are assumed when estimating the instability regions. Another option would be to assume the eccentricity distribution adopted by Brandeker et al. (2006, $f(e) = 2e$), or an empirically derived distribution based on stellar systems with orbital characterisation (e.g., Raghavan et al., 2010). However, this choice has very little impact on the results.

A range of eccentricity values have been tested in the simulations, verifying that the derived frequency remains constant in each case. Instability is then accounted for by ensuring that the calculated instability regions are counted as a non-detectable range, i.e., Monte Carlo simulated planets within this parameter space are counted as non-detections, even if they lie above the detection limits.

However, although this accounts for the bias introduced by the instability regions surrounding binary companions, it must be noted that the true frequency of wide giant planets around binary stars may be different than that around single stars. This hypothetical frequency discrepancy would (e.g.) be due to the influence that a binary companion will have on the planet formation process. While studies have found that binarity has a minimal effect on overall planet frequency (Bonavita & Desidera, 2007; Bergfors et al., 2013; Bonavita et al., 2016), it has been suggested that binary companions with separations $\lesssim$ 100 AU may result in a decrease in the number of planets formed through enhanced dynamical heating of the protoplanetary disk (Thalmann et al., 2014). While binary companions with separations $\lesssim$ 100 AU only account for 12 of the 43 binaries in our sample, an element of bias will be inherent in the statistical result derived from a combined single and binary star sample.

4.3 Estimation of Planet Frequency

With the determination of the average detection probability, $\langle p_j \rangle$, an upper limit on the frequency of planets hosting wide giants can be derived through the Bayesian approximation given in equation 4.7. The population analyses performed in this study derives an upper limit on the frequency of planets in the mass range [0.5, 13] M_J and the semi-major axis range [100, 1000] AU to be 9%. This value was calculated using the average detection probability $\langle p_j \rangle = 0.28$, across all 121 targets in the sample. If the P48 sample is excluded from the analysis, the average detection probability $\langle p_j \rangle = 0.42$, across the 73 P34 stars allows for the upper limit of the planet frequency to be constrained to 10%. Therefore, although the relatively high detection probabilities of young P34 stars dominate the determination of the frequency limit, the inclusion of the low detection probability old P48 stars in the analysis enables a slightly tighter constraint on planet frequency due to a favourable trade-off between $\langle p_j \rangle$ and increased sample size. For completeness, the frequency limit derived from analysis of the P48 sample in isolation ($\langle p_j \rangle = 0.08$, $N = 48$) is 78%, indicating

the lack of stringent constraints that can be placed on the planet population from systematic studies of old (> 1 Gyr) stellar populations.

As no previous survey has probed this parameter space to a similar degree of sensitivity there is no literature comparison to this result. However, the low-frequency findings certainly support the extension of previous survey findings of low-frequency at separations on the order of $10-100$ AU (see table 2.1), out to 1000 AU separations, and is in general agreement with the theory of Veras et al. (2009, see section 1.2.2.2), predicting a low-frequency population of 10^2-10^5 AU planets at ages > 50 Myr. Figure 4.3 shows planet frequency limits as a function of mass over constant separation range $100-1000$ AU. Figure 4.4 shows planet frequency as a function of separation with $a_{min} = 75$, 100, and 125 AU over constant mass range 0.5-13 M_J. While this study well constrains the population of $100-1000$ AU planets with masses ranging from 0.5 to 13 M_J, the planet frequency upper limit increases toward smaller mass and separation limits. This is a deterioration of the population constraint due to bias inherent in the detection technique, where imaging sensitivity, and therefore detection probability, decreases with decreasing mass (as planets become less luminous) and separation (as planets approach the residual PSF noise-limited core). However, planet frequency tends to be a smoothly varying function with respect to mass and separation, and Figure 4.4 shows that at separations $\gtrsim 700$ AU frequency values tend to be approximately constant, corresponding to the background noise-limited regime with approximately constant sensitivity. Thus there is no reason to expect that the choice of [0.5, 13] M_J and [100, 1000] AU boundaries are arbitrarily optimistic with regard to reasonably lower mass and separation limits.

4.4 Conclusions

In this study (spanning Chapters 3 and 4 of this Thesis) the results of a reanalysis of two archival Spitzer imaging surveys encompassing 121 targets with varying spectral types and ages have been presented. Previously, the large PSF associated with the 0.85 m Spitzer telescope diameter has severely limited its capability for directly imaging exoplanets. With the application of PCA, this study has removed the stellar PSF and opened up sensitivity to planetary mass companions over a broad range of separations. PCA has provided up to a magnitude sensitivity improvement at small separations with respect to conventional PSF subtraction methods, highlighting the

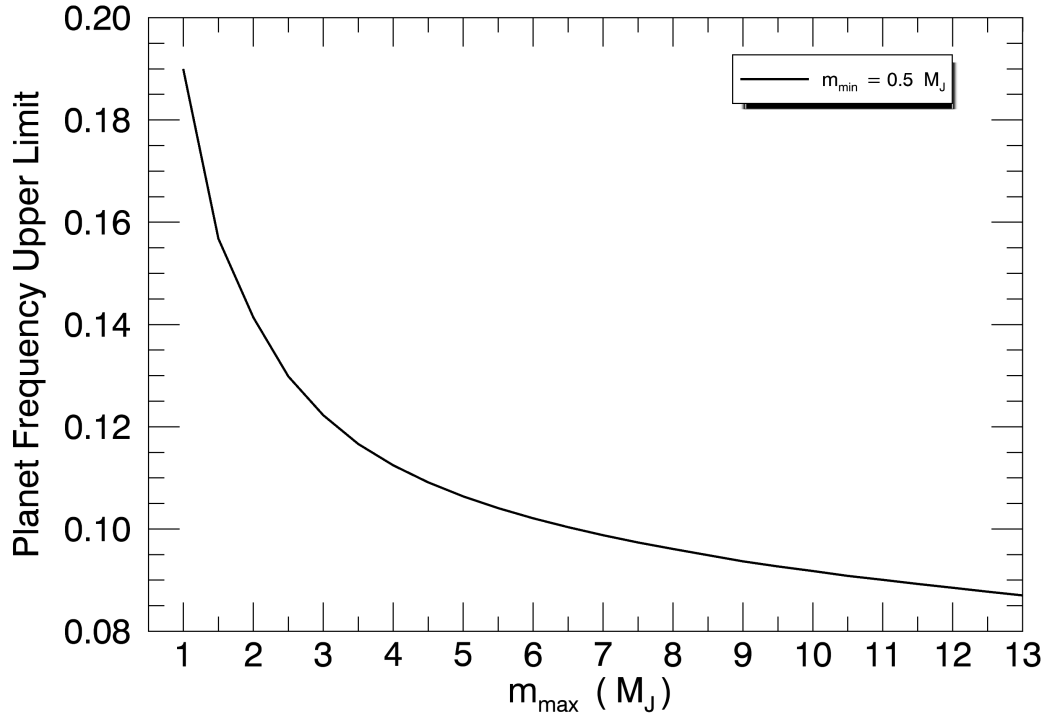

Figure 4.3: Planet frequency upper limit (at the 95% confidence level) as a function of mass. The x axis denotes the upper mass limit m_{max} with constant $m_{min} = 0.5$ M_J. The separation range is constant, $100 - 1000$ AU.

strength of the technique, even on a relatively unfavourable data set. Using theoretical mass-luminosity evolutionary models, it has been shown that sensitivity to planetary mass companions down to 0.5 M_J at separations on the order of $10^2 - 10^3$ AU has been achieved. This parameter space has not previously been systematically explored by imaging surveys to any comparable degree of sensitivity due to anisoplanatism and FOV limitations of ground-based surveys, and PSF contrast limitations of space-based surveys. Therefore, through the coupling of Monte Carlo simulations and a Bayesian analysis, for the first time the population of $0.5 - 13$ M_J, $100 - 1000$ AU planets has been constrained, producing an upper frequency limit of 9%. This is an extension of findings of low companion frequencies in numerous previous surveys at separations on the order of $10 - 10^2$ AU. Constraining this very wide giant planet population allows for previously untested formation and evolutionary theories to be adapted and constrained.

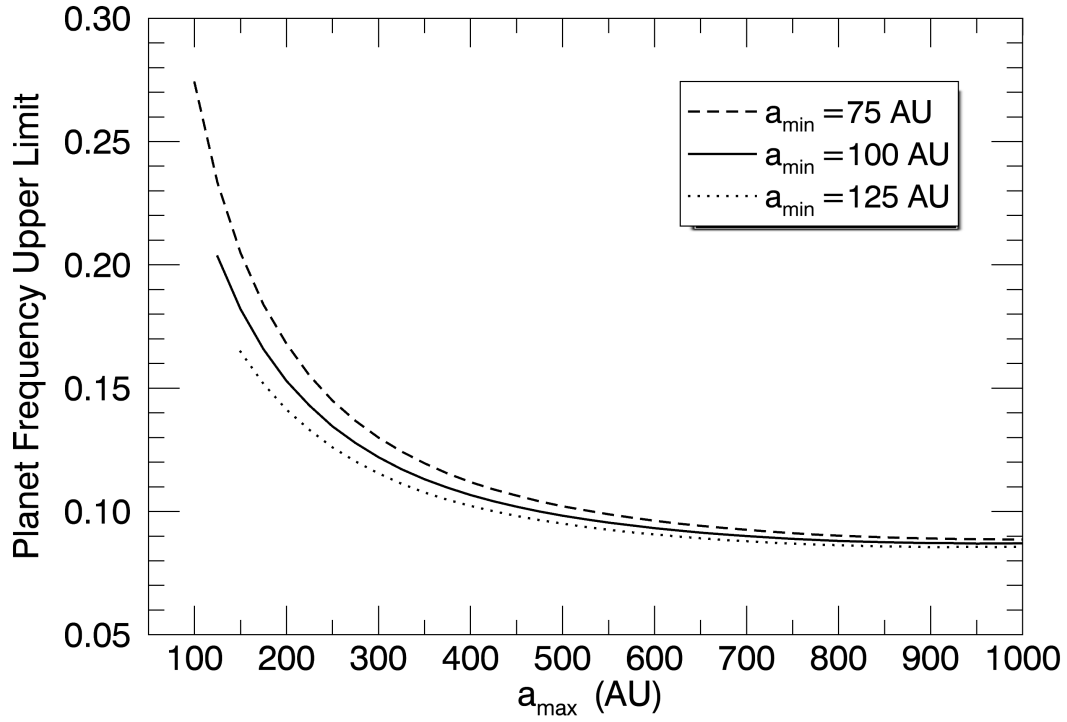

Figure 4.4: Planet frequency upper limit (at the 95% confidence level) as a function of separation. The x axis denotes outer separation limit amax with constant a_{min} = 75, 100, 125 AU. The mass range is constant, $0.5 - 13$ M_J.

Whilst these efforts provide an initial picture of the very wide planet population, planet detections and similarly stringent frequency limits are still lacking in this parameter space compared to closer separations. Extending sensitivity enhancement to additional imaging surveys with the goal of detecting planets within a previously elusive parameter space and building up a framework of robust wide planet population statistics is envisioned in future work (see section 7.1).

Chapter 5

A Radial Velocity Survey of Spatially Resolved Young, Low-Mass Binaries

The contents of this chapter have been accepted for publication in Astronomy and Astrophysics as the paper entitled 'A Radial Velocity Survey of Spatially Resolved Young, Low-Mass Binaries'. All of the work presented is my own, with the exception of the J053018BC mass ratio and systemic RV derivation (section 5.4.1), which was performed by co-author Josh Schlieder, and the limits on tidal synchronisation analysis (section 5.4.2), which was performed by co-author Markus Janson. A summary of the AstraLux multiplicity surveys is also given for which I have carried out a series of observations, leading to the publications Janson et al. (2017); Calissendorff et al. (2017).

As detailed in section 2.4.2, the identification and characterisation of low-mass binaries is of importance for a range of astrophysical investigations. To summarise, low-mass binaries in $\sim 10-100$ Myr YMGs in the solar neighbourhood (e.g., Zuckerman & Song, 2004; Torres et al., 2008) are of particular significance as they provide unique opportunities to calibrate stellar models and evaluate the ages and coevality of the groups themselves. This is critical for estimating the mass or initial entropy of planets and brown dwarfs in YMGs using mass-luminosity evolutionary models (e.g, Baraffe et al., 2003, 2015), where a precise system age is essential for deriving a precise object mass. Low-mass M-dwarfs have pre-main sequence lifetimes on the order of ~ 100 Myr and therefore are continually evolving along a mass-luminosity track throughout the YMG phase, providing ideal laboratories for precise isochronal dating, if a model-independent dynamical mass can be measured. AstraLux lucky

imaging multiplicity surveys (e.g., Bergfors et al., 2010; Janson et al., 2012c, 2014b, 2017) have recently identified hundreds of new YMG low-mass binaries, where a subsample of M-dwarf multiples have estimated orbital periods less than 50 years. A radial velocity survey of a sample of 29 such targets has been conducted to complement the astrometric data. This will allow enhanced orbital determinations and precise dynamical masses to be derived in a shorter timeframe than possible with astrometric monitoring alone, and allow for a more reliable isochronal analysis.

In this chapter I present the results of a radial velocity survey of spatially resolved young, low-mass binaries. I give a summary of the AstraLux multiplicity surveys and the survey results before describing the radial velocity follow-up sample. I then detail the RV observations with FEROS and the data reduction, going on to present the radial velocity measurements derived for the sample over several epochs. The detection of the three-component spectroscopic multiple 2MASS J05301858-5358483 is also presented, for which the C component is a new discovery, and forms a tight pair with the B component. Originally identified as a YMG member, this system is found to be a likely old field interloper, whose high chromospheric activity level is caused by tidal spin-up of the tight BC pair. One other, previously known, triple system with a tight pair exists in the sample (2MASS J04244260-0647313), but for the rest of the targets an analysis is presented which finds additional tidally synchronised companions are highly unlikely, providing further evidence that their high chromospheric activity levels are generally signatures of youth.

5.1 AstraLux Multiplicity Surveys

AstraLux Multiplicity surveys (e.g., Bergfors et al., 2010; Janson et al., 2012c, 2014b, 2017) have been ongoing for almost a decade. The aim of these surveys has been to identify and characterise YMG member M-dwarf binaries, with the primary goal of deriving dynamical masses for the components, enabling a precise isochronal dating that can then be applied to the full YMG of which they are members, for improved age constraints on the full population of stars.

Targets were typically selected for observation from multiple catalogues of late type stars on the basis of youth; indicated by high-probability YMG membership (e.g., Malo et al., 2013, 2014; Kraus et al., 2014b) and X-ray emission (Lépine &

Gaidos, 2011). To evaluate YMG membership six observational parameters are required to trace the target to a particular co-moving association. These parameters are the three dimensional galactic position (XYZ) and the three dimensional space velocity (UVW). As M-dwarfs are typically faint at visible wavelengths they often lack a parallactic distance measurement (Z) and a radial velocity measurement (W). However, Bayesian approximations using the BANYAN code of Malo et al. (2013); Gagné et al. (2014) can differentiate YMG members from field stars to high probability using R.A, .decl and measured proper motions (XY UV respectively) alone. Additional indicators of youth such as significant X-ray luminosity complement and lend confidence to the membership evaluation. X-ray emission is a product of the extreme temperatures (on the order of a million Kelvin) present in stellar corona that are driven by magnetic fields from within the star (e.g. Erdélyi & Ballai, 2007). X-ray luminosity is therefore considered a reliable proxy for magnetic activity. The stellar dynamo generating these large-scale magnetic fields is thought to depend on the shearing of magnetic field lines within the stellar interior due to differential rotation between the convective envelope and the radiative core in partially convective stars. Therefore, magnetic activity, and subsequently X-ray luminosity, is dependent on stellar rotation rate (e.g. Pizzolato et al., 2003; Wright et al., 2011). As stellar rotation rate decreases over time as a result of magnetic braking (e.g., Ivanova & Taam, 2003), where material in the stellar wind carries angular momentum away from the star, it is expected that X-ray luminosity decreases with stellar age, and indeed this has been observed (e.g., Jackson et al., 2012; Booth et al., 2017). As the AstraLux surveys target a wide range of M-dwarfs, some consideration must be given to the fully convective nature of targets with spectral types later than M3 (the boundary between partially and fully convective stars) as there will be no differential rotation between convective and radiative layers and thus the activity-rotation (and subsequently age) relationship may not be valid. However, Wright & Drake (2016) recently demonstrated that the activity-rotation relationship is indistinguishable between fully convective and solar-type stars. Therefore, compiling a youthful sample based on X-ray luminosity is valid, even though the dynamo process for later type M-dwarfs is not yet fully understood. Spectral type was confirmed from multiple catalogues of spectroscopically classified late type stars (through the measurement of molecule band and atomic line spectral features e.g., Riaz et al., 2006; West et al., 2011).

All observations were acquired with the AstraLux Norte (Hormuth et al., 2008) and AstraLux Sur (Hippler et al., 2009) cameras on the 2.2 m telescope at Calar Alto, Spain and the New Technology Telescope (NTT) at La Silla, Chile respectively. The cameras are an almost identical set of high-speed electron multiplying cameras allowing for exposures as short as 29 ms using the full 512×512 pixel FOV ($24'' \times 24''$ on AstraLux Norte and $16'' \times 16''$ on AstraLux Sur) or 15 ms using a 256×256 pixel sub-array. Therefore, these cameras are ideal for lucky imaging purposes (see section 2.1.1) and can achieve PSF FWHMs close to 100 mas. This approximate resolving power is well suited for M-dwarf multiplicity studies.

Typically 10,000 exposures of each target were acquired under the shortest possible exposure time, 15 ms in the sub-array mode, although this value increased for fainter targets or under poorer seeing conditions in order to achieve sufficient counts. The majority of targets were observed in both the Sloan Digital Sky Survey (e.g., Ahn et al., 2012) i' and z' band filters, with central wavelengths of 766 and 912 nm respectively, over two or more epochs. Each set of raw frames generated by the lucky imaging sequence were reduced on site with the dedicated AstraLux pipeline (Hormuth et al., 2008). This pipeline performs all standard flat field and bias corrections before oversampling using a Drizzle algorithm (Fruchter & Hook, 2002) to generate images with a pixel scale of ~ 23.3 mas and ~ 15.4 mas per pixel for AstraLux Norte and Sur respectively. Individual frame alignment is then carried out by aligning the brightest pixel throughout the 10,000 frames which should typically correspond to the core of the primary PSF in any multiple system. The pipeline then generates output images with different selection levels, e.g. a combination of all the frames, the 10% frames with the least distortion (largest Strehl ratio) and the 1% frames with the least distortion. A selection level of 10% is consistently chosen as a favourable trade off between image resolution (which improves with reduced frames due to better seeing) and image sensitivity (which reduces with reduced frames due to rejection of a portion of the measured flux).

To date AstraLux M-dwarf Multiplicity surveys have systematically studied $>$ 1000 X-ray active young M-dwarfs, many of which are also high probability YMG members. As one would expect, roughly 30% of these were identified as multiple systems, significantly increasing the number of close YMG M-dwarf binaries. A typical resolved AstraLux multiple can be seen in figure 5.1. Gaussian centroid fitting is applied to each resolved PSF in order to calculate position in detector coordinates

and relative flux for each component, allowing magnitude difference, projected separation and position angle to be calculated. For close binaries ($\lesssim 1''$) where centroid fitting becomes increasingly inaccurate (due to intricacies of Gaussian fitting to the combined PSF patterns of multiple stars), PSF fitting is conducted. This is done by taking the PSF of a single star as a reference and creating multiple star configurations (varying component brightness and position) to find the solution that minimises the residuals between the observed and reference data. The projected separations and position angles in detector coordinates are then translated into sky coordinates using the calibration of a standard stellar cluster, e.g., Trapezium or M15, by comparing relative detector positions of several stars calculated by Gaussian fitting to their recorded sky position in previous studies (e.g., McCaughrean & Stauffer, 1994; van der Marel et al., 2002). An example of the astrometric data that can be acquired through these surveys for a typical target and an initial orbital fit to the data can be seen in figure 5.2.

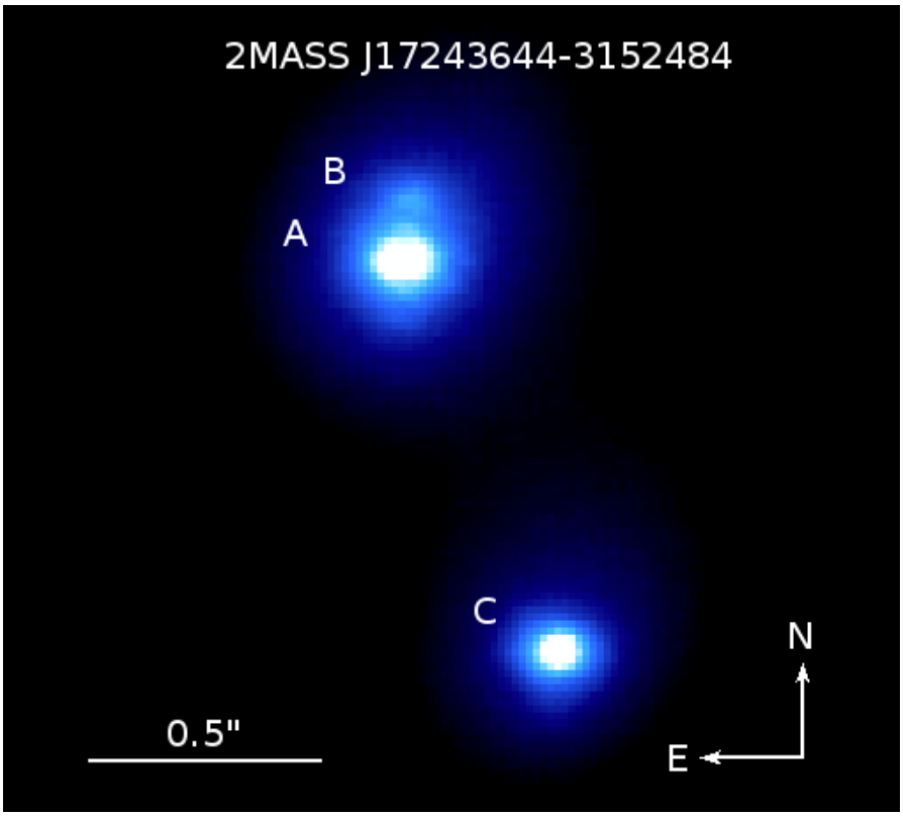

Figure 5.1: Example of the final image output of the AstraLux multiplicity surveys. Here the J17243644-3152484 triple system has been resolved for the first time (Janson, Durkan et al., 2017).

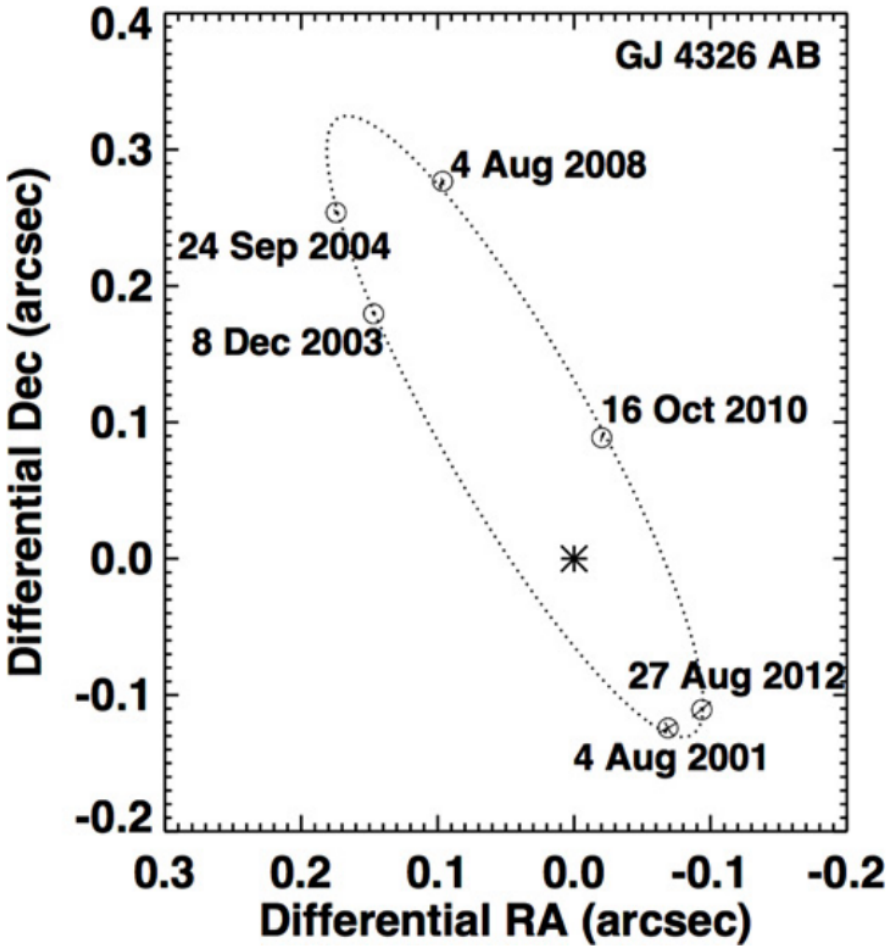

Figure 5.2: Example of the astrometric data acquired for a typical target in the AstraLux surveys, GJ 4326 (Janson et al., 2014a). The asterisk identifies the M3.0 primary, circles identify the measured position of the M4.5 secondary. This system has particularly good data coverage over a range of the orbital phase, almost closing the orbit. This allows for a good orbital fit to the data (dotted ellipse) and good constraints on all orbital parameters (except semi-major axis due to the large uncertainty in the systems distance estimate.

Individual spectral types for resolved components have been consistently derived following the method of Daemgen et al. (2007). This method assumes a flux weighted, linear relationship between integrated spectral type (adopted from spectral catalogues of e.g., Riaz et al. (2006)) and component spectral types;

$$SpT_{int} = \frac{f_A SpT_A + f_B SpT_B}{f_A + f_B} \tag{5.1}$$

This linear relationship is valid in the spectral type range M0-M7 where TiO and VO band strengths (from which spectral types are derived) behave linearly (Cruz & Reid, 2002). Here f_A and f_B are the respective flux values of the primary and secondary components. These values effectively act as flux weights that can be derived from the measured magnitude difference, $\Delta i'$ and $\Delta z'$. For example, if $\Delta z'$ is such that $x\%$ of the unresolved flux is due to the primary and $y\%$ is due to the secondary, then $f_A = x$ and $f_B = y$. SpT_{int} is then calculated for a grid of SpT_A and SpT_B values and the residuals between the measured integrated spectral type and the calculated values are computed. These residuals are plotted as a contour map for which an example is shown in figure 5.3. An additional relationship allows for further constraints to be placed on the resolved spectral types;

$$\Delta z' = M_{z'}(SpT_B) - M_{z'}(SpT_A) \tag{5.2}$$

Where $M_{z'}$ are the individual z' band magnitudes. For each grid value of SpT_A, $M_{z'}(SpT_A)$ is estimated from the empirical spectral-type - magnitude models of Kraus & Hillenbrand (2007). These models are given in table 5.1. The SpT_B corresponding to the $M_{z'}(SpT_B)$ value (again estimated from Kraus & Hillenbrand (2007)) which best matches the measured $\Delta z'$ given $M_{z'}(SpT_A)$ is recorded. These values are then overplotted on the residual contour map and the intersection of relations 5.1 and 5.2 produce an unambiguous determination of SpT_A and SpT_B for each system. An example of this determination is shown in figure 5.3. Final spectral type determinations are based on the z' band measurements, however, the same calculations are carried out using i' band values which give consistent spectral types, and therefore reasonable errors, to within ± 0.5 sub-classes. As shown in table 5.1, the empirical spectral-type - magnitude models of Kraus & Hillenbrand (2007) also provide an estimate of stellar mass as a function of spectral type. This allows for a model-dependant, rough approximation of individual component masses.

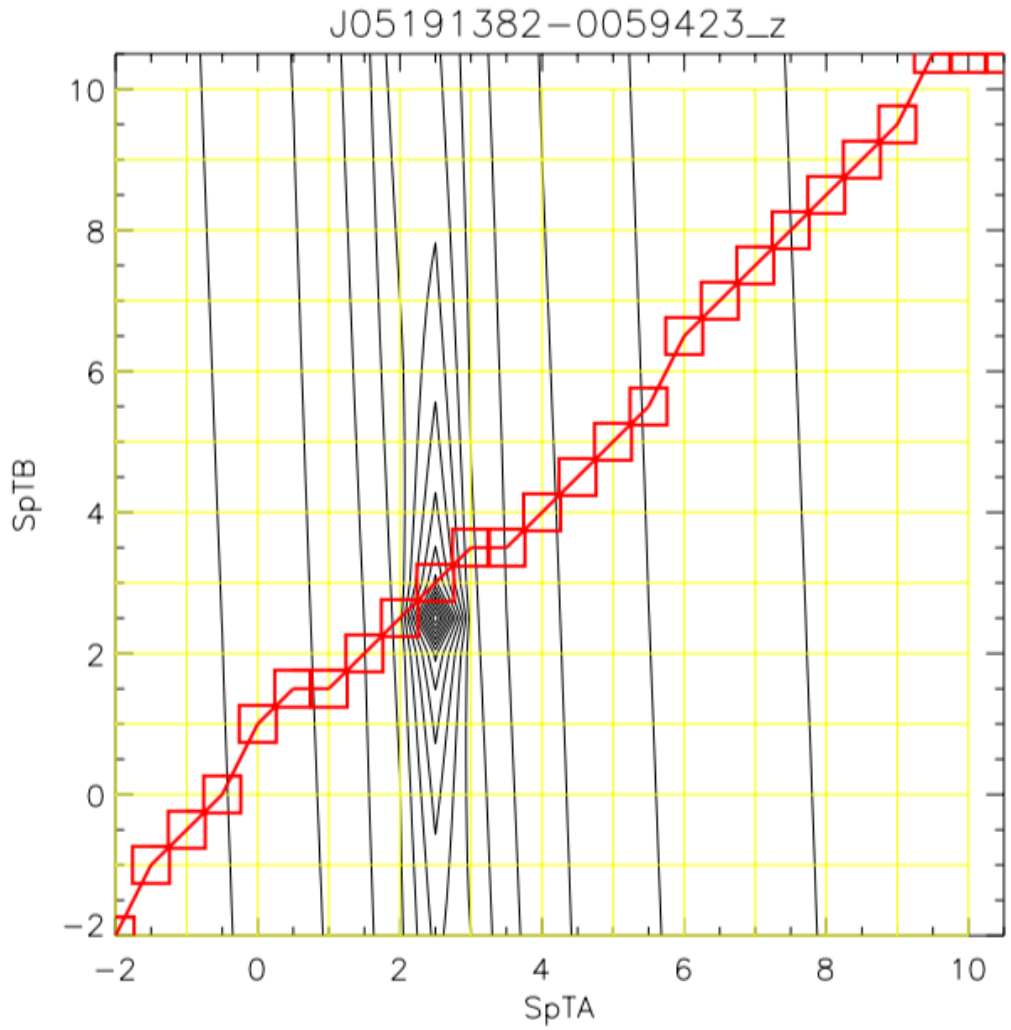

Figure 5.3: Example of resolved, individual spectral type determination for the target J05191382-0059423AB. The black contour plot is generated from residuals between measured SpT_{int} and that calculated from equation 5.1. Over plotted in red is the best estimate of SpT_B given the measured $\Delta z'$, the grid of SpT_A values and using the models of Kraus & Hillenbrand (2007) and equation 5.2. The intersection of these two calculations produce the spectral type determinations. For example, in this plot the two relationships intersect at [2.5, 3.0] and therefore SpT_A = M2.5 ± 0.5, SpT_B = M3.0 ± 0.5. Image: Unpublished Janson et al. (2012c)

Resolved multiple systems have been, and will continue to be, astrometrically monitored in order to fully sample and close binary orbits which would allow orbital parameters to be stringently constrained with the aim of deriving dynamical masses for individual components. This has recently been achieved by Calissendorff et al. (2017) for the young triplet 2MASS J10364483+1521394. A combined dynamical mass of 0.48 ± 0.14 $M_\odot$ and a mass ratio of 1.00 ± 0.03 was derived for the low-mass

Table 5.1: Kraus & Hillenbrand (2007) spectral-type - magnitude models

SpT	$M_{i'}$	$M_{z'}$	$M_\odot$
M0	7.83	7.46	0.59
M1	8.12	7.64	0.54
M2	8.73	8.15	0.42
M3	9.44	8.74	0.29
M4	10.48	9.64	0.20
M5	11.76	10.71	0.15
M6	12.98	11.88	0.12
M7	13.94	12.68	0.11
M8	14.83	13.21	0.102
M9	15.38	13.69	0.088

pair orbiting the M-dwarf primary. However, this system is particularly favourable to enabling robust mass determinations, due to its triple nature and the short orbital period (8.41 years) of the tight pair. The majority of the resolved sample has longer orbital periods, ensuring that orbits can only be closed and robust constraints derived over timescales on the order of decades. Exploiting dynamical masses for model calibration and isochronal dating that can then be applied across a wide range of YMGs is the underlying goal of our AstraLux multiplicity surveys.

However as mentioned in section 2.4.2, astrometric monitoring alone is often not enough to derive precise dynamical masses and enable a robust isochronal analysis, a complementary RV analysis is equally important for a range of purposes. To summarise, whilst relative astrometry is limited to providing the total system mass, an RV analysis provides information about the mass ratio of the system, allowing individual component masses to be derived when coupled with the astrometric information. RV data also provides a third dimension of information, outside the plane of the sky, providing much stronger constraints on mutual orbital parameters in a shorter timeframe than would be possible with either method in isolation (Tuomi et al., 2009). An additional importance to the RV observations is the ability to efficiently detect further close companions in the system that are unresolved in the images. Identifying such companions is of critical importance for isochronal analysis as any unresolved pair treated as a single star will lead to an incorrect age estimate or model calibration. This reasoning has motivated an RV monitoring survey of high-utility M-dwarf binaries to complement our astrometric observations. Potential Gaia astrometric measurements provided in future data releases will significantly enhance

the value of this survey, as the combination of RV, imaging and astrometry will allow for exceptional constraints on the orbits and physical parameters of these high utility systems.

5.2 Target Sample

AstraLux lucky imaging studies have detected > 300 confirmed M-dwarf binaries, the majority of which were previously undiscovered, and many are high probability YMG members. Janson et al. (2014a) identified a sub-sample of these binaries that exhibit strong indications of youth and estimated orbital periods less than 50 years. Orbital periods can be estimated using the component masses (calculated using Kraus & Hillenbrand (2007) models and component spectral type, see table 5.1), binary semi-major axis (estimated from the measured projected separation and target distance) and Kepler's third law. Although this only gives an order of magnitude basis for the orbital period, it is useful for identifying potentially rapidly orbiting systems. Orbits for these particular high-utility binaries could be closed on the scale of years to several decades, allowing full orbital parameters and dynamical masses to be constrained within reasonable timeframes.

The target sample in this study is primarily compiled from the Janson et al. (2014a). 20 targets are selected with orbital periods less than 40 years for complementary RV monitoring. This will allow for full orbital constraints and a robust isochronal analysis to be conducted on a much shorter time-scale than would be possible with astrometric monitoring alone. Three further youthful systems targeted in Janson et al. (2012c) are selected that appeared as single stars in the AstraLux images. However, these targets have either been previously resolved or are spectroscopic binaries, indicating short component separations and therefore rapid orbital periods. As the unresolved images reveal limited astrometric information, radial velocity monitoring of these targets is the most viable method for producing orbital determinations. From the literature, six additional resolved low-mass binary systems are selected that have strong indications of youth and short orbital periods for which additional RV measurements would significantly enhance orbital determinations. Due to the scientific aims of the project, the targets are chosen entirely on individual merit in terms of orbital properties and youth, with no particular considerations regarding sample uniformity in other respects. The sample is listed in table 5.2 along with

target spectral type, estimated binary orbital period and YMG / association membership. YMG ages adopted by Bell et al. (2015) give an estimate of target age; β Pic $= 24 \pm 3$ Myr, AB Dor $= 149^{+51}_{-19}$ Myr, Carina $= 45^{+11}_{-7}$ Myr, TW Hya $= 10 \pm 3$ Myr, Columba $= 42^{+6}_{-4}$ Myr, η Cha cluster $= 11 \pm 3$ Myr, along with the ages of; Argus $= 40 \pm 10$ Myr (Malo et al., 2013), Upper Scorpius $= 11 \pm 2$ Myr (Pecaut et al., 2012) and ϵ Cha $= \sim 6$ Myr (Torres et al., 2008).

5.3 Observations and Data Reduction

All RV monitoring was conducted using the Fiberfed Extended Range Optical Spectrograph (FEROS; Kaufer et al., 1999) mounted at the ESO-MPG 2.2 m telescope at La Silla Observatory. FEROS is an echelle spectrograph covering the wavelength range 3500-9200 Angstrom with a resolving power R $\approx 48,000$. This resolving power is defined as:

$$R = \frac{\lambda}{\Delta\lambda} \tag{5.3}$$

Where $\Delta\lambda$ is the spectral resolution of the instrument i.e., the smallest wavelength difference at which features can be distinguished. Echelle spectrographs use a reflecting grating to disperse incoming light into its component wavelengths. As a result, multiple orders of spectra are formed due to the diffraction of light over a range of reflection angles via;

$$m\,\lambda = \sigma\,(\sin\alpha + \sin\beta) \tag{5.4}$$

Where m is an integer defining the spectral order, σ is the groove spacing of the grating and α and β are angles of incidence and reflection respectively. However, the majority of incident light is preferentially diffracted into the m=0 order which gives no wavelength information. Furthermore, higher order diffracted light experiences larger angular dispersion. This enables smaller wavelength separated features to be resolved i.e., $\Delta\lambda$ decreases and R increases. Therefore, to concentrate more light

Table 5.2: Target Sample Properties

2MASS ID	SpT	Period estimate (Yr)	YMG / Association	YMG / Association Reference
J01112542+1526214	M5.0+M6.0	12	β Pic	M14, J17
J02451431-4344102	M4.0+M4.5	13	....	
J02490228-1029220	M1.5+M3.5+M3.5	30	β Pic?	B16
J03323578+2843554	M4.0+M4.5+M5.5	8	β Pic	M14, J17
J04244260-0647313	M4.0[1]	< 0.2[7]	Argus	M13
J04373746-0229282	M0.0+M3.0	29[8]	β Pic	M13
J04595855-0333123	M4.0+M5.5	9	Argus?	M13, J17
J05284446-6526463	M5.0+M5.5[2]	1.6[2]	AB Dor	LS06
J05301858-5358483	M3.0+M4.0+M6.0	25	AB Dor**	M14
J05320450-0305291	M2.0+M3.5	23	β Pic?	M14, J17
J06112997-7213388	M4.0+M5.0	8	Carina	M14
J06134539-2352077	M3.5+M5.0	13	Argus	M14, J17
J06161032-1320422	M3.5+M5.0	37	β Pic?	M13, J17
J07285137-3014490	M1.5+M3.5	33	AB Dor	M13
J08475676-7854532	M3.0[3]	....*	η Cha	LM13
J09075823+2154111	M2.0+M3.5	12	....	
J09164398-2447428	M0.5+M2.5	10	....	
J10140807-7636327	M4.0+M5.5	17	Carina	M14
J10172689-5354265	M6.0+M6.0[4]	5.15[4]	β Pic	M13
J11315526-3436272	M2.5+M9.0	5.94[9]	TW Hya	M14
J12072738-3247002	M1.0[5]	4.2[10][11]	TW Hya	M14
J12202177-7407393	M1.0[3]	....*	ϵ Cha	LM13
J13493313-6818291	M2.0+M4.0+M3.5	25	Argus	M13
J15573430-2321123	M1.0[6]	27[12]	Upper Scorpius	R15
J20163382-0711456	M0.0+M2.0	18	Argus?	M13, J17
J20531465-0221218	M3.0+M4.0	13	Argus?	M13
J23172807+1936469	M3.0+M4.5	33	β Pictoris?	M13, J17
J23205766-0147373	M4.0[1]	....*	Argus	M14
J23495365+2427493	M3.5+M4.5	38	β Pic / Columba?	M13, J17

NOTE – Individual spectral types taken from Janson et al. (2012c) unless otherwise noted. Estimated orbital period based on system mass and approximate semi-major axis taken from Janson et al. (2014a) unless otherwise noted. '?' in column 4 denotes ambiguity in association membership.

*Sources are partially resolved or previously resolved at small separations indicating rapid orbital periods (Köhler, 2001; Köhler & Petr-Gotzens, 2002; Daemgen et al., 2007).

** J053018 AB Dor membership is highly unlikely following our analysis detailed in section 5.4.1.

[1]Integrated spectral type (Int SpT); Alonso-Floriano et al. (2015), [2]Janson et al. (2007), [3]Int SpT; Riaz et al. (2006), [4]Bonnefoy et al. (2009), [5]Int SpT; Chauvin et al. (2010), [6] Int SpT; Carpenter et al. (2006), [7]Shkolnik et al. (2010), [8]Montet et al. (2015), [9]Konopacky et al. (2007), [10]Bailey et al. (2012), [11]Bonavita et al. (2016), [12]Lafrenière et al. (2014)

References – B16; Bergfors et al. (2016), J17; Janson et al. (2017), LM13; López Martí et al. (2013), LS06; López-Santiago et al. (2006), M13; Malo et al. (2013), M14; Malo et al. (2014), R15; Rizzuto et al. (2015), W94; Walter et al. (1994)

into higher orders the reflecting grating groves are tilted at what is called the Blaze angle. However, as a consequence of blazing into high values of m, the spectral orders spatially overlap and are unresolvable when mapped onto a detector. To negate this effect, a second dispersing element is used such as a grating, grism or in the case of FEROS, a prism. This cross-disperser disperses light perpendicular to the direction of spectral dispersion, spatially separating spectral orders to the degree that they can be resolved on the detector. An example of a 2d echelle spectrum can be seen in figure 5.4. FEROS blazes and spatially separates light into 39 different, high m value orders covering the wavelength range 3500-9200 Angstrom. FEROS has two 2.0″ aperture fibres that allow for simultaneous observation of a target and either the background sky or a lamp for wavelength calibration and to monitor spectrograph stability.

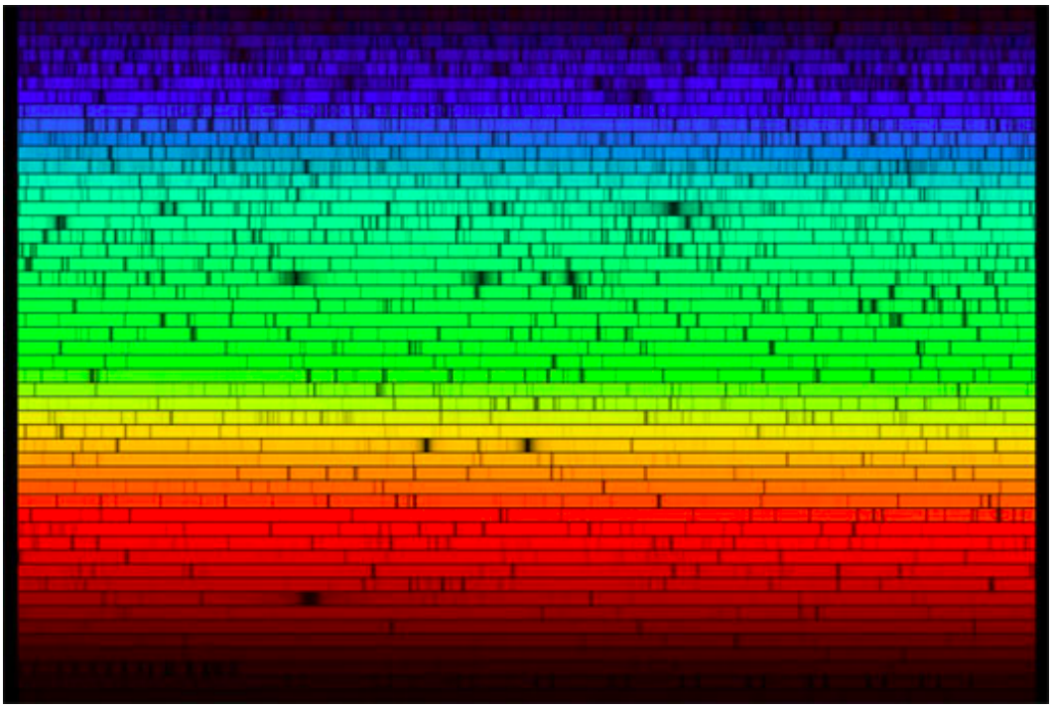

Figure 5.4: Example on a 2d spectrum of the sun taken with a high-resolution echelle spectrograph. Incident light is dispersed spectroscopically in the horizontal direction and each spectral order is dispersed spatially in the vertical direction. Dark lines across the orders are a result os solar absorption features Image: NASA.gov

The observations used in this survey were mainly taken in service mode under programs 093.A-9006(A) and 094.A-9002(A) between September 2014 and October 2015. A maximum of five spectra were taken per target as an optimal trade-off between initial number of RV data points and required observational time. Several

archival FEROS observations were also chosen to bolster the number of spectra for targets in which the ideal sample of five was not obtained. Observations were carried out in 'object + calibration configuration' in which one of the two FEROS optical fibres is centred on the star whilst the other simultaneously observes a ThAr+Ne lamp for wavelength calibration and stability monitoring. This lamp consists of a Thorium cathode, Argon filled lamp and a Neon bulb. Light from the separate bulbs is combined using a 50:50 transmission:reflection mirror. This configuration is preferable to the ThArNe lamp which has strongly saturated lines towards redder orders, resulting in a sub-par calibration over a valuable wavelength range were M-dwarfs emit more flux, providing great signal to noise data. On average, each target was observed for $\sim$ 30 minutes including overheads in order to obtain spectra with a signal to noise ratio of $\sim$ 30 per resolution element. Based on previous AstraLux RV follow-up studies under programs (086.A-9007(A) and 089.A-9013(A)), such spectra enable RV measurements to a precision of $\sim$ 200 m/s. This precision is reasonable given the active and variable nature of young, pre-main sequence M-dwarfs and is sufficient to constrain orbital parameters and component masses alongside the astrometric data. Afternoon calibrations such as bias frames and flat-fields were also taken for data reduction.

All standard spectroscopic data reduction procedures were carried out using the dedicated ESO-MIDAS based FEROS Data Reduction System (DRS). The DRS initially reduces sets of 5 bias frames, 10 flat-field frames and 6 ThAr+Ne wavelength calibration frames in order to perform bias correction, flat-fielding and bad pixel correction. The position of each of the 39 echelle orders is accurately traced from an averaged flatfield frame. Wavelength calibration is carried out using a global multi-parameter function solution to fit the positions of emission lines in the ThAr+Ne calibration lamp. The reduction is carried out in optimum extraction mode in which additional cosmic ray removal is performed, providing a gain in signal to noise compared to standard extraction (Kaufer et al., 1999). The DRS then re-bins and merges the separate wavelength calibrated echelle orders to produce an optimally reduced, continuous 1d spectrum with a wavelength spacing of 0.03 Angstrom. An example of a portion of this merged spectrum can be seen in figure 5.5. Müller et al. (2013) note that the barycentric correction applied by the DRS is inaccurate and introduces an artificial one year period. Therefore, this DRS correction is reversed (via equation 1.1) and an improved correction is applied using the IDL code baryvel.pro (based on

the algorithm of Stumpff (1980)), part of the IDL Astronomy Users Library.

In order to derive radial velocity measurements for the sample, observed spectra are cross-correlated with synthetic template spectra. The synthetic spectra are generated from the spectral libraries of Husser et al. (2013). This library is particularly well suited for cross-correlation with the target sample as it has been compiled using the ACES equation of state, which accounts for the formation of molecules at the low temperatures of M-dwarf atmospheres ($\sim 2400-4000$ K; Kraus & Hillenbrand, 2007). For each target a single synthetic template is used for cross-correlation. As will be detailed in the following section, the majority of systems are single lined binaries, and therefore a single template correlation is valid. The template is generated using surface gravity, temperature and metallically input parameters. Solar metallically is adopted for each target as our sample resides in the solar neighbourhood. Temperatures and surface gravity values are adopted from Baraffe et al. (1998) evolutionary models based on estimated target age (estimated from the YMG or association age) and mass. For example, an M4.0 primary will have a mass of 0.2 $M_{\odot}$ according to Kraus & Hillenbrand (2007). At the typical age of the AB Dor YMG this star is expected to have a temperature of 3298 K and a surface gravity of 4.99 log g. Therefore, the template for cross-correlation is generated using a temperature of 3300 K and 5.0 log g (input parameters have intervals of 100 K and 0.5 log g).

As mentioned in section 5.1, target masses are first order approximations, derived from primary component spectral type for resolved stars, and integrated spectral type for unresolved stars using the spectral type-mass relations of Kraus & Hillenbrand (2007). Therefore, synthetic templates generated using temperature and surface gravity values derived from these masses will also be first order approximations of the observed spectra. However, RV errors due to any observed - synthetic template spectral mismatch are expected to be well within the required ~ 200 m/s precision level. Indeed, this was found to be valid by trialling several separate templates within a reasonable range of temperatures (± 200 K) and surface gravity values (± 0.5 log g) from those calculated using the Baraffe et al. (1998) models. The synthetic spectra have a resolution of R $\approx 500,000$ between the 3500-9200 Angstrom range probed here. The template is not degraded or rotationally broadened as this is superfluous to deriving RV measurements to a ~ 200 m/s precision level. As the synthetic spectra are given at vacuum wavelengths they must be converted to air wavelengths following

the methods of Ciddor (1996);

$$\lambda_{air} = \frac{\lambda_{vac}}{f} \tag{5.5}$$

where;

$$f = 1.0 + \frac{0.05792105}{238.0185 - \sigma} + \frac{0.00167917}{57.362 - \sigma} \tag{5.6}$$

$$\sigma = \left(\frac{10^4}{\lambda_{vac}}\right)^2 \tag{5.7}$$

An example of a portion of a synthetic template spectra can be seen in figure 5.5.

The cross-correlation is carried out following the methods of Ciceri et al. (2016). The International Ultraviolet Explorer (IUE) Data Analysis Centers CRSTRIM and CRSPROD IDL routines are used to compute cross-correlation functions (CCFs). CRSPROD generates a normalised CCF for two spectra which are sampled on the same log(λ) wavelength scale. CRSTRIM interpolates spectral data to a common log(lambda) scale for CRSPROD application. A common log(λ) wavelength scale is required so that each pixel corresponds to a constant velocity interval. For example, equation 1.1 can be written as;

$$\frac{\Delta\lambda}{\lambda} = \frac{\Delta\, v}{c} \tag{5.8}$$

If the spectra are sampled in linear wavelength space then the velocity shift represent by each pixel is dependant on $\frac{\Delta\lambda}{\lambda}$ which varies across the spectrum with λ. However, spectra may instead be binned in equal increments of log(λ);

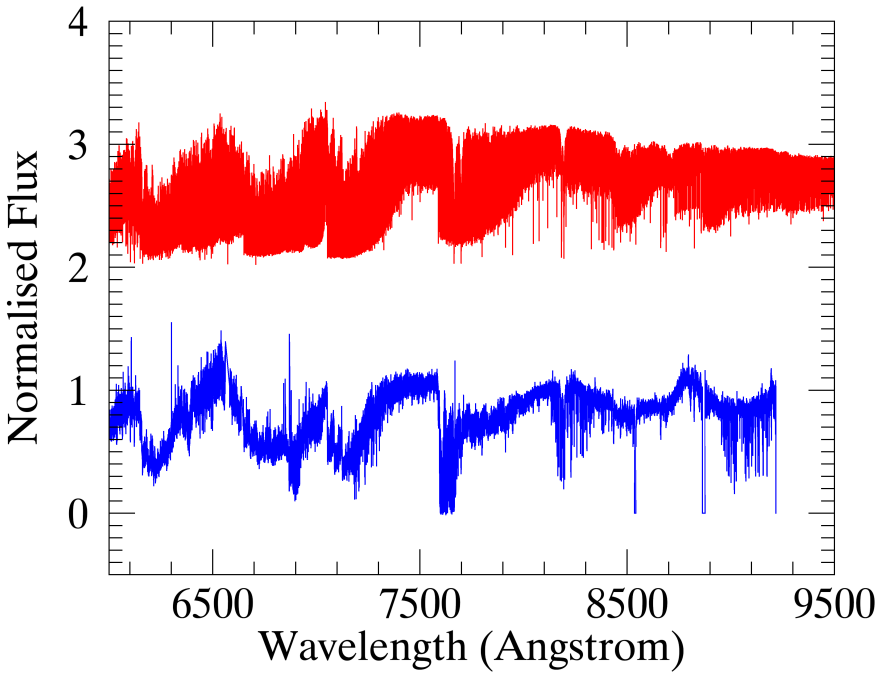

Figure 5.5: Example of a portion of the continuous 1d FEROS spectrum (in blue) for the target 2MASS J04244260-0647313. The spectral range 6000 - 9200 Angstrom is plotted, covering orders 26 -39. Also plotted is the corresponding synthetic spectrum (in red), generated with 3100 K and 5.0 log g input parameters from the Husser et al. (2013) spectral library. The synthetic spectrum has been arbitrarily shifted along the vertical axis for display purposes.

$$\Delta \log\lambda = \frac{\Delta\lambda}{\lambda} = \frac{\Delta \mathrm{v}}{\mathrm{c}} \tag{5.9}$$

Each pixel then corresponds to a constant velocity interval, $\Delta\, v = c\, \Delta \log\lambda$, which is independent of wavelength. As linear pixel shifts correspond to linear RV shifts, the CRSPROD routine effectively shifts the spectra with respect to one another by integer pixel values, recording the correlation between the two by multiplication and array summation at each shift (accompanied by a normalisation so that the largest total value across the range of shifts is given a value of 1.0). This correlation was carried out for each target at each epoch over multiple wavelength ranges. These ranges correspond to the wavelengths of individual echelle orders that are free from

telluric lines, strong stellar emission lines and instrumental effects. The edges of each order's wavelength range are also clipped to avoid edge of chip effects and any inaccuracy in the DRS order merging. The RV is measured across each range by fitting a Gaussian to the CCF, or multiple Gaussians for multiple component spectroscopic binaries. The final RV measurement for each spectrum is then derived by taking a weighted mean of these individual RV measurements and calculating the uncertainty by computing the standard error ($\sigma/\sqrt{n}$, where σ is the standard deviation in the individual measurements and n is the number of measurements/orders reduced). ~ 30 orders are suitable for cross correlation for each target, although this value decreases for later spectral types due to lower signal to noise data at bluer orders. An example of the RV measured across each order and the final RV measurement is given in table 5.3.

5.4 Results and discussion

The results of the RV monitoring survey for the sample of 29 M-dwarf multiples are presented in table 5.4. On average, individual RVs are derived to a precision of $\sim 200\,\mathrm{m/s}$, obtaining $\sim 3-4$ epochs of measurements per target. An example RV plot is shown in Figure 5.6. Several targets have RV's reported here for the first time. There are two three-component spectroscopic multiples present in this sample, one of which is a new discovery and is discussed in the following section.

Table 5.4: Radial Velocity Measurements

2MASS ID	Epoch (MJD)	RV ($\mathrm{kms^{-1}}$)	RV Error ($\mathrm{kms^{-1}}$)	f_c (Sect. 5.4.2)	Notes
J01112542+1526214	56915.351	3.14	0.24	0.915	SB1
	56978.061	3.44	0.22		SB1
J02451431-4344102	56161.302	31.59	0.14	0.964	SB1
	56912.268	30.74	0.18		SB1
	56979.144	31.23	0.30		SB1
	57058.048	31.18	0.21		SB1
	57070.103	27.99	0.21		SB1
J02490228-1029220	55613.082	16.40	0.16	0.995	SB1
	56161.326	16.85	0.13		SB1
	56978.203	16.80	0.12		SB1
J03323578+2843554	56979.165	10.73	0.20	—	SB1
J04244260-0647313	55790.421	7.81	0.46	—	SB3, Central Peak
	55790.421	-33.58	0.37		SB3, Blue Peak
	55790.421	57.52	0.49		SB3, Red Peak

Table 5.4: continued.

2MASS ID	Epoch (MJD)	RV (kms^{-1})	RV Error (kms^{-1})	f_c (Sect. 5.4.2)	Notes
	56912.297	-9.36	0.37		SB3, Central Peak
	56912.297	-48.67	0.48		SB3, Blue Peak
	56912.297	45.70	0.44		SB3, Red Peak
	56979.202	3.01	0.29		SB3, Central Peak
	56979.202	-50.21	0.71		SB3, Blue Peak
	56979.202	37.21	0.23		SB3, Red Peak
	57061.120	8.85	0.36		SB3, Central Peak
	57061.120	-13.54	0.26		SB3, Blue Peak
	57061.120	22.91	0.37		SB3, Red Peak
J04373746-0229282	53707.288	20.40	0.09	0.996	SB1
	55203.146	24.25	0.09		SB1
	56912.331	23.04	0.09		SB1
	56979.236	22.89	0.08		SB1
	57059.095	22.89	0.08		SB1
	57290.319	22.21	0.08		SB1
	57291.257	22.46	0.10		SB1
J04595855-0333123	56912.344	43.17	0.21	>0.999	SB1
	56980.125	43.03	0.17		SB1
	57060.127	43.00	0.19		SB1
	57291.272	42.80	0.19		SB1
J05284446-6526463	56701.124	30.08	0.31	—	SB1
J05301858-5358483	55525.295	31.69	0.22	—	SB3, 'A' component
	55525.295	1.48	0.24		SB3, 'B' component
	55525.295	69.93	0.28		SB3, 'C' component
	55615.023	32.03	0.29		SB3, 'A' component
	55615.023	66.16	0.36		SB3, 'B' component
	55615.023	-14.87	0.46		SB3, 'C' component
	56161.374	32.72	0.15		SB3, 'A' component
	56161.374	18.78	0.37		SB3, 'B' component
	56161.374	49.49	0.35		SB3, 'C' component
	56980.244	33.07	0.23		SB3, 'A' component
	56980.244	-4.14	0.21		SB3, 'B' component
	56980.244	78.27	0.32		SB3, 'C' component
	57060.161	33.67	0.22		SB3, 'A' component
	57060.161	68.15	0.26		SB3, 'B' component
	57060.161	-18.03	0.27		SB3, 'C' component
J05320450-0305291	55526.282	24.26	0.13	>0.999	SB1
	55615.041	24.24	0.12		SB1
	56164.407	24.80	0.14		SB1
	56980.258	24.82	0.14		SB1
	57059.134	25.23	0.13		SB1
J06112997-7213388	56980.288	19.33	0.29	0.943	SB1
	57058.223	19.54	0.26		SB1

Table 5.4: continued.

2MASS ID	Epoch (MJD)	RV (kms^{-1})	RV Error (kms^{-1})	f_c (Sect. 5.4.2)	Notes
J06134539-2352077	55522.312	21.28	0.21	>0.999	SB1
	56168.403	22.07	0.25		SB1
	56700.142	22.90	0.19		SB1
	56980.335	22.91	0.23		SB1
	57058.209	23.11	0.23		SB1
J06161032-1320422	56983.199	31.56	0.46	0.799	SB1
	57058.174	28.16	0.54		SB1
	57291.338	31.20	0.44		SB1
J07285137-3014490	55526.355	27.74	0.11	>0.999	SB1
	56173.407	28.08	0.10		SB1
	56980.349	28.91	0.12		SB1
	57058.295	28.74	0.12		SB1
	57166.001	28.90	0.13		SB1
J08475676-7854532	57058.309	18.75	0.15	0.943	SB1
	57118.129	18.51	0.15		SB1
J09075823+2154111	57059.178	-2.66	0.09	0.994	SB1
	57060.175	-2.68	0.10		SB1
J09164398-2447428	56984.343	21.21	0.12	0.997	SB1
	57059.297	20.43	0.15		SB1
	57060.209	20.54	0.15		SB1
	57166.015	19.66	0.16		SB1
J10140807-7636327	57058.344	17.16	0.22	0.972	SB1
	57118.165	17.25	0.22		SB1
J10172689-5354265	57059.310	13.05	0.23	0.998	SB1
	57059.330	12.96	0.25		SB1
	57060.222	13.19	0.22		SB1
	57166.032	12.75	0.21		SB1
J11315526-3436272	56708.278	12.13	0.24	0.997	SB1
	56816.146	11.90	0.20		SB1
	57062.297	11.86	0.26		SB1
J12072738-3247002	56816.160	9.33	0.22	>0.999	SB1
	57060.364	9.18	0.15		SB1
	57062.285	9.04	0.15		SB1
J12202177-7407393	56809.106	14.71	0.17	0.990	SB1
	57060.294	15.28	0.17		SB1
	57118.201	15.02	0.17		SB1
J13493313-6818291	56809.141	14.75	0.19	0.993	SB1
	57060.330	13.84	0.15		SB1
	57062.310	13.81	0.18		SB1
	57118.262	15.07	0.18		SB1
J15573430-2321123	56809.190	-5.49	0.10	0.970	SB1
	57119.295	-5.62	0.16		SB1
J20163382-0711456	56912.124	-23.31	0.06	>0.999	SB1

Table 5.4: continued.

2MASS ID	Epoch (MJD)	RV (kms^{-1})	RV Error (kms^{-1})	f_c (Sect. 5.4.2)	Notes
	56982.023	-23.10	0.06		SB1
	57166.263	-23.40	0.06		SB1
	57290.074	-23.93	0.06		SB1
	57291.068	-23.53	0.06		SB1
J20531465-0221218	56912.138	-39.57	0.13	0.996	SB1
	56979.057	-39.57	0.16		SB1
J23172807+1936469	56912.207	-0.06	0.14	0.861	SB1
	56979.091	-0.79	0.13		SB1
J23205766-0147373	56809.310	-5.99	0.17	0.984	SB1
	56912.173	-6.43	0.17		SB1
	56980.052	-5.93	0.17		SB1
J23495365+2427493	56912.233	-8.92	0.17	0.976	SB1
	56979.104	-9.13	0.14		SB1
	57291.090	-8.37	0.24		SB1

NOTE – SB1 and SB3 denote a singled-lined binary and a three-component spectroscopic multiple respectively. For SB3 system J042442 RV measurements are noted for the central CCF peak, and peaks towards the blue and red with respect to the central peak, as individual components cannot be distinguished between epochs. For SB3 system J053018 RV measurements are noted for the identified 'ABC' components, see section 5.4.1 for details.

5.4.1 High-Order Multiplicity of 2MASS J05301858-5358483

The system 2MASS J05301858-5358483, hereafter abbreviated as J053018, was previously known to be a M3.0+M4.0+M6.0 resolved triple system from AstraLux multiplicity surveys (Janson et al., 2012c). However, in each of the RV epochs a triple-peaked CCF is recovered and therefore J053018 is identified as a three-component spectroscopic multiple. An example triple-peaked CCF is shown in Figure 5.7. Janson et al. (2012c, 2014a) derive a separation of $\sim 0.2''$ for the tight M3.0+M4.0 pair, and a separation of $\sim 4''$ for the wide M6.0 companion. As the M6.0 companion falls outside the $2.0''$ FEROS fibre aperture, the third spectroscopic component is most likely due to an additional unresolved tight companion, making J053018 a quadruple system. As previously mentioned, identifying any unresolved components in a multiple system is of critical importance for an accurate isochronal analysis. The RV data for J053018 is plotted in Figure 5.8. The identification of which spectroscopic component is responsible for each individual RV measurement is possible by tracing CCF peak strength across each epoch. The strongest peak in each epoch is related to the 'A' component, occurring at ~ 30 kms^{-1} in Figure 5.7. The 2^{nd} strongest

Table 5.3: J04373746-0229282 RV Measurment

Order Number	Spectral Window ($\AA$)	RV (km/s)
07	3902-3960	23.93
08	4000-4093	21.82
09	4085-4190	22.88
10	4140-4265	22.95
11	4260-4320	22.47
12	4315-4430	22.21
13	4380-4515	23.14
14	4508-4605	23.34
15	4560-4692	23.32
16	4655-4795	23.28
17	4720-4860	23.60
18	4870-5005	22.67
19	4955-5110	23.48
20	5070-5235	23.22
21	5165-5360	22.84
22	5318-5482	23.17
23	5439-5604	23.09
24	5575-5755	23.13
25	5715-5885	23.27
26	5904-6050	23.08
27	6030-6225	22.085
28	6190-6275	22.93
29	6375-6500	22.31
30	6600-6670	23.38
31	6740-6840	22.38
34	7405-7592	22.66
35	7715-7875	22.48
36	7950-8100	23.10
38	8700-8800	22.84

Weighted mean RV = 23.04, Standard error = $\pm$0.09

NOTE – Errors used for weighted mean RV calculation are a measure of goodness of fit of the Gaussian to the CCF outputted by the gaussfit IDL routine.

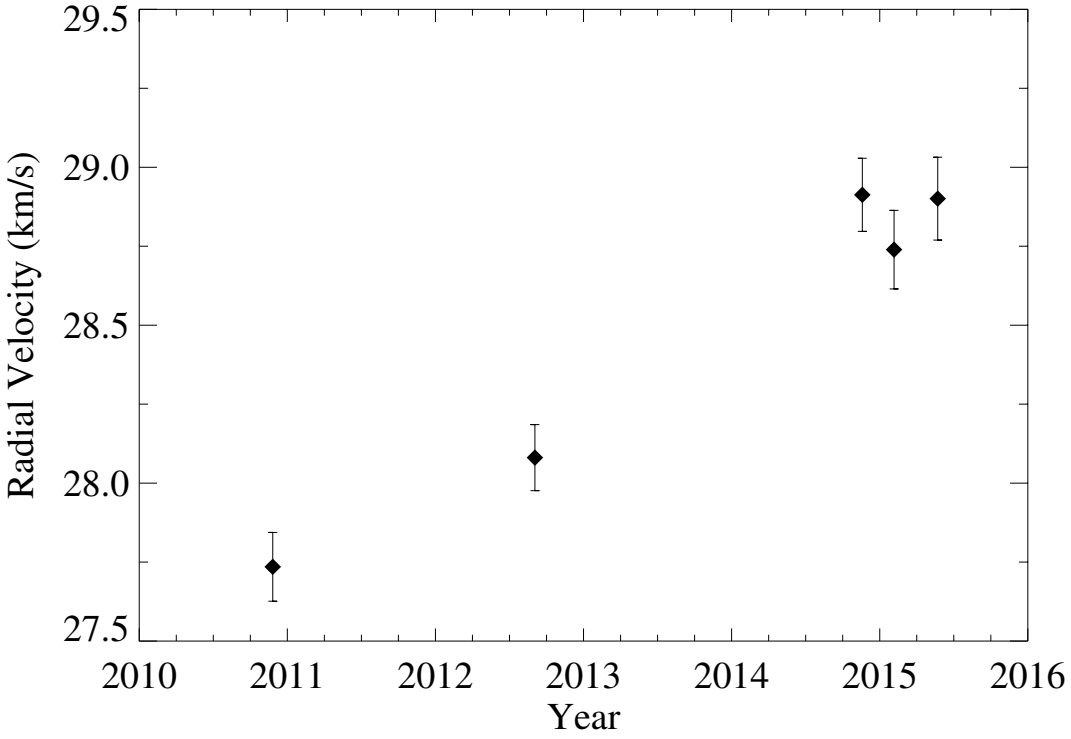

Figure 5.6: Example RV plot featuring data measured for the single-lined J07285137-3014490 system. RV motion is evident and will be combined with astrometric data in order to constrain the system orbit; Rodet et al. (in preparation).

CCF peak relates to the 'B' component and the lowest strength peak to 'C' component, occurring at ~ 0 kms^{-1} and ~ 70 kms^{-1} respectively in Figure 5.7. Figure 5.8 displays the slowly varying RV motion of the 'A' component, indicating that it is the $\sim 0.2''$ separation resolved component, whilst the 'B' and 'C' components display rapid RV motion, indicative of an unresolved tight spectroscopic binary. Figure 5.8 also indicates that the 'B' + 'C' pair are in anti-phase and have gone through ~ 180 degrees of motion, or some integer multiple of 180 degrees, between the 2010 and 2011 epochs (separated by ~ 90 days) and the 2014 and 2015 epochs (separated by ~ 80 days). Therefore, to first order the longest possible orbital period of the 'B' + 'C' pair is estimated to be ~ 170 days, and possibly factors of several shorter as multiple orbits may have been completed over the ~ 80 to 90 day baseline. Future RV monitoring over a baseline less than a year will significantly aid in constraining orbital parameters and resolve any remaining ambiguities in the system.

As the 'B' and 'C' component RVs can be distinguished, the mass ratio, r, and systemic RV, γ, of the pair can be calculated following the methods of Wilson (1941) via the equation;

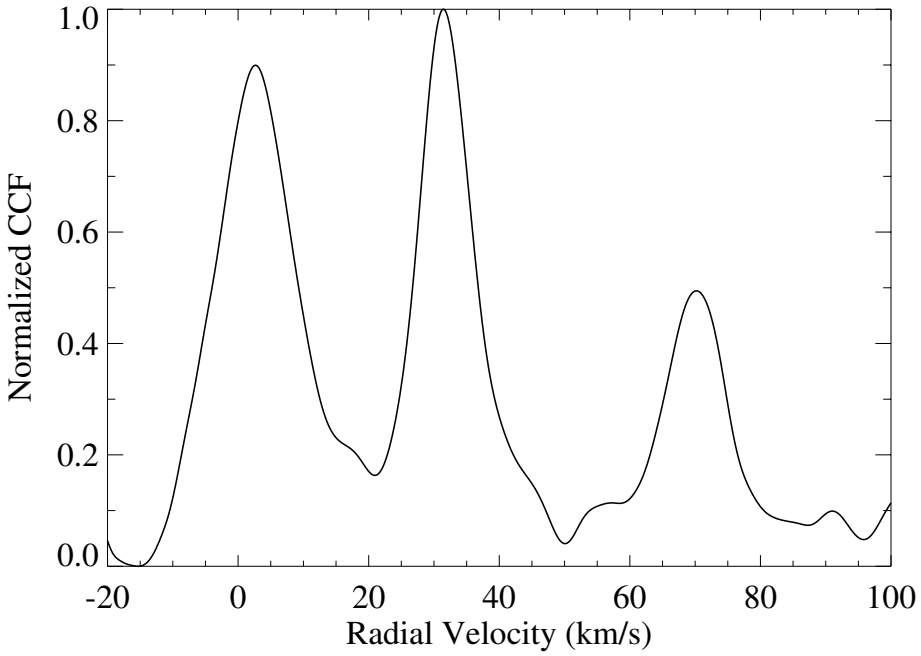

Figure 5.7: Example CCF plot for the J053018 system. Three individual peaks are clearly distinguishable, and therefore the system is identified as a three-component spectroscopic multiple. The CCF displayed has been measured for MJD = 55525.295, across the 36^{th} spectral order.

$$r = \frac{m_p}{m_s} = \frac{RV_p - \gamma}{\gamma - RV_s} \tag{5.10}$$

or

$$RV_p = \gamma\,(1 + r) - r\,RV_s \tag{5.11}$$

Where RV_P and RV_S are the radial velocities of the 'B' and 'C' components respectively. Equation 5.11 can be solved graphically as it is linear in both RV_P and RV_S. If the pairs of RV_P and RV_S measurements at each epoch are plotted, they define a straight line in the RV_P, RV_S plane. The negative of the slope of the line provides an estimate for the mass ratio of the pair, since $dRV_p/dRV_s = -r$ from equation 5.11. If the origin of the plot resides at [0,0] then r and γ can be measured from the line intercepts, RV_{p0} and RV_{s0} via;

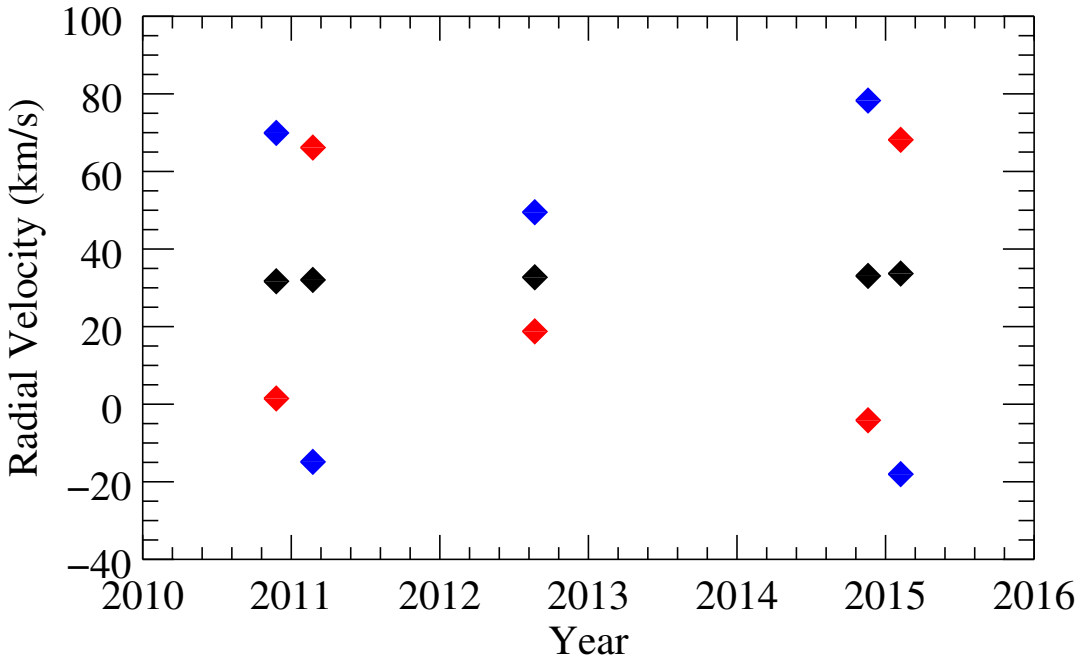

Figure 5.8: RV data for the J053018 system. Errors are on the order of ~ 0.3 kms^{-1} and therefore lie within the data point boundaries. Colour relates the measured RVs to individual spectroscopic components; black = 'A' component, red = 'B' component, blue= 'C' component, see text for details.

$$r = \frac{RV_{p0}}{RV_{s0}} \tag{5.12}$$

$$\gamma = \frac{RV_{p0}\, RV_{s0}}{RV_{p0} + RV_{s0}} \tag{5.13}$$

The component RVs for the 'B' and 'C' components of J053018 are plotted against each other in Figure 5.9. A mass ratio of 0.75 ± 0.01 and a systemic RV of 31.2 ± 0.3 kms^{-1} is measured for the pair using Figure 5.9 and equations 5.12 and 5.13 . This systemic RV is consistent with the 31.3 ± 0.2 kms^{-1} RV measured for the M3.0 primary by Malo et al. (2014). The RV measured by Malo et al. (2014) is also consistent with the RV measured here for the slowly varying 'A' component. Therefore, the 'A' component is identified as the M3.0 primary and the M4.0 companion as

the unresolved 'BC' pair. The 'BC' components are suspected to comprise of an M4.0 + M5.0 pair. This is based on relating the mass ratio of the pair, and the relative strengths of the CCF peaks, to the unresolved M4.0 spectral subtype.

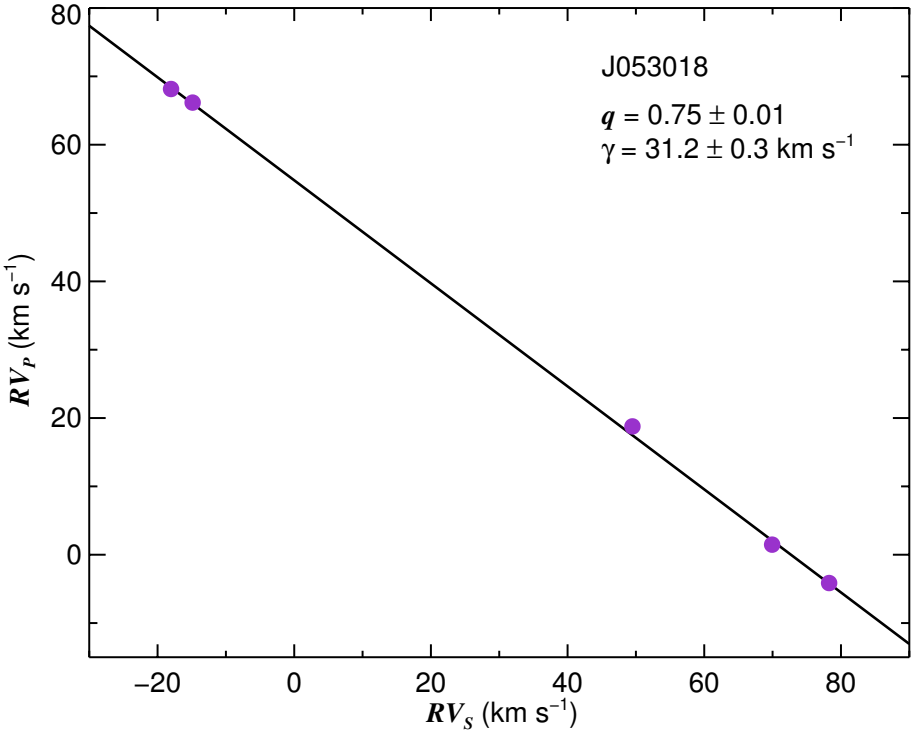

Figure 5.9: J053018 'B' and 'C' component RVs, denoted as RV_P and RV_S respectively. The negative gradient of the best-fit line is equal to the mass ratio of the system ($q = 0.75 \pm 0.01$), and a systemic RV (γ) of 31.2 ± 0.3 kms^{-1} is measured from the line intercepts.

J053018 was previously thought to be a high probability member of the AB Dor YMG with young age supported by significant X-ray emission (e.g., Lépine & Gaidos, 2011; Janson et al., 2012c). Using R.A, .decl, proper motions and their RV measurement for the M3 primary, Malo et al. (2014) derive an AB Dor membership probability of 97.7 % using the BANYAN code (see section 5.1). Whilst no parallactic distance measurement exists for this system, the Bayesian inference carried out by BANYAN is able to marginalise the weight of this parameter in membership probability determinations. The code is also able to produce a statistical prediction of the target distance based on the membership hypothesis that typically agrees with trigonometric distances to within 8%, if the hypothesis is trusted. The BANYAN code generated a statistical distance of 3 ± 1 pc for the J053018 system. The YMG membership is reevaluated here using the most recent online version of the BANYAN

code, BANYAN Σ (Gagné et al., 2018), and the systemic RV measured for the 'BC' pair. An AB Dor membership probability of $> 95\%$ and a statistical distance of 2.5 ± 0.8 pc is found in agreement with the Malo et al. (2014) findings. However, whilst no trigonometric distance exists for J053018, Janson et al. (2012c) derive a photometric distance of 23 ± 9 pc for the system using apparent and absolute magnitudes presented in Riaz et al. (2006). At this distance J053018 is highly unlikely to be an AB Dor member given its other kinematics and indeed, the BANYAN II tool returns a 0% membership probability. It is suspected that this system is instead an old field interloper, rather than a YMG member, that appears young and X-ray active because the rotational velocities of the tight 'BC' pair are high, due to spin-orbit locking. This argument is supported by a visual inspection of the FEROS spectra over Hα emission wavelengths. Similar to X-ray luminosity (see section 5.1), Hα emission is a reliable proxy for rotationally dependant magnetic activity (e.g., Newton et al., 2017) such that rapidly rotating, and therefore typically young, stars are expected to have significant Hα emission. Figure 5.10 shows the Hα emission region of several epochs of spectra. In each epoch prominent emission lines are visible at the predicted Hα position given the measured RVs of the 'B' and 'C' components. However, no significant emission is visible at the predicted Hα position given the measured RV of the 'A' component. This strongly suggests that the 'A' component is no longer active because it is old, whilst the 'B' and 'C' components are active due to tidal spin-up. This argument is further reinforced by an inspection of the CCF peaks. As seen in Figure 5.7, the 'B' and 'C' component peaks are significantly broader than the 'A' component peak. Although this may be due to a mis-match with the cross correlation template, this suggests that the 'BC' pair have larger rotational velocities than the 'A' component, supporting the theory that the pair has been spun-up. Whilst an upper limit of ~ 170 days was placed on the 'BC' orbital period from the apparent RV motion in Figure 5.8, the true orbital period is likely to be substantially shorter, probably on the order of $\sim 1 - 10$ days. This would allow the rotation of the components to be tidally locked to their orbit, and thus to be spun-up sufficiently to produce X-ray emission that matches the activity levels of a young (< 100 Myr) population (e.g., Herbst et al., 2007).

5.4.2 Limits on Tidal Synchronisation

As the case of J053018 shows, tidally synchronised pairs can mimic signatures of youth in low-mass systems, and can therefore critically bias isochronal analyses un-

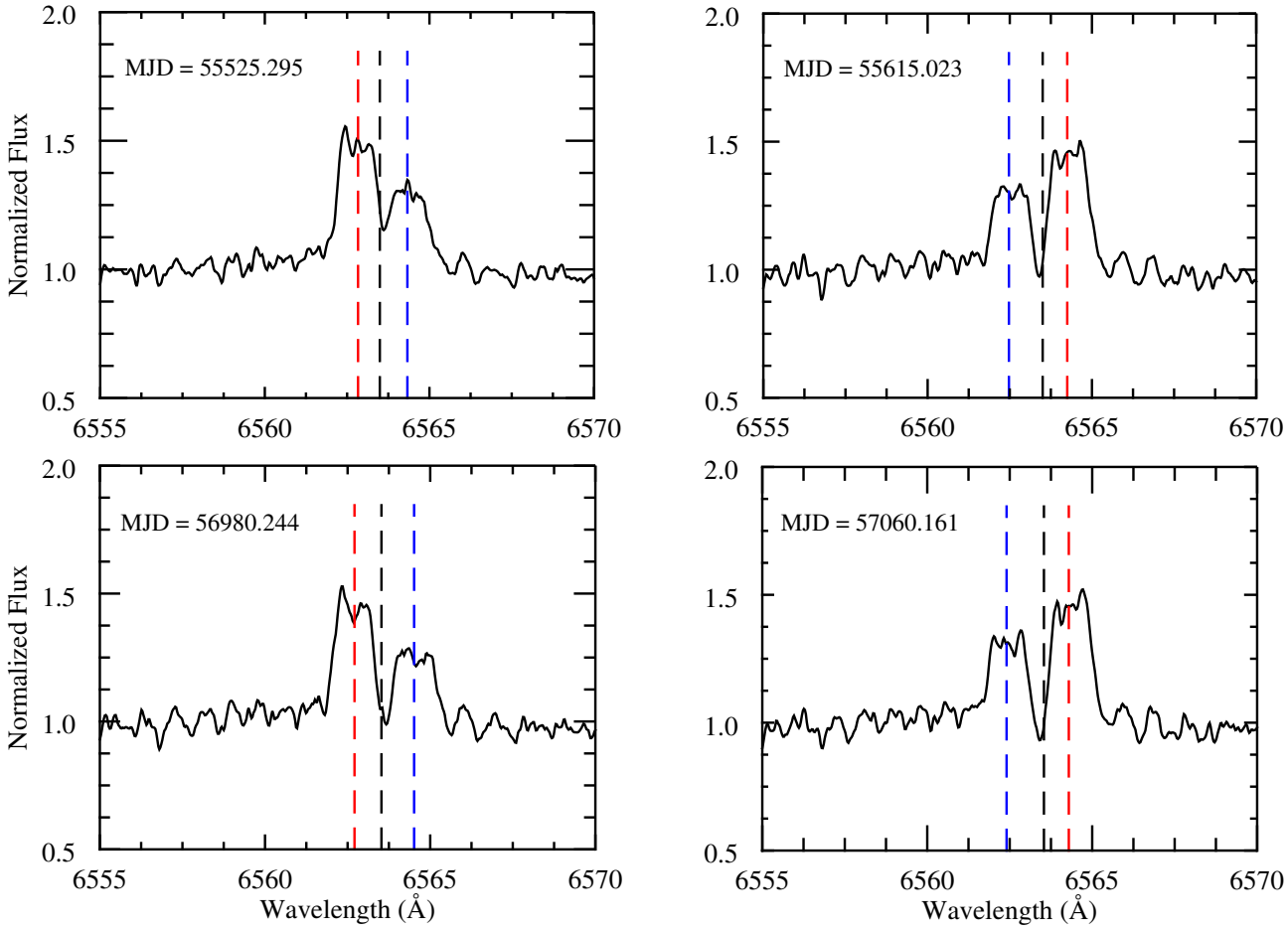

Figure 5.10: Four epochs of J053018 FEROS spectra covering Hα emission wavelengths. The dashed lines highlight the predicted positions of the Hα emission line given the measured RVs of the 'A' (black line), 'B' (red line) and 'C' (blue line) components. In each epoch, prominent emission lines are visible at the predicted Hα position given the measured RVs of the 'BC' pair, whilst no emission is visible at the predicted Hα position given the measured RV of the 'A' component.

less identified and discarded. Hence, the target sample is scanned for additional pairs of this nature, but only J053018 and the previously known J042442 (see Sect. 5.4.3) system show any such indications. In general, such systems should be easily identified, because at the necessary periods of <10 days for tidal synchronisation to occur over ∼100 Myr timescales (see e.g. Meibom et al., 2006), they can be expected to have velocity semi-amplitudes of >30 km/s, similar to the J053018 system. However, there are two effects that can hide an otherwise detectable pair: (i) The system inclination may be very close to face-on, leading to a very small fraction of the total velocity to be projected into the measurable radial component. (ii) Repeated RV measurements may accidentally sample the orbit in phases with similar instantaneous RV values. Both of these are low-probability effects, and the latter is particularly improbable if the RV has been sampled multiple times. Nonetheless, in a large enough sample, they should be expected to occur to some level, and it is therefore desirable to quantify to which extent they can be excluded for the targets in the sample without any detected signature. For this purpose, a series of Monte Carlo simulations are performed for each individual target, as described in the following paragraphs.

The total velocity semi-amplitude $K_{\rm tot}$ of a binary pair is a function of mass of each known star that is hypothesised to host a synchronising companion (hereafter named a 'synchroniser'), the mass ratio q of the pair, and their eccentricity and orbital period. If the system is a single lined binary (as is the case for the FEROS sample excluding the three component spectroscopic multiples J042442 and J053018);

$$K = \left(\frac{2\pi G}{P}\right)^{1/3} \frac{M_2 \sin i}{(M_1 + M_2)^{2/3}} \frac{1}{(1-e)^{1/2}} \tag{5.14}$$

Where M_1 is the mass of the observed primary and M_2 is the mass of the hypothesised synchroniser. Since only tidally synchronised pairs are of interest in this analysis, the orbital periods will be limited to $P < 10$ days as mentioned above. Setting $P = 10$ days will thus provide a lower limit on $K_{\rm tot}$. In such short-period systems, eccentricities are known to be very low (e.g. Raghavan et al., 2010), which is a natural consequence of the same tidal forcing that causes the period synchronization. Hence, $e = 0$ is set in the simulations. The mass ratio distribution of close-in and low-mass systems is strongly peaked toward $q = 1$, and do not show $q < 0.5$ stellar

systems even in surveys that are complete below this value (e.g. Reid & Gizis, 1997; Delfosse et al., 2004). Similarly to the P case, $q = 0.5$ is set to acquire a lower limit on $K_{\rm tot}$. The M_1 masses are assigned individually for the targets in our sample, based on their spectral types following the same relation as in Janson et al. (2012c).

For each system, $K_{\rm tot}$ is calculated using equation 5.14, adopting the parameters described above and initially assuming an orbital inclination of 0 degrees. 10^5 simulations are then performed in which $K_{\rm tot}$ is projected into a radial component assuming random orientations of the orbit and that the probability that orbital inclination $> i$ is governed by $\cos(i)$. Since the FEROS observations are taken at irregular intervals that are generally much longer than 10 days, it can be assumed that such short orbits are effectively randomly sampled. Thus, each simulated velocity curve is divided into a fine grid of small temporal segments, and $N_{\rm obs}$ segments are randomly selected for each of the 10^5 randomly projected orbits, where $N_{\rm obs}$ is the number of observations available for the target in question. The RV difference between adjacent pairs in the simulated ($\delta K_{\rm sim}$) and real ($\delta K_{\rm obs}$) observations is then evaluated, and the maximum difference among the $N_{\rm obs}-1$ pairs is chosen in both cases. If $\max \delta K_{\rm sim} > \max \delta K_{\rm obs}$, it is considered that the hypothesised synchroniser should have been detected in this random instance, while the opposite is true if $\max \delta K_{\rm sim} < \max \delta K_{\rm obs}$. The fraction among the 10^5 simulations for a given target in which the synchroniser should have been detected is denoted $f_{\rm c}$. If $f_{\rm c}$ is close to 1, it means that there is virtually no way to hide a synchroniser, and so the hypothesis of its existence can be discarded. If $f_{\rm c}$ is small, there is not yet enough data to conclude whether a synchroniser might exist. The motivation for using adjacent pairs of observations as opposed to, e.g., the minimum and maximum of the full set of observations is to mitigate the impact of the slower gradual RV trend that arises from the already known wider companions in the system.

All calculated $f_{\rm c}$ values are shown in table 5.4. For the two systems J033235 and J052844, only one epoch of observations exists, and for the J042442 and J053018 systems a close companion has already been identified, so for those systems no meaningful $f_{\rm c}$ can be calculated. However, for the other systems, $f_{\rm c}$ is generally very high – the lowest value is 0.799 for J061610, which still implies that it is unlikely that any synchroniser could hide from view, if such an object exists in the first place. The highest values are >0.999 for 6 systems, such that the synchroniser hypothesis can arguably be discarded entirely. This analysis implies that youth is the most probable

explanation for high chromospheric activity in the vast majority of the sample, as is often supported also through kinematic YMG analysis. For e.g. J024514, there is point-to-point RV scatter significantly exceeding the formal errors, which could imply that a close-in companion exists. However, in this case the f_c of 0.964 implies that any such companion has a lower RV amplitude than would be expected from a synchroniser. In other words, while an additional unseen companion could exist in that system, it could not be responsible for the high activity level of the system, so the conclusion of youth remains probable also in such a case. The value of f_c depends only weakly on the mass M_s, but depends quite strongly on the number of data points acquired; with only two data points it is relatively easy to miss a high RV variability if (e.g.) two epochs are accidentally separated by an integer multiple of the periodicity, but with a larger number of irregularly spaced observations, this becomes exceedingly unlikely.

5.4.3 Individual Target Discussion

Here, individual targets are discussed that merit particular attention.

J02490228-1029220: J024902 is a M1.5+M3.5+M3.5 resolved triple system for which three epochs of RV measurements are presented. Bergfors et al. (2016) present an earlier FEROS spectrum of J024902, recording a RV of 17.1 ± 1.1 kms^{-1} at MJD = 55901.121 along with a $v \sin i$ of 11 ± 3 kms^{-1}. Bergfors et al. (2016) also find J024902 to be a strong candidate member of the β Pic moving group, based on UVW galactic velocities and spectroscopic age indicators such as strong Li absorption. However, a parallax measurement is required to confirm group membership. Bergfors et al. (2016) additionally derive M4.0 ± 1.0 spectral types for both BC components from resolved SINFONI (Eisenhauer et al., 2003; Bonnet et al., 2004) spectra, consistent with the photometrically derived spectral types taken from Janson et al. (2012c).

J04244260-0647313: J042442 is a previously known, three-component spectroscopic multiple, first reported in Shkolnik et al. (2010). A triple-peaked CCF is recovered and RV measurements for all three components are derived in each epoch of observations. An example triple-peaked CCF is shown in Figure 5.11. Shkolnik et al. (2010) estimate M4.5, M5.5 and M5.7 ± 0.5 component spectral types from HIRES (Vogt et al., 1994) and ESPaDOnS (Donati et al., 2006) spectra using the methods of Daemgen et al. (2007). Using the spectral type - mass relations of Reid & Hawley

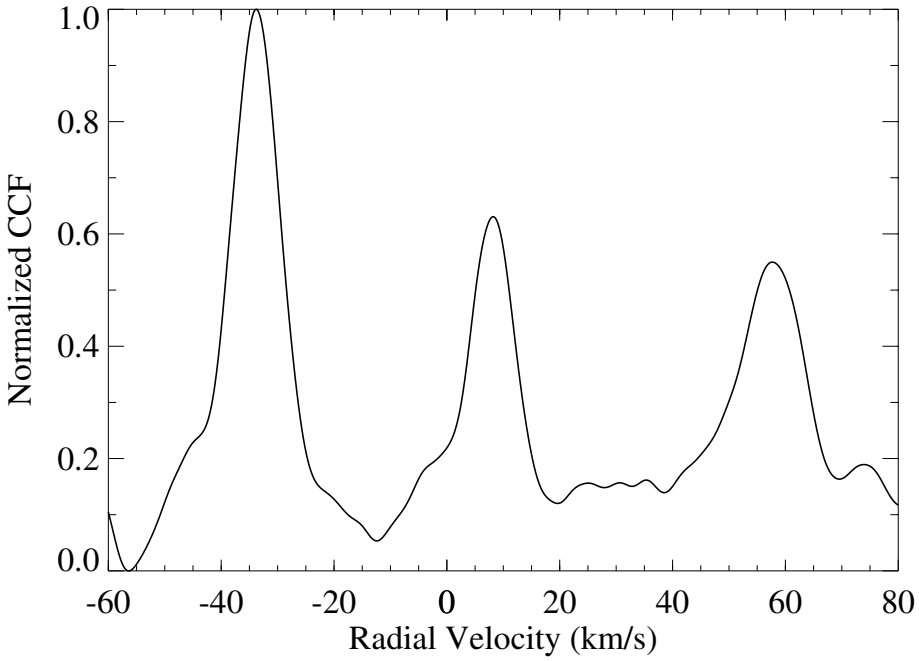

Figure 5.11: Example CCF plot for the J042442 system. Three individual peaks are clearly distinguishable, and therefore the system is identified as a three-component spectroscopic multiple. The CCF displayed has been measured for MJD = 55790.421, across the 35^{th} spectral order.

(2005) they then estimate component masses of 0.17, 0.12 and 0.1 $M_{\odot}$ and place an upper limit of 1.9 days on the orbital periods of the BC pair and 70.3 days on the orbit of the BC pair around the primary. Due to the tight nature of this system, < 0.25 AU ($\lesssim 7$ mas at 35 pc), it appears as a single star in AstraLux images. Therefore, aside from possible interferometric applications, the derived RV measurements and planned future RV monitoring currently provide the only viable means to fully constrain orbital parameters and derive model independent component masses for this system.

J04373746-0229282 (GJ 3305): GJ 3305 is a bona fide β Pic moving group member (Malo et al., 2013) and has a rich amount of astrometric data points, spanning $\sim$ 15 years of orbital motion. The binary is a wide ($\sim$ 2000 AU, Feigelson et al., 2006) companion to the exoplanet host 51 Eri. It is a prime target for isochronal analysis that can be used to date the β Pic group and test mass-luminosity evolutionary models. This has been accomplished by Montet et al. (2015) who exploit the wealth of astrometric information and a sample of complementary RV data from the literature to derive full orbital parameters and component masses to a good level

of precision. However, the mass uncertainties are dominated by the uncertainty in RV semi-amplitude. Montet et al. (2015) find BHAC15 evolutionary models (Baraffe et al., 2015) to be consistent with individual component masses to within 1.5σ and derive a system age of 37 $\pm$ 9 Myr, generally consistent with the overall β Pic age of 24 $\pm$ 3 Myr (e.g., Bell et al., 2015; Mamajek & Bell, 2014). This target is being densely monitored in both imaging and spectroscopy, and in future work, new orbital constraints will be deduced, with a considerable reduction in the error bars on the system age, allowing for a better comparison with the overall age of β Pic.

J07285137-3014490 (GJ 2060): GJ 2060 is a bona fide AB Dor moving group member (Malo et al., 2013) and has a large spread of astrometric data, sufficiently sampling and closing the binary orbit. In this study 5 new RV measurements are recorded for GJ 2060 which are plotted in Figure 5.6. These measurements will significantly aid in orbital determinations and place tighter constraints on individual component masses. A detailed orbital analysis of this system and complementary spectral analysis of the components is underway (Rodet et al., in prep.).

J08475676-7854532 (EQ Cha): EQ Cha is a member of the η Cha association (López Martí et al., 2013) and a suspected unresolved binary. Its binarity was first suspected due to its elevation in the Hertzsprung-Russell diagram (Lawson et al., 2001; Luhman & Steeghs, 2004). Surveys by Köhler & Petr-Gotzens (2002) and Brandeker et al. (2006) then revealed partially resolved images of J084756, supporting the binary nature of this system. By fitting the elongated, partially resolved PSF profile Brandeker et al. (2006) measure a binary separation of 40 mas ($\sim$ 4 AU at 97 pc (Bonavita et al., 2016)). This is within, or rapidly approaching, the diffraction limited resolution of the most advanced imaging instruments on 8m class telescopes. Therefore, again aside from possible interferometric applications, the derived RV measurements presented here and future RV monitoring currently provide the only viable means to produce a firm detection of the binary and derive orbital parameters and component masses.

J12072738-3247002 (TWA 23): TWA 23 is a bona fide member of the TW Hya association (Malo et al., 2014) for which three epochs of RV measurements are reported in table 5.4. It is noted that there exists two earlier epochs for this target listed in the FEROS archive which are additionally reduced, identifying two distinct peaks in the CCF. This suggests the system is a two-component spectroscopic binary and

that the individual CCF peaks have merged in later epochs due to the binary motion and spectrograph resolution. However, it is noted that the coordinates listed in the archive for the earlier epochs are offset by $\sim 1.0'$ from the actual target coordinates. Systems within a $2'$ radius of TWA 23 are > 6 magnitudes fainter, making it unlikely the target was misidentified within this region. However, Bailey et al. (2012) report RV measurements to a good level of precision ($\sim$60 m/s) for this system, identifying it as a single-lined spectroscopic binary from well sampled observations over the same timescale as the estimated orbital period, ~ 4 years. This suggests the early archival FEROS epochs, displaying a double peaked CCF, are not reliable. As it can not be confidently concluded whether or not TWA 23 was indeed observed during these epochs, the RVs measured for the components are excluded from table 5.4, however, they are listed here for completeness; MJD = 54170.258, RV = -5.59 $\pm$ 0.22 and 19.10 $\pm$ 0.41 kms^{-1}; MJD = 54228.241, RV = -3.51 $\pm$ 0.25 and 17.66 $\pm$ 0.41 kms^{-1}.

J15573430-2321123: J155734 is a high probability member of the Upper Scorpius subgroup of the Sco-Cen association (Rizzuto et al., 2015). Kraus et al. (2008) resolved this system using aperture masking interferometry, deriving a binary separation of $\sim$ 50 mas and estimating a mass ratio of 0.59 $\pm$ 0.06 from the measured contrast following the methods of Kraus & Hillenbrand (2007). Lafrenière et al. (2014) partially resolve the system and use a template to fit the elongated PSF profile to measure binary separation and contrast, which they use to estimate a mass ratio of 0.39 with uncertainties on the order of 10 - 30%. This system will notably benefit from the measurements presented here and future RV analysis over a longer baseline, allowing the mass ratio discrepancy reported in the literature to be resolved and full orbital parameters to be derived for this tight binary.

J20531465-0221218: J205314 is a potential member of the Argus moving group (Malo et al., 2013) for which two epochs of RV measurements are reported in table 5.4. As with TWA 23, it is noted there exists an additional archival epoch, which is reduced recovering a double peaked CCF, suggesting the system is a two-component spectroscopic where the individual CCF components have merged during our later epochs. Again however, the coordinates listed are offset by $\sim 1.0'$ from the actual target coordinates. As it can not be confidently concluded whether or not J205314 was observed in this archival epoch, this system is treated in a similar fashion to TWA 23 and the data is excluded from table 5.4, but listed here for completeness; MJD = 56809.274, RV = -45.32 $\pm$ 0.24 and -32.50 $\pm$ 0.30 kms^{-1}.

J23205766-0147373: J232057 is a high probability member of the Argus moving group (Malo et al., 2014) and was resolved by Daemgen et al. (2007) with a separation of $\sim 0.1''$. However, the system has since appeared as a single star in AstraLux images, indicating that the binary companion has moved inward. Therefore the RV measurements reported here are of significant importance for this system as they provide the most viable means of sampling the orbital motion over this timeframe, until the two components become visible again.

5.5 Summary and Conclusions

In this study the results of an RV monitoring survey of a sample of 29 young M-dwarf multiples are presented, many of which are high probability YMG members. These targets provide excellent laboratories for a range of astrophysical investigations and are prime candidates for isochronal analysis that can be used to calibrate low-mass stellar models and date individual systems. This dating can then potentially be applied to the full YMG of which they are members, for improved age constraints on the full population of stars. This sample has been monitored through various astrometric monitoring campaigns, primarily AstraLux multiplicity surveys, with the ultimate aim of deriving full orbital parameters and dynamical masses for the binary components. These model independent masses are essential for a robust isochronal analysis. The RV measurements reported here complement the imaging data, allowing enhanced orbital determinations and precise dynamical masses to be derived in a shorter timeframe than possible with astrometric monitoring alone. Furthermore, as illustrated by the case of J053018, RV allows for the identification of binary sub-pairs that are close enough to tidally synchronise, which increases their level of chromospheric activity. If such pairs go undetected, the age of the system can be drastically misestimated, which would invalidate any isochronal analysis. The majority of the sample has been shown to exhibit short-term RV variability on a level that is far lower than would be expected if they hosted $P < 10$ days stellar companions, even when accounting for the possibility of unfortunate orbit projections or non-optimal orbit sampling. Thus, nearly all of the targets are best interpreted as genuinely young binaries with spatially resolvable orbits of a few years to decades, confirming their suitability for isochronal analyses.

Whilst the ultimate goal of the AstraLux Multiplicity Surveys is to derive precise dynamical masses for M-dwarf binary components, enabling robust isochronal dating that can then be applied to YMGs, it is not feasible for the majority of the sample over the current survey lifetime due to the long orbital timescales. However, precise dynamical mass derivation and isochronal analysis is possible for several unique systems that already have a wealth of astrometric and RV data e.g, GJ 2060 (Rodet et al. in prep), 2MASS J10364483+1521394 (Calissendorff et al., 2017, see section 2.4.2). As mentioned in section 5.4.3, GJ 3305 in particular has a rich amount of astrometric data points. Combined with the array of new RV measurements presented here, orbital constraints and dynamical masses can be deduced to a good level of precision, allowing for a considerable reduction in the error bars on the system age. This analysis will be performed in future work and is discussed in Chapter 6 where a spectral analysis and preliminary isochronal dating demonstration is also presented.

Chapter 6

The case of GJ 3305

As noted in section 5.5, whilst the derivation of precise dynamical masses for the majority of AstraLux binaries will only become possible in the coming years, orbital and mass determinations are possible for several systems due to their particularly short orbital periods and wealth of additional astrometric and RV measurements in the literature. GJ 3305 is particularly favourable to mass determination and isochronal analysis due to the rich amount of astrometric and RV data points, both from the literature and AstraLux imaging / FEROS RV monitoring. The contents of this chapter are envisioned for publication in future work. In this chapter the GJ 3305 system is discussed, a spectral analysis is presented and a preliminary isochronal dating is demonstrated.

The unresolved GJ 3305 system, with integrated spectral type M0, was first identified as a wide ($\sim$ 2000 AU) companion to the F0 star 51 Eri, through common proper motion testing (both targets were previous known). Kasper et al. (2007) then identified GJ 3305 as a tight binary system using NACO on the VLT. The final component of this 4 body system was revealed by Macintosh et al. (2015) with the discovery of 51 Eri b, a ~ 2 M_J planet orbiting at ~ 13 AU from its F0 host. This mass was derived using hot-start evolutionary models and adopting a system age of 20 ± 6 Myr, Macintosh et al. (2015) own age estimate of the β Pic YMG , of which all components are members (e.g., Zuckerman et al., 2001; Malo et al., 2013).

Montet et al. (2015) exploit the wealth of astrometric data for this system (spanning ~ 15 years of orbital motion and including AstraLux multiplicity survey data) to calculate posterior distributions for orbital parameters and total system mass using an implementation of a Markov Chain Monte Carlo (MCMC) sampler, emcee (Foreman-Mackey et al., 2013). They derive an orbital period and semi-major axis

for the system of 29.03 ± 0.5 years and 9.78 ± 0.14 AU respectively. The astrometric data is also complemented by a small set of literature RV measurements (e.g., Bailey et al., 2012; Elliott et al., 2014) which enables a posterior distribution to be generated for the system mass ratio and subsequently the derivation of individual component masses. The dynamical masses of the primary and secondary components are estimated to be 0.67 ± 0.05 $M_{\odot}$ and 0.44 ± 0.05 $M_{\odot}$ respectively. Montet et al. (2015) then estimate the age of GJ 3305 by determining the age which produces the best match between BHAC15 (Baraffe et al., 2015) model predictions, the derived dynamical masses, and the observed combined and differential magnitudes. They estimate a system age of 37 ± 9 Myr, consistent with the β Pic age of 24 ± 3 Myr (e.g., Bell et al., 2015; Mamajek & Bell, 2014). The uncertainty in component mass is dominated by the uncertainty in the RV semi-amplitude which arises due to the lack of sufficient RV data points. Whilst additional astrometric data points will not aid in improving mass determinations, additional RV measurements are critical for deriving more precise masses. This will subsequently allow for an isochronal analysis that will improve the uncertainty on system age. Improved age constraints will have direct consequences for the inferred mass of the imaged planetary companion 51 Eri b, along with allowing for an assessment of dating robustness within the β pic YMG. 7 epochs of FEROS RV measurements for GJ 3305 are presented in table 5.4, increasing the sample of RV data points exploited by Montet et al. (2015) by a factor of ~ 2. Incorporating this sample into the MCMC analysis will provide a significant improvement on individual mass uncertainty and therefore system age. This MCMC analysis will be conducted in future work. However, a spectral analysis of this system and preliminary isochronal dating demonstration using the masses of Montet et al. (2015) is presented here.

6.1 Spectral Analysis

Individual spectral characterisation of each component is possible with the analysis of resolved spectra. Obtaining resolved spectra for this system is possible with the use of integral field spectroscopy (see section 2.2.3). GJ 3305 was observed with the AO assisted SINFONI (Eisenhauer et al., 2003; Bonnet et al., 2004) integral field spectrograph (IFS) on the VLT on the 17^{th} and 30^{th} October 2012. Observations were carried out on the separate nights using H+K and J gratings, covering the wavelength range 1.1 - 1.4 and 1.45 - 2.45 μm with a spectral resolution of R $\sim$ 2000 and

~ 1500 respectively. The SINFONI FOV is segmented into 32 images slices. Pre-slit optics are selected so that segment height is 25mas, producing a FOV of $0.8'' \times 0.8''$. Segmented FOV light is then dispersed to generate a 3d data cube with spatial information contained along two dimensions and spectral information along the third. 9 cubes were obtained with a direct integration time of 0.83 seconds for each grating. All standard IFS data reduction, such as flat-fielding, bias correction, pixel correction and wavelength calibration, was carried out using the SINFONI data reduction pipeline (Modigliani et al., 2007) and custom IDL routines following (Bonnefoy et al., 2010). Reduced individual data cubes were then merged into a master cube. GJ 3305 components were spatially resolved and individual 2d spectra were extracted by integrating the flux over 9×12.5 mas apertures across the wavelength dependant dimension. Telluric standard stars were also observed and reduced in order to identify and remove telluric lines from the GJ 3305 data (by dividing the respective spectra e.g., Bonnefoy et al., 2017).

In order to derive individual spectral types for the components, the individual spectra are compared against an empirical spectral catalogue of M0 - M9 V standard stars (Cushing et al., 2005; Rayner et al., 2009). The spectra are taken from the IRTF Spectral library, a compilation of solar-metallicity late-type spectra observed with SpeX (Rayner et al., 2003) at the NASA Infrared Telescope Facility covering the wavelength range 0.8 - 5 μm with a resolving power of R ~ 2000. The H+K spectra are divided into two separate wavelength ranges corresponding to H and K bands, $\sim 1.46 - 1.8\,\mu$m and $\sim 1.97 - 2.41\,\mu$m respectively, due to the lack of information between the two ranges as a result of the data reduction. The empirical spectra are similarly partitioned and degraded to the equivalent $R \sim 1500$ resolution (using the IDL Gaussfold routine). The J band SINFONI spectra are not suitable for comparison due to their sinusoidal shape as a result of a grating error at the time of the observations. IRTF spectra have all been shifted to zero RV. However, there is no need to shift GJ 3305 spectra to zero RV as SINFONI wavelength calibration can be off by 60 km/s due to systematics in the reduction process. GJ 3305's systemic RV, 20.76 ± 0.18 km/s (Montet et al., 2015), is well within this potential offset. Both SINFONI and IRTF spectra are given at vacuum wavelengths. Empirical IRTF spectra are normalised with respect to SINFONI spectra and interpolated to the same wavelength scale. For each GJ 3305 component and each H / K spectral range, the empirical spectra are subtracted from the SINFONI spectra and the residuals are recorded. The residuals can then be plotted as a function of the empirical spectral

type. Residual curves can be seen in figures 6.1 and 6.2 for the A and B components respectively. The spectral type of each component was estimated by averaging the H and K residual curves, fitting a 2^{nd} order polynomial, and taking the spectral type given at the polynomial minimum. Errors on the spectral type estimate were calculated by subtracting the polynomial fit from the residual curve, taking the standard deviation and propagating it along the spectral axis by determining the spectral class at the intercepts of the polynomial minimum $\pm\ \sigma$. This effectively projects the error in the polynomial fit into an error in the spectral type estimate. These fits can be seen in figures 6.1 and 6.2. The spectral types of the A and B components were determined to be $M0.0^{+1.5}_{-3}$ and $M3.5^{+1.5}_{-1}$ respectively. These are consistent with the spectral types derived by Janson et al. (2012c) using the magnitude - spectral type relations of Kraus & Hillenbrand (2007), M0.0 $\pm$ 0.5 and M3.0 $\pm$ 0.5 respectively. The larger lower bound error on the A component's spectral type is due to the lack of late K empirical spectra, particularly K8 - K9, which effects the gradient of the polynomial fit, resulting in a large projected error.

In order to derive individual temperatures for the components, the individual spectra are compared against a catalogue of synthetic spectra taken from the spectral libraries of Husser et al. (2013). These synthetic spectra are described in detail in section 5.3. The catalogue is composed of spectra with solar-metallicity, log g = 5.0 and temperatures in the range 2900 - 4700 K. The synthetic spectra have a resolution of R $\approx$ 500,000 across the wavelength ranges probed here, and therefore are degraded to R $\sim$ 1500 in the same fashion as the IRTF spectra degradation. Again, both SINFONI and Husser et al. (2013) synthetic spectra are given at vacuum wavelengths. Synthetic spectra are normalised with respect to SINFONI spectra and interpolated to the same wavelength scale. Figure 6.3 shows the H band portion of the GJ 3305A spectrum as an example, and a corresponding synthetic spectrum, highlighting the correlation between the two. Similar to the spectral type determination, for each GJ 3305 component and each H / K spectral range, the synthetic spectra are subtracted from the SINFONI spectra and the residuals are recorded and averaged. The residuals can then be plotted as a function of the synthetic spectra temperature. Residual curves can be seen in figures 6.4 and 6.5 for the A and B components respectively. Temperatures are estimated for both components by determining the temperature given at the residual curve minimum. The A and B component temperatures were determined to be 3800 ± 100 K and 3300 ± 100 K respectively. The $\pm$100 K errors are estimated from the difference in the minimum of individual H and K residual curves.

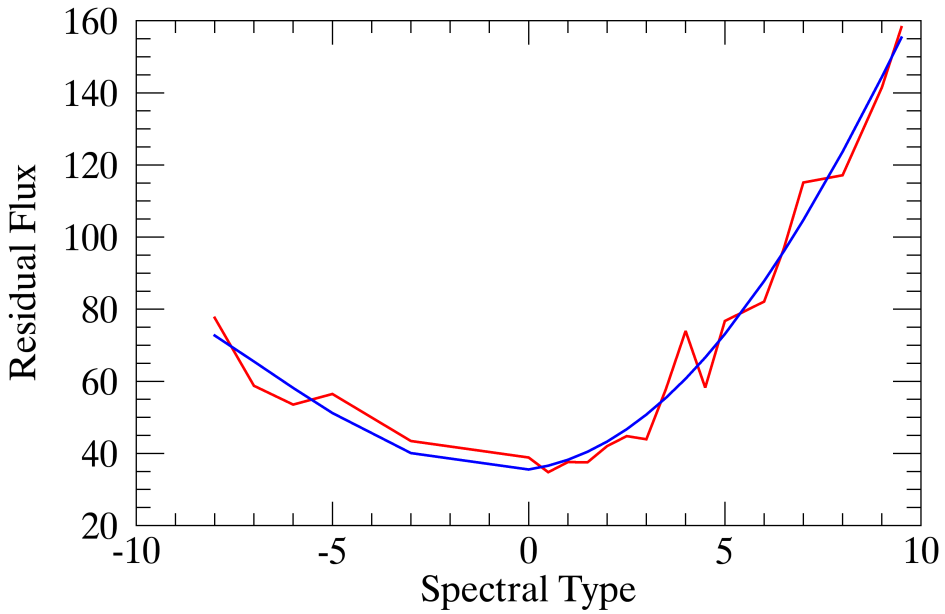

Figure 6.1: GJ 3305A Spectral Type determination. Residual flux in arbitrary units is plotted against spectral type with 0 = M0.0, 1 = M1.0, -1 = K9.0 etc. The SINFONI - Empirical IRTF spectra residuals, averaged across the H and K wavelength ranges, are plotted in red. The polynomial fit to the data is plotted in blue. The polynomial minimum occurs at 0.0, and therefore the spectral type of the A component is estimated to be M0.0$^{+1.5}_{-3}$. The lack of late K empirical spectra produces a flatter gradient towards the left of the polynomial minimum, producing a larger lower bound error.

The curves are quite smooth in nature, and therefore a polynomial fit is superfluous to minimum residual, and subsequently temperature, estimation. However, errors estimated through a polynomial fit (described in the previous paragraph) are consistent with the ±100 K error. This result is insensitive to the log g of the synthetic spectra (within the log g = 4.5 - 5.5 range), due to the low spectral resolution.

6.2 Isochronal Analysis

Now that individual temperatures have been estimated, a preliminary isochronal analysis of GJ 3305 is possible using the individual masses derived by Montet et al. (2015); 0.67±0.05 $M_\odot$ and 0.44±0.05 $M_\odot$ for the A and B components respectively. BHAC15 (Baraffe et al., 2015) temperature versus mass isochrones are used here. Isochrones

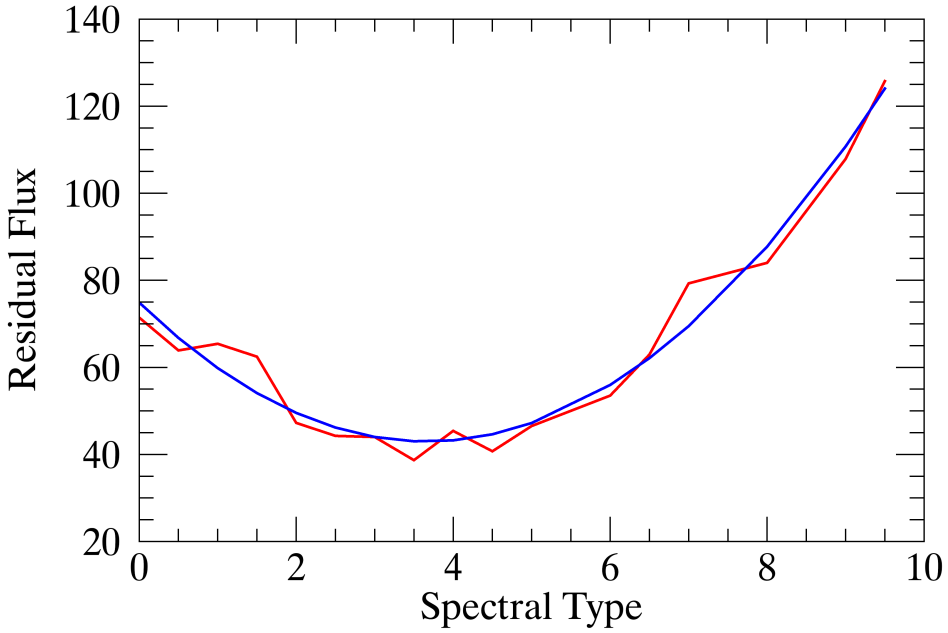

Figure 6.2: GJ 3305B Spectral Type determination. Residual flux in arbitrary units is plotted against spectral type with 0 = M0.0, 1 = M1.0, 2 = M2.0 etc. The SINFONI - Empirical IRTF spectra residuals, averaged across the H and K wavelength ranges, are plotted in red. The polynomial fit to the data is plotted in blue. The polynomial minimum occurs at 3.5, and therefore the spectral type of the B component is estimated to be $M3.5^{+1.5}_{-1}$.

spanning the age range 15 - 40 Myr are plotted in figure 6.6, along with the AB component measurements. As seen in figure 6.6, an isochronal analysis based on temperature provides limited information (over the age and mass range relevant to GJ 3305), as the isochrones converge and are very closely separated (with respect to component mass and temperature errors), as a result of pre-main sequence evolution. Therefore, no age constraints can be placed on the system from this analysis. However, it can be noted that although the isochrones are closely separated, they all lie well beyond the errors on the B component measurements. Similar to the results of Calissendorff et al. (2017), there is a possible discrepancy between dynamical and theoretical mass of the B component. However, it is more likely that the discrepancy is between observed and theoretical temperature, based on the analysis described in the following paragraphs.

In order to perform a more robust isochronal analysis and place reasonable con-

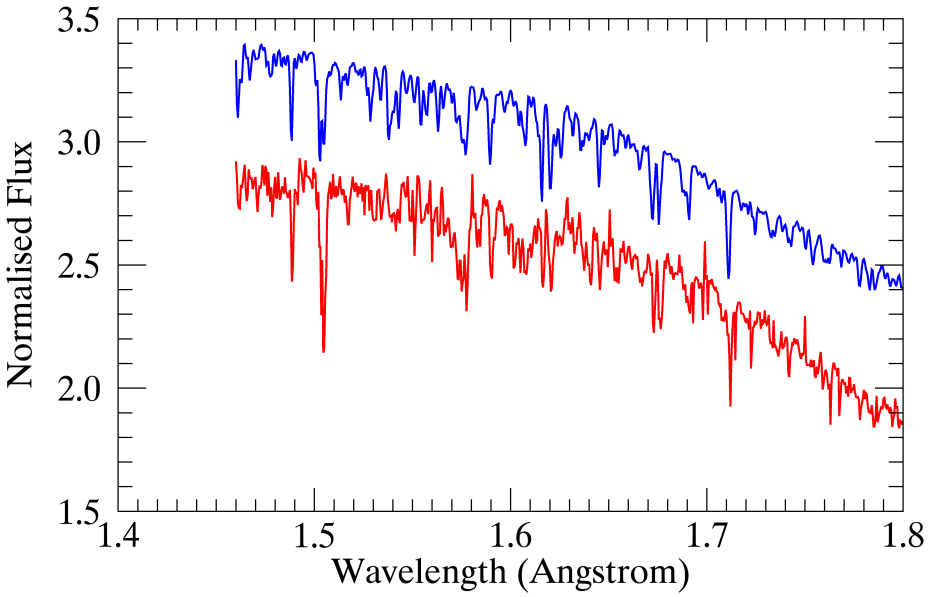

Figure 6.3: GJ 3305A H+K SINFONI spectrum over H band wavelengths, $\sim 1.46 - 1.8\mu$m, is plotted in red. Synthetic spectra of Husser et al. (2013), generated with a temperature of 3800 K, is plotted in blue. Spectra have been arbitrarily offset for display puproses.

straints on the age of GJ 3305, a bolometric luminosity based analysis can be performed. To derive resolved luminosities for each component, resolved J, H and K band magnitudes are first calculated. Montet et al. (2015) measures differential J, H and K band magnitudes for GJ 3305 which together with 2MASS (Cutri et al., 2003) J, H and K apparent unresolved magnitudes can be used to determine resolved magnitude via;

$$mA_{JHK} = m_{JHK} + 2.5\,log\,(1 + 10^{-\Delta m_{JHK}/2.5}) \tag{6.1}$$

$$mB_{JHK} = m_{JHK} + 2.5\,log\,(1 + 10^{\Delta m_{JHK}/2.5}) \tag{6.2}$$

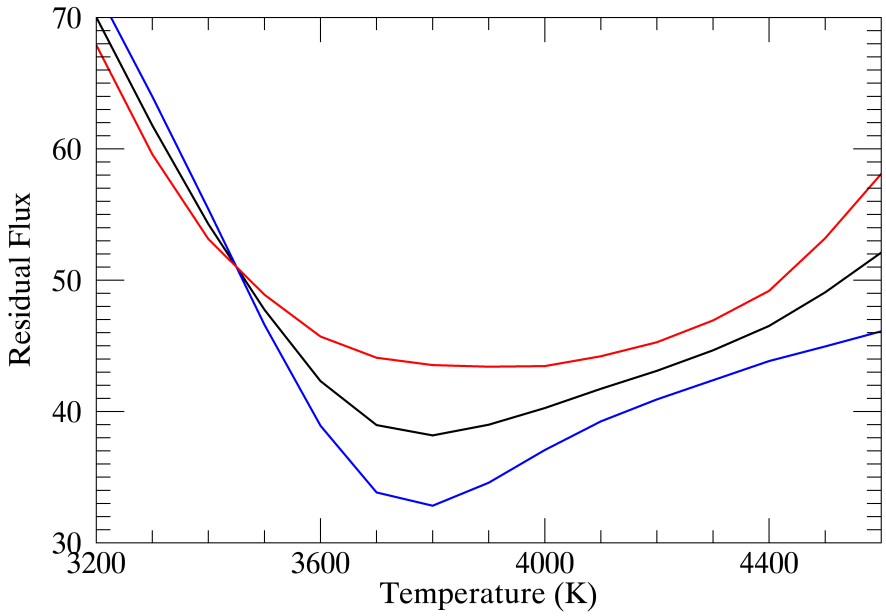

Figure 6.4: GJ 3305A Temperature determination. Residual flux in arbitrary units is plotted against synthetic template temperature. The SINFONI - synthetic spectra residuals, averaged across the H and K wavelength ranges, are plotted in black. The residual cure minimum occurs at 3800 K, and therefore the temperature of the A component is estimated to be 3800 ± 100 K. Individual H (red) and K (blue) residual curves are also plotted, which show difference of 100 K at their minimum, from which the $\pm$100 K error derives.

Table 6.1: GJ 3305 Unresolved and Differential Apparent Magnitudes

Magnitude	Magnitude Value	Reference
J	7.30 ± 0.02	Cutri et al. (2003)
H	6.64 ± 0.05	Cutri et al. (2003)
K	6.413 ± 0.02	Cutri et al. (2003)
ΔJ	0.97 ± 0.01	Montet et al. (2015)
ΔH	1.00 ± 0.01	Montet et al. (2015)
ΔK	0.94 ± 0.02	Montet et al. (2015)

Unresolved and differential magnitudes are given in table 6.1. Resolved magnitudes are calculated via equations 6.1 and 6.2 and presented in table 6.2. Resolved L' magnitudes measured by Kasper et al. (2007) are also included in this sample. To estimate the bolometric luminosity, the resolved magnitudes are compared to BHAC15 isochrones which also predict stellar magnitude and bolometric luminosity as a func-

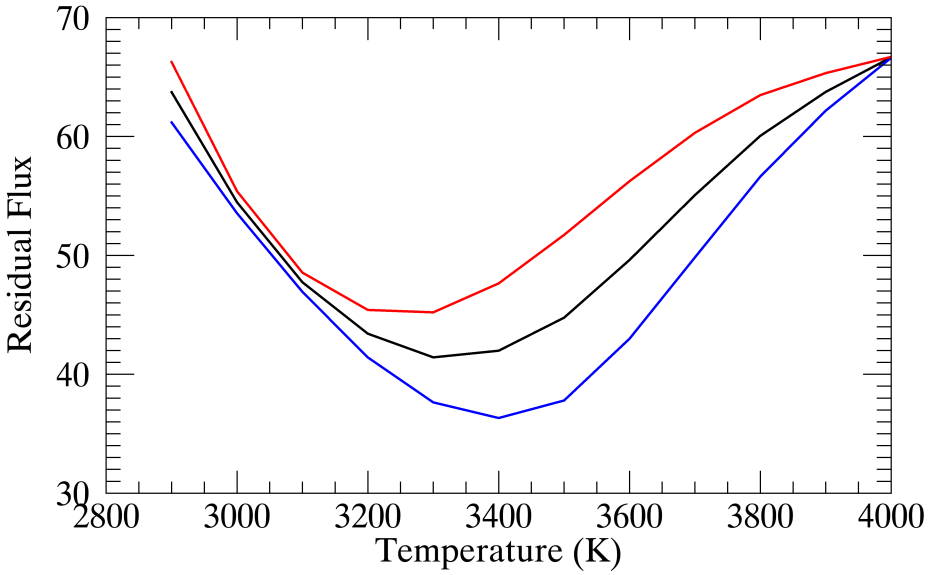

Figure 6.5: GJ 3305B Temperature determination. Residual flux in arbitrary units is plotted against synthetic template temperature. The SINFONI - synthetic spectra residuals, averaged across the H and K wavelength ranges, are plotted in black. The residual cure minimum occurs at 3300 K, and therefore the temperature of the B component is estimated to be 3300 ± 100 K. Individual H (red) and K (blue) residual curves are also plotted, which show difference of 100 K at their minimum, from which the $\pm$100 K error derives.

tion of mass and age. A chi-square test is performed on 5 - 100 Myr isochrones to determine which set of models best represents the observed resolved magnitudes. The chi-squared is calculated for each component as follows;

$$\chi^2 = \frac{J_{A/B} - J}{\Delta J^2} + \frac{H_{A/B} - H}{\Delta H^2} + \frac{K_{A/B} - K}{\Delta K^2} + \frac{L'_{A/B} - L'}{\Delta L'^2} \tag{6.3}$$

Where J, H, K and L' are the theoretical predictions which vary as a function of mass and age. However these predictions are absolute magnitudes and therefore the observed resolved apparent magnitudes are translated into absolute magnitudes using the system's distance. Since there is no parallactic measurement for GJ 3305, the trigonometric distance of its $\sim$ 2000 AU companion 51 Eri is adopted, 29.43 ± 0.30 pc (van Leeuwen, 2007), as it is unlikely the radial distance would be significantly

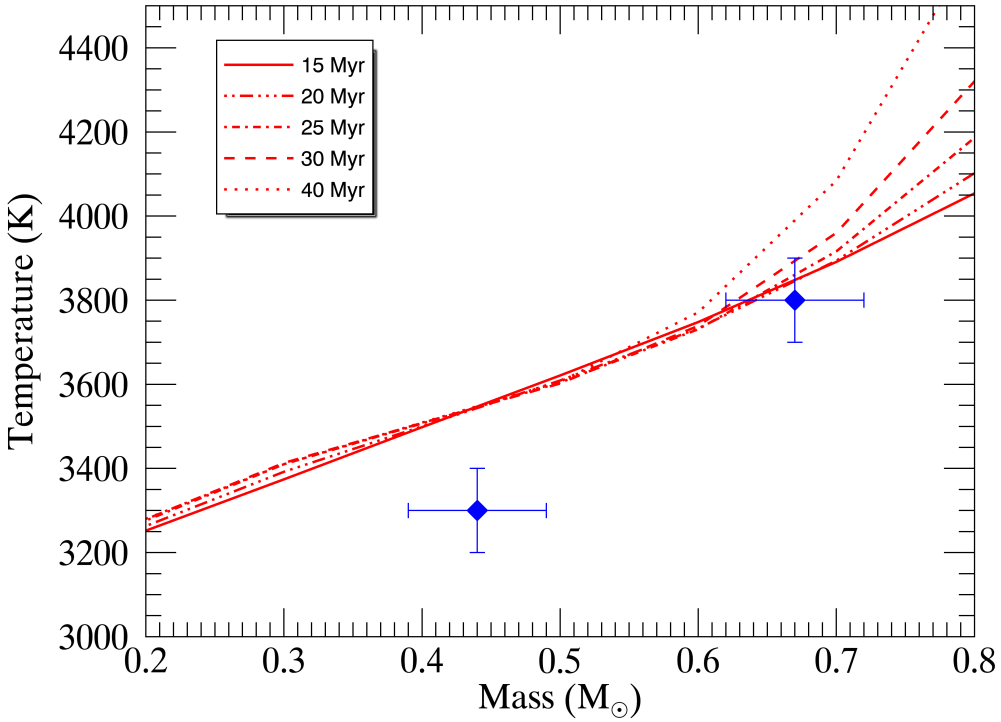

Figure 6.6: GJ 3305 temperature based isochronal analysis. BHAC15 isochrones are plotted as a function of mass and temperature spanning ages 15 - 40 Myr. The A component is the upper most diamond (T = 3800 ± 100 K, M = 0.67 ± 0.05 $M_\odot$), the B component is the lower most diamond (T = 3300 ± 100 K, M = 0.44 ± 0.05 $M_\odot$). Isochrones are closely separated and converge, providing limited information on system age. However, there is a discrepancy between the B component measurements and the theoretical predictions.

larger. The bolometric luminosity for each component is estimated as the luminosity corresponding to the mass and age that produces the minimum χ^2 value. The error on the luminosity is taken by selecting the luminosity of all models below a reasonable threshold χ^2 value, 20×the minimum χ^2, and taking the standard deviation. The A and B component luminosities are estimated to be log L/ $L_\odot$ = -0.91 ± 0.05 and -1.34 ± 0.04 respectively.

Now that individual luminosities have been estimated, a preliminary isochronal analysis of GJ 3305 is possible using luminosity versus mass BHAC15 isochrones. Isochrones spanning the age range 15 - 50 Myr are plotted in figure 6.7, along with

Table 6.2: GJ 3305 Resolved Apparent Magnitudes

	GJ 3305A	GJ 3305B
J	7.67 ± 0.02	8.64 ± 0.02
H	7.00 ± 0.05	8.00 ± 0.05
K	6.79 ± 0.03	7.73 ± 0.03
L'	6.50 ± 0.14	7.38 ± 0.24

the AB component measurements. This analysis is much more valuable than a temperature based isochronal analysis as the isochrones are well separated with respect to component errors in comparison to the closely spaced temperature dependant isochrones in figure 6.6, providing a tighter constraint on the system age. The masses and luminosities of both components are consistent with the theoretical predictions at these young (15 - 50 Myr) ages. Whilst the models converge towards higher masses in the range of the A component mass, providing limited information on system age, the B component can be dated to a reasonable level of precision in this preliminary analysis. The errors on the B component measurements are well constrained by 25 and 50 Myr isochrones as can be seen in figure 6.7. Therefore, the age of the B component, and thus the GJ 3305 and 51 Eri systems, can be constrained to 25 - 50 Myr. This is in agreement with the findings of Montet et al. (2015), 37 ± 9 Myr, and the age of the β Pic YMG, 24 ± 3 Myr. The uncertainty in the age is dominated by the uncertainty in the component mass, rather than the luminosity which is measured to a good level of precision. Therefore, the future MCMC analysis including the significantly increased sample of RV data points will be of vital importance to reducing the mass errors, and therefore improving the age constraints on the system.

6.3 Conclusions

In this chapter the preliminary results of a spectral analysis and isochronal dating of GJ 3305 are presented. GJ 3305 is a particularly valuable system as there exists a wealth of astrometric and RV data in the literature. Montet et al. (2015) exploit this data to derive dynamical masses of 0.67 ± 0.05 $M_{\odot}$ and 0.44 ± 0.05 $M_{\odot}$ for the primary and secondary components respectively and carry out an isochronal analysis to constrain the system age to 37 ± 9 Myr. The relatively large age uncertainty is is dominated by the mass uncertainty, which in turn stems from the uncertainty in the RV semi-amplitude which arises due to the lack of sufficient RV data points. The

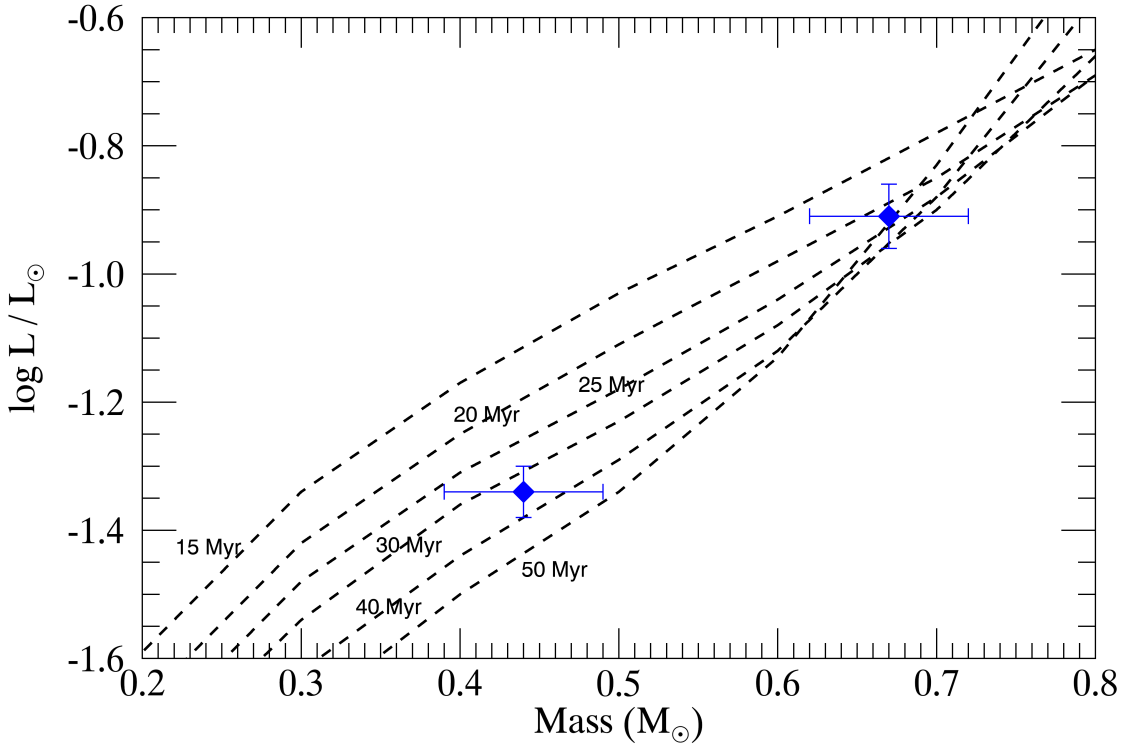

Figure 6.7: GJ 3305 bolometric luminosity based isochronal analysis. BHAC15 isochrones are plotted as a function of mass and luminosity spanning ages 15 - 50 Myr. The A component is the upper most diamond (log L/ $L_\odot$ = -0.91 ± 0.05, M = 0.67 ± 0.05 $M_\odot$), the B component is the lower most diamond (log L/ $L_\odot$ = -1.34 ± 0.04, M = 0.44 ± 0.05 $M_\odot$). Isochrones are well separated at lower masses, allowing the age of the B component to be constrained to 25 - 50 My. Both components are consistent with the theoretical predictions at young ($\lesssim$ 50 Myr) ages.

AstraLux RV follow up survey presented in Chapter 5 has increased the sample of available RV data points by a factor of ~ 2. Incorporating this sample into a future MCMC analysis will provide a significant improvement on individual mass uncertainty and therefore system age.

A spectral analysis of individual components was performed by comparing resolved SINFONI spectra against an empirical spectral catalogues of empirical and theoretical spectra. The spectral types of the A and B components were determined to be $M0.0^{+1.5}_{-3}$ and $M3.5^{+1.5}_{-1}$ respectively, consistent with the spectral types derived

by Janson et al. (2012c) using the magnitude - spectral type relations of Kraus & Hillenbrand (2007). The A and B component temperatures were determined to be 3800 ± 100 K and 3300 ± 100 K respectively. Preliminary temperature and luminosity based isochronal analysis of GJ 3305 was performed using the individual masses derived by Montet et al. (2015) and BHAC15 (Baraffe et al., 2015) isochrones. Whilst the temperature based analysis provides limited information, the luminosity based analysis constrains the age of the system to 25 - 50 Myr. This age will be significantly improved with enhanced mass estimates of future MCMC analysis.

Chapter 7

Conclusions - Future Work

In this thesis two specific limitations faced by the direct imaging field have been discussed: (i) the lack of detections and population constraints beyond 100 AU due to anisoplanatic limitations of large AO assisted ground based telescopes and FOV limitations of space based telescopes (see section 2.4.1). (ii) The lack of robust and consistent age estimates of typical imaging survey targets, YMG systems (see section 2.4.2). Efforts have been made to address these limitations in the two studies presented in this thesis: (i) a re-analysis of archival Spitzer imaging surveys with enhanced sensitivity through PCA PSF subtraction, enabling a systematic exploration for planetary mass companions beyond 100 AU, and the first robust constraints to be be placed on the planetary population out to 1000 AU. (ii) A radial velocity survey of a sample of spatially resolved young, low-mass binaries identified and astrometrically monitored through AstraLux multiplicity surveys which will allow for the derivation of precise component dynamical masses, followed by subsequent robust isochronal analysis which will place improved age constraints on the full population of YMG members.

In this chapter I detail future work that will continue to address these imaging limitations; extension of the high contrast imaging with Spitzer survey and the continuation of the AstraLux multiplicity surveys.

7.1 High Contrast Imaging with Spitzer Extension

In chapters 3 and 4 the results of a reanalysis of two archival Spitzer imaging surveys are presented. In summary, previously the large PSF associated with the 0.85m

Spitzer telescope diameter has severely limited its capability for directly imaging exoplanets. With the application of PCA, this study has removed the stellar PSF and opened up sensitivity to planetary mass companions over a broad range of separations. PCA has provided up to a magnitude sensitivity improvement at small separations with respect to conventional PSF subtraction methods, highlighting the strength of the technique, even on a relatively unfavourable data set. In the PSF noise-limited regime, sensitivity down to 0.5 M_J has been achieved at separations on the order of $10^2 - 10^3$ AU. Through the coupling of Monte Carlo simulations and a Bayesian analysis, for the first time the population of $0.5 - 13$ M_J , $100 - 1000$ AU planets has been constrained, producing an upper frequency limit of 9%. Constraining this very wide giant planet population allows for previously untested formation and evolutionary theories to be adapted and constrained.

Whilst these efforts provide an initial picture of the very wide planet population, planet detections and similarly stringent frequency limits are severely lacking over this parameter space. Therefore, it is envisioned that this enhanced sensitivity re-analysis will be extended to additional archival Spitzer imaging surveys to significantly enhance the prospect of exoplanet detection within a previously elusive parameter space. The population analysis that can be conducted with a larger sample of targets will build up a framework of robust wide planet population statistics, placing tighter constraints on the wide giant frequency and in turn allowing for various theories to be stringently constrained. Such studies are ideal precursors to imaging surveys with the JWST, aiding in target selection and optimising post-processing algorithms for space based imaging.

The two archival surveys chosen in this thesis for re-analysis encompass 121 targets observed during the cryogenic phase of the Spitzer mission between 2003 and 2004. A further three Spitzer imaging survey programs, executed between 2004 and 2006, have been identified that encompass an additional 191 targets that would be suitably similar for re-analysis. These surveys were effectively extensions of the original P34 and P48 surveys, and executed under the exact same observational parameters, in order to have a volume limited sample of systems within 50 pc of the Sun. Therefore, along with a further 191 systems to be probed for planetary companions and statistically analysed, these three surveys can be combined with the original P34 and P48 sample. This will provide significantly more PSF references, and therefore PCA modes, available for PSF construction than the original volume limited array of ~ 56

modes. This will allow for a more optimal PSF construction and provide greater image sensitivity upon subtraction, as sensitivity is currently limited at relatively small separations by residual PSF noise.

In the previous re-analysis, all sources within $\sim 1'$ of each target, $\sim$ 1000 AU at the median distance, were vetted for planet candidacy. This corresponds to the $2.01' \times 2.01'$ optimisation region. Along with candidate vetting and population analysis efficiency considerations, the $\sim 1'$ radius limit was chosen as PCA application beyond this separation would have proved fruitless; $> 1'$ separations are within the background noise-limited regime which PCA cannot reference and effectively subtract due to it's random nature. In fact, the background noise limited regime is estimated to occur at $> 20''$ separations as PCA provides no improvement over conventional PSF subtraction at these separations. Therefore, $>> 1'$ separations were not probed for planetary companions as PCA was not applied here. There was no sensitive improvement or additional data reduction performed with respect to the original observations and image generation. Therefore, it was assumed that no detectable companions existed over this parameter space, as they would have been revealed and presented in the original survey analysis. However, it is possible that this assumption was inaccurate and the recent discovery of planets at extremely wide separations >> 1000 AU (e.g., 2M2126b at $>$ 4500 AU; Deacon et al., 2016) motivates the extension of this survey to wider separations, as well as additional targets. This will increase the probability of exoplanet detection over a previously elusive parameter space and allow for constraints to be placed on the planet population at separations >> 1000 AU.

Extending enhanced space-based imaging capability beyond Spitzer to the Hubble space telescope (HST) is also of significant interest as the PSF stability of the HST (e.g., Anderson & Bedin, 2017) would prove ideal for PCA application. There is a vast array of archival HST data taken with a range of imaging instruments. Similar high contrast reprocessing of HST data is being carried out as part of the Archival Legacy Investigations of Circumstellar Environments (ALICE Hagan et al., 2018) program, which has identified $\sim$ 400 targets that would be particularly favourable for the enhanced imaging analysis proposed here.

All archival data is readily available, and the PCA algorithm is ready built and requires a very modest amount of CPU hours to execute. Therefore the completion of these proposed extensions is feasible within a reasonable time frame i.e., before

JWST is operational.

7.2 AstraLux Multiplicity Survey Continuation

In chapter 5 the motivations and data analysis of the AstraLux multiplicity surveys are discussed and the results of an RV monitoring survey of a sample of 29 high probability YMG M-dwarf multiples are presented. The ultimate goal of these surveys is to derive precise dynamical masses that will allow for an isochronal dating of individual systems that can then be applied to the full population of YMG members. Improved age constraints on YMG members is critical for estimating the mass or initial entropy of planets and brown dwarfs using mass-luminosity evolutionary models (e.g., Baraffe et al., 2003, 2015), where a precise system age is essential for deriving a precise object mass.

In order to derive dynamical masses orbital parameters must be derived to a good level of precision. Due to the resolving power of the AstraLux instruments and the typical distance of YMG systems, the shortest orbital period binaries that can be resolved and monitored have periodicities on the order of $\sim 10 - 40$ years (see table 5.2). In order to derive precise orbital parameters, orbits must be nearly closed and well sampled, which requires observations over the same timescale as an orbital period e.g, $\sim 10 - 40$ years. However, this timeframe reduces to the order of several years if there is sufficient RV data to complement the astrometry. Therefore, these surveys (AstraLux imaging and RV monitoring) are envisioned to be ongoing for the foreseeable future. Even if dynamical masses can be derived for the majority of the high-utility sample of 29 binaries within the next decade, continual monitoring beyond this is essential for closing orbits for longer period binaries, extending the possible isochronal analysis to a much larger sample of targets. This is of fundamental importance to covering a wider sample of YMGs and to assess dating robustness and coevality within individual YMGs, as well as allowing for evolutionary model calibration. In the immediate continuation of this survey, ~ 3 nights of FEROS observations of the high utility sample, along with several new binary discoveries, were taken in late 2017 and await analysis. Further astrometric monitoring has also been proposed for the 2018 period.

However, whilst the derivation of precise dynamical masses for the majority of the high utility sample will only become possible in the coming years, orbital and mass determinations are possible for several systems due to their particularly short orbital periods and wealth of additional astrometric and RV measurements in the literature. For example, the short ($\sim 8\,$yr) orbital period of the triple system 2MASS J10364483+1521394's BC pair has enabled Calissendorff et al. (2017) to derive a combined dynamical mass of 0.48 ± 0.14 $M_\odot$ and a mass ratio of 1.00 ± 0.03 for the components from AstraLux survey data alone. However, the discrepancy between dynamical and theoretical masses for J1036 noted by Calissendorff et al. (2017), in addition to the large mass uncertainty (stemming from the large error on the distance measurement; 20.1 ± 2.0 pc), make it difficult to isochronally date this particular system (see figure 2.11).

As mentioned in Chapter 6, GJ 3305 is also particular favourable to mass determination and isochronal analysis due to the rich amount of astrometric and RV data points, spanning $\sim$ 15 years of orbital motion. Montet et al. (2015) carried out an MCMC analysis to derive obrital parameters and masses for the system. The dynamical masses of the primary and secondary components are estimated to be 0.67 ± 0.05 $M_\odot$ and 0.44 ± 0.05 $M_\odot$ respectively. Through isochronal analysis Montet et al. (2015) estimate a system age of 37 ± 9 Myr. The relatively large age uncertainty is is dominated by the mass uncertainty, which in turn stems from the uncertainty in RV semi-amplitude. 7 epochs of FEROS RV measurements for GJ 3305 are presented in table 5.4, increasing the sample of RV data points exploited by Montet et al. (2015) by a factor of ~ 2. Incorporating this sample into a future MCMC analysis will provide a significant improvement on individual mass uncertainty and therefore system age.

Bibliography

Ahn, C. P., Alexandroff, R., Allende Prieto, C., et al. 2012, ApJS, 203, 21

Alexander, R. D. & Armitage, P. J. 2007, MNRAS, 375, 500

Alibert, Y., Mordasini, C., Benz, W., & Winisdoerffer, C. 2005, A&A, 434, 343

Allard, F., Hauschildt, P. H., Alexander, D. R., Tamanai, A., & Schweitzer, A. 2001, ApJ, 556, 357

Alonso-Floriano, F. J., Morales, J. C., Caballero, J. A., et al. 2015, A&A, 577, A128

Amara, A. & Quanz, S. P. 2012, MNRAS, 427, 948

Anderson, J. & Bedin, L. R. 2017, MNRAS, 470, 948

Anglada-Escudé, G., Amado, P. J., Barnes, J., et al. 2016, Nature, 536, 437

Babcock, H. W. 1953, PASP, 65, 229

Bailey, III, J. I., White, R. J., Blake, C. H., et al. 2012, ApJ, 749, 16

Baldwin, J. E., Tubbs, R. N., Cox, G. C., et al. 2001, A&A, 368, L1

Baraffe, I., Chabrier, G., Allard, F., & Hauschildt, P. H. 1998, A&A, 337, 403

Baraffe, I., Chabrier, G., & Barman, T. 2008, A&A, 482, 315

Baraffe, I., Chabrier, G., Barman, T. S., Allard, F., & Hauschildt, P. H. 2003, A&A, 402, 701

Baraffe, I., Homeier, D., Allard, F., & Chabrier, G. 2015, A&A, 577, A42

Barenfeld, S. A., Bubar, E. J., Mamajek, E. E., & Young, P. A. 2013, ApJ, 766, 6

Barnes, S. A. 2007, ApJ, 669, 1167

Barrado y Navascues, D. 1998, A&A, 339, 831

Barrado Y Navascués, D., Bayo, A., Morales-Calderón, M., et al. 2007, A&A, 468, L5

Basri, G. & Brown, M. E. 2006, Annual Review of Earth and Planetary Sciences, 34, 193

Batalha, N. M., Rowe, J. F., Bryson, S. T., et al. 2013, ApJS, 204, 24

Bate, M. R. 2009, MNRAS, 392, 590

Bate, M. R. 2012, MNRAS, 419, 3115

Baudoz, P., Rabbia, Y., & Gay, J. 2000, A&AS, 141, 319

Beaulieu, J.-P., Buchler, J. R., Marquette, J.-B., Hartman, J. D., & Schwarzenberg-Czerny, A. 2006, ApJL, 653, L101

Beckers, J. M. 1993, Annu. Rev. Astron. Astrophys., 31, 13

Bell, C. P. M., Mamajek, E. E., & Naylor, T. 2015, MNRAS, 454, 593

Bergfors, C., Brandner, W., Bonnefoy, M., et al. 2016, MNRAS, 456, 2576

Bergfors, C., Brandner, W., Daemgen, S., et al. 2013, MNRAS, 428, 182

Bergfors, C., Brandner, W., Janson, M., et al. 2010, A&A, 520, A54

Berkefeld, T., Glindemann, A., & Hippler, S. 2001, Experimental Astronomy, 11, 1

Berton, A., Gratton, R. G., Feldt, M., et al. 2006, PASP, 118, 1144

Beuzit, J.-L., Feldt, M., Dohlen, K., et al. 2008, in Proc. SPIE., Vol. 7014, Ground-based and Airborne Instrumentation for Astronomy II, 701418

Biller, B. A. & Close, L. M. 2007, ApJL, 669, L41

Biller, B. A., Close, L. M., Masciadri, E., et al. 2007, ApJS, 173, 143

Biller, B. A., Kasper, M., Close, L. M., Brandner, W., & Kellner, S. 2006, ApJL, 641, L141

Biller, B. A., Liu, M. C., Wahhaj, Z., et al. 2013, ApJ, 777, 160

Bitsch, B., Lambrechts, M., & Johansen, A. 2015, A&A, 582, A112

Bloemhof, E. E. 2003, ApJL, 582, L59

Bonavita, M. & Desidera, S. 2007, A&A, 468, 721

Bonavita, M., Desidera, S., Thalmann, C., et al. 2016, A&A, 593, A38

Bond, I. A., Bennett, D. P., Sumi, T., et al. 2017, MNRAS, 469, 2434

Bond, I. A., Udalski, A., Jaroszyński, M., et al. 2004, ApJL, 606, L155

Bonnefoy, M., Chauvin, G., Dougados, C., et al. 2017, A&A, 597, A91

Bonnefoy, M., Chauvin, G., Dumas, C., et al. 2009, A&A, 506, 799

Bonnefoy, M., Chauvin, G., Rojo, P., et al. 2010, A&A, 512, A52

Bonnet, H., Conzelmann, R., Delabre, B., et al. 2004, in Proc. SPIE., Vol. 5490, Advancements in Adaptive Optics, ed. D. Bonaccini Calia, B. L. Ellerbroek, & R. Ragazzoni, 130–138

Booth, R. S., Poppenhaeger, K., Watson, C. A., Silva Aguirre, V., & Wolk, S. J. 2017, MNRAS, 471, 1012

Borucki, W. J. & Summers, A. L. 1984, Icarus., 58, 121

Boss, A. P. 1997, Science, 276, 1836

Boss, A. P. 2001, ApJ, 563, 367

Boss, A. P. 2006, ApJL, 637, L137

Bowler, B., Kraus, A., Bryan, M., et al. 2017, ArXiv e-prints

Bowler, B. P. & Hillenbrand, L. A. 2015, ApJL, 811, L30

Bozza, V., Mancini, L., & Sozzetti, A., eds. 2016, Astrophysics and Space Science Library, Vol. 428, Methods of Detecting Exoplanets

Brandeker, A., Jayawardhana, R., Khavari, P., Haisch, Jr., K. E., & Mardones, D. 2006, ApJ, 652, 1572

Brandt, T. D., Kuzuhara, M., McElwain, M. W., et al. 2014, ApJ, 786, 1

Bubenicek, J., Palous, J., & Piskunov, A. E. 1985, , 29, 625

Burgasser, A. J., Reid, I. N., Siegler, N., et al. 2007, Protostars and Planets V, 427

Burkert, A., Bate, M. R., & Bodenheimer, P. 1997, MNRAS, 289, 497

Burrows, A., Hubbard, W. B., Lunine, J. I., & Liebert, J. 2001, Reviews of Modern Physics, 73, 719

Burrows, A., Sudarsky, D., & Lunine, J. I. 2003, ApJ, 596, 587

Calissendorff, P., Janson, M., Köhler, R., et al. 2017, A&A, 604, A82

Cameron, A. C. 2012, Nature, 492, 48

Carpenter, J. M., Mamajek, E. E., Hillenbrand, L. A., & Meyer, M. R. 2006, ApJL, 651, L49

Carson, J. C., Eikenberry, S. S., Smith, J. J., & Cordes, J. M. 2006, AJ, 132, 1146

Carson, J. C., Marengo, M., Patten, B. M., et al. 2011, ApJ, 743, 141

Cassan, A., Kubas, D., Beaulieu, J.-P., et al. 2012, Nature, 481, 167

Chabrier, G., Baraffe, I., Allard, F., & Hauschildt, P. 2000, ApJ, 542, 464

Chabrier, G., Johansen, A., Janson, M., & Rafikov, R. 2014, Protostars and Planets VI, 619

Chapman, S. 1939, ApJ, 90, 309

Charbonneau, D., Brown, T. M., Latham, D. W., & Mayor, M. 2000, ApJL, 529, L45

Chatterjee, S., Ford, E. B., Matsumura, S., & Rasio, F. A. 2008, ApJ, 686, 580

Chauvin, G., Desidera, S., Lagrange, A.-M., et al. 2017, A&A, 605, L9

Chauvin, G., Lagrange, A.-M., Bonavita, M., et al. 2010, A&A, 509, A52

Chauvin, G., Lagrange, A.-M., Dumas, C., et al. 2004, A&A, 425, L29

Chauvin, G., Lagrange, A.-M., Dumas, C., et al. 2005, A&A, 438, L25

Chauvin, G., Vigan, A., Bonnefoy, M., et al. 2015, A&A, 573, A127

Ciceri, S., Mancini, L., Southworth, J., et al. 2016, MNRAS, 456, 990

Ciddor, P. E. 1996, Applied Optics LP., 35, 1566

Cruz, K. L. & Reid, I. N. 2002, AJ, 123, 2828

Cumming, A., Butler, R. P., Marcy, G. W., et al. 2008, PASP, 120, 531

Cushing, M. C., Rayner, J. T., & Vacca, W. D. 2005, ApJ, 623, 1115

Cutri, R. M., Skrutskie, M. F., van Dyk, S., et al. 2003, VizieR Online Data Catalog, 2246, 0

Daemgen, S., Siegler, N., Reid, I. N., & Close, L. M. 2007, ApJ, 654, 558

Daemgen, S., Todorov, K., Quanz, S. P., et al. 2017, ArXiv e-prints

Dainty, J. C., Hennings, D. R., & Odonnell, K. A. 1981, Journal of the Optical Society of America (1917-1983), 71, 490

Dale, D. A., Bendo, G. J., Engelbracht, C. W., et al. 2005, ApJ, 633, 857

Davies, R. & Kasper, M. 2012, Annu. Rev. Astron. Astrophys., 50, 305

Davis, S. S. 2005, ApJL, 627, L153

De Silva, G. M., D'Orazi, V., Melo, C., et al. 2013, MNRAS, 431, 1005

de Zeeuw, P. T., Hoogerwerf, R., de Bruijne, J. H. J., Brown, A. G. A., & Blaauw, A. 1999, AJ, 117, 354

Deacon, N. R., Schlieder, J. E., & Murphy, S. J. 2016, MNRAS, 457, 3191

Delfosse, X., Beuzit, J.-L., Marchal, L., et al. 2004, in Astronomical Society of the Pacific Conference Series, Vol. 318, Spectroscopically and Spatially Resolving the Components of the Close Binary Stars, ed. R. W. Hilditch, H. Hensberge, & K. Pavlovski, 166–174

Delorme, P., Gagné, J., Girard, J. H., et al. 2013, A&A, 553, L5

Delorme, P., Lagrange, A. M., Chauvin, G., et al. 2012, A&A, 539, A72

Diolaiti, E., Conan, J.-M., Foppiani, I., et al. 2010, in Proc. SPIE., Vol. 7736, Adaptive Optics Systems II, 77360R

Dodson-Robinson, S. E., Veras, D., Ford, E. B., & Beichman, C. A. 2009, ApJ, 707, 79

Donati, J.-F., Catala, C., Landstreet, J. D., & Petit, P. 2006, in Astronomical Society of the Pacific Conference Series, Vol. 358, Astronomical Society of the Pacific Conference Series, ed. R. Casini & B. W. Lites, 362

Duchêne, G. & Kraus, A. 2013, Annu. Rev. Astron. Astrophys., 51, 269

Dumusque, X., Pepe, F., Lovis, C., et al. 2012, Nature, 491, 207

Dupuy, T. J. & Liu, M. C. 2012, ApJS, 201, 19

Dupuy, T. J., Liu, M. C., & Ireland, M. J. 2009, ApJ, 692, 729

Duquennoy, A. & Mayor, M. 1991, A&A, 248, 485

Durkan, S., Janson, M., & Carson, J. C. 2016, ApJ, 824, 58

Ehrenreich, D., Lagrange, A.-M., Montagnier, G., et al. 2010, A&A, 523, A73

Eisenbeiss, T., Ammler-von Eiff, M., Roell, T., et al. 2013, A&A, 556, A53

Eisenhauer, F., Abuter, R., Bickert, K., et al. 2003, in Proc. SPIE., Vol. 4841, Instrument Design and Performance for Optical/Infrared Ground-based Telescopes, ed. M. Iye & A. F. M. Moorwood, 1548–1561

Ellerbroek, B. L. & Tyler, D. W. 1998, PASP, 110, 165

Elliott, P., Bayo, A., Melo, C. H. F., et al. 2014, A&A, 568, A26

Erdélyi, R. & Ballai, I. 2007, Astronomische Nachrichten, 328, 726

Fazio, G. G., Hora, J. L., Allen, L. E., et al. 2004, ApJS, 154, 10

Feigelson, E. D., Lawson, W. A., Stark, M., Townsley, L., & Garmire, G. P. 2006, AJ, 131, 1730

Fekel, F. C., Bopp, B. W., Africano, J. L., et al. 1986, AJ, 92, 1150

Fischer, D. A. & Valenti, J. 2005, ApJ, 622, 1102

Ford, E. B. & Chiang, E. I. 2007, ApJ, 661, 602

Foreman-Mackey, D., Hogg, D. W., Lang, D., & Goodman, J. 2013, PASP, 125, 306

Fortney, J. J., Marley, M. S., Saumon, D., & Lodders, K. 2008, ApJ, 683, 1104

Fried, D. L. 1965, Journal of the Optical Society of America (1917-1983), 55, 1427

Fried, D. L. 1966, Journal of the Optical Society of America (1917-1983), 56, 1380

Fried, D. L. 1978, Journal of the Optical Society of America (1917-1983), 68, 1651

Fritz, T., Gillessen, S., Trippe, S., et al. 2010, MNRAS, 401, 1177

Fruchter, A. S. & Hook, R. N. 2002, PASP, 114, 144

Fuhrmann, K. 2004, Astronomische Nachrichten, 325, 3

Fuhrmann, K. 2008, MNRAS, 384, 173

Fusco, T., Petit, C., Rousset, G., et al. 2006, in Proc. SPIE., Vol. 6272, Society of Photo-Optical Instrumentation Engineers (SPIE) Conference Series, 62720K

Gagné, J., Lafrenière, D., Doyon, R., Malo, L., & Artigau, É. 2014, ApJ, 783, 121

Gagné, J., Lafrenière, D., Doyon, R., Malo, L., & Artigau, É. 2015, ApJ, 798, 73

Gagné, J., Mamajek, E. E., Malo, L., et al. 2018, ApJ, 856, 23

Gaidos, E. J., Henry, G. W., & Henry, S. M. 2000, AJ, 120, 1006

Gammie, C. F. 2001, ApJ, 553, 174

Gardner, J. P., Mather, J. C., Clampin, M., et al. 2006, Space Sci. Rev., 123, 485

Gaudi, B. S. 2010, Microlensing by Exoplanets, ed. S. Seager, 79–110

Gaudi, B. S. 2012, Annu. Rev. Astron. Astrophys., 50, 411

Geballe, T. R., Knapp, G. R., Leggett, S. K., et al. 2002, ApJ, 564, 466

Getman, K. V., Feigelson, E. D., Luhman, K. L., et al. 2009, ApJ, 699, 1454

Gilles, L., Ellerbroek, B., & Véran, J.-P. 2006, in Proc. SPIE., Vol. 6272, Society of Photo-Optical Instrumentation Engineers (SPIE) Conference Series, 627236

Gillon, M., Triaud, A. H. M. J., Demory, B.-O., et al. 2017, Nature, 542, 456

Gliese, W. & Jahreiss, H. 1991, NASA STI/Recon Technical Report A, 92, 33932

Goldreich, P. & Tremaine, S. 1979, ApJ, 233, 857

Goldreich, P. & Tremaine, S. 1980, ApJ, 241, 425

Guyon, O., Pluzhnik, E. A., Kuchner, M. J., Collins, B., & Ridgway, S. T. 2006, ApJS, 167, 81

Hagan, J. B., Choquet, E., Soummer, R., & Vigan, A. 2018, ArXiv e-prints

Haisch, Jr., K. E., Lada, E. A., & Lada, C. J. 2001, ApJL, 553, L153

Hekker, S., Snellen, I. A. G., Aerts, C., et al. 2008, A&A, 480, 215

Herbst, W., Eislöffel, J., Mundt, R., & Scholz, A. 2007, Protostars and Planets V, 297

Hernández, J., Hartmann, L., Calvet, N., et al. 2008, ApJ, 686, 1195

Hippler, S., Bergfors, C., Brandner Wolfgang, et al. 2009, The Messenger, 137, 14

Holman, M. J. & Wiegert, P. A. 1999, AJ, 117, 621

Hormuth, F. 2007, AstraLux: High Angular Resolution Astronomy with an Electron Multiplying CCD Diploma Thesis University of Heidelberg

Hormuth, F., Brandner, W., Hippler, S., Janson, M., & Henning, T. 2007, A&A, 463, 707

Hormuth, F., Hippler, S., Brandner, W., Wagner, K., & Henning, T. 2008, in Proc. SPIE., Vol. 7014, Ground-based and Airborne Instrumentation for Astronomy II, 701448

Houck, J. R., Roellig, T. L., van Cleve, J., et al. 2004, ApJS, 154, 18

Hufnagel, R. 1966, Restoration of Atmospherically Degraded Images, 3, 11

Husser, T.-O., Wende-von Berg, S., Dreizler, S., et al. 2013, A&A, 553, A6

Ingrosso, G., Novati, S. C., de Paolis, F., et al. 2009, MNRAS, 399, 219

Isella, A., Carpenter, J. M., & Sargent, A. I. 2009, ApJ, 701, 260

Ivanova, N. & Taam, R. E. 2003, ApJ, 599, 516

Jackson, A. P., Davis, T. A., & Wheatley, P. J. 2012, MNRAS, 422, 2024

Janson, M., Bergfors, C., Brandner, W., et al. 2014a, ApJS, 214, 17

Janson, M., Bergfors, C., Brandner, W., et al. 2014b, ApJ, 789, 102

Janson, M., Bonavita, M., Klahr, H., & Lafrenière, D. 2012a, ApJ, 745, 4

Janson, M., Bonavita, M., Klahr, H., et al. 2011, ApJ, 736, 89

Janson, M., Brandner, W., Lenzen, R., et al. 2007, A&A, 462, 615

Janson, M., Brandt, T. D., Kuzuhara, M., et al. 2013, ApJL, 778, L4

Janson, M., Carson, J. C., Lafrenière, D., et al. 2012b, ApJ, 747, 116

Janson, M., Durkan, S., Hippler, S., et al. 2017, A&A, 599, A70

Janson, M., Hormuth, F., Bergfors, C., et al. 2012c, ApJ, 754, 44

Janson, M., Quanz, S. P., Carson, J. C., et al. 2015, A&A, 574, A120

Jeffries, R. D., James, D. J., & Bromage, G. E. 1994, MNRAS, 271, 476

Jenkins, J. M., Twicken, J. D., Batalha, N. M., et al. 2015, AJ, 150, 56

Jódar, E., Pérez-Garrido, A., Díaz-Sánchez, A., et al. 2013, MNRAS, 429, 859

Johansen, A., Youdin, A., & Klahr, H. 2009, ApJ, 697, 1269

Johnson, J. A., Aller, K. M., Howard, A. W., & Crepp, J. R. 2010, PASP, 122, 905

Johnson, J. A., Winn, J. N., Cabrera, N. E., & Carter, J. A. 2009, ApJL, 692, L100

Jurić, M. & Tremaine, S. 2008, ApJ, 686, 603

Karhunen, H. 1947, Ann. Acad. Science. Fenn, Ser. A.I. 37

Kasdin, N. J., Vanderbei, R. J., Spergel, D. N., & Littman, M. G. 2003, ApJ, 582, 1147

Kasper, M., Apai, D., Janson, M., & Brandner, W. 2007, A&A, 472, 321

Kaufer, A., Stahl, O., Tubbesing, S., et al. 1999, The Messenger, 95, 8

King, J. R., Villarreal, A. R., Soderblom, D. R., Gulliver, A. F., & Adelman, S. J. 2003, AJ, 125, 1980

Klahr, H. H. & Bodenheimer, P. 2003, ApJ, 582, 869

Koch, D. G., Borucki, W. J., Basri, G., et al. 2010, ApJL, 713, L79

Köhler, R. 2001, AJ, 122, 3325

Köhler, R. & Petr-Gotzens, M. G. 2002, AJ, 124, 2899

Köhler, R., Ratzka, T., Petr-Gotzens, M. G., & Correia, S. 2013, A&A, 558, A80

Konacki, M., Torres, G., Jha, S., & Sasselov, D. D. 2003, Nature, 421, 507

Konopacky, Q. M., Barman, T. S., Macintosh, B. A., & Marois, C. 2013, Science, 339, 1398

Konopacky, Q. M., Ghez, A. M., Duchêne, G., McCabe, C., & Macintosh, B. A. 2007, AJ, 133, 2008

Kouwenhoven, M. B. N., Goodwin, S. P., Parker, R. J., et al. 2010, MNRAS, 404, 1835

Kraus, A. L. & Hillenbrand, L. A. 2007, AJ, 134, 2340

Kraus, A. L., Ireland, M. J., Cieza, L. A., et al. 2014a, ApJ, 781, 20

Kraus, A. L., Ireland, M. J., Martinache, F., & Lloyd, J. P. 2008, ApJ, 679, 762

Kraus, A. L., Shkolnik, E. L., Allers, K. N., & Liu, M. C. 2014b, AJ, 147, 146

Kroupa, P. & Bouvier, J. 2003, MNRAS, 346, 369

Kuchner, M. J. & Traub, W. A. 2002, ApJ, 570, 900

Lafrenière, D., Doyon, R., Marois, C., et al. 2007a, ApJ, 670, 1367

Lafrenière, D., Jayawardhana, R., & van Kerkwijk, M. H. 2008, ApJL, 689, L153

Lafrenière, D., Jayawardhana, R., & van Kerkwijk, M. H. 2010, ApJ, 719, 497

Lafrenière, D., Jayawardhana, R., van Kerkwijk, M. H., Brandeker, A., & Janson, M. 2014, ApJ, 785, 47

Lafrenière, D., Marois, C., Doyon, R., Nadeau, D., & Artigau, É. 2007b, ApJ, 660, 770

Lagrange, A.-M., Bonnefoy, M., Chauvin, G., et al. 2010, Science, 329, 57

Lambrechts, M. & Johansen, A. 2012, A&A, 544, A32

Laughlin, G. & Bodenheimer, P. 1994, ApJ, 436, 335

Lawson, W. A., Crause, L. A., Mamajek, E. E., & Feigelson, E. D. 2001, MNRAS, 321, 57

Leconte, J., Soummer, R., Hinkley, S., et al. 2010, ApJ, 716, 1551

Lenzen, R., Hartung, M., Brandner, W., et al. 2003, in Proc. SPIE., Vol. 4841, Instrument Design and Performance for Optical/Infrared Ground-based Telescopes, ed. M. Iye & A. F. M. Moorwood, 944–952

Lépine, S. & Gaidos, E. 2011, AJ, 142, 138

Levison, H. F., Morbidelli, A., Gomes, R., & Backman, D. 2007, Protostars and Planets V, 669

Liebes, S. 1964, Physical Review, 133, 835

Lin, D. N. C. & Papaloizou, J. 1986, ApJ, 309, 846

Lloyd, J. P. 2011, ApJL, 739, L49

Lodders, K. 2004, ApJ, 611, 587

Loève, M. 1948, in Processes Stochastiques et Mouvement Brownien, ed. P. Lèvy (Paris: Hermann)

López Martí, B., Jiménez-Esteban, F., Bayo, A., et al. 2013, A&A, 556, A144

López-Santiago, J., Micela, G., & Montes, D. 2009, A&A, 499, 129

López-Santiago, J., Montes, D., Crespo-Chacón, I., & Fernández-Figueroa, M. J. 2006, ApJ, 643, 1160

Low, C. & Lynden-Bell, D. 1976, MNRAS, 176, 367

Luhman, K. L., Joergens, V., Lada, C., et al. 2007, Protostars and Planets V, 443

Luhman, K. L. & Steeghs, D. 2004, ApJ, 609, 917

Lyot, B. 1939, MNRAS, 99, 580

Macintosh, B., Graham, J. R., Barman, T., et al. 2015, Science, 350, 64

Macintosh, B. A., Graham, J. R., Palmer, D. W., et al. 2008, in Proc. SPIE., Vol. 7015, Adaptive Optics Systems, 701518

Makarov, V. V., Zacharias, N., & Hennessy, G. S. 2008, ApJ, 687, 566

Makarov, V. V., Zacharias, N., Hennessy, G. S., Harris, H. C., & Monet, A. K. B. 2007, ApJL, 668, L155

Maldonado, J., Martínez-Arnáiz, R. M., Eiroa, C., Montes, D., & Montesinos, B. 2010, A&A, 521, A12

Malo, L., Artigau, É., Doyon, R., et al. 2014, ApJ, 788, 81

Malo, L., Doyon, R., Lafrenière, D., et al. 2013, ApJ, 762, 88

Mamajek, E. E. & Bell, C. P. M. 2014, MNRAS, 445, 2169

Mamajek, E. E. & Hillenbrand, L. A. 2008, ApJ, 687, 1264

Marconi, A., Di Marcantonio, P., D'Odorico, V., et al. 2016, in Proc. SPIE., Vol. 9908, Ground-based and Airborne Instrumentation for Astronomy VI, 990823

Marengo, M., Megeath, S. T., Fazio, G. G., et al. 2006, ApJ, 647, 1437

Marengo, M., Stapelfeldt, K., Werner, M. W., et al. 2009, ApJ, 700, 1647

Marley, M. S., Fortney, J. J., Hubickyj, O., Bodenheimer, P., & Lissauer, J. J. 2007, ApJ, 655, 541

Marois, C., Doyon, R., Racine, R., & Nadeau, D. 2000, PASP, 112, 91

Marois, C., Lafrenière, D., Doyon, R., Macintosh, B., & Nadeau, D. 2006, ApJ, 641, 556

Marois, C., Lafrenière, D., Macintosh, B., & Doyon, R. 2008a, ApJ, 673, 647

Marois, C., Macintosh, B., Barman, T., et al. 2008b, Science, 322, 1348

Marois, C., Zuckerman, B., Konopacky, Q. M., Macintosh, B., & Barman, T. 2010, Nature, 468, 1080

Martin, R. G., Lubow, S. H., Pringle, J. E., & Wyatt, M. C. 2007, MNRAS, 378, 1589

Masciadri, E., Mundt, R., Henning, T., Alvarez, C., & Barrado y Navascués, D. 2005, ApJ, 625, 1004

Mason, B. D., Wycoff, G. L., Hartkopf, W. I., Douglass, G. G., & Worley, C. E. 2001, AJ, 122, 3466

Matsuo, T., Shibai, H., Ootsubo, T., & Tamura, M. 2007, ApJ, 662, 1282

Mayer, L., Quinn, T., Wadsley, J., & Stadel, J. 2002, Science, 298, 1756

Mayor, M., Marmier, M., Lovis, C., et al. 2011, ArXiv e-prints

Mayor, M., Pepe, F., Queloz, D., et al. 2003, The Messenger, 114, 20

Mayor, M. & Queloz, D. 1995, Nature, 378, 355

McCaughrean, M. J. & Stauffer, J. R. 1994, AJ, 108, 1382

McKee, C. F. & Ostriker, E. C. 2007, Annu. Rev. Astron. Astrophys., 45, 565

Meibom, S., Mathieu, R. D., & Stassun, K. G. 2006, ApJ, 653, 621

Mesa, D., Gratton, R., Zurlo, A., et al. 2015, A&A, 576, A121

Meshkat, T., Kenworthy, M. A., Quanz, S. P., & Amara, A. 2014, ApJ, 780, 17

Modigliani, A., Hummel, W., Abuter, R., et al. 2007, ArXiv Astrophysics e-prints

Moeckel, N. & Bate, M. R. 2010, MNRAS, 404, 721

Montes, D., López-Santiago, J., Fernández-Figueroa, M. J., & Gálvez, M. C. 2001a, A&A, 379, 976

Montes, D., López-Santiago, J., Gálvez, M. C., et al. 2001b, MNRAS, 328, 45

Montet, B. T., Bowler, B. P., Shkolnik, E. L., et al. 2015, ApJL, 813, L11

Mróz, P., Udalski, A., Skowron, J., et al. 2017, Nature, 548, 183

Müller, A., Roccatagliata, V., Henning, T., et al. 2013, A&A, 556, A3

Naef, D., Mayor, M., Beuzit, J. L., et al. 2004, A&A, 414, 351

Nagasawa, M., Ida, S., & Bessho, T. 2008, ApJ, 678, 498

Nakajima, T. & Morino, J.-I. 2012, AJ, 143, 2

Naoz, S., Farr, W. M., Lithwick, Y., Rasio, F. A., & Teyssandier, J. 2011, Nature, 473, 187

Naud, M.-E., Artigau, É., Malo, L., et al. 2014, ApJ, 787, 5

Newton, E. R., Irwin, J., Charbonneau, D., et al. 2017, ApJ, 834, 85

Nielsen, E. L. & Close, L. M. 2010, ApJ, 717, 878

Nielsen, E. L., Close, L. M., Biller, B. A., Masciadri, E., & Lenzen, R. 2008, ApJ, 674, 466

Oppenheimer, B. R. & Hinkley, S. 2009, Annu. Rev. Astron. Astrophys., 47, 253

Parker, R. J., Goodwin, S. P., Kroupa, P., & Kouwenhoven, M. B. N. 2009, MNRAS, 397, 1577

Parker, R. J. & Quanz, S. P. 2012, MNRAS, 419, 2448

Pecaut, M. J., Mamajek, E. E., & Bubar, E. J. 2012, ApJ, 746, 154

Pepe, F., Molaro, P., Cristiani, S., et al. 2014, Astronomische Nachrichten, 335, 8

Perets, H. B. & Kouwenhoven, M. B. N. 2012, ApJ, 750, 83

Perryman, M. 2011, The Exoplanet Handbook

Perryman, M. A. C., Brown, A. G. A., Lebreton, Y., et al. 1998, A&A, 331, 81

Petit, C., Sauvage, J.-F., Fusco, T., et al. 2014, in Proc. SPIE., Vol. 9148, Adaptive Optics Systems IV, 91480O

Pizzolato, N., Maggio, A., Micela, G., Sciortino, S., & Ventura, P. 2003, A&A, 397, 147

Plavchan, P., Werner, M. W., Chen, C. H., et al. 2009, ApJ, 698, 1068

Pollacco, D. L., Skillen, I., Collier Cameron, A., et al. 2006, PASP, 118, 1407

Pollack, J. B., Hubickyj, O., Bodenheimer, P., et al. 1996, Icarus., 124, 62

Pueyo, L., Crepp, J. R., Vasisht, G., et al. 2012, ApJS, 199, 6

Quintana, E. V., Barclay, T., Raymond, S. N., et al. 2014, Science, 344, 277

Racine, R., Walker, G. A. H., Nadeau, D., Doyon, R., & Marois, C. 1999, PASP, 111, 587

Raghavan, D., McAlister, H. A., Henry, T. J., et al. 2010, ApJS, 190, 1

Rameau, J., Chauvin, G., Lagrange, A.-M., et al. 2013, A&A, 553, A60

Rasio, F. A. & Ford, E. B. 1996, Science, 274, 954

Rauer, H., Catala, C., Aerts, C., et al. 2014, Experimental Astronomy, 38, 249

Rayner, J. T., Cushing, M. C., & Vacca, W. D. 2009, ApJS, 185, 289

Rayner, J. T., Toomey, D. W., Onaka, P. M., et al. 2003, PASP, 115, 362

Reid, I. N. & Gizis, J. E. 1997, AJ, 114, 1992

Reid, I. N. & Hawley, S. L. 2005, New light on dark stars : red dwarfs, low-mass stars, brown dwarfs

Riaz, B., Gizis, J. E., & Harvin, J. 2006, AJ, 132, 866

Ricker, G. R., Winn, J. N., Vanderspek, R., et al. 2014, in Proc. SPIE., Vol. 9143, Space Telescopes and Instrumentation 2014: Optical, Infrared, and Millimeter Wave, 914320

Riedel, A. R., Finch, C. T., Henry, T. J., et al. 2014, AJ, 147, 85

Rieke, G. H., Young, E. T., Engelbracht, C. W., et al. 2004, ApJS, 154, 25

Rigaut, F., Neichel, B., Boccas, M., et al. 2014, MNRAS, 437, 2361

Rizzuto, A. C., Ireland, M. J., & Kraus, A. L. 2015, MNRAS, 448, 2737

Roddier, F., Northcott, M., & Graves, J. E. 1991, PASP, 103, 131

Rouan, D., Riaud, P., Boccaletti, A., Clénet, Y., & Labeyrie, A. 2000, PASP, 112, 1479

Rousset, G., Lacombe, F., Puget, P., et al. 2003, in Proc. SPIE., Vol. 4839, Adaptive Optical System Technologies II, ed. P. L. Wizinowich & D. Bonaccini, 140–149

Samland, M., Mollière, P., Bonnefoy, M., et al. 2017, A&A, 603, A57

Sandler, D. G., Stahl, S., Angel, J. R. P., Lloyd-Hart, M., & McCarthy, D. 1994, Journal of the Optical Society of America A, 11, 925

Santos, N. C., Israelian, G., & Mayor, M. 2004, A&A, 415, 1153

Schlieder, J. E., Lépine, S., & Simon, M. 2012, AJ, 143, 80

Schneider, J., Dedieu, C., Le Sidaner, P., Savalle, R., & Zolotukhin, I. 2011, A&A, 532, A79

Schnupp, C., Bergfors, C., Brandner, W., et al. 2010, A&A, 516, A21

Shkolnik, E. L., Hebb, L., Liu, M. C., Reid, I. N., & Collier Cameron, A. 2010, ApJ, 716, 1522

Sivaramakrishnan, A., Koresko, C. D., Makidon, R. B., Berkefeld, T., & Kuchner, M. J. 2001, ApJ, 552, 397

Song, I., Schneider, G., Zuckerman, B., et al. 2006, ApJ, 652, 724

Song, I., Zuckerman, B., & Bessell, M. S. 2012, AJ, 144, 8

Soummer, R., Aime, C., & Falloon, P. E. 2003, A&A, 397, 1161

Soummer, R., Ferrari, A., Aime, C., & Jolissaint, L. 2007, ApJ, 669, 642

Soummer, R., Pueyo, L., & Larkin, J. 2012, ApJL, 755, L28

Sparks, W. B. & Ford, H. C. 2002, ApJ, 578, 543

Spergel, D., Gehrels, N., Breckinridge, J., et al. 2013, ArXiv e-prints

Spiegel, D. S. & Burrows, A. 2012, ApJ, 745, 174

Spiegel, D. S., Burrows, A., & Milsom, J. A. 2011, ApJ, 727, 57

Stauffer, J. R., Hartmann, L. W., Prosser, C. F., et al. 1997, ApJ, 479, 776

Stumpff, P. 1980, A&AS, 41, 1

Sumi, T., Abe, F., Bond, I. A., et al. 2003, ApJ, 591, 204

Sumi, T., Kamiya, K., Bennett, D. P., et al. 2011, Nature, 473, 349

Tabernero, H. M., Montes, D., & González Hernández, J. I. 2012, A&A, 547, A13

Tanaka, H., Takeuchi, T., & Ward, W. R. 2002, ApJ, 565, 1257

Tetzlaff, N., Neuhäuser, R., & Hohle, M. M. 2011, MNRAS, 410, 190

Thalmann, C., Desidera, S., Bonavita, M., et al. 2014, A&A, 572, A91

Todorov, K., Luhman, K. L., & McLeod, K. K. 2010, ApJL, 714, L84

Tokovinin, A. 2004, PASP, 116, 941

Toomre, A. 1964, ApJ, 139, 1217

Torres, C. A. O., Quast, G. R., Melo, C. H. F., & Sterzik, M. F. 2008, Young Nearby Loose Associations, ed. B. Reipurth, 757

Traub, W. A. & Oppenheimer, B. R. 2010, Direct Imaging of Exoplanets, ed. S. Seager, 111–156

Tsiganis, K., Gomes, R., Morbidelli, A., & Levison, H. F. 2005, Nature, 435, 459

Tuomi, M., Kotiranta, S., & Kaasalainen, M. 2009, A&A, 494, 769

Udalski, A. 2009, in Astronomical Society of the Pacific Conference Series, Vol. 403, The Variable Universe: A Celebration of Bohdan Paczynski, ed. K. Z. Stanek, 110

van Dam, M. A., Bouchez, A. H., Le Mignant, D., et al. 2006, PASP, 118, 310

van der Marel, R. P., Gerssen, J., Guhathakurta, P., Peterson, R. C., & Gebhardt, K. 2002, AJ, 124, 3255

van Leeuwen, F. 2007, A&A, 474, 653

Veras, D. & Armitage, P. J. 2004, MNRAS, 347, 613

Veras, D., Crepp, J. R., & Ford, E. B. 2009, ApJ, 696, 1600

Vernin, J. & Munoz-Tunon, C. 1994, A&A, 284, 311

Vican, L. 2012, AJ, 143, 135

Vigan, A., Bonavita, M., Biller, B., et al. 2017, A&A, 603, A3

Vigan, A., Patience, J., Marois, C., et al. 2012, A&A, 544, A9

Vogt, S. S., Allen, S. L., Bigelow, B. C., et al. 1994, in Proc. SPIE., Vol. 2198, Instrumentation in Astronomy VIII, ed. D. L. Crawford & E. R. Craine, 362

Wahhaj, Z., Cieza, L. A., Mawet, D., et al. 2015, A&A, 581, A24

Walter, F. M., Vrba, F. J., Mathieu, R. D., Brown, A., & Myers, P. C. 1994, AJ, 107, 692

Ward, W. R. 1997, Icarus., 126, 261

Werner, M. W., Roellig, T. L., Low, F. J., et al. 2004, ApJS, 154, 1

West, A. A., Morgan, D. P., Bochanski, J. J., et al. 2011, AJ, 141, 97

Wilson, O. C. 1941, ApJ, 93, 29

Wöllert, M., Brandner, W., Reffert, S., et al. 2014, A&A, 564, A10

Wolszczan, A. & Frail, D. A. 1992, Nature, 355, 145

Wright, N. J. & Drake, J. J. 2016, Nature, 535, 526

Wright, N. J., Drake, J. J., Mamajek, E. E., & Henry, G. W. 2011, ApJ, 743, 48

Youdin, A. N. & Goodman, J. 2005, ApJ, 620, 459

Zhou, G., Bayliss, D., Hartman, J. D., et al. 2014, MNRAS, 437, 2831

Zhou, G., Bayliss, D., Hartman, J. D., et al. 2015, MNRAS, 451, 2263

Zuckerman, B., Bessell, M. S., Song, I., & Kim, S. 2006, ApJL, 649, L115

Zuckerman, B., Rhee, J. H., Song, I., & Bessell, M. S. 2011, ApJ, 732, 61

Zuckerman, B. & Song, I. 2004, Annu. Rev. Astron. Astrophys., 42, 685

Zuckerman, B., Song, I., & Bessell, M. S. 2004, ApJL, 613, L65

Zuckerman, B., Song, I., Bessell, M. S., & Webb, R. A. 2001, ApJL, 562, L87

Zuckerman, B., Vican, L., Song, I., & Schneider, A. 2013, ApJ, 778, 5